RESIDUAL STRESS MEASUREMENT IN ENGINEERING COMPONENTS BY NEUTRON DIFFRACTION

BY

MARK. A.M. BOURKE

A thesis submitted for the degree of

Doctor of Philosophy

of the

University of London

and for the

Diploma of Imperial College

May 1990

Imperial College of Science, Technology & Medicine

Department of Mechanical Engineering

London SW7 2BX

Abstract

The presence of residual stress in engineering components can effect their mechanical properties and structural integrity. It can be introduced either by differential thermal behaviour or by regions of localised yielding caused by overstressing. The final stress state in a component is often a superimposition of the two effects, in practice resulting from heat treatment and forming processes such as extrusion or cold working. Generally compressive stresses are beneficial while tensile stresses can accelerate fracture mechanisms such as fatigue crack growth, stress corrosion cracking and intergranular failure. Since residual stresses can be close to the yield stress a knowledge of their magnitude and direction can be crucial in lifetime assessments.

By measuring the interplanar crystalline spacing, neutron diffraction can give non destructive strain measurements in the interior of metallic engineering components. This thesis presents developments to improve both the spatial and strain resolution of the neutron diffraction technique. Measurements taken on a continuous neutron source are contrasted with those taken on a pulsed source and their respective advantages examined.

Particular attention has been paid to measurements in regions of steep stress gradients. The deconvolution of strain and position due to finite sampling volumes is discussed. Specimen manipulation has been addressed by the installation of a modular translation and rotation system. The implication of prior plastic deformation on the results is also examined.

Experimental results have been obtained for Aluminium, Steel and metal-matrix composite components. These include autofrettaged tubing, pre-stressed single edge notch bend specimens, peened plate and sections of rail. Where possible comparisons are made with conventional strain measurements. Computational predictions were made using finite element and boundary element methods. All results are discussed in the context of fracture and failure models.

To Ania, Tish, Lucy and my parents

Acknowledgements

First and foremost the author would like to thank his supervisor Professor George Webster for his enduring help and support during the course of this research. Thanks are are also due to Dr David Smith, Dr Kamran Nikbin, Dr Roger Allen, Dr Steve Hull and Dr Peter Webster.

The translation of this document from "wordy" to acceptable was effected with the, much appreciated, help of Hugh MacGillivray and thanks are also due to Sheila Webster for being "out" at a vital moment.

Finally: Thanks Lucy for a sterling job on the photocopier and for putting up with me in the darkest periods of my creative phase.

Table of Contents

		Page Number
Title Page		1
Abstract		2
Dedication		3
Acknowledgements		4
Contents		5
Notation		9
Chapter 1 : The origins and measurement of residual stress		
1.1	Introduction	10
1.2	Background	10
1.3	Origins of residual stress	12
1.4	Superposition principle and yield criteria	14
1.5	Fracture mechanics concepts	15
1.6	Conventional measuring techniques	17
1.7	Discussion	19
Figures 1.1 to 1.3		21-22
Chapter 2 : Principles of neutron scattering stress measurement		
2.1	Introduction	23
2.2	Neutron characteristics	23
2.3	Neutron formalism	26
2.4	Diffraction from metals and the Bragg equation	27
2.5	Powder diffraction	28
2.6	Lattice strain	28
2.7	Unstressed lattice spacing	30
2.8	Theory of stress measurement	31
2.9	Different stress types	32
2.10	Peak broadening	33
2.11	Discussion	34
Appendix A2.1	Neutron attenuation in materials	
A2.1.1	Linear attenuation coefficient	35
A2.1.2	Scattering from a single element	36
A2.1.3	Attenuation coefficient for an alloy	38
A2.1.4	Application to a nickel base alloy	38

Appendix A2.2

	Neutron detection	39
	Figures 2.1 and 2.2	41-42
	Figure A2.1	43

Chapter 3 : Calibration using a uniaxial stress rig

3.1	Introduction	44
3.2	Background	44
3.3	Theory	45
3.4	Stress rig description and operation	47
3.5.1	Mild steel results	48
3.5.2	Mild steel discussion	49
3.6.1	Metal matrix composites	50
3.6.2	Results for an Al SiC composite	52
3.6.3	Discussion of composite results	53
3.7	Discussion and suggestions	54
3.8	Conclusions	56
	Figures 3.1 to 3.10	58-69

Chapter 4 : Equipment development at the I.L.L.

4.1	Introduction	70
4.2	General	70
4.3	The high resolution powder diffractometer D1A	72
4.4	Definition of a sampling volume	72
4.5	Effect of the input aperture position on the beam profile	74
4.6	Calibration using a powder cell	75
4.7	Manipulation system	
4.7.1	Specification	77
4.7.2	Hardware	77
4.7.3	Control system	78
4.8	Data processing	79
4.9	Recommendations	80
4.10	Conclusions	81
	Figures 4.1 to 4.16	83-95

Chapter 5 : Measurement in cracked autofrettaged rings

5.1	Introduction	96
5.2	Background	96
5.3	Specimens	97

5.4	Experimental measurements	98
5.5	Boundary integral method	101
5.6	Application of boundary integration to 9RDMA	103
5.7	Discussion	104
5.8	Conclusions	105
Figures 5.1 to 5.13		107-118

Chapter 6 : Residual stress distributions in cracked beams

6.1	Introduction	119
6.2	Background	119
6.3	Specimens	121
6.4	Experimental results	
6.4.1	Deformation response under reverse yield conditions	122
6.4.2	Sampling volume and θ_0 determination	123
6.4.3	Measurements ahead of the crack tip	124
6.4.4	Measurements normal to the crack tip	125
6.4.5	Plastic zone size	125
6.5	Finite element (FE) prediction	
6.5.1	FE description	126
6.5.2	Residual stresses	127
6.5.3	Plastic region	127
6.6	Discussion	128
6.7	Recommendations	130
6.8	Conclusions	130
Figures 6.1 to 6.24		132-146

Chapter 7 : Residual stresses in railway rails

7.1	Introduction	147
7.2	Background	147
7.3	Residual stress in rails	148
7.4	Failure mechanisms	149
7.5	Strain gauge results	150
7.6	Cold expanded bolt hole	151
7.7	Representative rail specimen sizes	153
7.8	Survey of an unused rail	
7.8.1	Overview	154
7.8.2	Stress free θ_0 for rail specimens	155
7.8.3	Longitudinal variations	156
7.8.4	Measurement in a longitudinal plate	157

7.8.5 Measurement in a transverse slice 157
7.8.6 Measurement in a gauge corner specimen 158
7.9 Conclusions 159
Figures 7.1 to 7.20 160-177

Chapter 8 : Strain measurements at ISIS
8.1 Introduction 178
8.2 Background 178
8.3 Instruments and profile refinement 180
8.4 Samples 182
8.5 Collimation and manipulation 183
8.6 HRPD results 184
8.7 POLARIS results 186
8.8 Comparison with D1A and discussion 188
8.9 Recommendation for futher study 189
8.10 Conclusions 190
Figures 8.1 to 8.18 191-207

Chapter 9 : Additional measurements
9.1 Introduction 208
9.2 Measurements in a shot-peened plate
9.2.1 Shot-peening 208
9.2.2 Experimental results 209
9.2.3 Discussion of peened plate 212
9.3 Compact tension (CT) specimen
9.3.1 Introduction 212
9.3.2 Experimental results 213
9.3.3 Discussion of CT specimen 214
9.4 Conclusions 215
Figures 9.1 to 9.9 216-223

Chapter 10 : Concluding remarks
10.1 General discussion 224
10.2 Recommendation for further work 225
10.3 Overall conclusions 227
Figures 10.1 and 10.2 229-230

References 231-241

Notation

a	Crack length
a_0	Lattice parameter
d_{hkl}	Interplanar lattice spacing
d_0	Unstrained lattice spacing
E	Young's modulus
hkl	Miller indices
H	Peak height
I	Peak intensity
K_I	Opening mode stress intensity factor
K_{IC}	Critical stress intensity factor
K_{eff}	Effective stress intensity factor
K_i	Incident wave vector
K_f	Scattered wave vector
K_{LS}	Stress intensity due to applied load
K_{RS}	Stress intensity due to residual stress
r_p	Plastic zone radius
R	Instrumental resolution
S_{ij}	Single crystal elastic compliances
t	Time of flight
t_o	Time of flight for unstrained material
W	Peak width
ε	Strain
λ	Wavelength
μ	Linear attenuation coefficient
ν	Poisson's ratio
σ^{LS}	Loading stress
σ^{RS}	Residual stress
σ_i	Principal stress (i)
σ_{eq}	Equivalent stress (Tresca or Von-Mises)
σ_a	Nuclear scattering cross section
σ_s	Nuclear absorption cross section
σ_{xyz}	Stress in x,y or z direction
θ	Diffraction scattering angle
θ_0	Scattering angle for unstrained material
K_B	Boltzmann's constant
h	Planck's constant
N_A	Avogadros number

CHAPTER 1

The origins and measurement of residual stress

1.1 Introduction

Most materials in engineering applications are subject to residual stresses. These are the self equilibriating stresses which exist in a free body, under uniform thermal conditions in the absence of any external forces. They are sustained either by regions of inhomogeneous plastic deformation or by incompatibility resulting from thermal effects. Their presence can be beneficial or detrimental according to their sign and magnitude because they affect the probability and mechanisms of failure in loaded components. Conventional techniques are available for measuring residual stress but are subject to a variety of limitations. Neutron diffraction offers a non-destructive alternative to conventional measurements. In this chapter the origins and conventional measurement of residual stress are described. A brief outline of fracture mechanics is given, showing where residual stresses enter into calculations of failure and lifetime prediction.

1.2 Background

Metals are polycrystals consisting of grains which are usually of random alignment. The crystal lattice of an individual grain is, for the most part, a regular array of atoms. However, in real materials there are irregularities or dislocations. When a metal is loaded beyond a limiting value the dislocations respond to shear stress by moving in a variety of ways. The process is called slip and dislocations move to reduce the energy of a stressed system by allowing atoms in adjacent planes to slide over one another through an interatomic distance. Under these circumstances plastic deformation will occur, in which volume is conserved (Poisson's ratio 0.5). The shear stress in an annealed single crystal, at which plastic deformation first occurs is called the critical resolved shear stress (CRSS) and is dependent on the crystal structure and direction within the lattice (Reid, 1973).

Examination of the stress-strain curves for different materials indicates that plastic deformation is governed by many variables including strain rate, prior plastic deformation, crystal structure, stress state and temperature. The best known effect is

due to work hardening which results from deformation hindering the movement of dislocations (which are trapped at grain boundaries) and hence a progressively higher force is needed to move the remainder. Work hardening at crack tips can be substantial. Since slip is partly thermally activated, plasticity is also affected by temperature and at low temperatures the yield strength of body centered cubic steels increases dramatically giving rise to a ductile to brittle transition temperature.

Not all directions in a lattice are susceptible to slip under an applied load. In grains where the CRSS is not attained, the strain due to an applied load will remain elastic and will be recoverable on unloading. This contrasts with grains which have been plastically strained and which will maintain a permanent set. Inhomogeneous plastic deformation of a material is the main cause of residual stresses and is discussed in 1.3.

The state of stress in a metal is related to its metallurgy and crystallinity. For a complete description of the processes contributing to residual stress a metal cannot be treated as a homogeneous material. However, most design applications do consider it as homogeneous and models of material behaviour must take this into account. The most important material parameters pertinent to residual effects are the yield stress and compliance. The stress at which permanent deformation is first induced when a material is subjected to a load is called the yield stress. It is usually determined by a simple uniaxial test but may differ in compression or tension. It can be affected by the past history of a component, as for example occurs due to the Bauschinger effect (Zyczkowski, 1981). Beyond the yield stress the plastic strain caused by deformation is usually larger than the elastic strain and there is no simple linear relationship between stress and strain.

Metals can sustain internal stresses over three distinct scales (Macherauch, 1986) which are described in chapter 2. However, for practical purposes they can be split into macro and microstresses. The former vary over dimensions comparable to those of the component while the latter vary in and around individual grains. Although both are relevant to material failure and can coexist in a material, most of the work in this thesis concerns macrostresses. In either case the associated forces and moments must balance

over plane sections, though it is difficult to account for microstresses in real analyses.

A component can fail by brittle or ductile fracture and the mode of failure is affected by the state of stress, such as plane strain or plane stress. Regions where brittle failures are likely include notch tips where a triaxial tensile stress can exist or the centre of thick samples where high constraint, plane strain conditions prevail. The likelihood of failure at any point depends on the complete state of stress which results from a combination of the residual and applied contributions. The yield stress is incorporated into failure calculations by defining yield criteria.

The origins of residual stress in materials are complex and their effects touch many different fields. These include the initiation and growth of fatigue cracks (Berns, 1986), stress corrosion (Harris, 1982) and load bearing characteristics. Particular examples of problems associated with residual stress include the distortions which result from stress redistribution during sectioning or the exposure of regions of tensile residual stress during machining which constitute a fatigue risk. There have been many review articles and conferences in the field over the last ten years. In this chapter a necessarily brief review is made of the origins, uses and measurements of residual stresses.

1.3 Origins of residual stress

The origins of residual stress are associated with inhomogeneous plastic deformation, inhomogeneous thermal treatment or volume incompatibility. When one region of a body is plastically extended with respect to another, and elastically strained material is constrained then a residual stress distribution is produced. For example, in a rolled plate friction at the rollers may cause an extension of the surface relative to the interior leaving a compressive stress at the surface which will diminish with depth. The nature of the stress profile will depend on the plate thickness, degree of reduction and roll size. Most processing methods cause localised deformation of the surface and lead to residual stresses (McMeeking, 1982). Other examples of fabrication processes which induce residual stress include machining, grinding, turning, milling, planing, drilling, drawing, forging, pressing and spinning.

One well-characterised example of residual stress due to plastic deformation is a bending beam. Consider a beam which is deformed to produce plastic yield in

compression and tension as shown in figure 1.1. On removal of the bending load, the interior of the beam is prevented from relaxing by the plastically deformed regions. A compressive stress will be induced near surface A and a tensile stress near surface B. The stress distributions in bending beams can be predicted and have been examined using neutron diffraction by Allen (1986). The case of a plastically deformed cracked beam is discussed in chapter 6.

In most cases inhomogeneous plastic deformation is induced by bending however residual stresses can occasionally be caused by homogeneous deformation. For example in a uniaxial tensile test if plastic deformation occurs and dislocations are trapped near the edges of the specimen, preferential work hardening will occur in the skin. This will lead to an increase in the yield stress at the surface and consequently the interior of the specimen will strain more than the skin. On relaxation of the load a tensile stress will result in the surface, balanced by a compressive stress in the interior.

The second major cause of residual stress is inhomogeneous heating and cooling in a solid object. An important example concerns the stresses produced by welding. Contraction of molten weld metal during solidification is resisted by the colder surrounding material. In most cases a biaxial stress state is induced as the weld contracts, with stresses lying across and perpendicular to the welding bead (Smith, 1988). Alternatively, rapid thermal quenching can "freeze" a surface faster than the interior of a component, which will cool more slowly and during the subsequent contraction a compressive stress will be produced at the surface.

Thermal effects are often superimposed on the third major cause of residual stress, which is due to volume incompatibility. Phase transformations, such as martensitic hardening, can be associated with a dilatation of the crystalline lattice. Surrounding material will be strained and the effect can be sufficient to cause localised plastic yield in or near the intrusive phase. Similarly, composite materials consisting of two phases with different thermal coefficients can contain residual stresses on cooling from fabrication temperatures. Thermal and transformation effects are discussed by Ericsson (1982) who showed that although experimentally they are too rapid to follow, computer models can be used to predict material behaviour.

Transformation hardening is a standard technique for improving material qualities. For example, during a martensitic transformation, resulting from the quenching of steel, carbon atoms can be trapped in interstitial positions and strain the lattice leaving a hard brittle material. Phase transformations are closely dependent on cooling rates and tempering is often used to relieve residual stresses.

In the previous examples the residual stresses are a by-product of the fabrication or forming of a component. However processes are often applied to introduce a residual stress which will be beneficial for a particular application. Examples include autofrettage which is described in chapter 5, rapid quenching of the interior of a pipe and cold expansion of bolt holes (chapter 7). One common and easily applied technique is shot peening, in which a component is bombarded by small shot at high speed causing plastic deformation of the surface layer. The surface is extended relative to the interior but is also constricted by it (figure 1.2). The resulting compressive stress at the surface decreases to zero and is balanced by a tensile stress in the interior of smaller magnitude than the maximum at the surface. The stress distribution depends on parameters which include the relative hardness of the shot and workpiece, the shot velocity, size and shape (Wohlfahrt, 1982). Compressive stress at a surface is often important for the inhibition of fatigue crack growth and initiation. Measurements made on a peened plate are described in chapter 9.

1.4 Superposition principle and yield criteria

To incorporate residual stresses into stress analyses the superposition principle is assumed. This states that the stress due to two or more loads acting together is equal to the sum of the stresses due to each load acting separately. Provided a body behaves elastically the stress at any point in the body is the sum of the applied and residual contributions. Thus, if the principal axes of a residual stress state, σ^{RS} coincide with those of a loading stress, σ^{LS} the total effective stress, σ^{TOT} may be written,

$$\sigma_i^{TOT} = \sigma_i^{LS} + \sigma_i^{RS} \qquad (1.1)$$

with i=1,2,3. (Macherauch,1986)

Deviation from simple elastic behaviour occurs at the yield stress, σ_y but if it is

not clearly identifiable a proof stress can be used instead. A proof stress is defined as a stress which produces 0.1 or 0.2% permanent strain. The yield or proof stress are usually determined by a uniaxial test, but the stress at which plastic deformation occurs depends on the stress state in three dimensions due to the principal stresses. The uniaxial yield or proof stress may be related to the three dimensional case by an "equivalent stress" which is defined in terms of the principal stresses.

The Tresca or maximum shear stress criterion defines an equivalent stress σ_{eq} for plastic flow as:

$$\frac{\sigma_{eq}}{2} = \frac{\sigma_1 - \sigma_2}{2} \text{ or } \frac{\sigma_2 - \sigma_3}{2} \text{ or } \frac{\sigma_3 - \sigma_1}{2} \qquad (1.2)$$

Alternatively the Von Mises yield criterion is deduced in terms of shear strain energy and defines an equivalent stress by:

$$\sigma_{eq} = \frac{1}{\sqrt{2}}\left[(\sigma_1 - \sigma_2)^2 + (\sigma_2 - \sigma_3)^2 + (\sigma_3 - \sigma_1)^2 \right]^{\frac{1}{2}} \qquad (1.3)$$

In either case plastic deformation is assumed to occur when the maximum value of the equivalent stress at any point in a body exceeds the yield stress. Residual stresses can be included in the yield criteria by using the superposition principle. Thus the stresses σ_i in equations 1.2 and 1.3 can be replaced by σ_i^{TOT}.

1.5 Fracture mechanics concepts

Residual stress effects fatigue problems because crack initiation and growth are inhibited in the presence of a compressive stress but accelerated by a tensile stress. Cracks can propagate under cyclic compressive applied loading only if a tensile residual stress maintains some or all of the fatigue cycle in a tensile regime. Fracture mechanics has been developed to predict the behaviour of cracked bodies in the presence of direct, residual or cyclic stresses.

The presence of a crack in a body acts as a stress raiser. In principle the stress at a crack tip tends to infinity however in practice, subject to the amount of plasticity, the stress can be several times greater than the bulk average. The stress magnification at the crack tip is defined by a stress intensity factor, K_I:

$$K_I = Y \sigma (\pi a)^{\frac{1}{2}} \qquad (1.4)$$

where σ is a measure of the applied stress

a is half the crack length for an internal crack or the crack length for an external crack.

Y is a configuration factor.

The subscript I on the stress intensity factor indicates that the cracking is opening mode I, which is the simplest geometry. Sliding and tearing modes also exist denoted by the suffixes II and III (figure 1.3). For the simplest case of an infinite plate under mode I loading Y=1, but in general is dependent on the specimen geometry and loading and can be obtained from reference handbooks (Rooke, 1976). In equation 1.4 as the stress increases there is a proportional increase in K_I until fracture occurs at a critical stress intensity termed the fracture toughness. A lower limit exists for plane strain conditions (maximum constraint) and is identified by K_{IC}. In energy terms the lower limit of the fracture toughness denotes the point at which the total energy of the stressed system can be reduced by extending the crack.

Beyond the plastic zone, the stress ahead of a crack tip is expected to show an $r^{-1/2}$ dependence where r is the distance from the crack tip with a constant of proportionality, K (equation 6.1). The applicability of linear elastic fracture mechanics (LEFM) depends on the degree of plasticity. For small plastic zones estimates of the plastic zone size at a crack tip for plane stress and plane strain are given in equations 6.4 and 6.5. The shape and blunting of a crack are critical, since a rounded crack may not magnify a stress sufficiently to break bonds even though local plasticity can occur. All problems involving cracks are governed by K although the criteria used to define failure may not necessarily be based on linear elastic fracture mechanics. The solution for K is important since this is where residual stresses enter an analysis. In LEFM nothing is specified about the micro-mechanism of fracture.

Fatigue crack growth kinetics are governed by the level of the stress intensity, K and by the stress intensity range ΔK applied during the fatigue process. Residual stresses modify both according to superposition. In fatigue analyses the time for a crack

to become unstable and result in failure is often the desired result. The failure criterion which determines the critical crack size depends on the operating conditions but is usually defined in terms of exceeding a critical value of the stress intensity factor. The effective stress intensity factor, K_{eff} in a cracked body subject to applied and residual stresses is the sum of the stress intensity factor due to each stress:

$$K_{eff} = K_{LS} + K_{RS} \tag{1.5}$$

In regions of compressive stress K_{RS} will be negative, and although in the absence of an applied load this is of no physical significance, it reduces K_{eff} and can inhibit the growth of fatigue cracks under cyclic loading. Numerical and analytical procedures have been developed for incorporating residual stresses into predictions of fatigue strength (Stacey, 1984 or Webster, 1989a). The fracture mechanics formalism can be extended to include other phenomena such as the effect of residual stress on stress corrosion cracking (Harris, 1982).

1.6 Conventional measuring techniques

The need for measurement and monitoring of residual stress was recognised long before neutron diffraction was applied to the problem and there are a variety of conventional techniques available. The most widely used are strain gauging and X-ray diffraction, although other techniques relying on ultrasonic, magnetic and optical principles are available. In all cases the measurements are underpinned by the basic themes of linear elasticity and stresses are inferred from measurements of strain. Particularly in the case of diffraction, care must be taken to distinguish the macroscopic or microscopic origin of the measured stresses. One problem which is common to all techniques is the identification of completely stress free material for calibration purposes.

Strain gauge methods infer the residual stress by removing a portion of material and noting the relaxation which occurs at a position in close proximity. In blind hole drilling a gauge rosette is attached to a surface and a small hole is drilled at its centre (Beaney, 1973). The introduction of the hole causes stress redistribution and at the hole surface the radial stress must reduce to zero. By noting the strain distortion which occurs around the hole after the surrounding material has relaxed and assuming elastic

behaviour, the original stresses can be inferred. Typically the hole is 1-2mm in diameter with a depth equivalent to or greater than its diameter. The component is usually thick compared to the hole diameter.

The technique is semi-destructive since the hole is comparatively small and can be filled after the measurement. A possible source of error is the possibility of plastic deformation due to the action of the hole as a stress concentrator. Depending on the stress state near the hole a stress as small as one third of the yield stress could induce localised plastic yielding which would contribute to the distortion around the hole and induce an error in the calculated stress (Beaney, 1973). Other errors can result from a failure to achieve concentricity with the center of the strain gauge rosette and stresses introduced into the material by the drilling operation itself. This has been the subject of considerable attention and air abrasion using a high pressure jet containing fine abrasive particles offers a favourable method for forming the holes without introducing unwanted stress effects (Bynum, 1981). Interpretation of results from blind hole drilling can also be complicated by steep stress gradients in the region of the hole. Only a partial relaxation of the original strains around the hole is recorded thus any of the above errors can seriously affect the results.

An alternative to hole drilling is sectioning which is completely destructive. In the Sachs boring method which is applicable to thick cylinders, successive layers are removed while measuring the relaxation on the opposing face after each cut (Denton, 1966). An extrapolation from the relaxation due to each cut is made to infer the original stress state. The material is removed by boring or electropolishing and an assumption concerning the principle axes is required. The errors are cumulative and are largest at the surface near the strain gauges.

X ray methods described by Hauk (1982) rely on the same physical principles as neutron diffraction by using the crystalline lattice spacing as an "atomic strain gauge". The strain is inferred from the change in position of Bragg reflections. It is convenient but can only be applied at surfaces because X rays rarely penetrate more than 100 microns into a metal. In common with all other techniques it is primarily used to measure elastic strain but is also qualitatively sensitive to plastic deformation. One

major advantage of diffraction techniques can be for studies of two phase materials, since they allow the determination of the strain tensor in each phase, however in the case of X rays depth profiles can only be obtained by removing surface layers using electropolishing or etching. X ray measurements can be complicated by shear stresses and texture effects.

Ultrasonic techniques measure residual stress by recording its effect on the propagation of sound waves in a material (Clark, 1986). Residual stresses effect the elastic constants in a material which alters the propagation velocity, and by varying the frequency the sampling depth can be moved. Microstructural effects, texture and plastic deformation all inhibit the technique. Magnetic techniques rely on the effect of local strain centers which impede the magnetization of a material during the application of an electric field (Theiner, 1986). This causes oscillations in the magnetization which can be detected by a sensitive probe.

1.7 Discussion

The introduction of residual stress in components is almost inevitable during fabrication processes. Its origins are diverse and since avoidance is rarely possible, prediction, control and measurement are important. Processes are often applied to attempt to eliminate residual effects or to superimpose a beneficial treatment over them. However the stress state is not necessarily stable and can alter due to fatigue, wear or ageing processes. The final state of a material is governed by a mixture of macroscopic and microscopic stresses which are limited by equilibrium considerations of force and moment in free bodies. The effects are demonstrable in a variety of fatigue and fracture processes and on the load bearing capability under the influence of a direct stress. In particular fatigue cracks can be arrested by a compressive residual stress field. Fracture mechanics models can and must be modified to include residual stresses for reliable fatigue lifetime assessments.

Conventional measuring techniques are available but suffer from a variety of drawbacks. Strain gauge measurements present an average response of the stress strain curve for many grains. X rays can only penetrate into the surface layers of a sample which may not be representative of the interior. Neutron diffraction which is described

in the following chapter offers a non-destructive bulk measurement of crystalline strain at a granular level. It requires a minimum of inferences concerning the state of stress at the measuring position and is useful for validating conventional methods or computer predictions. It may also be used for complicated shapes where conventional methods are impeded.

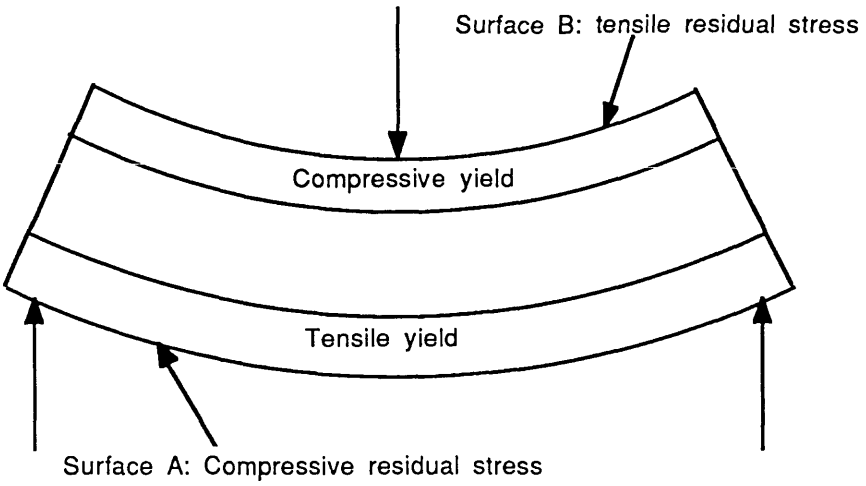


Figure 1.1: Yield in a bending beam

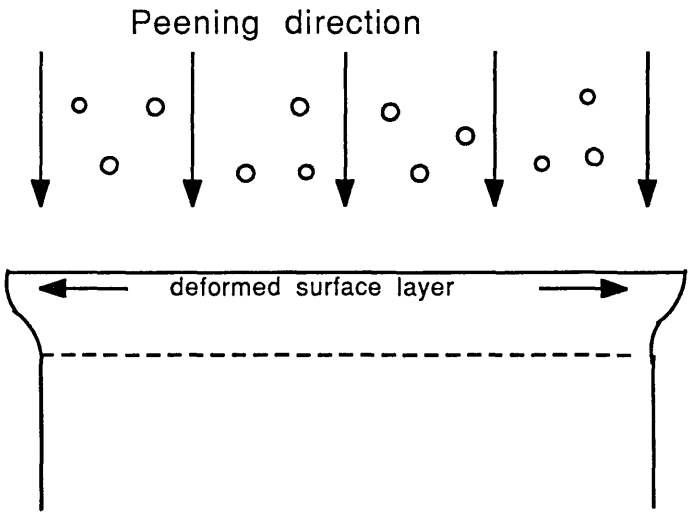


Figure 1.2: Example of shot peening

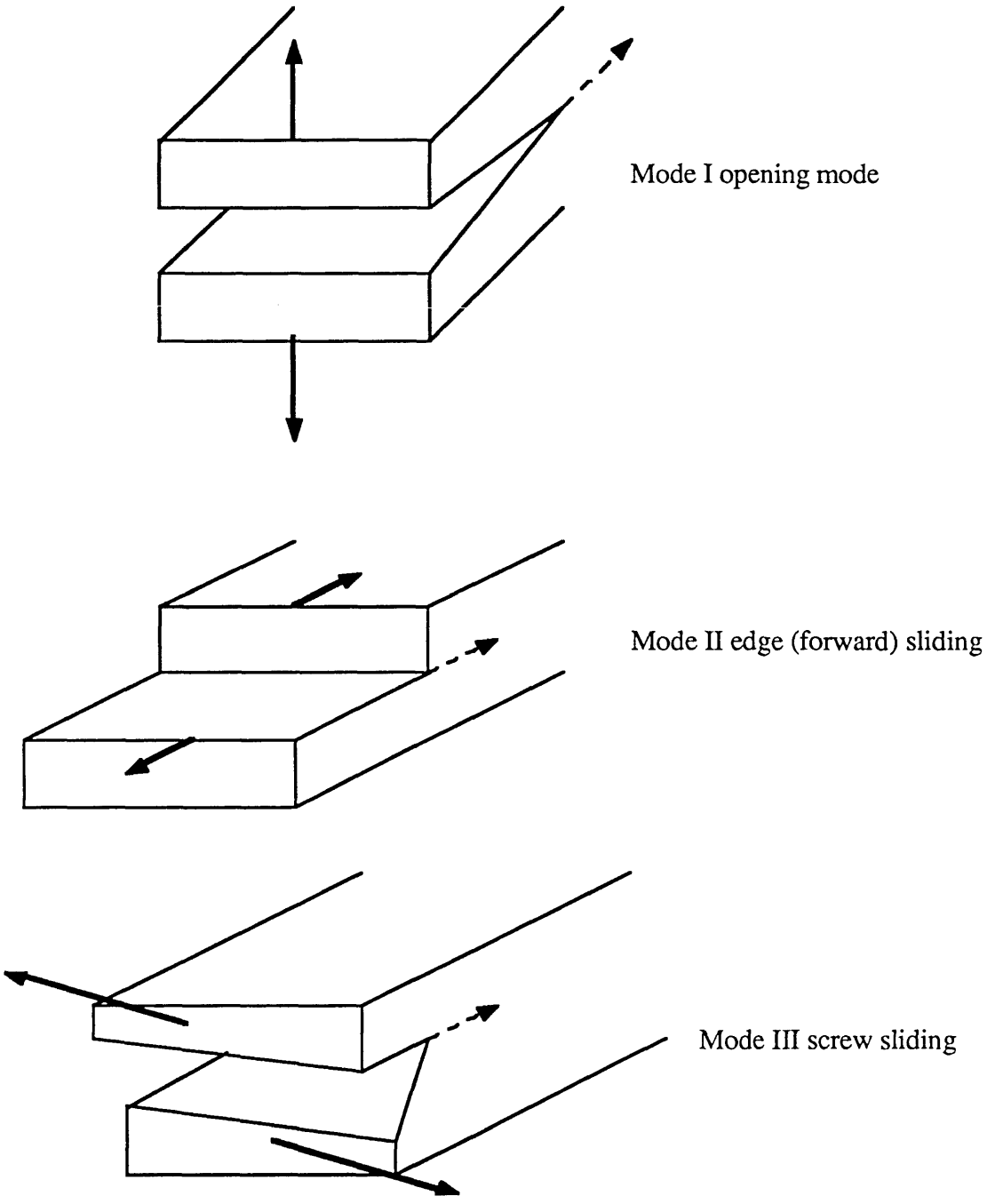


Figure 1.3: Fatigue failure modes

CHAPTER 2

Principles of neutron scattering stress measurement

2.1 Introduction

The field of neutron scattering is well developed and includes many applications other than stress measurement. Before examining the application of neutrons to residual stress the characteristics which make them appropriate for materials examination are described. The different scattering techniques which have been or could be used in engineering science are listed briefly as well as the processes by which neutrons may be produced and the procedures which are adopted to select neutrons for different measurements. Although the literature describing neutron scattering dates back to the 1930's, the earliest references to stress measurement by neutron diffraction date from the early 80's and the field currently represents a small but increasing activity at most neutron sources.

2.2 Neutron characteristics

Neutrons are atomic particles of no electric charge, no electric field and of rest mass $1.675\ 10^{-27}$kg. They possess a spin of 1/2 and a magnetic moment by which they can couple with magnetic nuclei. The previous characteristics are all associated with particles, however neutrons may also be treated as a wave motion with a wavelength related to their energy. They are produced by nuclear reactions in which bound atomic neutrons are freed from nuclei. Several different reactions exist by which neutrons may be produced but only fission and spallation are employed to produce beams of neutrons for materials science.

The usefulness of neutrons as a material probe results from the nature of their interaction with atomic nuclei which is by the strong nuclear force. The short range of the strong nuclear force limits the interaction probability of an incident neutron with a target nucleus. Most of the volume in a solid is not occupied by matter hence neutrons penetrate more effectively than other radiations which may, in the case of X rays, interact with the electrons around the nucleus. Since the interaction is with the nucleus the range of the scattering vector is not limited by an atomic form factor and neutrons can

penetrate comparatively deeply into most materials. The constraints on penetration in solid materials are given in Appendix A2.1.

Most neutrons which impinge on a material are transmitted without interaction. However some are scattered. There are three distinct origins of neutron scattering which are; small angle neutron scattering (SANS), diffraction and inelastic scattering. SANS occurs when there is a disparity in the scattering characteristics between a matrix and a defect within it. It is determined by the contrast factor which expresses the difference in scattering characteristics of the medium and the inhomogeneity. Diffraction is an elastic scattering process resulting from the periodic three dimensional arrangement of atoms in crystals. It forms the basis for neutron stress measurement and is discussed in section 2.4. Inelastic scattering occurs when both momentum and energy of the incident neutrons are exchanged with the nuclei in the specimen.

Coherent scattering processes give information concerning the spatial and temporal correlations of atoms in a lattice while incoherent scattering results from translational, rotational and vibrational atomic motion, not necessarily in a solid. Thus inelastic scattering can, for example, provide information about excitational states or the presence of adsorbed material.

For completeness the neutron radiography technique can also be mentioned, in which a transmitted image is obtained. Contrast is produced by the different scattering characteristics of atoms in the specimen, although artificial enhancement of features of interest can be obtained by selective introduction of a strong scatterer. Radiography is used extensively for non-destructive detection of defects.

Neutrons are produced by a variety of nuclear processes which include fission, fusion, photofission, charged particle reactions and spallation, the latter two being based on accelerator technology. Until recently most neutrons for scattering science have been produced by fission in research reactors. However pulsed spallation sources (discussed in chapter 8) have recently begun to make a contribution and offer some advantages over reactor sources. The initial energy of neutrons produced in nuclear reactions is measured in MeV and they have wavelengths too small to be of use for diffraction.

Most scattering experiments need larger wavelengths and diffraction, in particular, requires wavelengths comparable to the interatomic distance of condensed matter. Consequently the energy (velocity) of the epithermal neutrons must be reduced. This is performed with a moderator.

Moderators are inherent to all reactors since a chain reaction is only possible when sufficient neutrons are slowed to energies where the probability of fission is large. Typically moderators are light or heavy water (hydrogenous material) or graphite. These are light atoms which have reasonable scattering cross sections without a large probability of absorption. Neutrons which undergo many collisions with the moderator material achieve thermal equilibrium with their surroundings. By opening an aperture to the moderator in a reactor, a continuous Maxwellian distribution of neutron energies is obtained in which the maximum intensity is determined by the moderator temperature (equation 2.2). By maintaining a moderator at an elevated or lowered temperature the maximum intensity can be moved to higher or lower energies.

When compared to current spallation sources most reactors produce a comparatively high continuous flux of neutrons. Sufficient neutrons are produced to allow energy selection by diffraction or velocity differentiation using spinning choppers. In either case inefficient use is made of the continuous energy spectrum emerging from the reactor since most of the neutrons in a "white" beam are discarded.

Since neutrons can probe solid objects, exceptional conditions may be obtained using pressure cells, cryostats and furnaces. Texture and stress are frequently examined with neutrons. Microstructural analysis and determination of atomic scattering cross sections are also important in understanding material behaviour and the defects in materials.

Neutron scattering is not without drawbacks. These include comparatively low beam intensity (quanta/cm^2/sec) in comparison to X rays. Count times to obtain diffracted spectra by neutrons generally take longer than X rays and larger sampling volumes are required because of their weak interaction. There are a limited number of neutron sources with fluxes sufficient to permit measurements in engineering components. The highest flux sources that are in existence including the Institut Laue

Langevin (ILL) high flux reactor are close to the maximum flux possible without a breakthrough in thermodynamic design since the limiting factor is the temperature drop between the coolant and the fuel (Carpenter 1986). Finally for some elements activation can take place leaving the sample radioactive.

2.3 Neutron formalism

Neutrons with energies in the MeV range are too energetic to be of use in most scattering experiments. Consequently neutrons produced in reactors and spallation sources are brought into contact with a moderator with which they achieve thermal equilibrium.

Neutrons with velocity v (momentum,p=mv) have an intrinsic de Broglie wavelength given by:

$$\lambda = \frac{h}{m v} \tag{2.1}$$

where h is Planck's constant

m is the neutron mass

v is the neutron velocity

λ is the neutron wavelength

If neutrons achieve thermal equilibrium with a moderator of temperature,T, they will possess energies of the order of $K_B T$ where K_B is Boltzmann's constant. Then by equating the kinetic energy of the neutron to its thermal energy:

$$\frac{h^2}{2 m \lambda^2} = K_B T \tag{2.2}$$

From equation 2.2 a moderator temperature of ≈300K will give a neutron spectrum with a maximum intensity close to 2 Angstroms. Thus the wavelength of thermal neutrons is ideal for diffraction experiments.

To describe the scattering process a scattering vector, $\underline{Q}$ is defined by:

$$\underline{Q} = \underline{k}_i - \underline{k}_f \tag{2.3}$$

where $\underline{k}_i$ is the incident wave vector,

$\underline{k}_f$ is the scattered wave vector.

This is illustrated in figure 2.1. For diffraction, $\underline{Q}$ is the direction in which the separation of the lattice planes, and hence strain, is measured.

2.4 Diffraction from metals and the Bragg equation

Crystallography and the formalism describing it is covered in many text books. The discussion here is limited to those aspects which pertain to stress measurement by neutron diffraction.

Crystals are made up of repeating units called unit cells. They are subject to conditions of symmetry which limit the number of different cells which can exist. To characterise a crystal it is sufficient to specify its unit cell and its space group. In practice there are 14 distinct space groups the simplest of which is the cubic lattice. Within a crystal a set of lattice planes or the direction normal to them may be labelled using the Miller indices, hkl.

Stress measurement by neutron diffraction is limited to crystalline materials. Most metals are polycrystals consisting of a network of individual grains. In the absence of preferred orientation or texture the metal can be treated as a powder of randomly orientated particles.

When neutrons of wavelength λ fall on a crystalline material they may undergo elastic scattering i.e. diffraction. In specific directions constructive interference can take place giving maxima in scattered intensity. The condition for constructive interference is when the scattering vector $\underline{Q}$ is a reciprocal lattice vector of the crystal. This condition may be written as Bragg's equation by:

$$n \lambda = 2 d_{hkl} \sin \theta \qquad (2.4)$$

where λ is the wavelength,

d_{hkl} is the lattice plane spacing in the direction $\underline{Q}$,

n is an integer,

and θ is half the scattering angle as given in figure 2.2.

Diffraction of monochromatic radiation from a single crystal produces a three dimensional array of directional maxima while a randomly orientated powder gives

diffraction maxima in the form of Debye cones depicted in figure 2.3.

The relationship between the lattice spacing, d_{hkl} and the lattice parameter, a_0 for the unit cell for cubic crystals is:

$$d_{hkl} = \frac{a_0}{\sqrt{(h^2 + k^2 + l^2)}} \tag{2.5}$$

2.5 Powder diffraction

The information obtained by diffraction from a powder is considerably degraded compared with a single crystal measurement. In practice the locations of the reflections indicate the shape and size of the unit cell while their relative intensities indicate its make up. One reason for the success of the powder diffraction technique is the Rietveld refinement package (Von Dreele, 1982). If the type of lattice is known then peak positions and intensities corresponding to different crystallographic directions can be combined using the Rietveld refinement technique, to determine the lattice parameter and structure. Profile refinement is discussed in chapter 8 in the context of time of flight measurements made on a pulsed source.

An example of a powder diffraction pattern for steel is given in figure 8.12. To produce a good diffraction pattern the sampled material must contain sufficient crystallites of the appropriate size. The optimal size for crystallites is in the range of 10 - 50 microns since particles of this size generally give sharp well defined peaks. When grains larger or smaller than the optimal size occur, size effects may be observed in the diffracted peaks. Generally, small crystallites which are less than 100 Angstroms in diameter give broad diffraction peaks which may be indistinguishable from the background. At the other extreme, individual grains exceeding about 0.1mm in diameter are close to single crystals for the purposes of powder diffraction.

2.6 Lattice strain

Generally in investigations of crystal structure the unknown in the Bragg equation is the lattice spacing d_{hkl}. Experimentally a specimen can be examined using either monochromatic or polychromatic neutron radiation. The two alternatives are associated with reactor and pulsed sources respectively.

a) **Constant wavelength.** For reactor based instruments which employ an intense continuous beam of neutrons, it is conventional to scan the lattice spacings d_{hkl} at a fixed wavelength,λ_0 and variable 2θ. Then from equation (2.4):

$$0 = 2\Delta(d_{hkl})\sin(\theta) + 2d_{hkl}\Delta(\theta)\cos(\theta) \tag{2.7}$$

and:

$$\frac{\Delta(d_{hkl})}{d_{hkl}} = -\Delta(\theta_{hkl})\cot(\theta_{hkl}) \tag{2.8}$$

If a crystal is subjected to a load then its unstressed lattice spacing d_0 will undergo a change $\Delta(d_{hkl}) = d_{hkl} - d_0$. Thus equation 2.8 defines the strain, ε in a material, i.e. extension divided by the original length. From equation 2.8 there is an implied change $\Delta\theta$ in the direction of the scattered maximum (positive for compression negative for tension). The change is observed as a shift in the peak centre of the Bragg reflection. Using a high resolution diffractometer, peak shifts as small as five thousandths of a degree can be recorded which, for a scattering angle of typically 120° 2θ corresponds to approximately 50 microstrain. The cotθ term in equation 2.8 means that larger peak shifts occur at larger scattering angles.

b) **Constant scattering angle.** On a pulsed source a continuous spectrum of neutron energies is produced in every pulse (after moderation) and the energy or wavelength of a diffracted neutron is determined by its time of flight (TOF) from creation to detection. The lattice spacing, d_{hkl} is determined by maintaining a constant scattering angle, θ_0 at the detector and scanning the wavelength. Therefore from equation (2.4),

$$\Delta\lambda_{hkl} = 2\Delta d_{hkl}\sin\theta_0 \tag{2.9}$$

and since the TOF is proportional to neutron velocity, by Equation 2.1) then:

$$\frac{\Delta d_{hkl}}{d_{hkl}} = \frac{\Delta\lambda_{hkl}}{\lambda_{hkl}} = \frac{\Delta t_{hkl}}{t_{hkl}} \tag{2.10}$$

Thus a lattice strain, ε may be determined from the small change in time of flight, Δt_{hkl} for the diffracted maximum provided there is no change in the path length. On

reactor sources wavelength scans can be performed by selecting and varying the neutron velocity using choppers rotating at different angular velocities.

Thus, when a load is applied to a crystal lattice deformation takes place. If the yield stress, σ_y is not exceeded the deformation is a reversible change of distance between atomic planes in the unit cell. If the yield stress is exceeded then the deformation includes a plastic component due to irreversible shear which occurs when planes of atoms slide in suitable directions. However, as strain measurement by neutron diffraction determines the separation of lattice planes, the technique only records the elastic strain in a specimen. In some cases the degree of plastic deformation may also be inferred from the peak shape, although the results are often ambiguous (cf section 2.10).

2.7 Unstressed Lattice spacing

In equations 2.8 and 2.10, $\Delta\theta$ and Δt correspond to the difference between the measured value of θ or t and the corresponding values for stress free material, θ_0 and t_0; i.e:

$$\Delta\theta = \theta - \theta_0 \tag{2.11}$$

$$\Delta t = t - t_0 \tag{2.12}$$

To calculate the absolute strain in a sample, θ_0 or t_0 must be known. If θ_0 or t_0 are measured experimentally then any variation due to structural change must be less than the variation due to the engineering strain. In practice the unstressed response of material identical to the sample is measured for a coupon with a maximum dimension less than 1cm (small enough to be assumed stress free in an engineering analysis). Alternatively when a complete stress profile through a sample has been obtained then, subject to symmetry and continuity assumptions, the strain free zero can be inferred from equilibrium constraints in which the load or moment must balance across a plane section. By applying both force and moment equilibrium, two independent calculations of the strain free value can be calculated and have, in practice, shown good agreement. In principle the stress free value can also be inferred from the physical condition that the stress normal to a free surface must be zero. Although measurements at free surfaces

can usually be made it is difficult to use this method since surface stress gradients can be extremely steep, the surface may not be representative of the bulk material and accuracy in this region is limited.

At present the best method for determining stress free zeros is by equilibrium balance of force and moment over plane sections in a sample. This has the limitation that it cannot be applied when a complete traverse through a sample has not been made either because of time or geometrical constraints. Measurements of θ_0 on small, carefully annealed cubes which should, in principle, be stress free have shown variations larger than the inherent accuracy of the technique making it hard to measure small strains with sufficient precision. This problem is examined in chapter 7 and it is a weakness of the method that specimens less than $1cm^3$ cannot always be relied on to give a stress free value.

2.8 Theory of stress measurement

Engineering design is usually dependent not on the strain but on the stress in a component. For a constant wavelength and specific lattice reflection the scattering vector Q remains fixed in space. By reorienting the specimen with respect to Q, the strain can be measured in different directions. Theory relating stress to strain is covered in many text books and is applied for neutron diffraction by Allen (1985). To fully specify the stress tensor at least six strain measurements are required unless some symmetry is assumed.

The strain tensor defined relative to orthogonal axes (x,y,z) in a sample may be determined from measurement of the strain, ε in different directions. If the orientation of Q relative to the sample axes is given by the direction cosines (l'm'n') then:

$$\varepsilon(l'm'n') = l'^2\varepsilon_{xx} + m'^2\varepsilon_{yy} + n'^2\varepsilon_{zz} + 2l'm'\varepsilon_{xy} + 2m'n'\varepsilon_{yz} + 2l'n'\varepsilon_{zx} \qquad (2.13)$$

Once the strain tensor is determined the principal axes may be found by diagonalisation. Then the principal stresses may be calculated using the macroscopic Young's modulus, E and Poisson's ratio,ν for isotropic materials by:

$$\begin{bmatrix} \sigma_x & & \\ & \sigma_y & \\ & & \sigma_z \end{bmatrix} = \frac{E}{1+\nu} \begin{bmatrix} \varepsilon_x & & \\ & \varepsilon_y & \\ & & \varepsilon_z \end{bmatrix} + \frac{(\nu E)(\varepsilon_x+\varepsilon_y+\varepsilon_z)}{(1-2\nu)(1+\nu)} \begin{bmatrix} 1 & & \\ & 1 & \\ & & 1 \end{bmatrix} \tag{2.14}$$

In practice the value of E depends on the elastic constants for the particular lattice planes used in the measurement. Anisotropic strain response for different lattice reflections cannot be ignored and is examined in chapter 3. Experimentally it is better to use a lattice reflection whose response is known to be close to the macroscopic modulus.

In special cases such as plane stress or plane strain where σ_x or ε_x respectively are zero equation 2.14 is simplified. For plane stress one principal stress is zero, (σ_x=0) and:

$$\sigma_y = \frac{E}{(1-\nu^2)}(\varepsilon_y + \nu\varepsilon_z) \tag{2.15}$$

$$\sigma_z = \frac{E}{(1-\nu^2)}(\varepsilon_z + \nu\varepsilon_y) \tag{2.16}$$

For plane strain $\varepsilon_x = 0$, and the stress relations are:

$$\sigma_x = \frac{E\nu}{(1-2\nu)(1+\nu)}(\varepsilon_y + \varepsilon_z) \tag{2.17}$$

$$\sigma_y = \frac{E}{(1-2\nu)(1+\nu)}[(1-\nu)\varepsilon_y + \nu\varepsilon_z] \tag{2.18}$$

$$\sigma_z = \frac{E}{(1-2\nu)(1+\nu)}[(1-\nu)\varepsilon_z + \nu\varepsilon_y] \tag{2.19}$$

2.9 Different stress types

Metals are polycrystals made up of many individual grains which have grown together in a randomly aligned melt. The stress state of a polycrystal is complicated by the diverse origins of stress within it. Different types can be classified according to their wavelength in the specimen (Macherauch, 1987 or MacEwen, 1987).

Type 1 or macrostresses correspond to engineering stresses which vary over the macroscopic dimensions of the component. These include the stresses produced by directly applied loads.

Type 2 or grain interaction stresses vary over distances corresponding to the grain size. They are generally attributable to differences in the mechanical or thermal properties of two phases or components. The effects of anisotropic plastic deformation also fall in this category.

Type 3 or microstresses refer to the stresses produced within grains.

The design engineer is generally concerned with type 1 stresses resulting from either direct or residual origin. With neutron diffraction, type 1 stresses can usually be resolved over distances small compared to their variation except in regions of steep stress gradient, for example, near a crack tip or a peened surface. Type 2 stresses cannot be resolved between grains although their effects over many grains can be observed as for example in a composite (cf chapt 3). Type 3 microstress originating from the variation in stress within individual grains may not be determined from the shifts of individual Bragg reflections although they do give rise to peak broadening.

2.10 Peak Broadening

Plastic deformation of a material modifies the shape of Bragg reflections through the introduction of crystal imperfections and stacking faults. In certain cases semiquantitative estimates of prior plastic strain can be made. In order to relate peak shapes to plastic strain, other effects such as grain size or stress gradients must be accounted for. For example small grains can cause broadening above the instrumental resolution. This effect is described by the Scherrer formula:

$$B = \left(\frac{K\lambda}{L}\right) \sec\theta \qquad (2.20)$$

where B is the line broadening above the intrinsic line width

L is the average length of a crystallite

λ is the wavelength

θ is half the scattering angle

K is the Scherrer constant.

Alternatively, peak broadening can occur when the sampling volume is in a region of steep stress gradient. The Scherrer formula and other causes of broadening are described by David (1986).

In practice, it is rarely possible to separate the effects on peak shape of prior plastic strain from the causes noted above. One successful study was made by Smith (1987) on simple cylindrical test pieces. They demonstrated that prior deformation increases the width of Bragg reflections in aluminium and A533B steel but is indistinguishable for tension or compression and appears to saturate for prior plastic strains of between 5 and 10 % in either sense.

2.12 Discussion

The implications of variable and directionally dependent crystalline compliance within the unit cell are examined in chapter 3. The practical aspects of neutron diffraction strain measurement are covered in chapter 4. For the experimental results quoted in this thesis the principal stress directions have been assumed, either because of simple specimen geometries or because of symmetry. However, in general to calculate the strain tensor a minimum of six independent strain measurements are required. Priesmeyer (1989) gives an example of the general calculation for a friction welded tube and notes that the accuracy can be substantially improved by making in excess of six measurements. In the case of neutron diffraction a compromise must be made between accuracy and use of beam time.

Vacancies, voids and dislocations associated with plastic strain or fatigue damage must be considered with the residual stresses in components if their service life is to be assessed. The effects of plastic strain are not easily addressed by neutron diffraction. One non destructive alternative which has been employed in conjunction with the neutron technique is positron annihilation (Allen 1987). By noting the shape of the gamma ray spectrum produced when positrons annihilate in a material inferences can be made concerning the plastic damage.

Appendix 2.1 Neutron attenuation in materials

A 2.1.1 Linear attenuation coefficient

When a neutron falls on a specimen one of three processes will occur: transmission, absorption or scattering. The intensity of transmitted radiation reduces as the distance traversed by the neutrons through the material increases. The strength of attenuation determines the maximum distance in a specimen over which neutrons may travel and still have sufficient intensity for a scattering measurement. In principle, the maximum path length for engineering strain measurements is limited by multiple scattering, however it is rare for path lengths to be used where this is an issue. Nevertheless engineering components can necessitate path lengths of up to several centimeters and the measurements are usually determined by the available beam time.

Increasing thickness of an absorber in a neutron beam causes an exponential decay in the intensity of transmitted radiation. The decay may be derived by assuming that the reduction in transmitted intensity caused by a small thickness of absorber is proportional both to the initial intensity and the thickness:

$$dI = -\mu I\, dt \qquad \text{(A2.1)}$$

where μ is the linear attenuation coefficient.

dt is a small increase in thickness.

I is the intensity.

If the incident intensity on a sample of thickness, t is I_0 then by integration:

$$I = I_0 e^{-\mu t} \qquad \text{(A2.2)}$$

The constant of proportionality in A2.1, μ has units of inverse length. The penetration in a material is often specified by the attenuation length, μ^{-1} (or the mean free path) which represents the thickness of material associated with a reduction in the incident intensity by e^{-1}. From equation A2.2 the thickness for 50% absorption is $\mu^{-1}\ln 2$.

The scattering probability for neutrons impinging on a specimen is related to the cross sectional area presented by the nuclei in it. By considering target cross sections, first at an atomic level then for the bulk material, μ can be inferred by reference to equation A2.7. Examples of μ and the thickness (cm) of material to give 50%

absorption are given in table A2.1.

Table A2.1: Absorption coefficients for different elements

Element	Fe	Ni	Al	Ti	Cd	Gd
μ (cm^{-1})	1.12	1.86	0.10	0.45	117.4	$1.5\ 10^{4}$
μ^{-1}ln2 (50%)	0.62	0.37	7.05	1.55	$5.9\ 10^{-3}$	$4.6\ 10^{-5}$

The mean free path of neutrons in most metals is at least several centimeters. While this precludes measurements with path lengths in metallic materials in excess of about 50mm, neutron penetration is considerably greater than for X rays which typically penetrate less than 100 microns. Exceptional materials such as cadmium, boron and gadolinium are very strong neutron absorbers and possess mean free paths of a fraction of a millimeter. Consequently cadmium and boron are frequently employed for shielding and collimation. Gadolinium is used as a moderator poison at the spallation neutron source, ISIS.

A2.1.2 Scattering from a single element

If the wavelength of the incident neutrons is much larger than the range of the strong nuclear force then the target nuclei can be treated as identical, non-interacting particles of constant cross section. The strength of interaction is characterized by a scattering length, b which depends on the atomic species, isotope and spin state. The sign and magnitude of b change irregularly with atomic mass and number. When atoms of one species scatter in the same way the scattering is coherent and is associated with a cross section, σ_c (here σ denotes a cross section not a stress). Random fluctuations in the isotopic distribution and spin alignments cause incoherent scattering described by a cross section σ_i. Absorption also causes attenuation and is described by σ_a. The scattering intensity depends on whether the the nucleus is fixed or free to recoil in the scattering process. For most condensed matter experiments the fixed atom is a reasonable approximation and it is conventional to quote bound atom values for scattering cross sections. The scattering and absorption cross sections have been

measured for most elements and isotopes and are typically of the order of 10^{-28} m^2 or 1 barn.

A slab of material consisting of a single elemental species is illustrated in figure A2.1. If the material has density ρ then the mass of the slab is $\rho l^2 dt$ and the number of atoms, n in the slab is given by:

$$n = \frac{\rho l^2 dt}{A} . N_A \qquad \text{(A2.3)}$$

Where N_A is Avogadro's number,

A is the atomic mass of the element.

Each nucleus in the slab will present a cross section for interaction with the incident neutrons given by $\sigma_s + \sigma_a$, where $\sigma_s = \sigma_c + \sigma_i$. The total macroscopic cross section, σ_{tot} of the slab presented to the incident neutrons is:

$$\sigma_{tot} = \frac{\rho l^2 dt}{A} . N_A . (\sigma_s + \sigma_a) \qquad \text{(A2.4)}$$

The probability, p of a neutron interacting with a target nucleus is obtained by dividing A2.4 by l^2:

$$p = \frac{\rho (\sigma_s + \sigma_a) N_A}{A} . dt \qquad \text{(A2.5)}$$

but from equation A2.1 the probability of interaction is also:

$$p = \frac{dI}{I} = -\mu dt \qquad \text{(A2.6)}$$

Thus the attenuation coefficient for an element may be calculated from its density, atomic mass, Avogadro's number and the total scattering cross section of its nuclei by:

$$\mu = \frac{\rho (\sigma_s + \sigma_a) N_A}{A} \qquad \text{(A2.7)}$$

Elemental iron (Fe) has an atomic mass of 55.85, density 7.88 gcm^{-3} and $(\sigma_s+\sigma_a)$ of $(11.66+2.56)\ 10^{-24} cm^2$. Taking Avogadro's number as $0.6022\ 10^{24}$ per gram mole gives a value for μ of $-1.21 cm^{-1}$ or $0.121 mm^{-1}$. This agrees exactly with the value of μ measured for an A533B steel by Smith (1987).

A2.1.3 Attenuation coefficient for an alloy

Many metals of engineering interest may be treated as single elements in attenuation calculations since they only contain small or negligible amounts of alloying elements. In A2.1.2 the attenuation coefficient calculated for pure iron agrees with the measured value for A533B steel. However if appreciable alloying species (denoted by the suffix i) are present or in the case of composite materials, the calculation for the modified attenuation coefficient μ_{al} is obtained by analogy to equation A2.7 and accounting for each atomic constituent:

$$\mu_{al} = \rho_{al} N_A \sum_i \frac{w_i (\sigma_s + \sigma_a)_i}{A_i} \qquad \text{(A2.8)}$$

where w_i is the weight fraction of species i and:

$$\Sigma_i w_i = 1$$

As in the single element case the penetration length l_{al} is given by μ_{al}^{-1}.

A 2.1.4 Application to a nickel base alloy

The attenuation coefficient may be determined experimentally by a minimum of two measurements of the transmitted intensity with and without an absorber of known thickness in the beam, allowing equation A2.2 to be solved for μ. Ideally, intensity measurements are obtained for a variety of absorber thicknesses which allow μ to be determined from the gradient of a lnI versus thickness plot.

Waspaloy is a nickel based superalloy which has good high temperature strength and is used in gas turbines where components have to operate at sustained high temperatures. Experimental measurement at the ILL on a sample approximately 10mm thick yielded a value for the attenuation coefficient of 0.1795 mm^{-1}.

Waspaloy is approximately 58% by weight nickel however it also contains appreciable amounts of chromium, molybdenum and other elements. The data below shows how μ may be calculated from the chemical compositional data.

Element†	Wt %(W_i)	σ_T ($=\sigma_s+\sigma_a$)*	$w_i.\sigma_T.A_i^{-1}$
Ni	56.3	22.06	0.212
Cr	19.5	6.54	0.025
Co	13.5	43.33	0.099
Mo	4.3	8.45	0.004
Ti	3.0	10.16	0.006
Fe	2.0	14.22	0.005
Al	1.4	1.74	0.001
B	0.006	772.01	0.004
	Σ=100%		Σ=0.356

† Not including traces of carbon, manganese, silicon, zirconium, copper and sulphur all of which are considerably less than 1 % by weight.
* units of $10^{-24}cm^2$

Then by equation A2.8,

$$\mu_{wasp} = - 8.8 * 6.22\ 10^{23} * 0.356\ 10^{-24} \quad cm^{-1}$$

Thus the calculated value for μ_{wasp} is $1.95cm^{-1}$ or $0.195mm^{-1}$ which is in reasonable agreement with the measured value.

Appendix 2.2 Neutron detection

Neutrons penetrate deeply in materials because they are neutral particles. Consequently they do not directly produce ionisation and are not easily detected. Their detection relies on observing the ionisation caused by the products of absorption or fission reactions. Practical neutron detection falls into one of three categories: fission chambers, gas detectors and scintillation counters.

In fission chambers neutrons interact with a fissile coating and the energetic, electrically charged fragments cause ionisation of a gas in the detector, which in the presence of an electric field produces a current pulse. Fission reactions release a large amount of energy in each event which leads to a large voltage pulse. The fission cross section for Uranium 235 with thermal neutrons is 582 Barns.

In gas detectors the large absorption cross section of neutrons with boron or helium is exploited. The relevant reactions are:

$$^1n + {}^{10}B = {}^7Li + {}^2\alpha + 2.792MeV \qquad (A2.9)$$

$$^1n + {}^3He = {}^3H + {}^1p + 765KeV \qquad (A2.10)$$

The respective interaction cross sections are 4000 Barns for the boron reaction and 5400 barns for helium (at 2200m/s). At n.t.p. the lithium and tritium reaction products have path lengths of approximately 5mm producing on average 10^4 ion pairs (Bacon, 1962). The cross section of both the boron and helium reactions decreases with energy which gives preferential sensitivity to thermal neutrons. One disadvantage of boron is that its gaseous compound, boron trifluoride BF_3, is highly reactive. By contrast helium three is relatively rare and the higher range of protons compared with alpha particles necessitates higher filling pressures.

Despite the lower energy deposited for each event in gas detectors (compared to fission counters) their larger interaction cross sections give higher sensitivities. However BF_3 counters tend to saturate between 10^4 and 10^5 counts/second depending on their size and area. Consequently a fission chamber is generally employed to monitor intense incident fluxes while gas detectors are used to record low intensity scattered radiation.

Recently scintillation counters have been extensively adopted (Leadbetter, 1985). The salient reaction is:

$$^1n + {}^6Li = {}^4\alpha + {}^3H + 4.78MeV \qquad \text{(A2.11)}$$

At 2200m/s the cross section is 940 Barns. Lithium has no usable gaseous compound and cannot be used in conventional gas detectors. However lithium 6 can be supported in glass with an active cerium component for scintillation. As the products of A2.11 cause ionisation pairs, the electrons excite the cerium resulting in a flash of light which is detected by conventional photomultipliers. Advantages of scintillation counters include good efficiency, short dead times, flexible shape and cost, however their sensitivity to gamma radiation can be a problem.

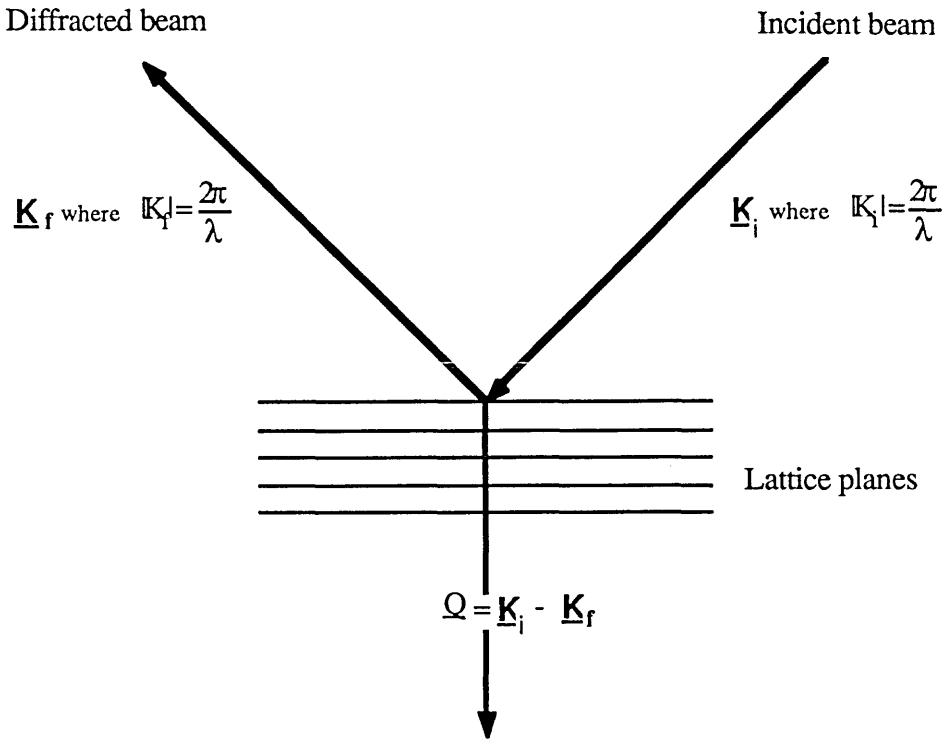


Figure 2.1: Definition of the scattering vector, Q

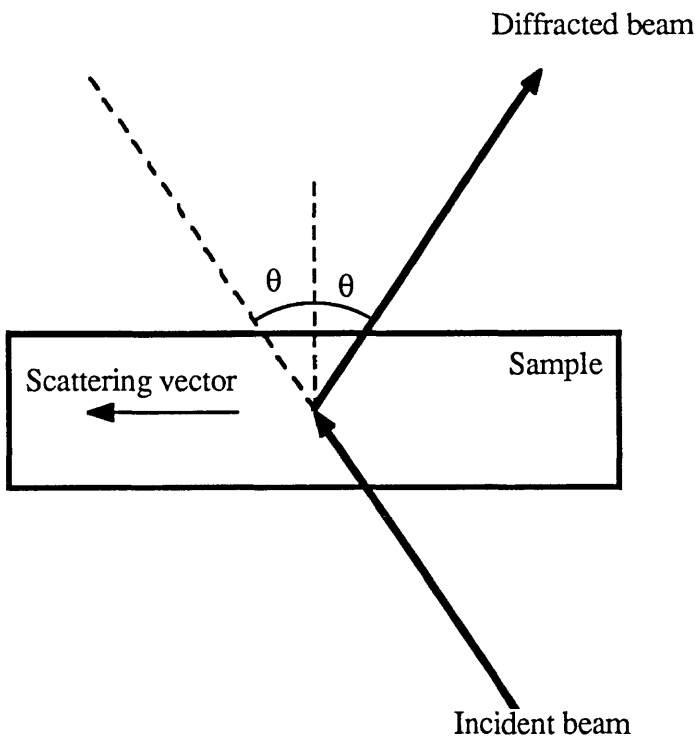


Figure 2.2: Bragg law diffraction

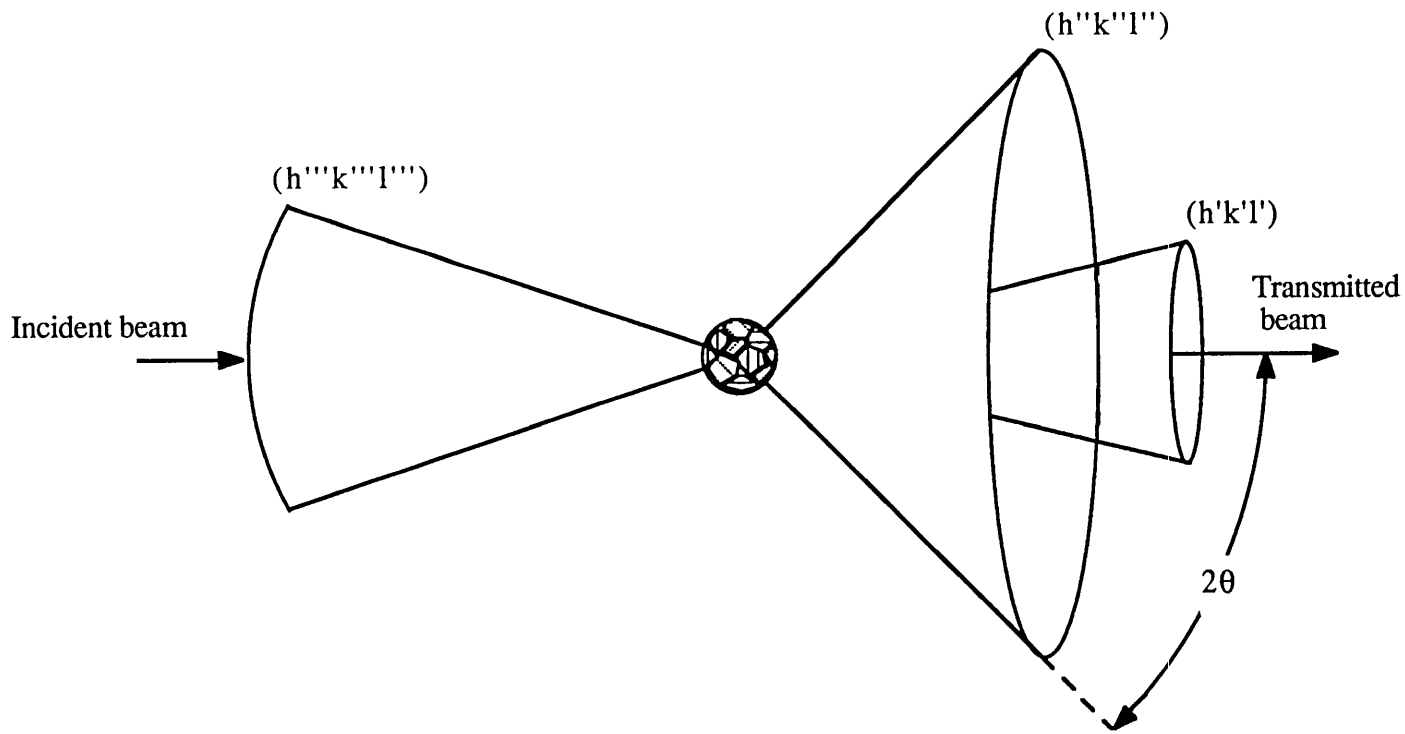


Figure 2.3 Debye Scherrer scattering cones

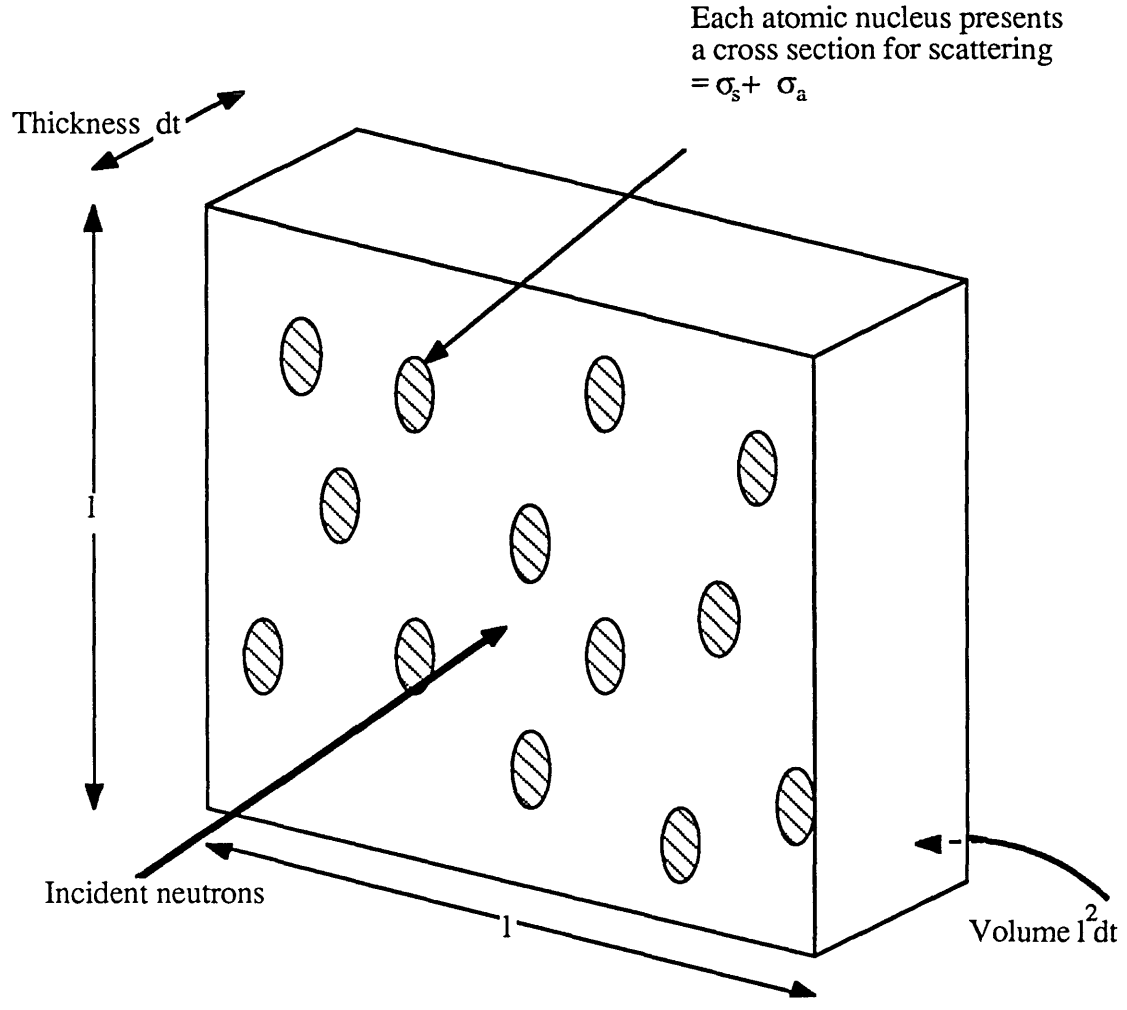


Figure A2.1 : Scattering cross sections presented to incident neutrons

CHAPTER 3

Calibration using a uniaxial stress rig

3.1 Introduction

In most engineering designs, steel is usually treated as homogeneous in which, stresses are assumed to be continuous. In chapter 2 a general expression (2.15) was given for converting strain measurements to stress. It uses a value for Young's modulus, E which is quoted as a macroscopic material parameter. However, when strain is inferred by diffraction, the information comes from a subset of grains with lattice planes normal to the strain direction. Thus a diffraction measurement is an average of the strains in a group of grains of atypical alignment. In most crystals the strain response in the unit cell is directionally dependent. Another effect pertinent to strain measurement by diffraction is the preferred slip in specific directions in the lattice. When both elastic anisotropy and slip are considered, it is clear that at the scale of individual grains a polycrystalline material cannot be treated as homogeneous.

Conventional strain gauge measurements offer little information concerning the details of intergranular load sharing and deformation. In this chapter the anisotropic strain response due to an applied load is examined for a low carbon steel and an aluminium silicon carbide composite. The effect of plastic strain is considered and whether the strain in different grains or phases rises monotonically and whether relaxation occurs. The residual strains induced on unloading are also measured. The low attenuation of neutrons enables many grains to be examined in each measurement which gives a representative average. The strain response of different reflections are calibrated with respect to the macroscopic behaviour and are discussed in the context of their relevance to stress measurement in engineering components.

3.2 Background

Although models for intergranular behaviour were proposed by Reuss (1929) and Voigt in (1928) the first extensive experimental examinations were made by Greenough (1949, 1951 and 1952). He noted that the fundamental issue is to allow for crystal interactions during deformation and that it is not possible for both stress and

strain to be constant across the grain boundary of two anisotropic crystals of different orientations. Early measurements of strain anisotropy relied on X-rays to give information on residual stress and plastic deformation from the displacement and shape of Bragg reflections. The study of peak shape is important because although the position of a Bragg reflection relates to the relative positions of atoms in a crystal lattice it does not distinguish the bulk movement of atoms. Strain associated with slip, in which one atom is replaced by its neighbour will be indistinguishable if only examined by the position of a diffracted reflection.

Although X-rays are still used (Honda, 1989) in the examination of strain response they are restricted by their lack of penetration. X-rays rarely penetrate more than a grain diameter in most materials and measurements are restricted to accessible surfaces which are often unrepresentative of the bulk material. Recently the use of neutron diffraction has led to a resurgence in interest in investigating the strain response in polycrystals.

As well as the deformation response under applied load the residual stress in the aggregate after application of a stress in excess of yield is also of interest. It will depend on the resultant equilibrium state between grains which have been plastically or elastically strained. Honda (1989) demonstrated that certain grains in mild steel can exhibit residual tensile stresses even when the macroscopic state of the material is compressive. Residual stresses due to anistropic yield are likely in dual phase or composite materials and it is not surprising that similar effects are noted in single phase materials. Preferred orientation which results from fabrication processes such as rolling, extrusion or welding must also be considered. The grains in textured materials cannot be treated as randomly aligned and a theoretical treatment has been devised to allow for their orientation by Sayers (1984).

3.3 Theory

The macroscopic properties of polycrystals result from the combined effects of single crystal elasticity and grain interactions. The elastic properties of single crystals are expressed by their elastic constants or compliances. Treatments for the strain response in a single crystal are given by Sayers (1984) or Love (1944). However for

the specific case of diffraction the elastic strain, $e^{//}_{hkl}$ in a direction normal to the lattice planes for an applied uniaxial stress, σ is given by Allen (1985) as

$$e^{//}_{hkl} = \sigma (S_{11} - 2SA_{hkl}) \tag{3.1}$$

where $S = S_{11} - S_{12} - S_{44}/2$ and S_{ij} are the elastic compliances

σ is a uniaxial stress

hkl are the Miller indices of the lattice planes

and

$$A_{hkl} = \frac{(h^2k^2+k^2l^2+l^2h^2)}{(h^2+k^2+l^2)^2} \tag{3.2}$$

In a direction normal to the applied stress, if the Reuss limit is applied then the elastic strain, $e^{\perp}$ is given by,

$$e^{\perp}_{hkl} = \sigma (S_{12} + SA_{hkl}) \tag{3.3}$$

From equation 3.1 the effective Young's modulus, E_{hkl} for a direction normal to the lattice planes (described by the Miller indices hkl) is:

$$E_{hkl} = \frac{1}{(S_{11} - 2SA_{hkl})} \tag{3.4}$$

The value of A_{hkl} varies from 0 to 0.333. For ferritic steel (with S_{11}=7.632 10^{-3} GPa^{-1} S_{12}=-2.788 10^{-3} GPa^{-1} and S_{44}= 8.547 10^{-3} GPa^{-1}) E_{hkl} for the compliant [200] direction is 131GPa and for the stiffest [222] direction is 282GPA (Allen, 1985).

Theoretical limits of behaviour were proposed by Reuss (1929) and Voigt (1928). Reuss proposed that each crystallite experienced the same stress field while Voigt suggested that each crystallite experienced the same strain field. A more realistic model was proposed by Kroner (1958) in which crystallites are assumed to be embedded in a homogeneous elastic medium with elastic properties equal to those of the bulk material. The implications of the three models are discussed by Sayers (1984). The Voigt model implies that no strain anisotropy will be observed for different lattice reflections while the Reuss model predicts that strains in the polycrystalline aggregate will depend on the orientation of the crystallites with respect to the applied stress.

Strain and stress in polycrystalline aggregates are also affected by plastic deformation resulting from slip. However there is little theory available for the plastic

region where shear stresses cause slip. Experimental measurement of its effects are complicated by the presence of interstitial impurities such as nitrogen or carbon which affect material properties, as well as uncertainties resulting from voids and changes in cohesion at grain boundaries. On relaxation of an applied load, grains in different orientations which had different yield stresses can be driven into compression or held in tension. Neutron diffraction measurements of lattice strains are elastic and inferred residual stresses in a small free sample must result from grain interaction. The net residual stress across any plane section will equal zero.

3.4 Stress rig description and operation

To examine the strain response of polycrystalline samples under applied loads a uniaxial tensile stress rig was used (fig 3.1). The rig permitted unobstructed diffraction measurements through at least 100° in horizontal and vertical orientations and was accommodated on the omega table of the D1A diffractometer. Tensile samples were 60mm long and 3mm in diameter except at the ends where they were attached to the rig using split cones. The force was monitored with a load cell and the stress level, ramp rate and hold time were controlled by a microprocessor. A piezoelectric extensiometer was attached to the sample. The applied force, macroscopic strain and time were printed at periodic intervals on a dedicated printer. The sample orientations for measurement of strain parallel to and perpendicular to the applied load are shown in figure 3.2(a,b). In figure 3.2a the sample is horizontal and the strain measurement is parallel to the applied stress. In figure 3.2b the sample is vertical and the strain measurement is perpendicular to the applied stress. Different samples were used for the measurements in the two orientations. For each Bragg reflection the rig was reoriented to maintain the scattering vector, Q parallel or perpendicular to the sample.

The samples were subjected to stresses to between 400MPa and 550MPa in steps of 50MPa. At each level the sample was held at constant stress to permit diffraction measurements from several reflections. On completion of the maximum stress level the samples were unloaded to half the maximum stress and then to zero. For strain measurements perpendicular to the loading axis the strains are related to the applied stress by Poisson's ratio. Tension and compression are indicated by positive

and negative strain values respectively. Changes in lattice strain are expressed as μstrain.

3.5.1 Mild steel results

The measurements on mild steel had two objectives; to relate the strain anisotropy of different reflections to the bulk response and to investigate non-linear strain response at high stress levels due to limited plasticity.

The regular shape of the specimen and the uniaxial applied stress made definition of a sampling volume unnecessary, although care was taken to mask the split cones and the piezoelectric extensiometer with cadmium. Typically a 10mm length of the specimen was exposed to the neutron beam. Lattice reflections were observed at approximately 50Mpa stress intervals to a maximum of 520MPa. For each reflection the wavelength was selected to maximize the diffracted angle thereby giving the best accuracy. An example of the peak shifts obtained for the iron [310] reflection (at 101.5°) with $\underline{Q}$ parallel to the applied stress between zero and 500MPa is given in figure 3.3. The change in the position over this stress range is approximately 0.39 °2θ.

Individual measurements took between 15 and 40 minutes and the total hold period at each stress level was approximately 100 minutes. Below 350MPa the macroscopic creep remained less than 0.001% over the duration of each stress level. At 420, 470 and 520 MPa the macroscopic strain increased by 0.040, 0.073 and 0.0153% respectively over the duration of the measurements. At 520 MPa the creep rate was approximately 0.01%/hour.

The lattice strains for a variety of reflections parallel and perpendicular to the applied stress are given in figures 3.4a and 3.4b. The peak positions at a nominal zero stress, typically 7MPa (sufficient to lock the specimen in position) were taken as zero strain values. The measured reflections include the compliant [200] direction and the stiff [222] direction. In figures 3.5a and 3.5b the strains on unload are plotted. Residual strains retained by grains in specific orientations are denoted by the intersections with the horizontal axis.

The strain errors are determined by the accuracy of the Gaussian fits to the data and are approximately $\pm$ 50μstrain. The accuracy of the load cell gave an error in the

applied stress of ± 5MPa. Peak widths were between 0.5 and 0.6 °2th with errors of ± 0.01°. No systematic variations in peak width were observed except for a 10% increase in width for the [200] reflection with Q parallel to the applied load. Above 400MPa small variations from Gaussian peak shapes were observed for some reflections, notably in the [222] and [211] directions. These included the formation of sub peaks which may indicate the selective relaxation of some grains.

3.5.2 Mild steel discussion

The Young's modulus for mild steel is 207GPa which is close to the single crystal compliance of 219GPa normal to the [211] or [110] lattice planes (A_{hkl}=0.25). Figure 3.6 shows the lattice strain of the [211], [110] and [220] reflections parallel to the applied stress plotted with the strain recorded by the extensiometer. Over the range 0 to 500MPa the measured compliances of the [211] and [110] reflections are 226 and 241GPa respectively. Although these values are larger than the predicted single crystal values there is good agreement with the extensiometer up to 350MPa. Beyond 350MPa the macroscopic strain shows conventional post yield behaviour and there is increasing divergence. At 500MPa the disparity between the extensiometer and the [211] lattice strain is 1000μstrain.

In figure 3.6 the relationship between the lattice strain in the [211] ([110] or [220]) direction and the applied stress remains linear at high stress levels. This implies that the majority of the grains with the [211] direction parallel to the applied stress continue to deform elastically while slip occurs in some grains of differing alignment to account for the macroscopic yield. Non linear response is observed in figure 3.4a for the [200] reflection. Neutron diffraction only measures the elastic strain in crystals. Non-linear strain response can occur because the lattice strain in grains of specific alignment is plotted against the average stress applied to the aggregate. The stress measured by the load cell is an average of the stresses existing in all the grains. This is illustrated in figure 3.7. In a polycrystal containing adjacent grains A and B of different alignment, if grain B can deform by slip then (ignoring the constraint from surrounding grains and boundary effects) it will relax and to maintain a constant stress on the specimen (as is the case with the stress rig): then grain A must experience a larger stress

(fig 3.7b). In practice slip and grain interaction processes determine the behaviour of strained polycrystalline aggregates.

Information concerning plastic deformation in a specimen can sometimes be inferred from the shape of neutron diffraction reflections. However for most of the stress rig measurements the statistical accuracy of each peak is only sufficient for accurate determination of the peak centre not of the peak shape. The assessment of peak shapes is limited to qualitative observations and quantitative assessment is not possible.

If strain is to be inferred from a single lattice reflection, as is usual for monochromatic measurements, it is preferable to use a reflection which is demonstrably close to the bulk response and which is unlikely to slip in response to shear stresses. In cubic crystals lattice reflections with A_{hkl}=0.25 appear to meet this criterion. More compliant reflections offer larger peak shifts but may lead to an underestimate of the bulk stress unless appropriate corrections are applied.

At 500MPa the order of strain measurements is in accordance with the simple theory of single crystal compliances. The disparity in strains for different reflections show that the material behaviour differs from the Voigt limit which predicts equal strains in all grains. To assess the data with respect to the Reuss limit the inverse of the compliance E^{-1}_{hkl} for each reflection is plotted against A_{hkl} in the parallel and perpendicular direction (fig. 3.8). In the Reuss limit equation 3.1 predicts a linear relationship with gradient -2S and intersection with the vertical axis at S_{11}. In figure 3.8 an approximately linear relationship does exist between E^{-1}_{hkl} and A_{hkl} which indicates that the spread in strain is largely caused by crystalline anisotropy. However the gradient in the parallel direction is 53% of that predicted for a simple Reuss model of mild steel. The elastic compliances perpendicular to the strain axis lie close to the Reuss limit when Poissons ratio (0.3) is taken into account.

3.6.1 Metal Matrix Composites

Metal matrix composites (MMC) offer high strength and good creep resistance at lower densities than conventional engineering materials. The essential requirement for a good composite is effective load transfer between the stiff reinforcement and soft matrix. However the difference in coefficients of thermal expansion between the two phases is

often considerable and significant plastic strain can occur on cooling from fabrication temperatures. Composites inevitably experience residual stresses. Results are presented for an investigation by neutron diffraction of load sharing between two phases of a metal matrix composite in the presence of a uniaxal tensile stress. The behaviour of the material was also recorded on unload from a stress in excess of the yield stress of the material.

Continuous fibre composites offer good mechanical properties but discontinuous chopped fibre or particulate composites are cheaper and easier to shape. The stress response of fibre composites can be divided into three stages:

Stage 1- Both the matrix and the fibre are elastic.

Stage 2- The matrix deforms plastically while the fibre remains elastic.

Stage 3- Both the matrix and fibres deform plastically.

When both components behave elastically (stage 1) the effective Young's modulus, E_c for a composite is given by the rule of mixtures.

$$E_c = E_f V_f + E_m (1-V_f) \qquad (3.5)$$

where E_f and E_m are the moduli of the fibre and matrix respectively. V_f is the volume fraction of the stiffener component.

Once stage 2 is reached the introduction of residual stresses during unloading is inevitable. The value of diffraction measurements in metal matrix composite materials was recognised by Cheskis and Heckel (1970) who made in situ strain measurements on loaded continuous-fibre composites. Using a loading rig mounted on an X-ray diffractometer they examined the matrix and fibre of aluminium tungsten and aluminium boron composites at a variety of stress levels. They also noted the residual stresses induced on unloading. The rule of mixtures was shown to be effective only if prior residual stresses were taken into account. Their measurements were confined to a single lattice reflection.

X-ray examination of composites do not give a representative average for the bulk behaviour in the material because they penetrate only a short distance into the material. Swe den Tsai (1987) has made a merit of this by attempting measurements at the interface between fibres and matrix. The difficulties in exposing the interface in a

manner which does not destroy the residual stresses are considerable. Although neutrons do not have the spatial discrimination to assess interface behaviour they offer selective, non-destructive measurements of either phase averaged over a volume measured in a few cubic millimeters with little or no sample preparation.

3.6.2 Results for an Al SiC composite

Using the stress rig described in section 3.4 the lattice strain was measured in the matrix and reinforcement of a composite material. Two specimens were powder pressed and extruded from an aluminium alloy matrix (Al 2014) containing 20% by volume of 10μm β SiC particulate material. The aluminium and β silicon carbide are both face centered cubic although some hexagonal, α SiC was noted in a powder scan of the tensile specimens. It is worth noting that all of the measured silicon carbide reflections can be indexed to a hexagonal lattice structure. Prior to examination a "T6" solution treatment at 500° C was applied followed by ageing at 180°C. The strain response of several lattice reflections in both phases were examined up to 450MPa in increments of 50MPa (figs 3.9ab). A comparison specimen of pure aluminium alloy was also examined with Q parallel to the applied stress (fig 3.10). Separate samples were examined in the parallel and perpendicular directions. The diffraction peaks were all fitted with Gaussian line shapes to determine the diffraction angle.

The fabrication residual stresses in a composite of aluminium and silicon carbide fibre were found to leave the aluminium matrix with a tensile stress of 140MPa parallel to the plane of the fibres (Allen 1986). However the fabrication stresses in a particulate composite are likely to be hydrostatic and the strain at 7MPa was taken as zero for all reflections. Thus the quoted lattice strains do not include any residual strains. Typical experimental errors are $\pm$ 5MPa and $\pm$ 100 μstrain respectively.

Figures 3.9a and 3.9b show the lattice strains parallel and perpendicular to the applied stress for three Bragg reflections in the matrix and reinforcement. Owing to texture and restrictions imposed by the experimental geometry, not all the same reflections were examined in the two directions. The SiC [200] is absent in the parallel direction as are the Al [222] and SiC [222] in the perpendicular direction. The elastic strain responses with E_{Al} and E_{SiC} of 72GPa and 420GPa respectively are included in

figure 3.9a. The predicted Poisson's ratio effects are included in figure 3.9b for $\nu(Al)=0.3$ and $\nu(SiC)=0.22$.

The residual strains induced in the composite on unload are shown in table 3.1.

Table 3.1: Residual strains induced on unloading

Material	Reflection	Strain parallel to σ (μstrain)	Strain perpendicular to σ (μstrain)
Al	[111]	-10 ± 60.....	..... -151 ± 120
Al	[220]	-241 ± 70	
Al	[311]	65 ± 50.....	..... -195 ± 60
Al	[420]	-274 ± 200	
Al	[200]	8 ± 200.....	..... 45 ± 60
SiC	[111]	-169 ± 80	
SiC	[220]	52 ± 50.....	..... 417 ± 100
SiC	[422]	130 ± 50	
SiC	[311]	148 ± 50.....	..... 39 ± 40
SiC	[400]		170 ± 70

3.6.3 Discussion of composite results

Using E_{Al} of 72GPa, E_{SiC} of 420GPa and taking the volume fraction as 20% the predicted composite modulus,E_c is 142GPa (equation 3.5). The predicted response for E_c is also included in figure 3.9a. From the extensiometer value it is clear that the initial response of the composite is stiffer than predicted by the simple model. However the strains in the matrix and particulate lie between the elastic responses for pure silicon carbide and aluminium (fig 3.9a). The Voigt limit is clearly inappropriate and the data lies closer to the Reuss prediction of constant stress.

Little anisotropy is observed in figure 3.10 for different reflections in the pure matrix material although the magnitudes qualitatively follow the Reuss prediction with the (002) reflection being the most compliant and the (111) the least. The measured strains closely follow the extensiometer measurements. The measurements are in

agreement with the single crystal constants for aluminium which predict almost isotropic directional strain response.

Normal to the applied stress the different reflections of the each phase are close to -ν times the parallel strains as would be expected for isolated components. Despite the experimental errors (which are similar in both measurement orientations, but form a larger fraction of the strains in the perpendicular direction) the silicon carbide (400) and (220) reflections exhibit erratic behaviour which includes tensile strains at low stress levels. This may be due to the constraining effect of the matrix on the particulate material.

Prediction of the residual stresses and internal loading induced in both phases of composite materials requires a model for the material behaviour and the manner of deformation. The model must account for localised stress fields, the aspect ratio, size and alignment of the inclusions. Plastic deformation may cause stress redistribution in which the stiffener can take more of the load. Also material behaviour can be further complicated by the growth of voids around the stiffening phase.

One model which is appropriate for these results is that of equivalent homogeneous inclusions (Eshelby, 1957). It has already been applied to a short fibre metal matrix composite (Withers, 1987). Preliminary application of the Eshelby model to the data reported here has shown that the measured strains can be explained in terms of the expected elastic (and at high stresses plastic) transfer of load towards the stiff included phase (Allen, 1990). Diffusional and plastic relaxation processes in which atoms move to reduce the total energy of a stressed system probably play a major part in determining the residual strains on unload (compressive in the matrix and tensile in the reinforcement). For these measurements each stress level was maintained for 3 hours and relaxation is likely at stress levels in excess of 350MPa. However the neutron diffraction technique cannot directly address the processes by which such relaxation may occur.

3.7 Discussion and suggestions

The relevance of the stress rig results to the measurement of residual stress, stems from the selection of a single Bragg reflection to infer bulk properties during

monochromatic measurements. Limited beam time, strong attenuation and long path lengths, in specimens large enough to be representative, usually preclude the examination of more than one lattice reflection per position for monochromatic measurements. Thus it is of importance that a strain reflection is selected with a calibrated compliance and which is not susceptible to yield effects.

The residual stresses produced in composites by thermal effects and quenching from different temperatures can be considerable. When tensile residual stresses are produced in the matrix plastic flow will occur at lower stresses than expected. One area which neutrons cannot explore concerns the material behaviour at the interface between the matrix and stiffener material. The best spatial resolution which can currently be obtained by neutron diffraction techniques is 0.2mm in any direction. Thus it is impossible to measure only at the interface, unless a distinct interface phase exists in sufficient quantity to produce a discrete diffracted spectrum.

The stress rig results demonstrate the potential of neutrons both in calibration of the strain response of materials under an applied load but also in recording the residual strains produced in the two phases upon unload. Some anomalous effects have been observed. These include kinks in the strain response for the Fe (310) in the perpendicular direction between 150 and 200MPa and a similar effect for the composite aluminium (111) parallel to the applied stress. Also the strain response of the silicon carbide perpendicular to the applied stress appears initially to be in the "wrong" direction. These effects may be related to localised yield of grains in particular orientations. Yield effects are apparent in the detailed shape of applied load versus lattice strain curves as discussed in 3.5.2.

One area which appears to be worth further investigation are the effects on peak shape of the application of stresses in excess of the yield stress, both during and after the application of loads. During the measurements reported in this chapter, variations in the shapes of diffracted reflections were noted which included broadening and the development of sub peaks. By studying these effects in the context of the metallurgy of yield, dislocation densities and slip systems it may be possible be possible to identify the preferred yield mechanisms in polycrystals which would help to predict the internal

lattice strains. Artificial enhancement of the processes of interest could be made by making the measurements at elevated temperatures where creep and dislocation movement can occur more readily. Alternatively by making strain measurements at an angle of 45 degrees to the applied load the lattice planes most susceptible to slip may be observed directly.

One feature which has been ignored in this discussion is texture. Production processes like hot rolling, powder pressing or extrusion often introduce preferred orientation The induced texture may preclude the observation of reflections in specific directions and can make the material properties directionally dependent.

3.8 Conclusions

The lattice strains in a mild steel and a metal matrix composite have been examined by neutron diffraction at stress levels up to and beyond the yield stress. Lattice strains have been recorded which offer a detailed picture of the grain response in both specimens under an applied stress. Strain anisotropy is seen in both the elastic and plastic regions.

The relationship between lattice strain and applied stress for mild steel Bragg reflections with A_{hkl} =0.25 is linear in the elastic and plastic regions. Their compliance is close to the bulk response. This makes them suitable for residual stress measurement in engineering components since corrections for yield and crystalline compliance need not be applied to infer the bulk properties. More generally the measured compliances for different reflections with normals parallel to the applied load follow a Reuss like variation with A_{hkl} but with slope reduced to 53% of that expected in the simple model for mild steel. The perpendicular strains are related to the parallel results by Poissons ratio ν=0.3.

Neutron diffraction has been used to follow the strains in two phases of a metal matrix composite. When subjected to a uniaxial stress the strains parallel to the loading direction in the components of a silicon carbide particulate reinforced aluminium composite behave closer to a uniform stress situation than uniform strain. However the strain in the silicon carbide normal to the loading axis exhibited anomalous behaviour and appeared to show tensile strain at low stress levels. The measured residual strains

induced on unload can be used to verify the theories of strain response in composite materials.

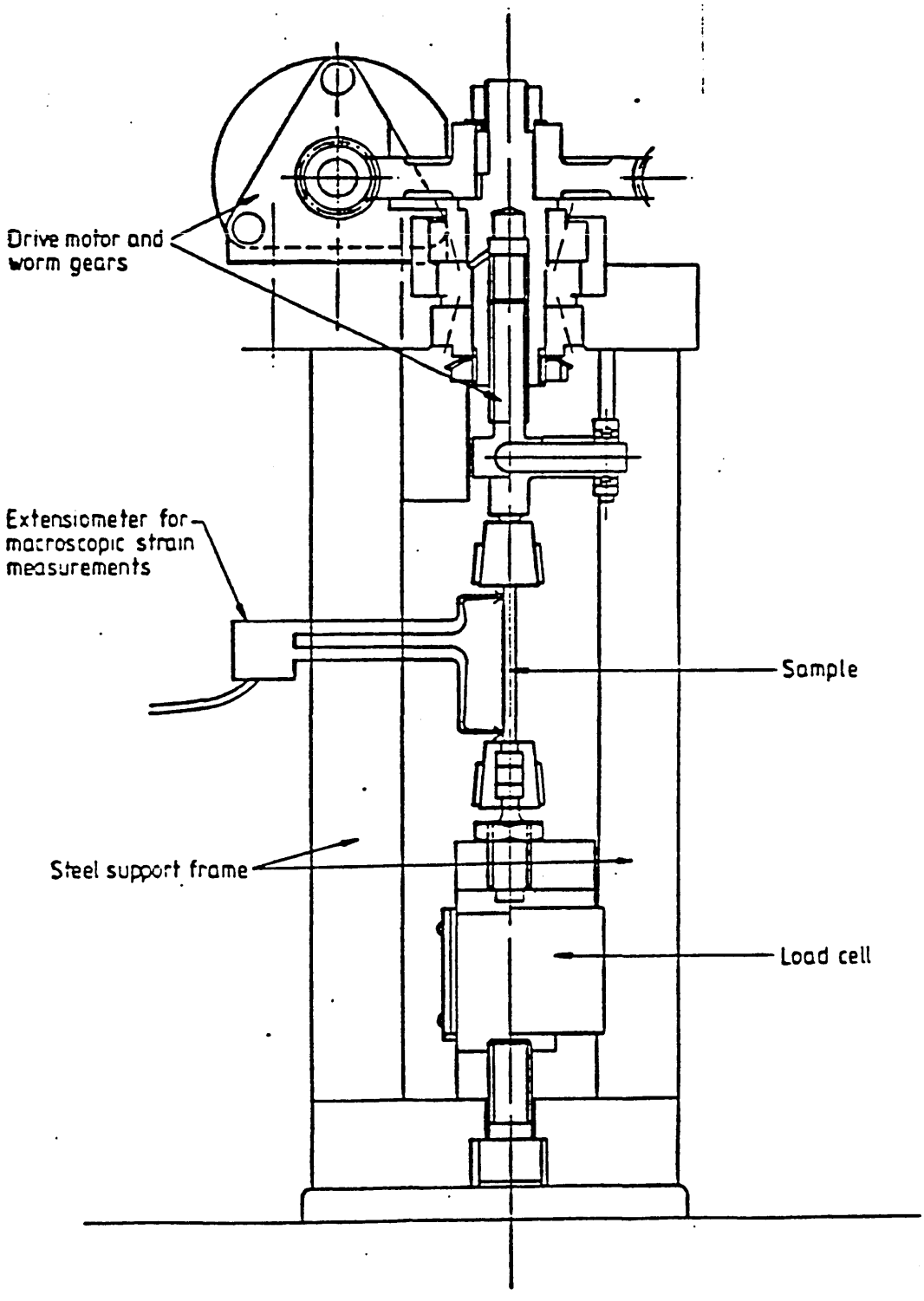
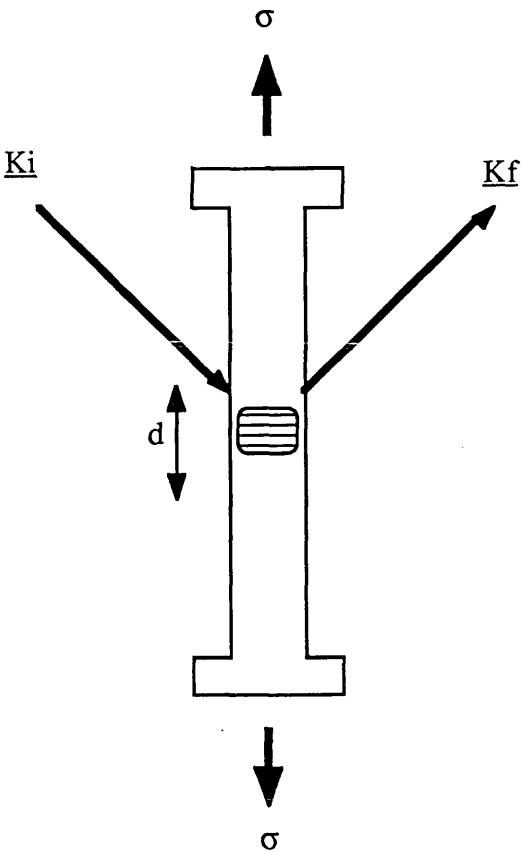


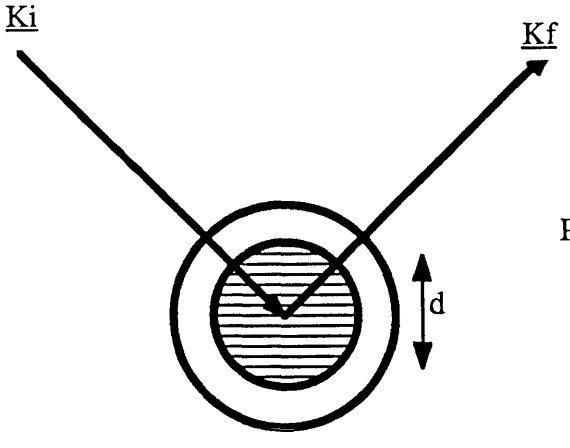
Figure 3.1: Compact tensile stress rig for calibration measurements



Plan view, not to scale

[Sample horizontal]

Figure 3.2a: Tensile specimen, Q parallel to applied load



Plan view, not to scale

[Sample vertical]

Figure 3.2b: Tensile specimen, Q perpendicular to applied load

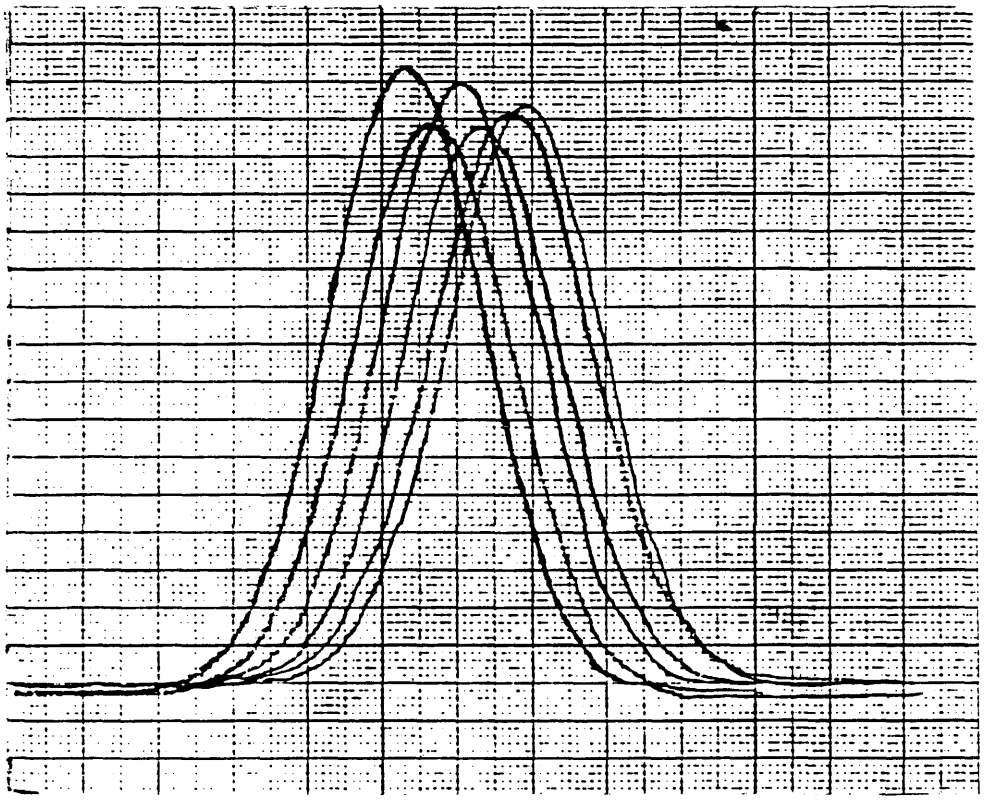


Figure 3.3: Peak shifts of iron 310 reflection between 0 and 500MPa.

[Peak centre at 101.5°2θ, width ≈0.5°2θ]

Figure 3.4a: Mild steel strain anisotropy parallel to applied load.

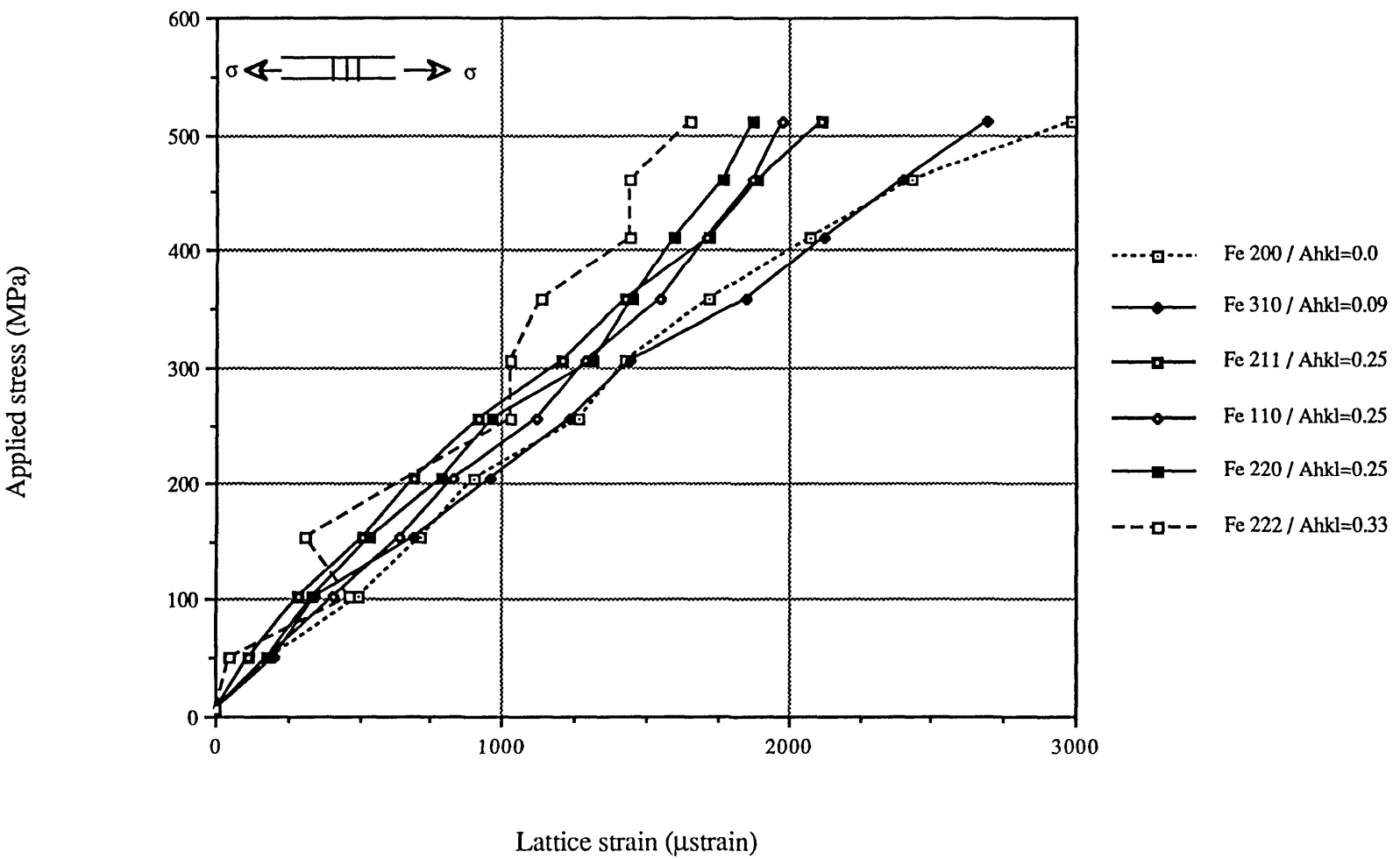


Figure 3.4b: Mild steel strain anisotropy perpendicular to applied load.

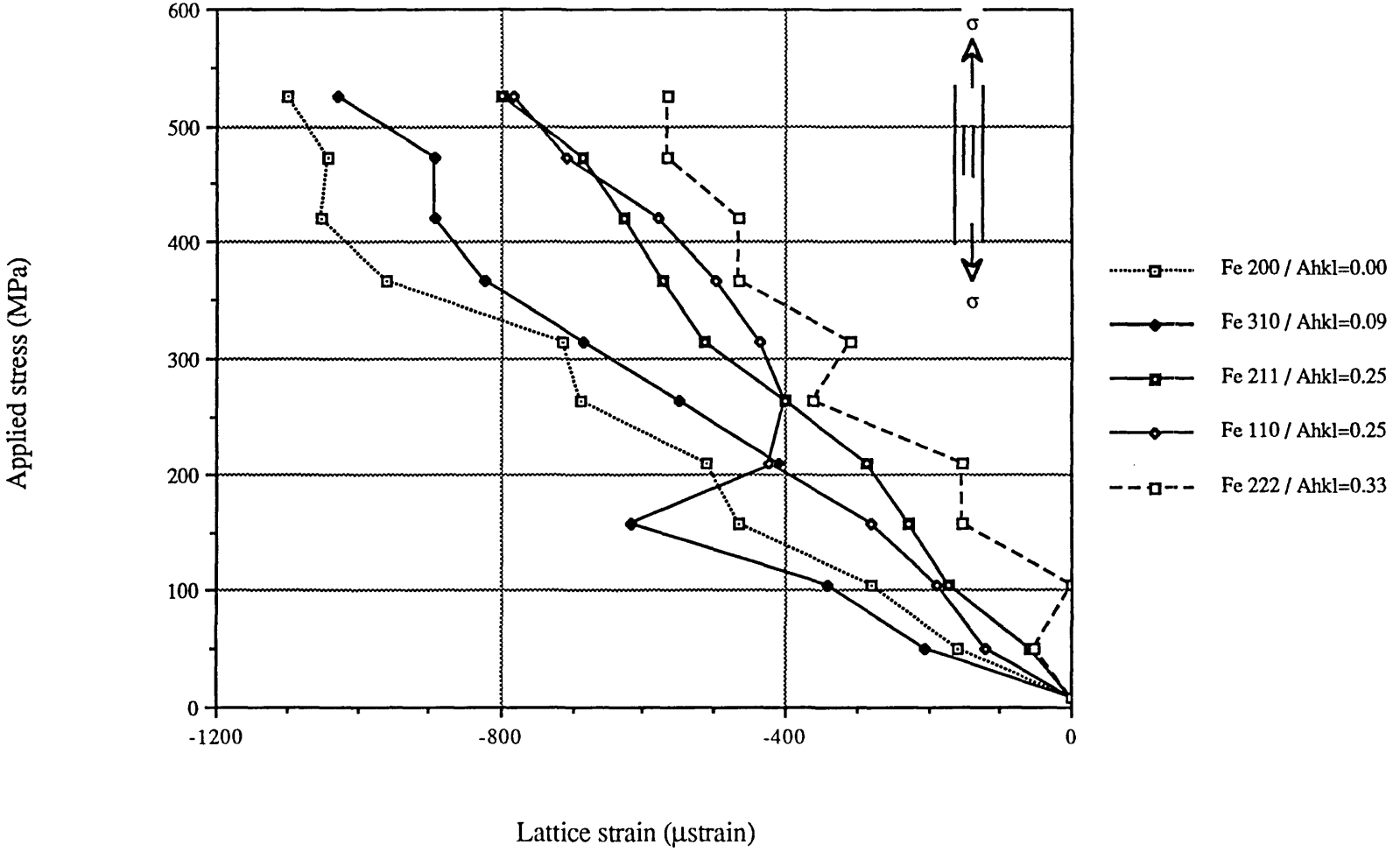


Figure 3.5a: Mild steel residual strain parallel to loading direction

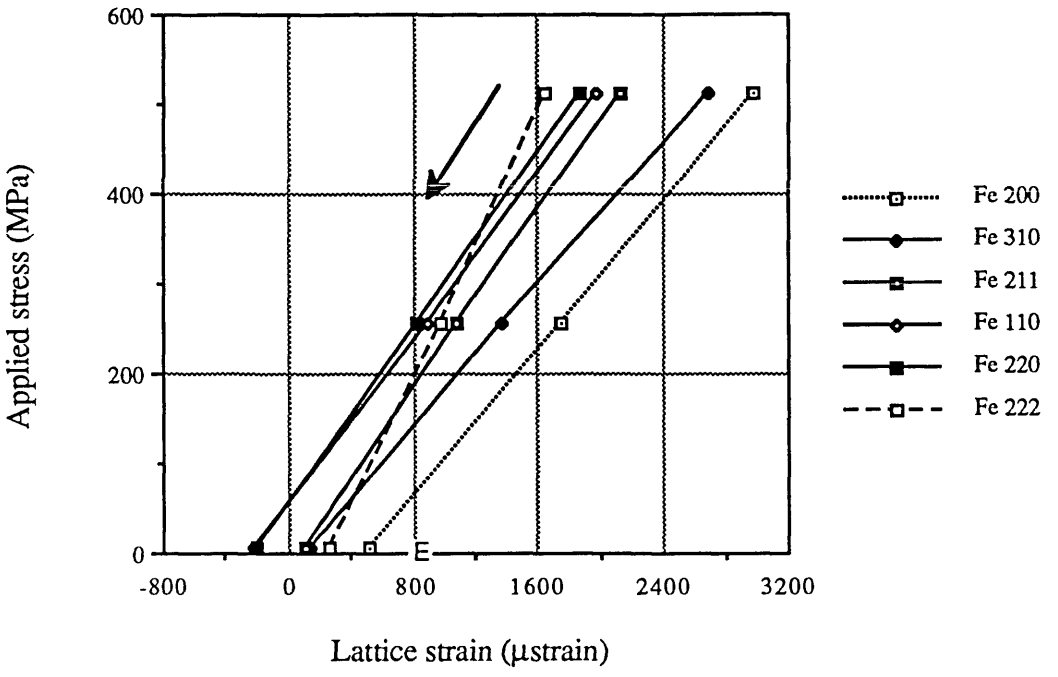


Figure 3.5b: Mild steel residual strain perpendicular to loading direction

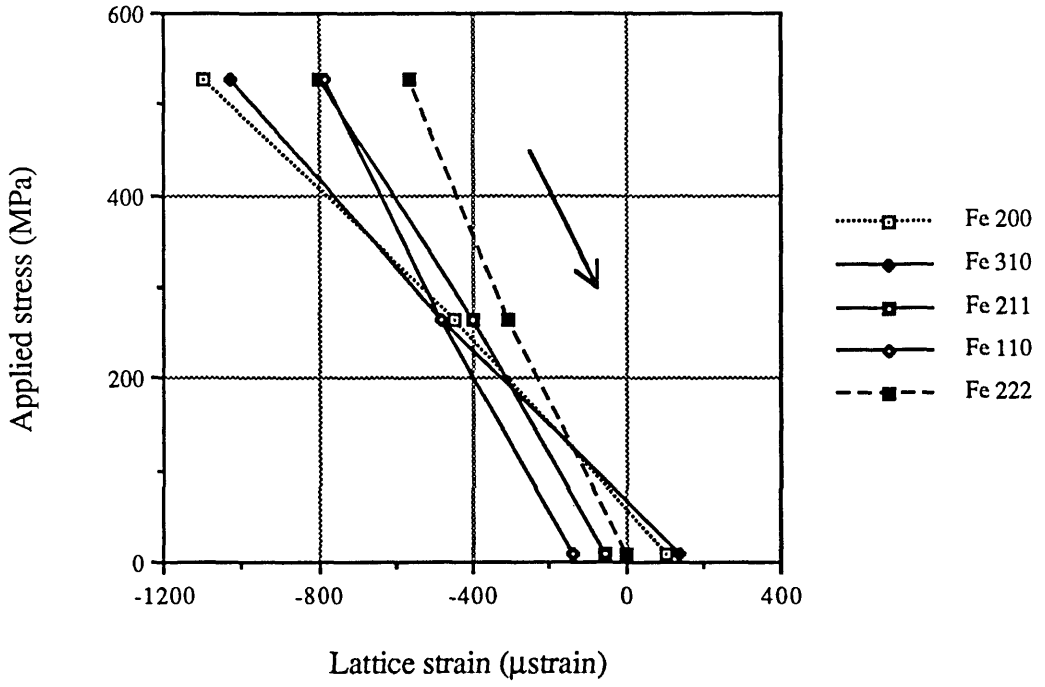
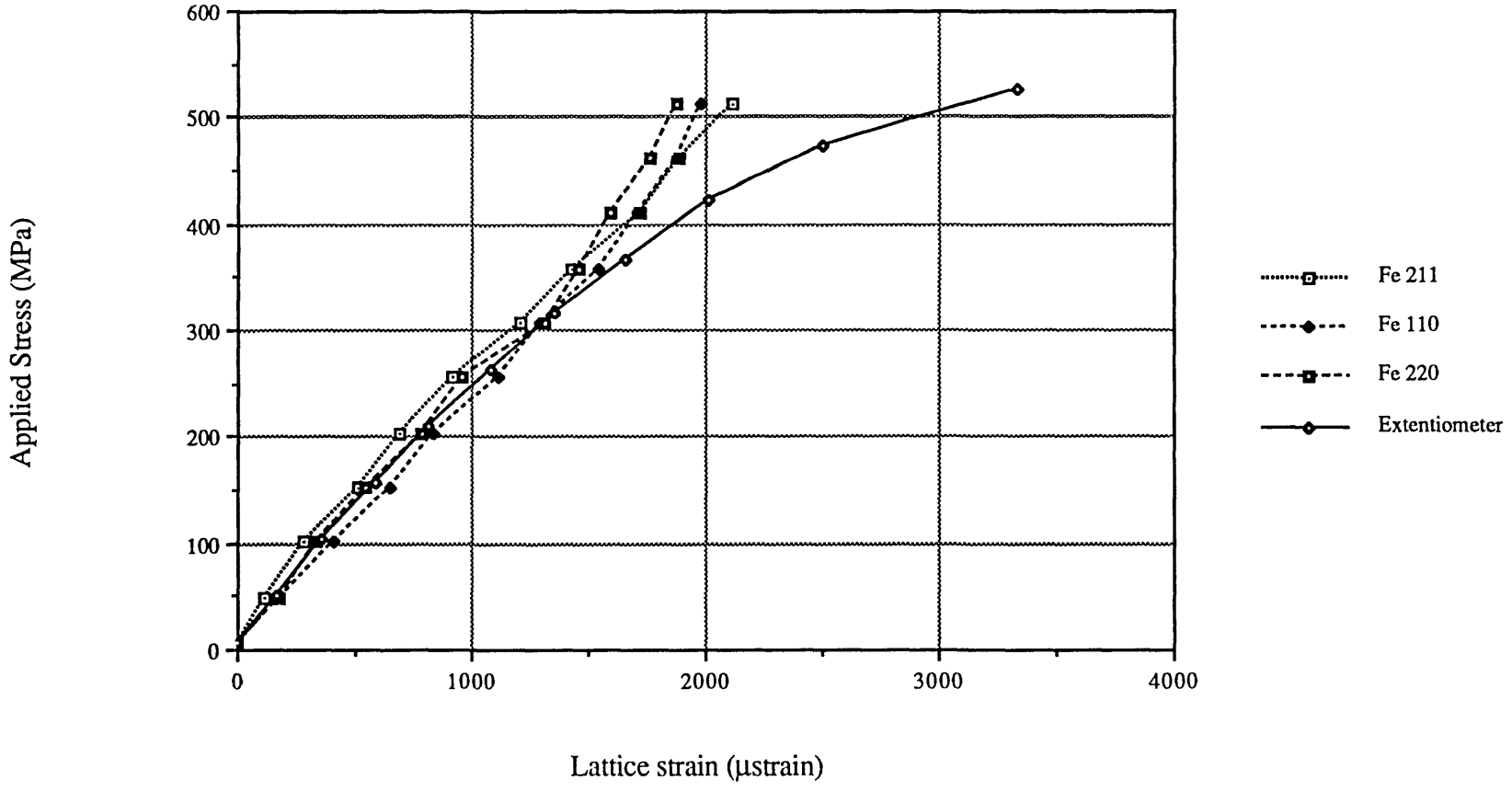


Figure 3.6: Mild steel, macroscopic strain vs. [211], [110] and [220] lattice strains.



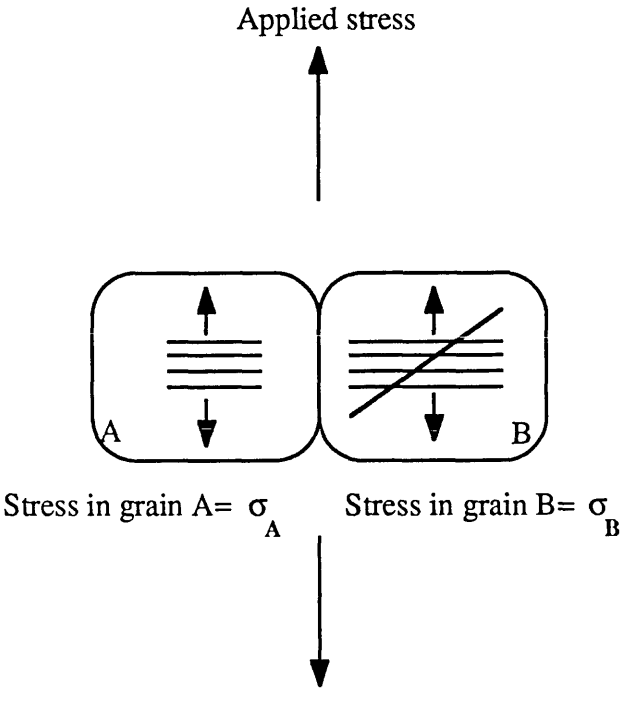


Figure 3.7a

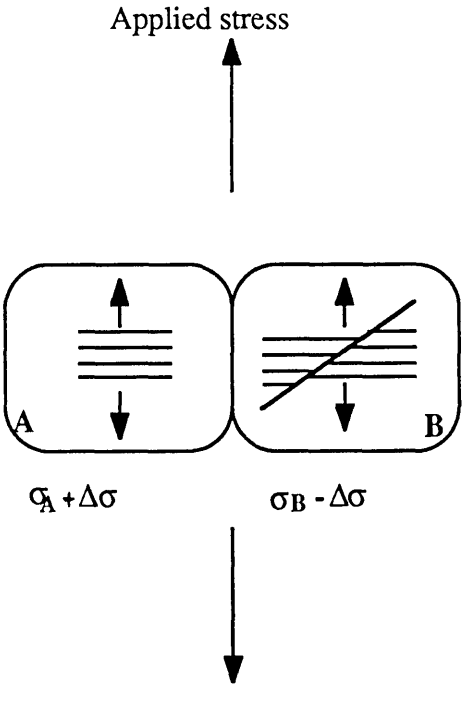


Figure 3.7b

Figure 3.7ab: Simple model of stress redistribution resulting from localised slip under conditions of constant applied stress

Figure 3.8: hkl dependence of elastic compliance in mild steel.

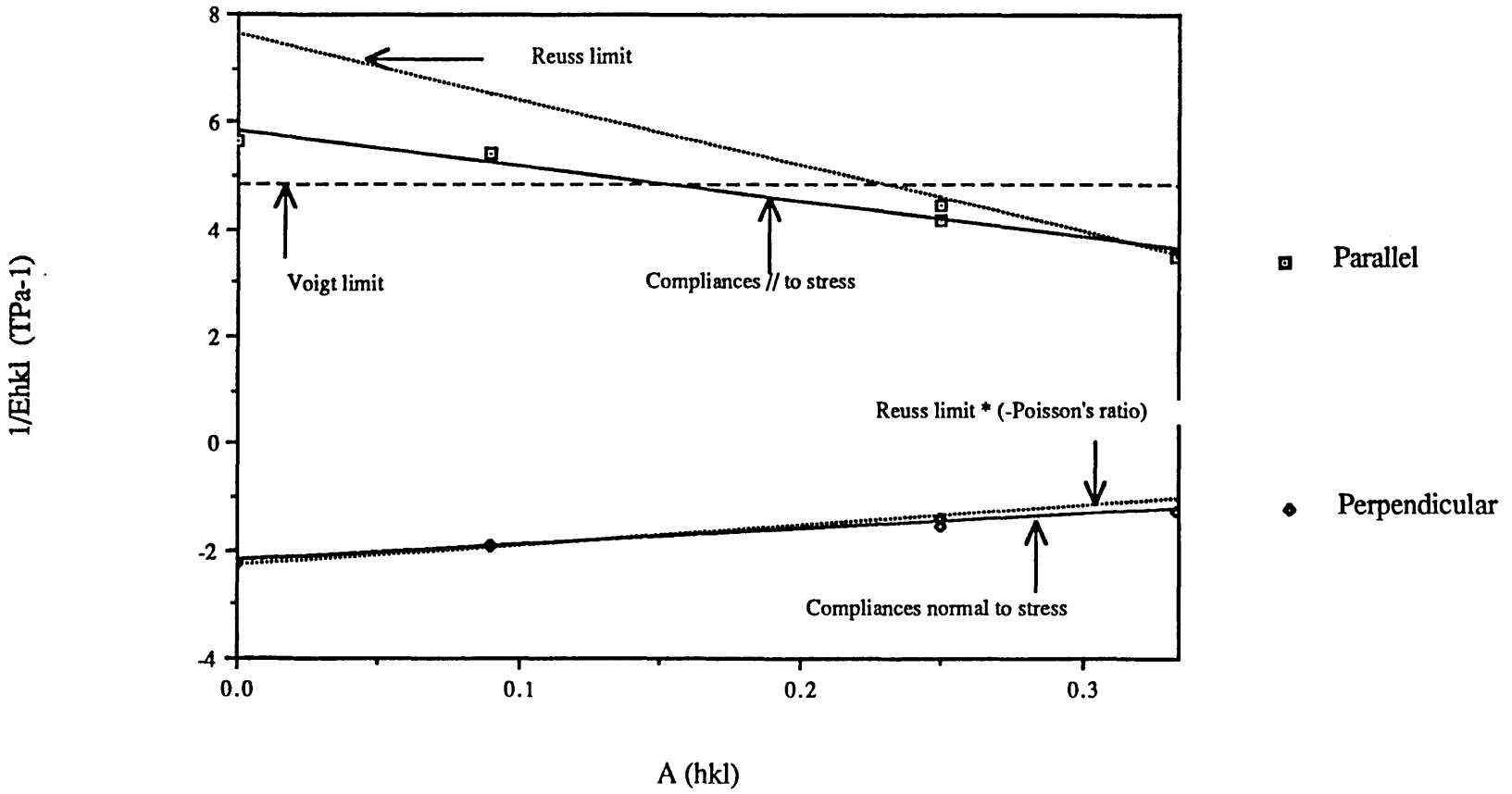


Figure 3.9a: hkl dependence of lattice strain parallel to an applied load in an Al-SiC MMC.

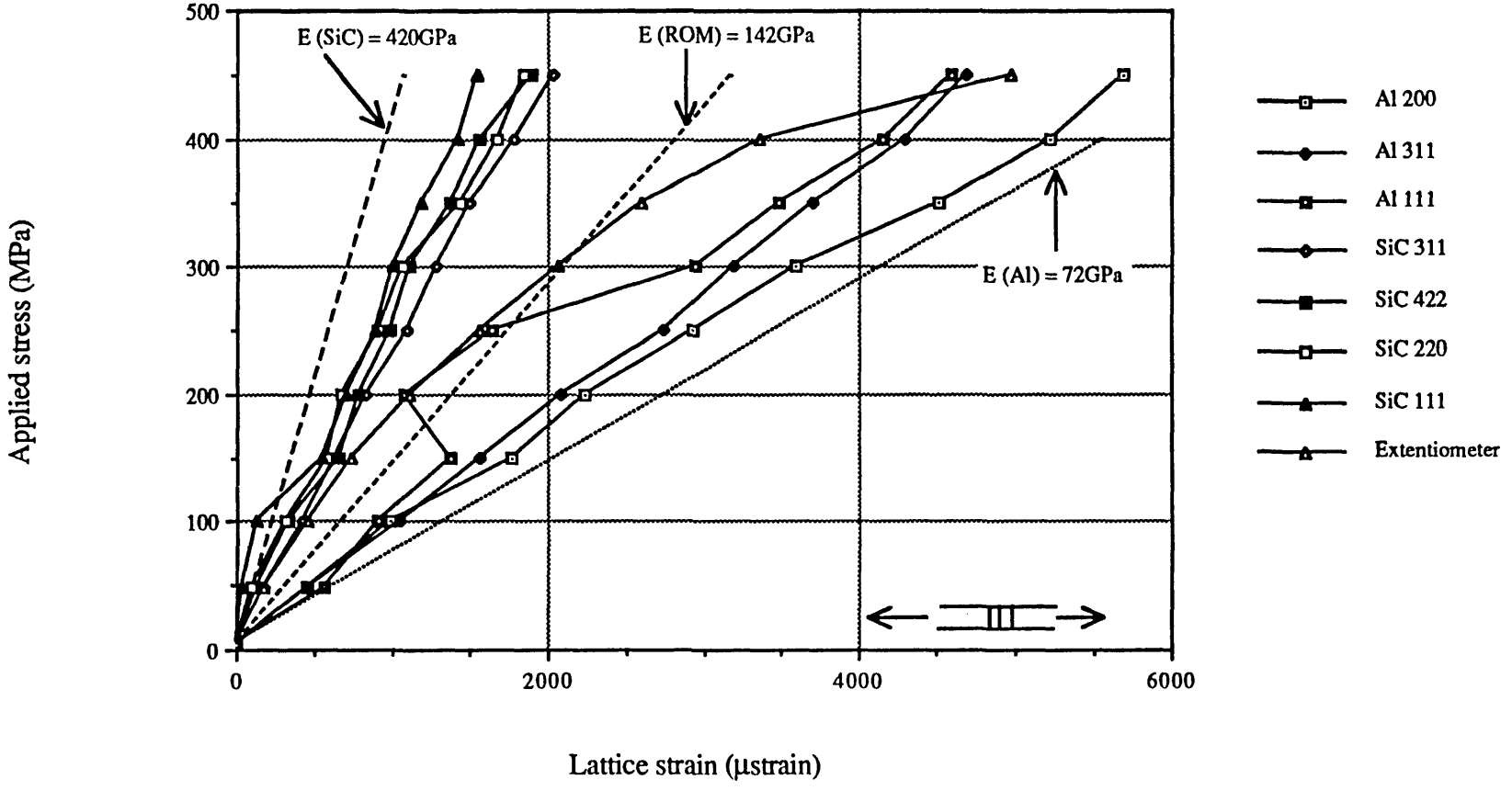


Figure 3.9b: hkl dependence of lattice strain perpendicular to an applied load in an Al-SiC MMC.

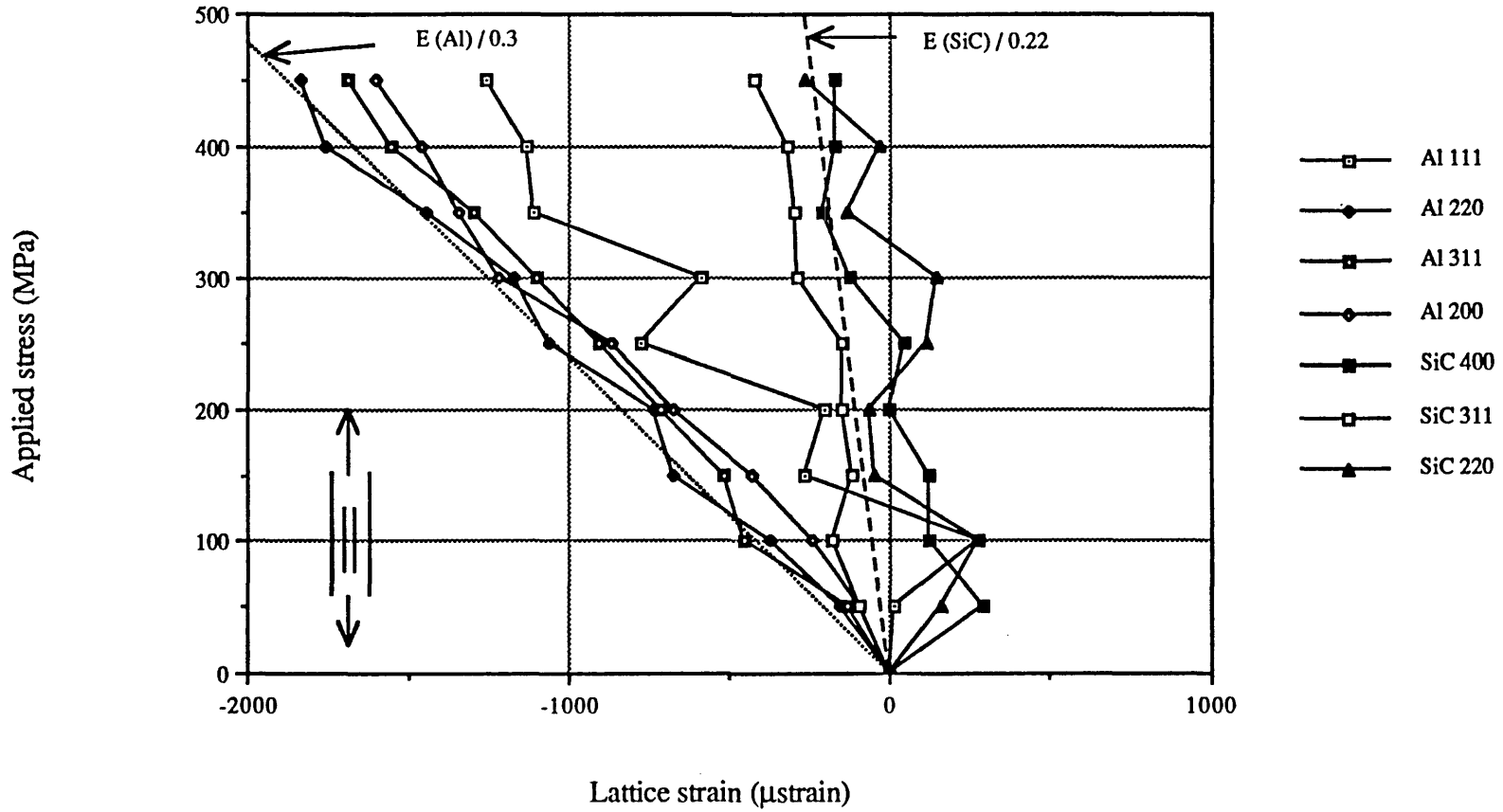
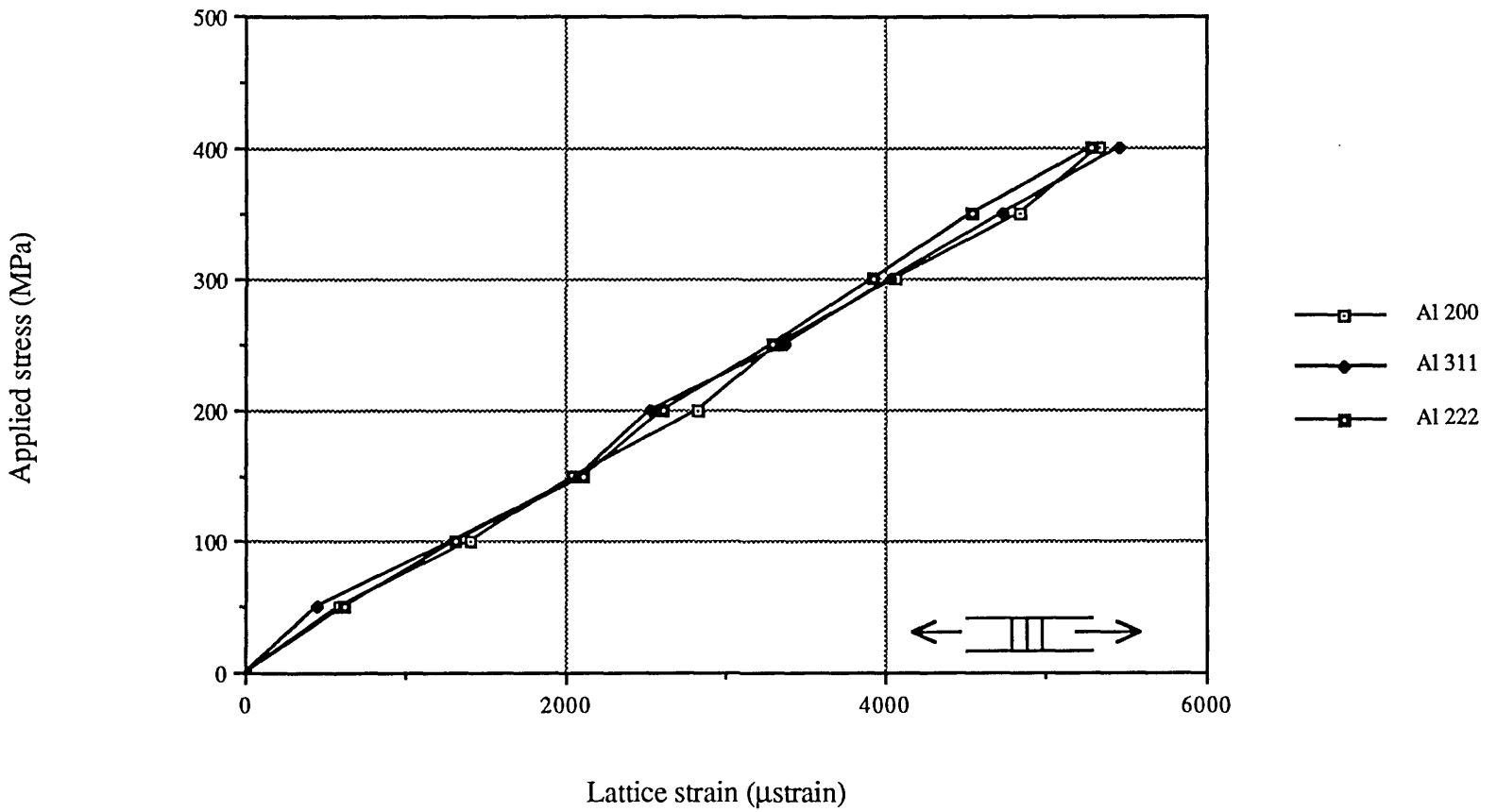


Figure 3.10: Lattice strains parallel to an applied stress in Al 2014 alloy.



CHAPTER 4

Equipment development at the I.L.L.

4.1 Introduction

Efficient stress measurement at the I.L.L. has been inhibited by three features; long preparation times, limited specimen movement and labour-intensive data processing. Refinements to the alignment procedure for the incident and exit masks permit faster and more accurate definition of the sampling volume. Use of a theodolite has been adopted and specimens can now be positioned to at least $\pm$ 0.1mm relative to a fixed point. A modular manipulation system has been designed, tested and installed on D1A. It gives precise, repeatable remotely controlled sample movement in the neutron beam and can be operated from a personal computer. The system is capable of installation on any neutron instrument and the 5 motion axes can be assembled in different configurations for specific applications. Finally, the data processing route has been modified to minimise operator intervention, allowing real-time analysis and the flexibility to alter the experimental program during the measurements.

4.2 General

For monochromatic radiation the displacement of a Bragg reflection due to engineering strains can be as small as 0.01° depending on the diffraction angle. Thus a diffractometer must have sufficient instrumental resolution to detect the small shifts in angle. The resolution of a diffractometer using a crystal monochromator is determined from the uncertainty in wavelength and diffracted angle. The former is dependent on the angular resolution before and after the monochromator and also on its mosaic spread (Windsor, 1986). The latter is dependent on the length and width of the soller collimation between the sample and the detector. An expression for the instrumental resolution, $\Delta d/d$ is given by Allen (1985):

$$\left[\frac{\Delta d}{d}\right]^2 = \left[\cot\theta_M \Delta\theta_M\right]^2 + \left[\cot\theta_S \Delta\theta_S\right]^2 \qquad (4.1)$$

where θ_M is the monochromator Bragg angle

$\Delta\theta_M$ is the collimation angle of the beam from the monochromator

θ_S is the sample diffraction angle

$\Delta\theta_S$ is the uncertainty in diffraction angle.

(The equivalent equation for a time of flight spectrometer is given in chapter 8, equation 8.1). By equation 4.1 the best resolution on a monochromatic diffractometer is achieved at a large scattering angle from the monochromator. The sensitivity to change in lattice strain primarily depends on counting time but can be defined as some fraction of the instrumental resolution.

Most diffractometers were designed for crystallography applications and their configuration is not ideal for engineering strain measurements. In general, there is limited space around the sample position for a manipulation system, particularly if the component itself is large. Also, since most conventional experiments attempt to maximise the specimen volume in the neutron beam there is rarely any facility for defining a small incident beam profile. On some instruments, notably HRPD and POLARIS at ISIS, the sample position is enclosed in a vacuum tank which further hampers installation of a manipulation system and positioning of specimens.

Three issues must be addressed to adapt a diffractometer for measurements of engineering strain. First, a point in space corresponding to the centre of the sampling volume must be repeatably identifiable. Second, incident and exit collimation is necessary to define a sampling volume. Third, a system for translating and rotating specimens with respect to the sampling volume must be installed.

On D1A preparation for strain measurements takes between 8 and 24 hours depending on the required precision. This is often an appreciable fraction of the beam time available for the experiment and its minimisation is highly desirable. In this chapter changes to the existing system are described which reduce the set-up time and improve the spatial resolution of the sampling volume.

Initially a robotics option was examined for sample reorientation. However a robot arm would have to stand up to 1metre from the sample position and massive samples would apply severe torques. In view of the positioning precision and repeatability required, the size and cost of an appropriate system precluded its consideration for use on D1A. Instead a modular movement system was selected.

4.3 The high resolution powder diffractometer D1A

To reach D1A thermal neutrons from a 50MW reactor pass along a guide tube to a monochromator with a take-off angle of 123°. The monochromator consists of a mosaic of germanium mounted on a substrate out of the scattering plane, which has a focussing effect and gives a beam profile at the sample position with dimensions 20mm by 20mm. The convergence in the vertical plane is approximately 6° and in the horizontal plane the edges of the neutron beam are parallel. Rotation of the monochromator offers a selection of wavelengths.

Plan and horizontal section diagrams of the instrument are given in figures 4.1 and 4.2. The height of the neutron beam over the diffractometer table is 500mm and the distance between the axis of rotation of the base and the front of the detector is only 350mm. The detector bank consists of ten He^3 tubes (at 5 atmospheres) each of which is 50mm in diameter and 100mm long. Each tube is separated from its neighbour in the horizontal plane by 6°, thus 60° 2θ can be scanned during each 6° movement of the detector bank. A total of 0 - 160°2th is accessible around the sample position. Sollers slits with an effective area 100mm high by 20mm wide collimate the neutrons between the sample and each detector tube. The collimation has a horizontal divergence of 10' and 6.6° in the vertical direction. The blades of the sollers are 25 micron thick aluminized mylar foil, coated with 25 microns of gadolinium oxide paint.

4.4 Definition of a sampling volume

The strain resolution, measuring direction and sampling volume are all affected by the diffraction angle. Good strain resolution is achieved for large scattering angles due to the cotθ term in equation 2.8. The best spatial resolution in the specimen is achieved for 90° scattering and the measuring direction in space depends on the lattice reflection. Thus in contrast to conventional powder diffraction and despite the fact that all lattice reflections contain strain information, strain measurements with monochromatic neutrons usually address a single lattice reflection during each measurement. Its selection is usually a compromise between the noted features and its intensity.

The sampling volume is determined by the intersection of the incident and

diffracted neutron beams. By appropriate masking, the two beams can be restricted so that the detector can only receive neutrons which are scattered from a volume defined by the masks. Generally an approximately cubic sampling volume is used which remains constant in space for a particular scattering geometry. In some specimens symmetry exists and the shape of the sampling volume may be modified accordingly (Pintschovius, 1982). Precise definition of the incident and exit beams is critical for measurements in regions of steep stress gradients. Coarse alignment can be performed using Polaroid photographs with neutron sensitive film but a more precise method is required.

The first step in preparing D1A for strain measurement is to identify a reference position which corresponds to the centre of the sampling volume. The detector collimation is directed over and parallel to radii from the table centre. Thus the axis of rotation of the omega table defines the reference position in one plane. The centre of the beam is 500mm above the base of the diffractometer which identifies the reference position in a second plane. By measuring the height above the diffractometer base and observing a spike with the theodolite during rotation of 180° by the omega table the reference position can be identified. The theodolite and cathetometer are aligned on the reference position approximately normal and at a shallow angle to the incident beam (figure 4.1). In practice the positions of the theodolite and cathetometer are determined by the space available near the instrument instead of the ideal situation where they would both be placed at the beam height and separated by 90°. Nevertheless, they provide an optical identification of the centre of the sampling volume which remains unchanged for the duration of each experiment. The quality of the optics in the theodolite permits specimens to be positioned with an accuracy of $\pm$ 0.1mm. All alignment is performed optically. Some attempts have been made to use a laser to show the direction of the incident beam however it proved inconvenient and did not facilitate the alignment or subsequent positioning of specimens.

A section of optical bench is mounted above the incident beam to support the input aperture. Using manual Microcontrol translators the optical bench is adjusted until it lies on a radius to the reference position. This is achieved by placing a thin vertical

aperture at the reference position and supporting an equivalent slit as an input aperture. By noting the transmitted intensity for different orientations of the optical bench and with the equivalent slit at different radial positions from the central axis, the correct orientation can be calculated. If the optical bench is not parallel to the incident beam then a horizontal displacement of the sampling volume will be noted for different radial positions of the input mask. This is illustrated in figure 4.3. If the input mask is retracted along line AB then the effective sampling volume will be displaced by a distance δ. Different size samples necessitate the radial displacement of the input mask so this alignment is important. A selection of precise incident aperture masks have been fabricated from cadmium and can be changed in a few seconds. The input mask holder is shown in figure 4.4 with a vertical 2mm input aperture.

During each measurement on D1A only one detector is used to record a diffracted reflection. Diffracted radiation lies on the surface of a Debye cone and the exit beam is restricted by installing a vertical slit between the specimen and the detector. The usable width of each detector on D1A is approximately 20mm. Initially a detector is masked by a 4mm cadmium slit. Then an extendible support is attached above the detector from which a narrower exit slit can be supported close to the sample (fig 4.5). A rotation and translation procedure similar to alignment of the incident aperture is used to orientate the extender. Alignment of the slit in the diffracted beam is initially performed optically and is refined by using a diffracted reflection from a 1mm diameter steel pin. A variety of exit slits from 3mm to 0.3mm are available. Changing the exit slit without disturbing the alignment is a delicate operation but can be performed in a few minutes.

4.5 Effect of the input aperture position on the beam profile

The 6° vertical convergence of the neutron beam complicates the definition of an accurate beam profile. The vertical extent of the beam passing through the reference position increases with radial displacement of the input mask. The effect was examined by measuring the transmitted intensity during traverses of a 0.5mm cadmium slit through the reference position for different positions of a 2 * 2mm input aperture. Results were obtained with the input aperture between 20 and 60mm from the reference

position.

The intensity profiles obtained from a horizontal traverse from a vertical slit and a vertical traverse of a horizontal slit are given in figures 4.6 and 4.7. The horizontal limits of the beam are almost unchanged for the 20 and 60mm displacement of the input aperture from the reference position (fig 4.6). However in the vertical plane the extent of the beam increases by a factor of 2 between aperture positions of 20 and 60mm from the reference point (fig 4.7). At 20mm the vertical extent of the intensity profile is approximately 2mm but each subsequent 10mm displacement of the aperture from the sampling volume increases its extent by approximately 0.5mm. The broadening is asymetrical and the effective centre of the sampling volume is displaced downwards for increasing radial separation of the input mask from the reference position.

Thus the horizontal definition of the incident beam is independent of the position of the input aperture. In the vertical plane, accurate vertical definition of the beam profile requires the input aperture to be not more than 20mm from the reference position.

4.6 Calibration using a powder cell

A further check on the positioning accuracy and definition of the sampling volume was made with a hollow aluminium cell filled with 6-9 micron iron powder. The cell was flat sided approximately 8cm square with an inner thickness of 6mm. The variation in intensity for a diffracted reflection was recorded as the cell was completely traversed through the sampling volume. Since free unconfined powder cannot support a macrostress, the peak centre for each measurement was not expected to vary. Near-surface measurements were made to examine the effect of partial submersion of the sampling volume in the material.

The iron (211) reflection with a wavelength of 1.905Å was used, which gave a diffraction angle of 109.5° 2th. A 2mm square input aperture was combined with a 2mm exit slit. In plan view the sampling volume was a rhombus (fig 4.8). Traverses were made on a line normal to the cell face; first with the scattering vector in the plane and second normal to the face of the plate (fig 4.9 ab). Due to the shape of the rhombus the effective dimension of the sampling volume in the direction of the traverse was different for the two orientations. In figure 4.9a the scattering vector is parallel to the

cell face and the shorter diagonal ac of the rhombus enters the surface first. With the scattering vector normal to the surface of the cell the longer diagonal db enters first (fig 4.9b). The distinction is important because the apparent width of the specimen will vary in the two cases and is also relevant to positional corrections at surfaces.

The intensity profile of a diffracted peak as a specimen is translated into a sampling volume provides the least ambiguous determination of its position relative to the probe region. Peak intensity profiles for the two scans through the powder plate are given in figures 4.10 and 4.11. The shapes are different for the two orientations because of differing path lengths in the material. For the in-plane measurement (fig 4.10) the path length of neutrons through the material is constant and equal to pbq (fig 4.9a). For the measurements normal to the surface the path length increases with the depth of measurement (fig 4.9b). This causes increasing absorption which gives the asymetric shape in figure 4.11.

If the peak intensity is assumed to be proportional to the area of the rhombus submerged in the material, the intensity variation can be predicted for the two orientations. For the normal direction the absorption is included by using an exponential decrease in intensity with a linear absorption coefficient of 0.121 mm^{-1}. The agreement between the predicted and measured intensities (figs 4.10 and 4.11) is good and indicates that the shape of the sampling volume is close to that depicted in figure 4.8.

The peak centres for the two orientations are given in figures 4.12a and 4.12b. The scatter for the normal measurements is larger than the planar results because the scans were limited to four points over the peak. The significant feature in figure 4.12a is the apparent strain of 250μstrain at the surface. This is an artifact of the peak fitting routine and was shown to result from a systematic error in the fitting program which occurred as the peak height fell below 50 counts (background <5). A similar effect was not noted in the Z orientation since the intensity did not drop below 50. It is concluded that reflections with a peak height less than 50 should not be used.

4.7 Manipulation system

4.7.1 Specification

Strain measurements are made at different positions in a component by moving it through the sampling volume. For a wavelength and lattice reflection combination, the direction of strain measurement is altered by varying the orientation of the specimen relative to the scattering vector. Thus, the minimum requirement for a manipulation system is reliable and accurate multi-axis movement of a component. The system must support specimens with masses from a few grammes to many kilogrammes. Control must be possible from an instrument computer and also as a stand-alone facility. The system described below was designed for D1A but is self-sufficient and can be interfaced with other instruments. The translator and rotary stages were purchased from Time and Precision Ltd and the control system from Quin Systems Ltd.

4.7.2 Hardware

The new 5 axis motion system is illustrated in figure 4.13. A modular combination of translators and rotary stages are mounted on a base plate which is attached to the diffractometer omega table. The base plate can be rotated and then locked into position to give the system a specific orientation on the omega table. Apart from the small rotary stage (mounted at the top in figure 4.13) each stage is doweled to permit precise relocation in any combination. If necessary, one or more slides can be removed. Adaptor and spacer plates are available to customise the system for special requirements. Two low profile linear translators provide approximately 250mm of horizontal translation in two normal directions in the horizontal plane. The vertical elevator provides 100mm of vertical travel and is driven by a toothed drive belt which raises a table on four vertical columns. This design is ideal for use in this application because there is no protrusion above the raising platform. The large rotary stage can be mounted with its axis vertical or horizontally using a right angle bracket. A photograph of the manipulation system in position on D1A is shown in figure 4.14.

The slides can quickly be dismounted and are easily transportable. All the stages are driven by DC servo motors which offer better reliability than digital stepper motors.

Each stage is fitted with a datum sensor and an encoder to give absolute positional measurements. The horizontal translators can be positioned to within 5 microns and the vertical translator to within 1 micron. The linear translators and the elevator are fitted with hardware limit switches to prevent overrun. Apart from on the small rotary stage, samples up to 50 Kg can be moved by each of the four axes (although it is unlikely that this upper limit will ever be required). A Psion Organiser hand-held micro computer with an RS232 communication module provides manual control of the manipulator by the instrument and reduces the labour-intensive aspects of alignment and testing.

4.7.3 Control system

The manipulator control system is housed in a purpose built rack which also contains the motor amplifiers. A schematic of the control system is given in figure 4.15. Each axis is controlled by a separate microprocessor and can be addressed individually, sequentially or simultaneously. In practice sample movement time is short compared to measuring time and all movements are performed as a simple sequence of movements on each axis.

The control of each axis is comprehensive and all operating parameters can be set from the software interface. The proportional gain and feedback constants were optimised prior to installation on the instrument. The velocity, acceleration and setting precision are also treated as fixed parameters though they are occasionally changed. If the highest precision is required the settling time can be some tens of seconds. Positions can be demanded as encoders pulses or if a scaling factor is used as absolute or relative positions in millimeters or centimeters. The scaling factor can be set by the operator. The position of a stage can be zeroed at any arbitrary point on its travel. For example a surface can be moved to the reference position and the translator zeroed at that point. Software limits for the maximum and minimum travel can be set which if exceeded disable the motor. Control commands are two letter mnemonics, such as MA for "move absolute" followed by a numeric input. A detailed description of the available commands is given in the "Quin Systems- Programmable Transmission System User's Manual".

The control system can be addressed via an RS232 serial interface by the Psion,

a microcomputer or by the D1A Microvax. The D1A diffractometer is controlled using a standard software package called MAD. This enables users to operate the instrument by setting scans, count times etc. The D1A software has been adapted so that the manipulator may be addressed from within MAD, instructions are simply prefixed by the letter Q. Thus, list files containing a sequential mixture of instrument and manipulation commands can be operated from within MAD.

4.8 Data processing

On a monochromatic diffractometer, Bragg reflections are measured by scanning the detector through the peak. Typically scans are made in steps of 0.1° to one degree on either side of the position of maximum intensity. The resultant peak in neutron intensity as a function of diffraction angle is fitted to give its height, width and centre. Gaussian or Lorentzian shapes are the standard peaks fitted to reflections obtained on monochromatic diffractometers. The definitions are given in equations 4.2 and 4.3 where H is the peak height, W as the full width at half maximum (FWHM) and C as the centre:

$$\text{Gaussian, } y = H \exp\left(-\left(\frac{(x - C)}{(0.60056 * W)}\right)^2\right) \tag{4.2}$$

$$\text{Lorentzian, } y = \frac{I * \left(\frac{W}{2}\right)}{\pi (x - C)^2 + \left(\frac{W}{2}\right)^2} \tag{4.3}$$

In equation 4.3, I is the integrated intensity of the peak which is related to the height by:

$$I = \frac{H * \left(\frac{W}{2}\right)}{\pi} \tag{4.4}$$

Powder samples produce Gaussian peak shapes. Similarly, most engineering components containing regions of uniform or linear stress variation also give single Gaussian peaks, although their width varies with the gradient of the stress variation. However, if the sampling volume is centered on an irregular stress variation or for example over the boundary of a heat affected zone, departures from single Gaussian behaviour has been observed. Also, in regions of extensive plastic damage Lorentzian

peak shapes sometimes offer better fits than Gaussians. The interpretation of peak shapes and line broadening is covered by Noyan (1987).

Peaks are fitted using the PKFIT program at the I.L.L. For each fit, noisy data can be removed or altered and the number and type of fits can be selected. Any combination of up to 6 peaks may be fitted to each scan, although most engineering scans only require a single Gaussian fit for each measurement. The operator inputs an estimate of the peak parameters from which the program attempts a refinement. A constant background is usually applied to engineering scans and is important for consistent results. Any of the parameters may be constrained although this is rarely applied unless, for example a contamination peak is observed. The fitting routine performs an iterative least squares fit on the data and outputs the final parameters and a χ^2 value which relates to the goodness of fit. χ^2 is defined by:

$$\chi = \sum \frac{(y_{val}(i) - y_{cal}(i))}{n_v - n_p} \qquad (4.4)$$

where n_v is the number of data points in the fit,

n_p is the number of parameters,

y_{val} is the data point value,

y_{cal} is the calculated values.

A typical engineering traverse through a component may generate between 10 and 50 scans of the same Bragg reflection. A data processing route has been developed to permit automatic fitting of a sequence of the same Bragg reflection. The raw data is stored in tabular form and is automatically sorted according to a position given in the title of each scan. The intensity is normalised to the incident monitor and the strains and stresses are calculated using a value of θ_0 selected by the operator or by applying an equilibrium constraint. The resultant strains and stresses may be plotted on linear or contour graphs as appropriate. The processing route is illustrated in figure 4.16.

4.9 Recommendations

The largest issue for engineering strain measurement on D1A remains the time taken to prepare the positioning and aperture systems. Despite the improvements described in this chapter setting up remains time consuming. In particular, the aperture

systems are vulnerable to accidental misalignment if touched during specimen traverses. If this occurs the operator is faced with a time consuming realignment procedure. The software limits on each translator do help but the variety of specimens, geometries and orientations mean that they rarely give complete protection. One solution involve the installation of a photosensitive cell system which could be aligned adjacent to the masks and which would disable the motors if mask interference threatened. A number of small practical problems still need to be addressed. These include the large quantity of cable associated with each translator. Since each motor is allocated 10m of shielded cable for both the drive and the encoder the total is unwieldy and a distributive drum would improve their storage around the instrument and would help to avoid their interference with the detector bank rotation. A large accessible emergency stop button would also be an advantage. Finally most specimens which have been examined to date have had a flat face or a convenient geometry however some attention should be addressed to gripping unusual specimen, in particular for rotating specimens about a horizontal axis.

4.10 Conclusions

The peak shift due to a lattice strain at 120°2th is approximately double the shift due to the same strain at 80°. Measurement accuracy is optimised by selecting a large scattering angle provided this does not unacceptably compromise the shape of the sampling volume or the intensity of the reflection. The shape of the sampling volume produced by a 2mm square input aperture combined with a 2mm exit slit has been examined using transmitted and diffracted radiation. Severe defocusing, due to the convergent monochromator, was observed in the vertical plane as the input aperture was moved away from the sampling volume. However in a horizontal plane the neutron beam is parallel for aperture positions up to 60mm from the sampling volume. If accurate vertical definition of the neutron beam is required the input aperture must not be more than 20mm from the sampling volume. Measurements made on a powder plate indicated that the sampling volume is well defined in a horizontal plane but that peaks less than 50 should not be used.

A 5 axis manipulator has been interfaced to the D1A instrument controller although it can also be independently operated. Precise location of a component relative

to a fixed point in the neutron beam is possible. Positioning accuracies of better than 10μm can routinely be obtained and samples up to 50kg can be moved. A variety of design features have been incorporated into the operating system to facilitate experimental operation. Finally the data processing route has been improved to permit faster on line analysis.

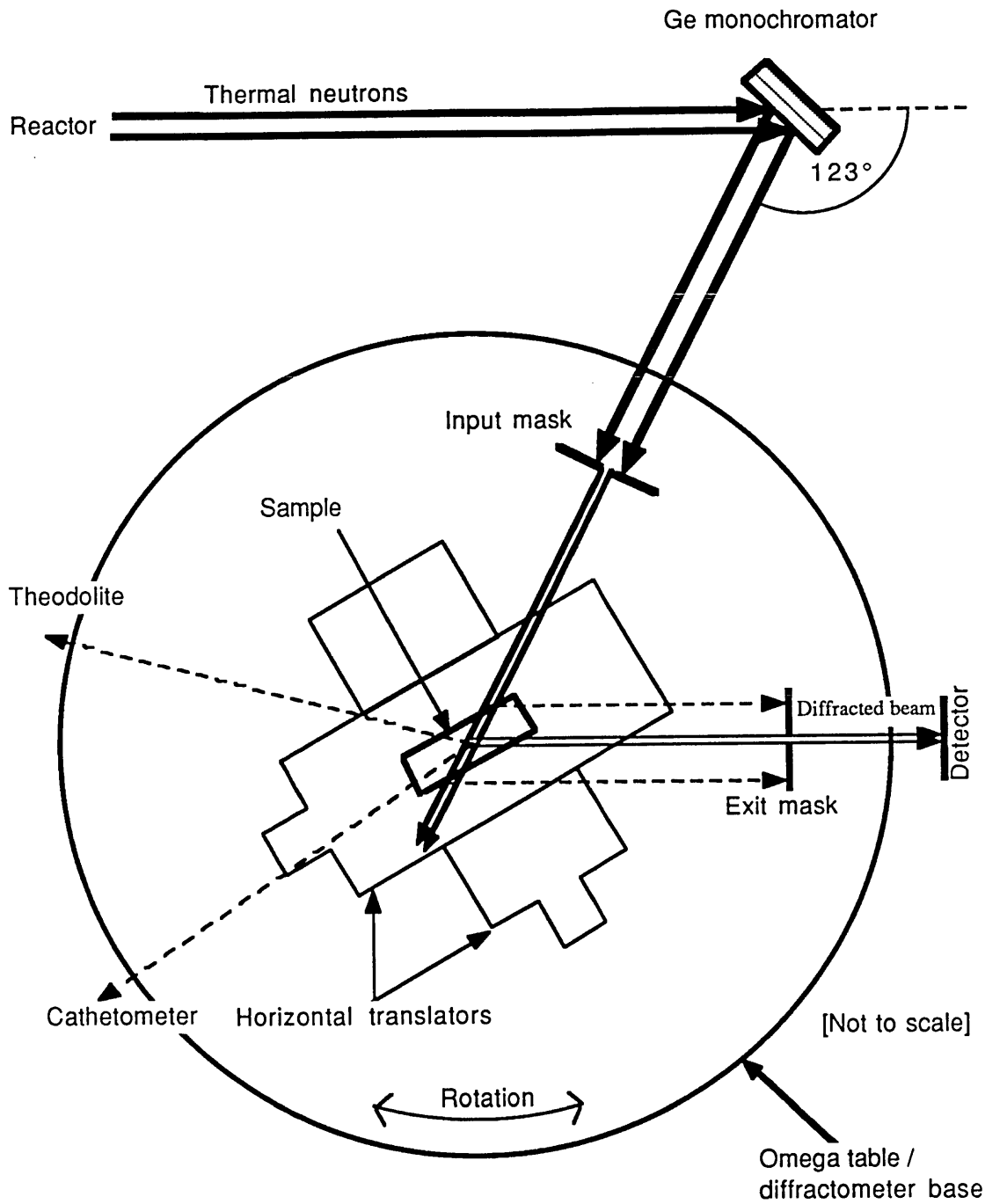


Figure 4.1 : Plan view of D1A

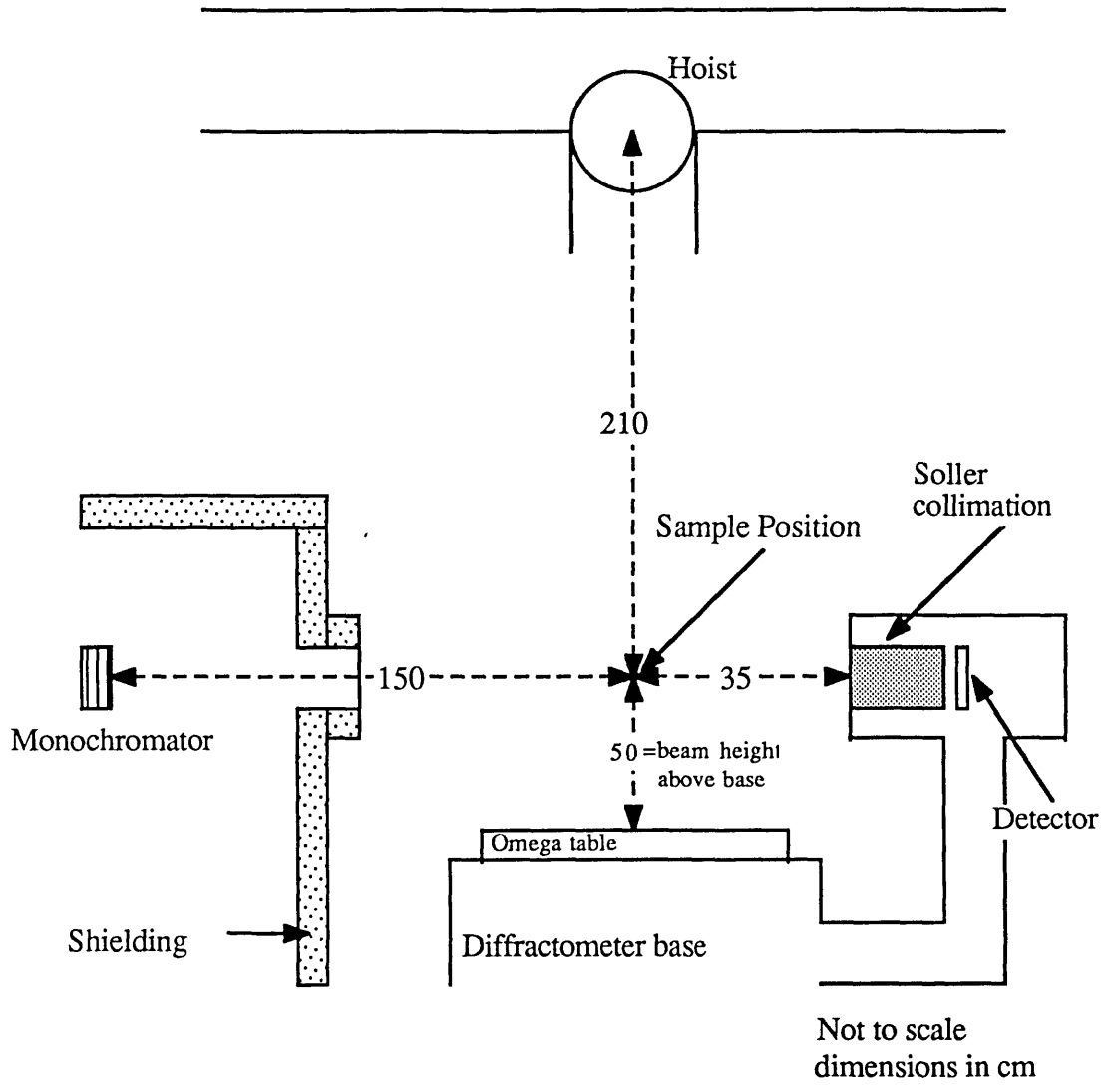


Figure 4.2: Horizontal view through D1A

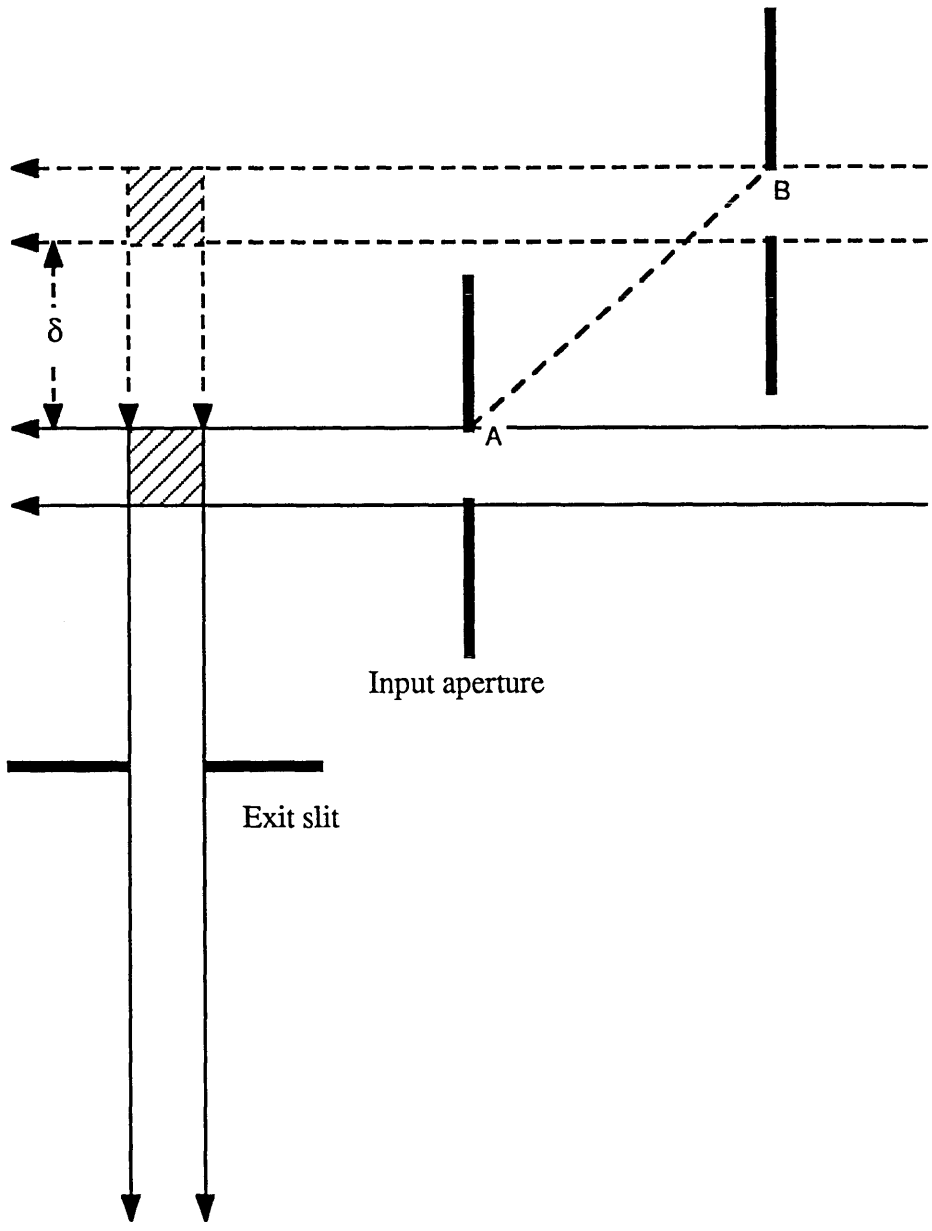


Figure 4.3: Displacement of sampling volume if input aperture is not retracted along a radius from the sampling volume

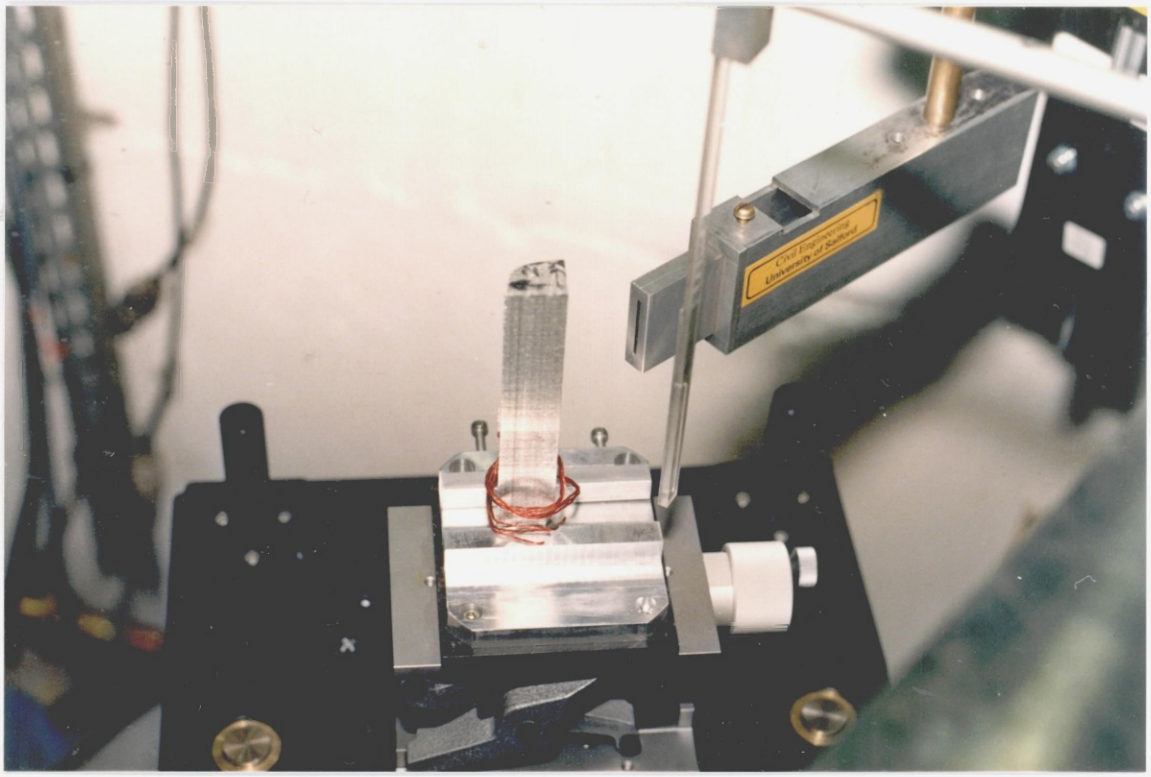


Figure 4.4: 2mm Input slit on D1A (rail gauge corner specimen)

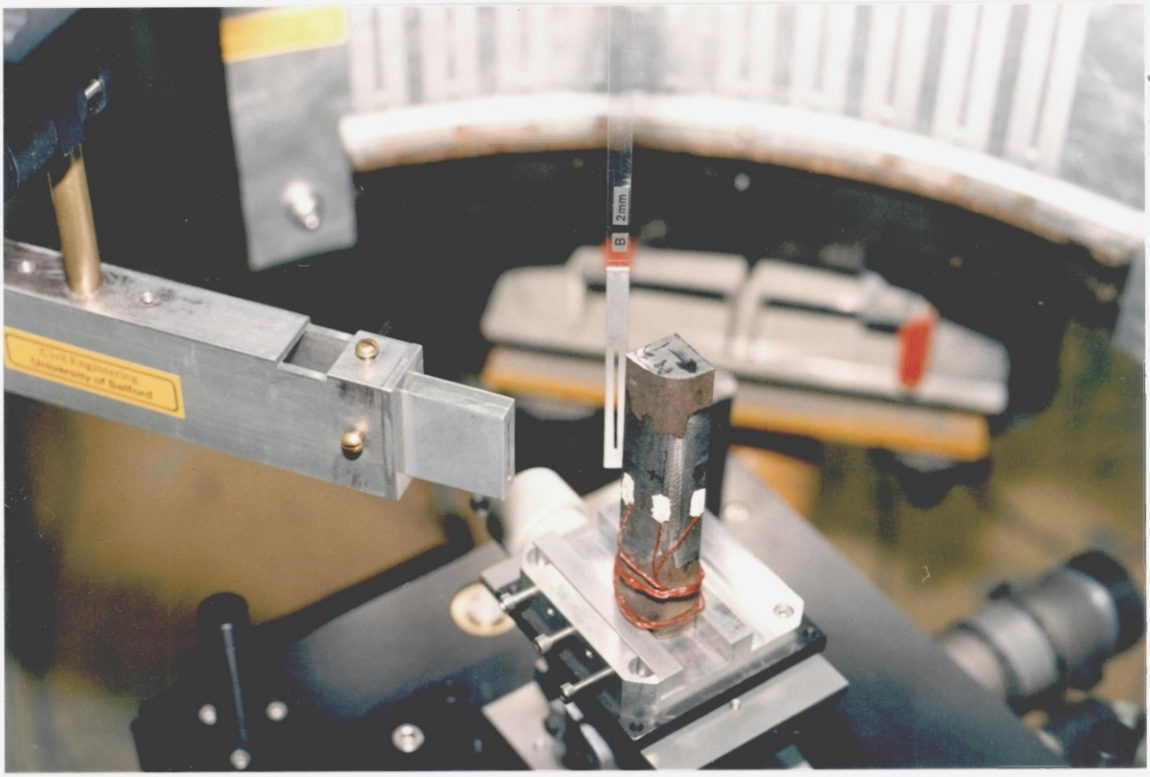


Figure 4.5: 2mm Exit slit on D1A (rail gauge corner specimen)

Figure 4.6: Transmitted intensity profiles in a horizontal plane.

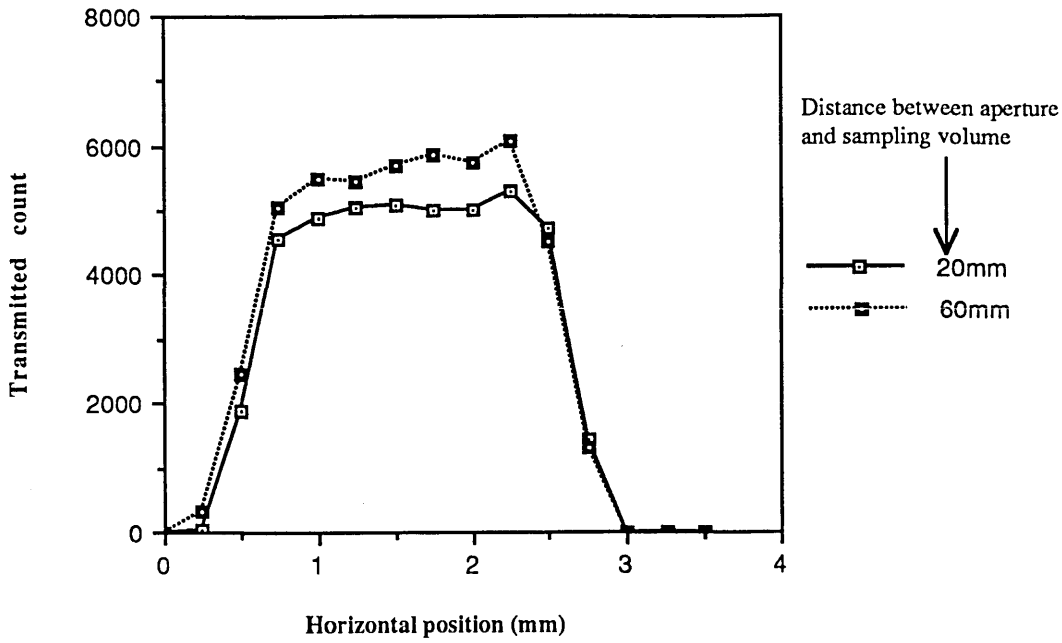
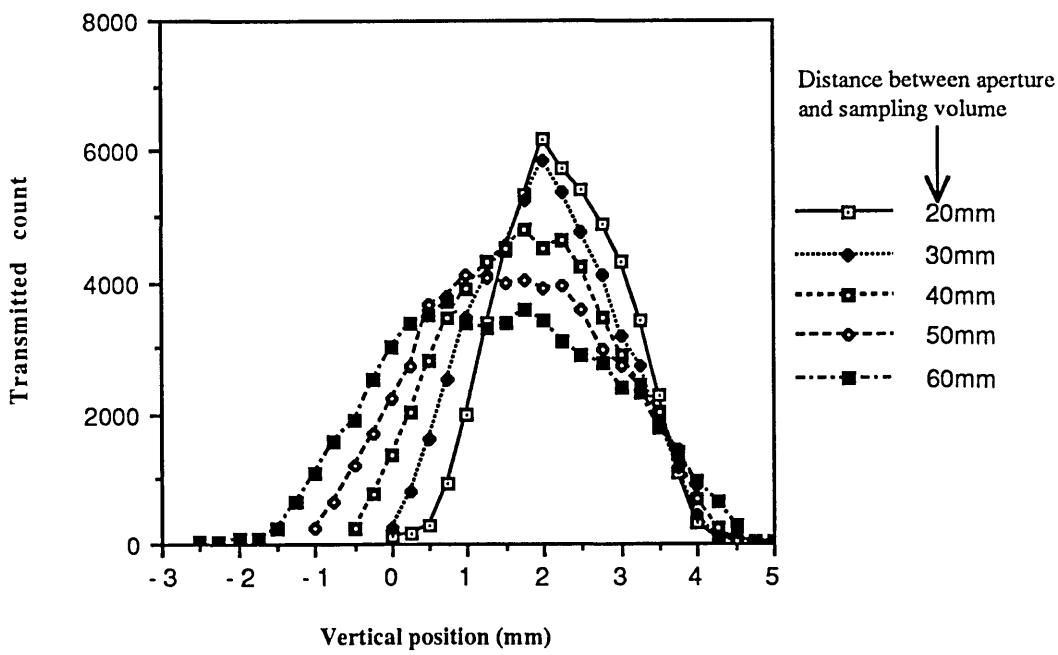


Figure 4.7: Transmitted intensity profiles in a vertical plane.



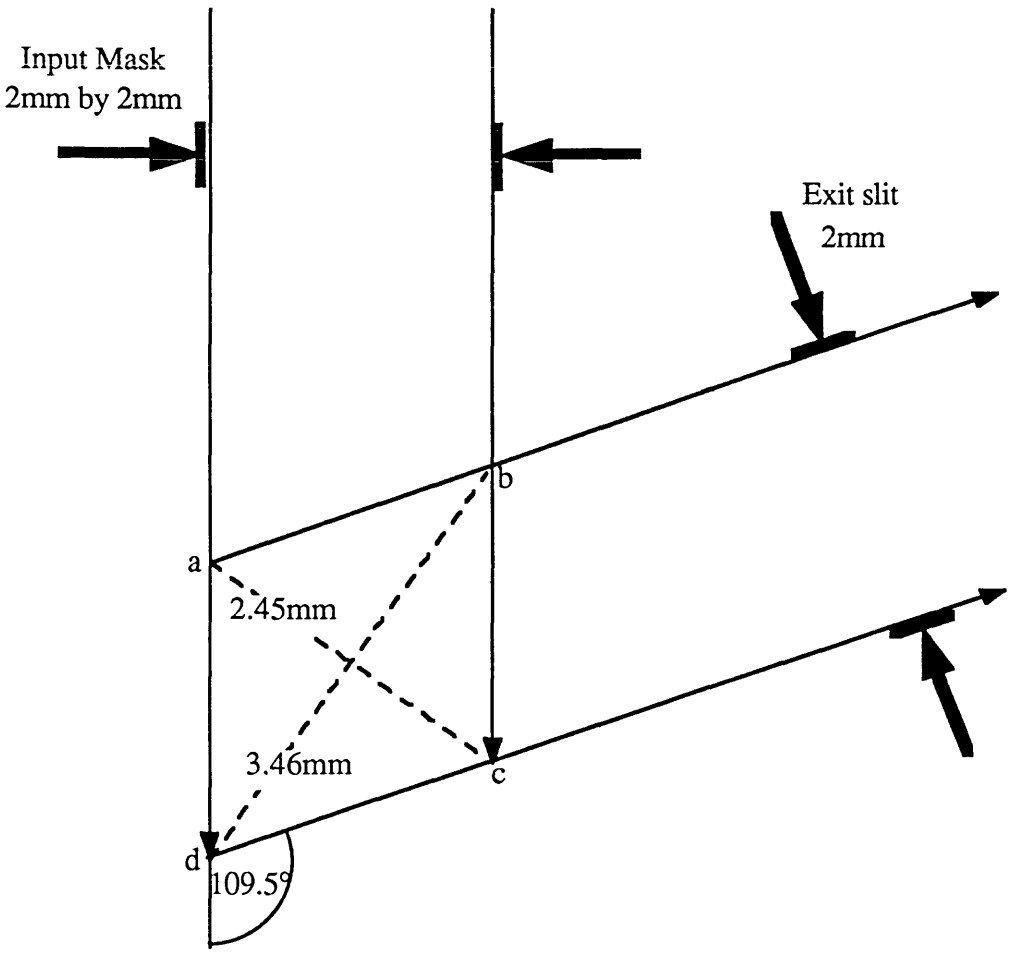


Figure 4.8 : Plan view of sampling volume used for powder plate

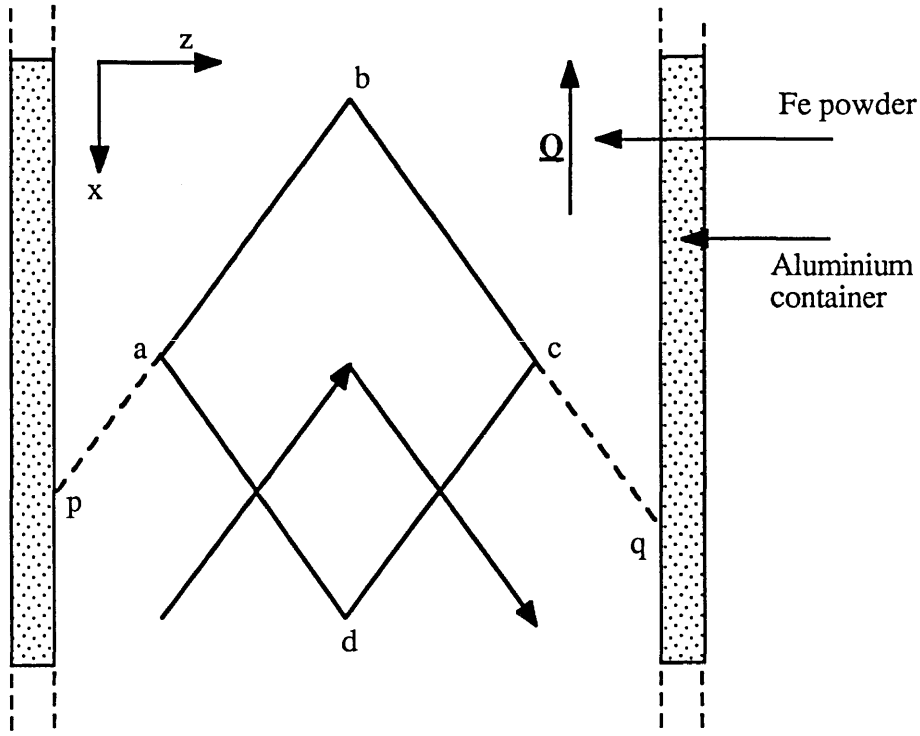


Figure 4.9a: Iron powder calibration Q in plane

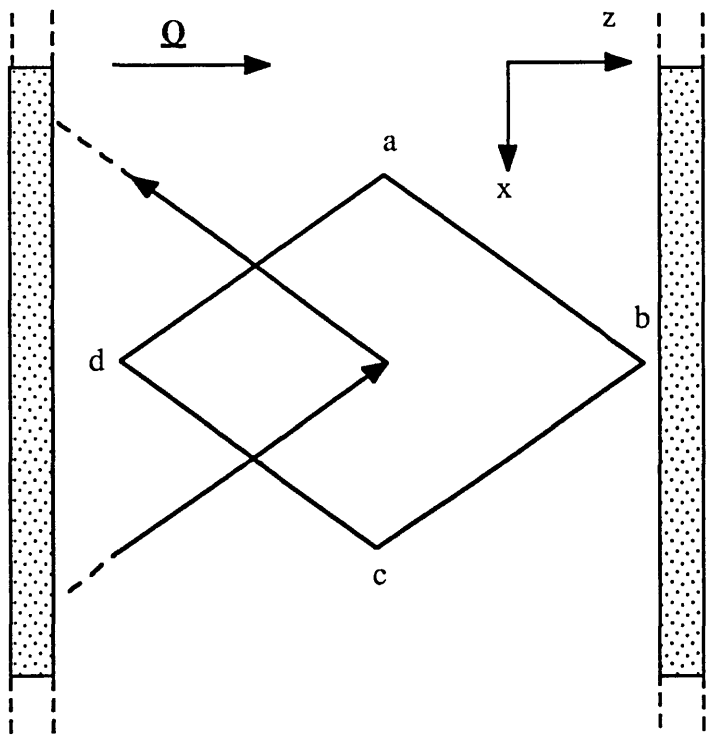


Figure 4.9b: Iron powder calibration Q normal to plane

Figure 4.10: Powder cell X orientation, measured and calculated intensity

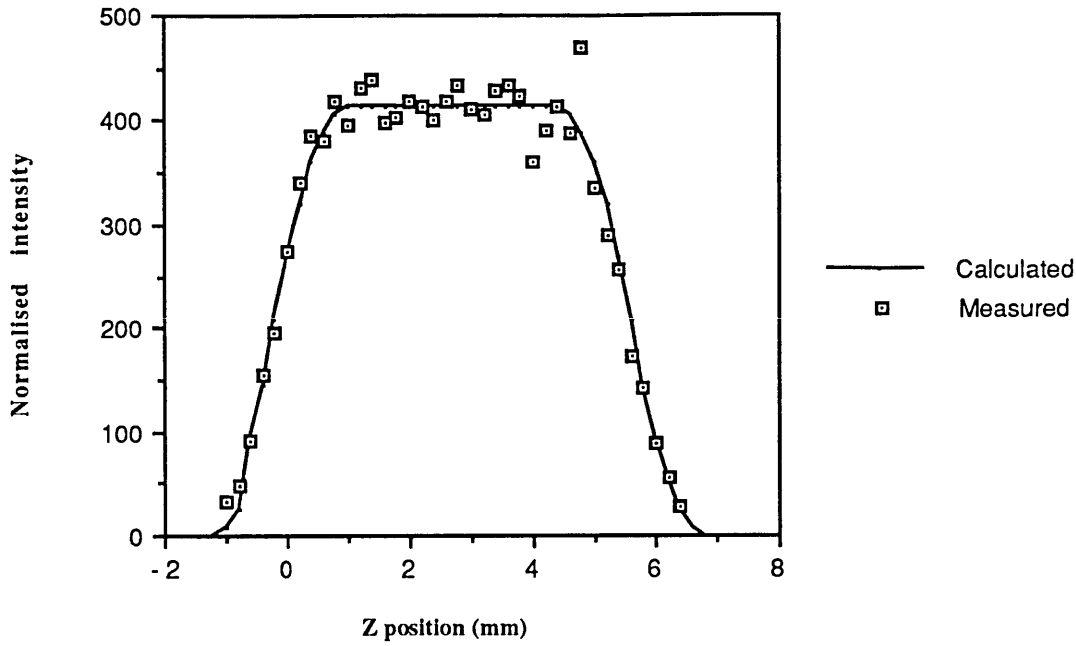


Figure 4.11: Powder cell Z orientation, measured and calculated intensity

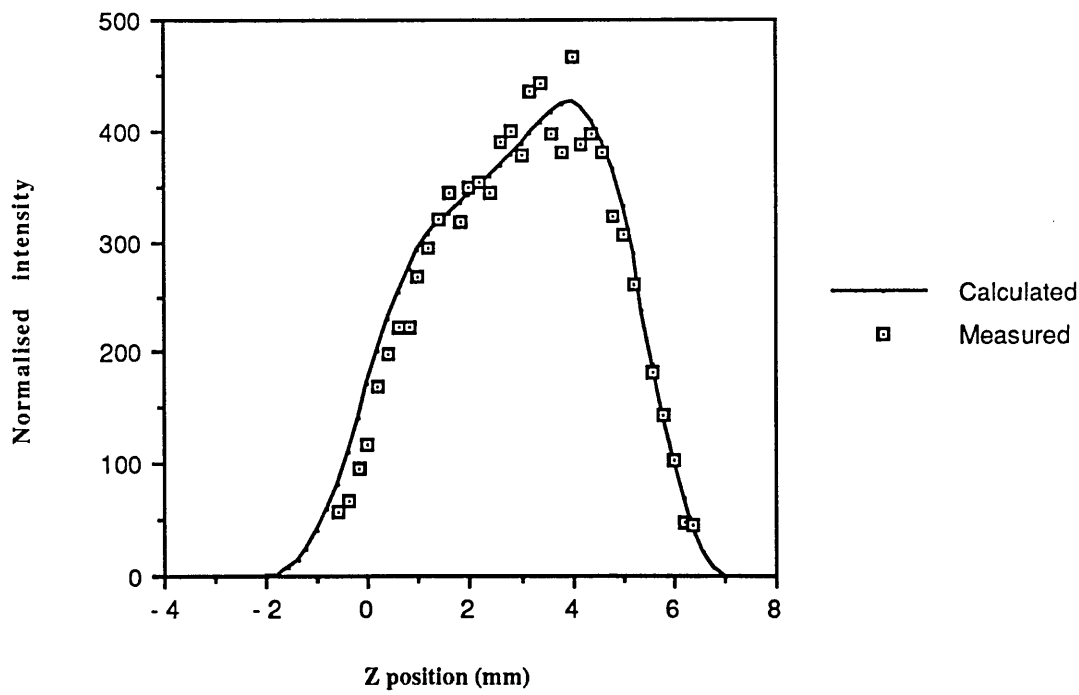


Figure 4.12a: Powder plate X orientation peak centre

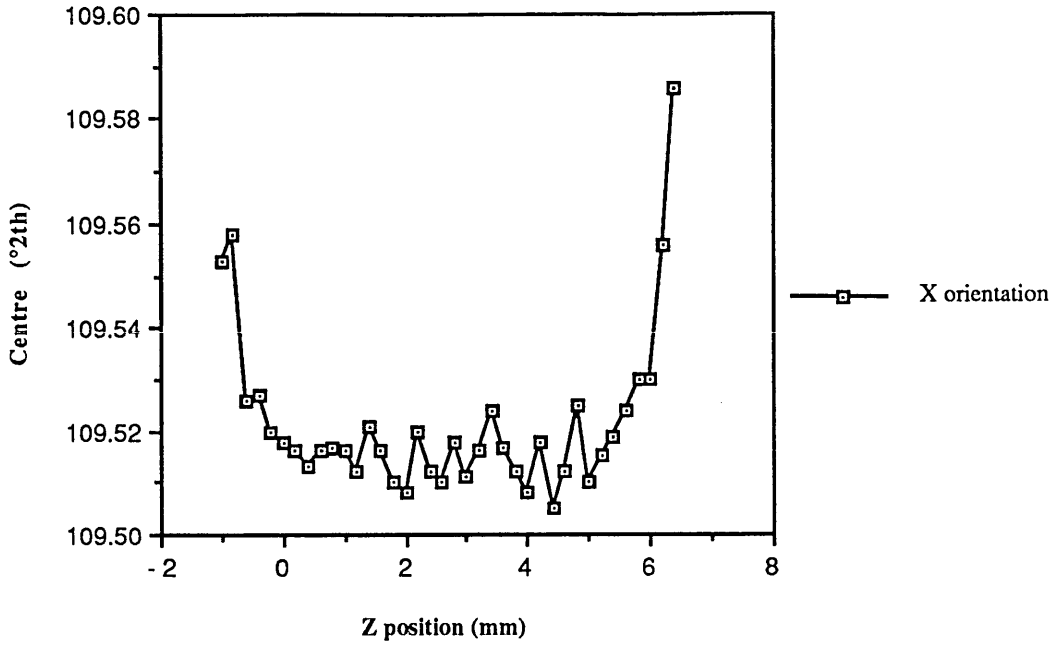
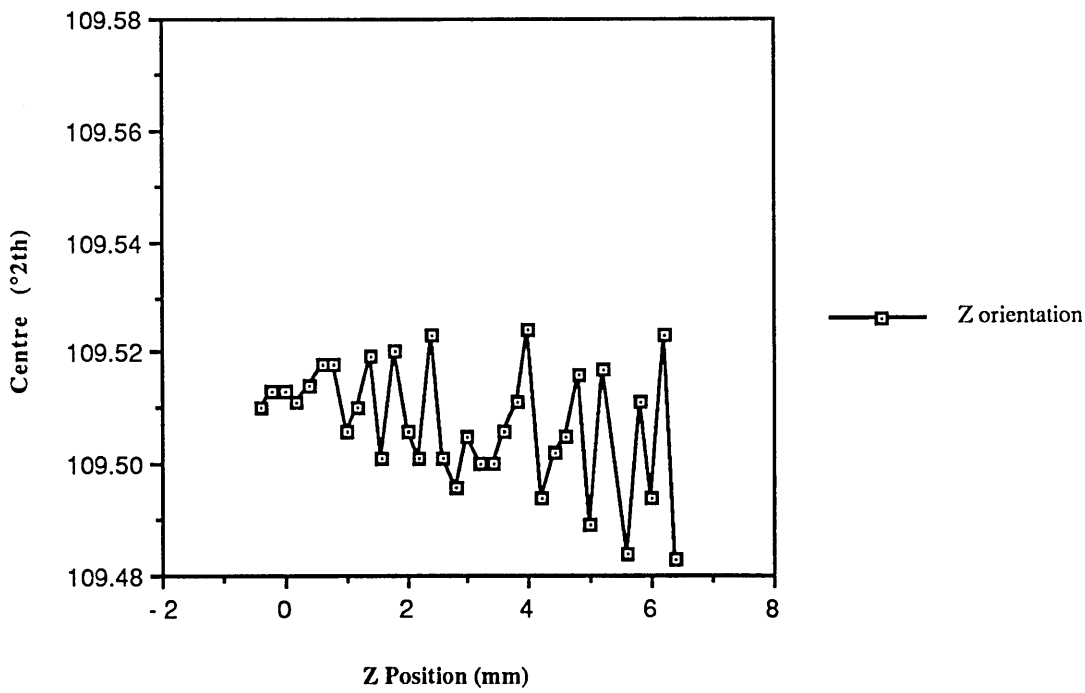


Figure 4.12b: Powder plate Z orientation peak centre



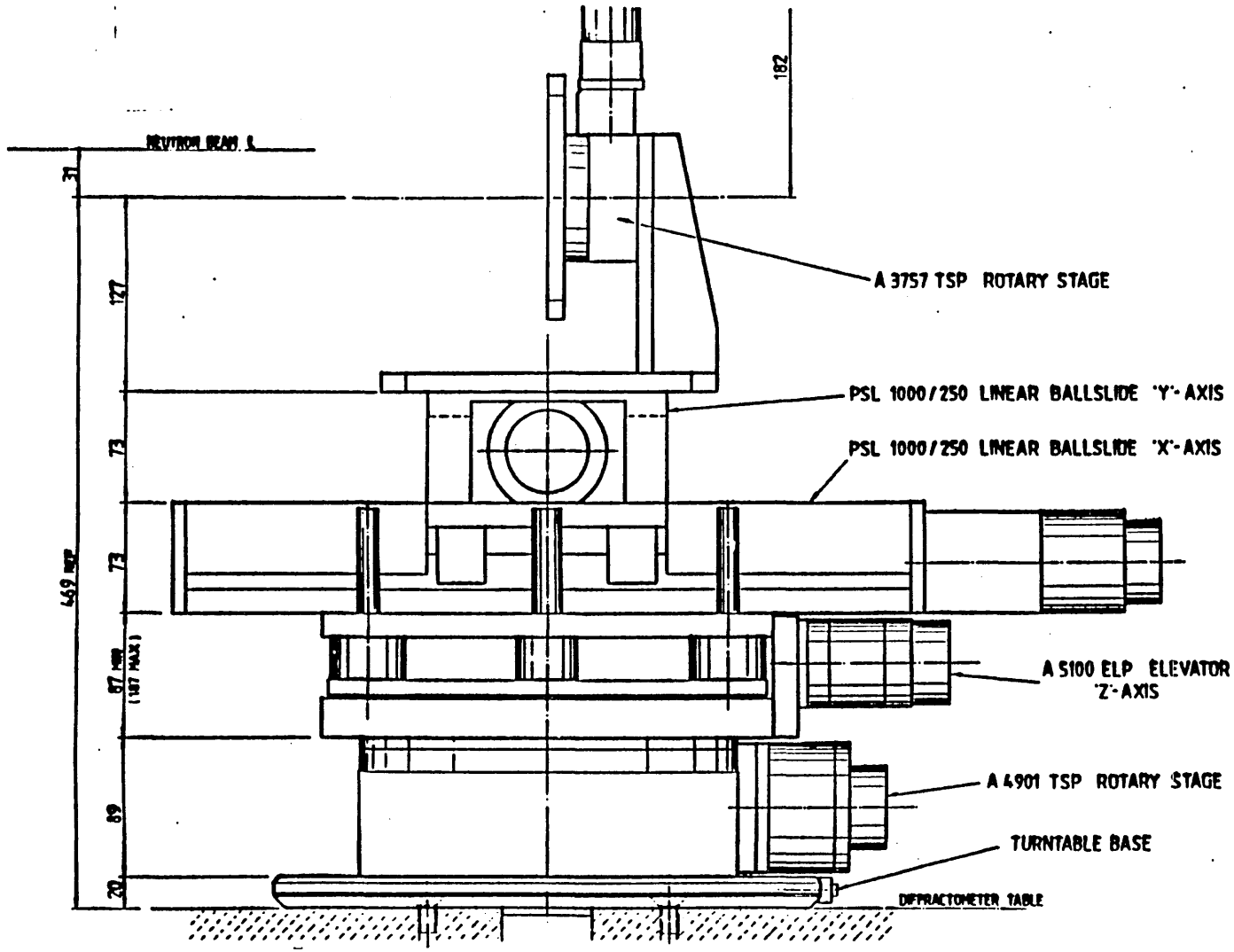


Figure 4.13: 5 Axis manipulator in position on D1A

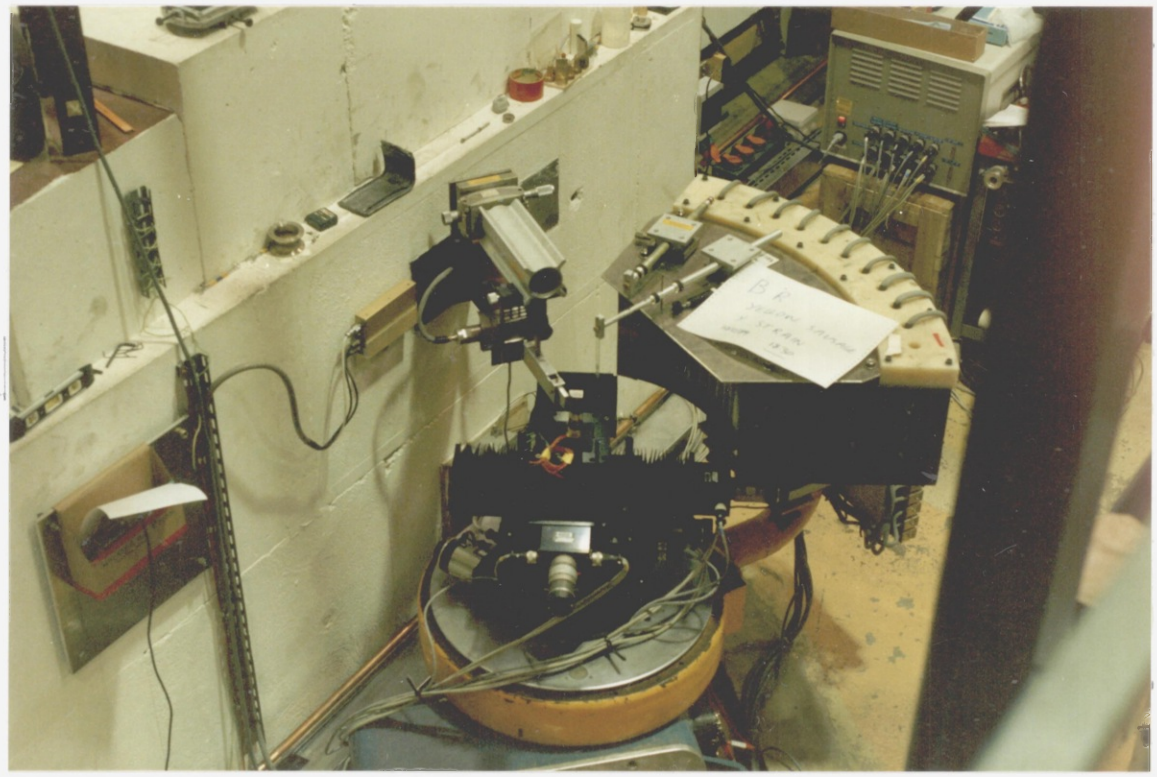


Figure 4.14: 5 Axis manipulator in position on D1A

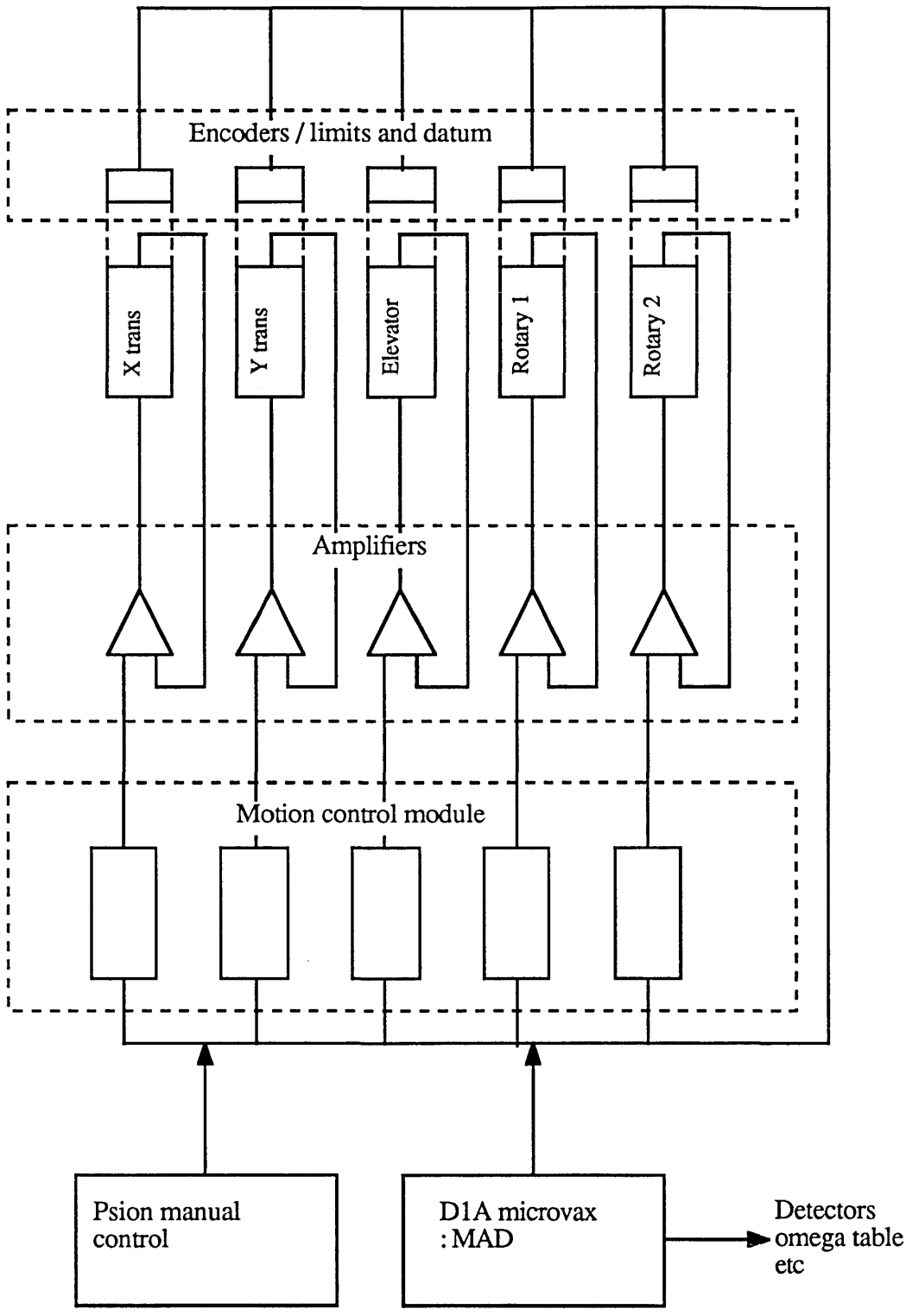


Figure 4.15 : Control system for 5 axis manipulator

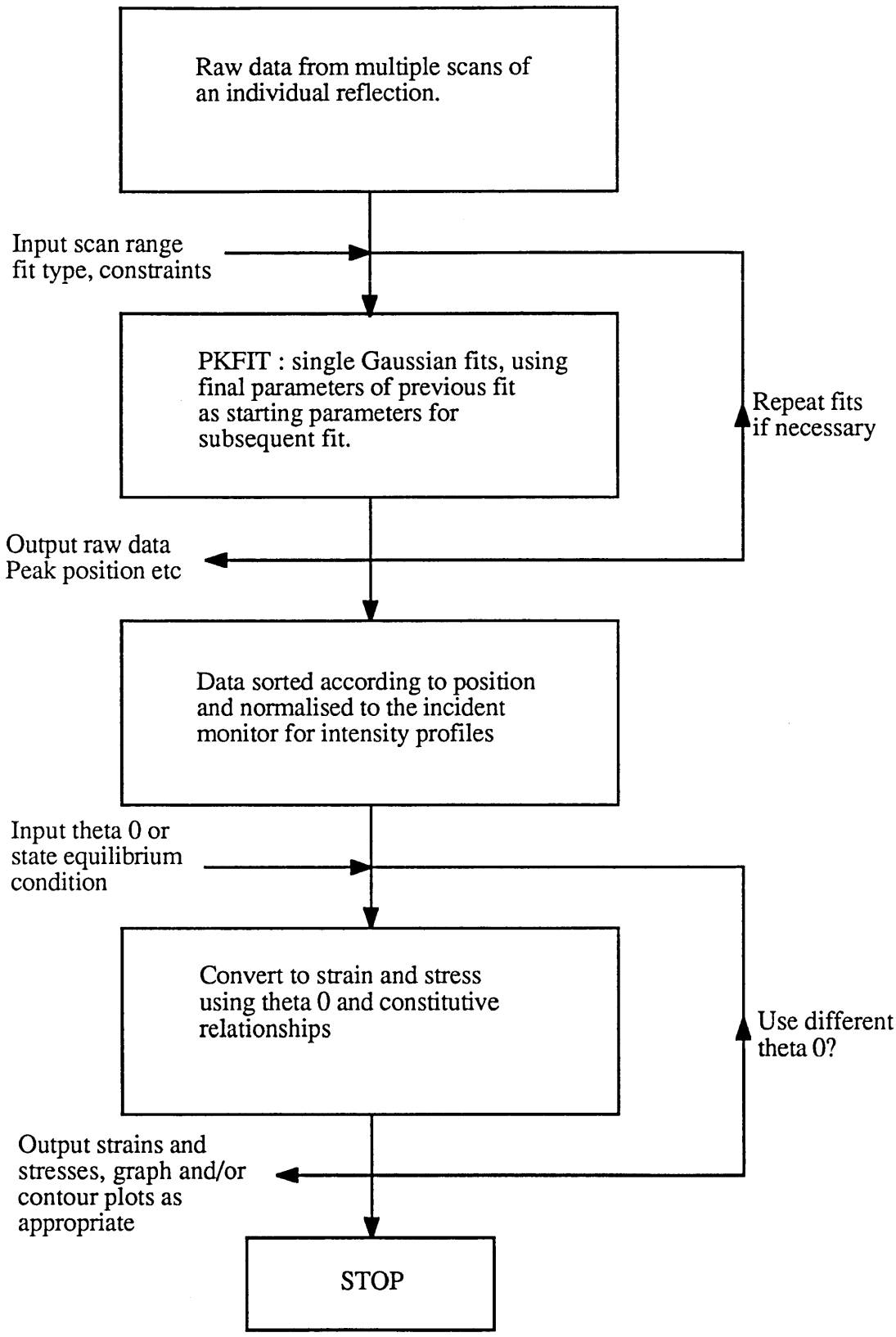


Figure 4.16 : Data processing for data from D1A

CHAPTER 5

Measurements in cracked autofrettaged rings

5.1 Introduction

Thick walled tubing is used in a variety of high pressure, military and chemical engineering applications. When subject to cyclic internal pressure, fatigue cracks can propagate from the bore of the tube and cause failure. Autofrettage provides some protection against this type of failure by applying internal pressure of sufficient magnitude to cause partial yield through the wall thickness. This introduces a compressive residual hoop stress at the bore which is balanced by a tensile stress at larger radii. The redistributed autofrettage residual stress has been examined following the growth of fatigue cracks from the bore. Three crack lengths were examined corresponding to different fractions of the wall thickness. Prediction of the redistribution was attempted using a boundary element method. The effects of the stress relieved by the crack were calculated and combined with the uncracked stress distribution using the principle of superposition. Qualitative agreement was achieved between the measured and predicted results.

5.2 Background

Pulsating internal pressures which are often found in polyethylene production plants can cause fatigue cracks at the bore of thick walled tubing (fig 5.1). The benefits of autofrettage in improving the fatigue life of tubing have been documented (Stacey, 1984). In the autofrettage process an over-pressure is applied which causes plastic yield from the bore through a fraction of the wall thickness. The magnitude of the over-pressure determines the limit of the plastic zone and the shape of the stress distribution through the wall. Subsequent applied loading must first overcome the compressive residual hoop stress before cracks can propagate from the bore. Experimental measurements combining X-ray and neutron diffraction techniques on autofrettaged tube with inner and outer diameters of 9mm and 28mm respectively indicated that removing thin rings does not substantially alter the residual hoop stresses (Pintschovius, 1986). By contrast finite element calculations for thin walled tubing

suggest that significant reduction in the hoop stresses can be incurred by removal of thin slices (Sorem, 1990)

The stress produced by autofrettage in identical but uncracked specimens to those examined in this chapter has been measured by neutron diffraction and conventional methods (Stacey, 1985ab). The measurements described here are an extension of that work but examine the effect on the residual stress distribution of propagating fatigue cracks in a radial direction from the bore through the wall. When the crack remains in the compressive region little redistribution is expected since the crack plane continues to transmit a compressive force. However, when the crack enters a region which originally contained a balancing tensile stress, redistribution occurs since the cracked region cannot transmit a tensile load.

5.3 Specimens

A thick walled tube of internal diameter 60mm and external diameter 124mm (diameter ratio 2.07) was subjected to an internal pressure of 662MPa. The bore is defined as R=0 and the outer edge as R=32mm. Yielding through 40% of the 32mm wall thickness was expected. The tube material was a high strength, low alloy steel containing principal alloying additions of 0.34%C, 1.67%Ni and 0.8%Cr (designated AISI 4333M4). The autofrettage was applied without producing end loading on the tube and corresponded to plane stress. The yield stress was 1070MPa and the U.T.S. was 1150MPa.

After autofrettage three rings, each of thickness 5mm were removed (fig 5.2). A 2.5mm deep notch was introduced at the bore of each ring from which fatigue cracks 4.5, 8.5 and 16mm in length (including the notch) were propagated. The rings were designated 7RDMA, 8RDMA and 9RDMA corresponding to failure through ≈14% , 25% and 50% of the wall thickness respectively (fig 5.3). Previous measurement indicated that the change from compression to tension occurs approximately 8mm from the bore (Stacey, 1985).

5.4 Experimental measurements

The experimental measurements described in this chapter were made on three separate visits to the I.L.L. in 1987. During that period the alignment and collimation procedures for strain measurement on D1A, were undergoing refinement. Changes were made to the masking system in the diffracted beam and to the optical alignment procedure. In particular the sensitivity of the vertical dimension of the sampling volume to the position of the input mask was not recognised until the end of 1987. Consequently although the data are presented as a complete set, the early measurements must be considered in the light of these facts and it is believed that poor spatial resolution may explain a number of anomalies. For reference, a table detailing the measurement type and date is included in table 5.1.

All measurements were made on D1A using the (211) reflection from steel at $2\theta=109.5°2\theta$. When a crack is grown beyond the compressive zone the circular symmetry of the stress distribution produced by the autofrettage is disrupted. Consequently a compact sampling volume is required in order to resolve the changes near the crack tip. The input mask for all measurements was a square of side 2mm. The exit slit was 2mm wide although for the early measurements it was attached directly to the front of the detector and not supported close to the specimen. The specimens were placed with the measuring volume on the centre plane at mid thickness. Hoop, radial and axial strains were measured along each crack plane and on the opposite uncracked radius.

θ_0 was calculated by assuming that the force acting across the plane of measurement on the uncracked side must balance to zero. The difference in stress calculated by assuming moment instead of force equilibrium proved to be less than 10MPa. Count times were typically 20 minutes per measurement with strain resolution of $\pm$ 40μstrain.

The strains for the uncracked and cracked sides of the three rings are plotted in figures 5.4. and 5.5. The stresses are plotted in figures 5.6 and 5.7. Comparison for the different rings in figures 5.4abc and 5.6abc show that the presence of fatigue crack up to half way through the bore on the opposite side causes no detectable redistribution

of stress on the uncracked side. The measured hoop strains and stresses are, within experimental accuracy, the same as quoted by Stacey (1985) for an uncracked ring subject to the same autofrettage process. In figure 5.6 the maximum compressive hoop stress seen at the bore is -300MPa which reduces to zero within 7.5mm and attains a maximum tensile value of ≈80MPa approximately 10mm from the bore. On the uncracked side the radial and axial stresses remain within about ± 50MPa throughout the wall thickness.

On the cracked sides the hoop and axial strains show consistent changes but the radial strains do not form a pattern. In figure 5.5a the hoop strains for 7RDMA follow the uncracked value observed in figure 5.4a but are displaced by the notch. In 7RDMA the maximum disparity in the magnitude of the hoop strain between the cracked and uncracked sides coincides at R=2.5mm where there is a 20% difference. However this reduces with increasing radius and the change from compressive to tensile strain coincides at R≈7.5mm. The hoop strains for 9RDMA demonstrate a characteristic shoulder between R=6 and R=14mm along which the hoop strain is constant and compressive (fig 5.5a). Beyond R=14mm the hoop strain becomes increasingly tensile and attains a maximum value of 1400 μstrain between R=16 and R=17mm. 8RDMA shows limited evidence for a compressive hoop strain shoulder at R=6mm and an increase in tensile strain compared to an uncracked ring but smaller in magnitude than 9RDMA.

On the crack plane of each ring the axial strains maintain a tensile strain in the cracked region. At the crack tip there is a sharp discontinuity to give a compressive strain along the remaining ligament (fig 5.5c). The discontinuity is less pronounced for 7RDMA which may reflect reduced spatial resolution.

On the cracked side the radial strain behaviour of 7RDMA does not fall into the pattern (fig 5.5b). Since the hoop and axial strains of 7RDMA are close to the uncracked values the same is expected of the radial strain, at least in the uncracked ligament. However between R=0 and R=12mm the radial strain differs from the uncracked side values and moves in the opposite sense to the data from the rings containing the longer cracks. Beyond R=12mm the radial strains converge for the three

rings and are subsequently close to the behaviour on the uncracked side. It seems likely that the 7RDMA radial strain results were in some way corrupted. However the measured results have been used in calculation of stresses.

The stresses on the cracked side follow the strains. The compressive hoop stress shoulder in 9RDMA is -80MPa and a maximum tensile stress of 300MPa is reached at R=17mm (fig 5.7a). In figure 5.7a the tensile hoop stress begins between R=14 and R=15mm which is closer to the bore than the nominal crack tip position at 16mm. Since a crack cannot support a tensile stress this indicates that either the positioning or the visual identification of the crack tip position is in error. Comparison of the hoop and axial strain profiles with the intensity profiles obtained near the edges of the rings suggest that the crack tip is in fact less than 16mm from the bore. To assess the resolution and positioning accuracy in 9RDMA, hoop strain measurements were recorded in an array near the crack tip (fig 5.8). The results suggest that the crack tip lies between R=13.5 and 15.5mm which is ahead of the optically measured value but do not discount the possibility of a positioning error for the sampling volume relative to the ring.

The radial stresses in figure 5.7b follow the strains as is expected. The values for 8 and 9 RDMA lie close to zero at the outer edge as they must at a free surface. However the 7RDMA radial stress gives a value of -100MPa at the outer edge. Clearly a problem exists with the 7RDMA results and the radial strain data has been discounted until repeat measurements can be made.

The peak widths for the measurements on the cracked and uncracked sides in the axial direction are included in figure 5.9abc. Similar results were noted in the hoop and radial directions. On the uncracked side of each ring there is an approximate 16% reduction in the width of the diffracted peaks from the bore to the outer edge. On the cracked sides there is a further increase in peak width associated with the presence or passage of the fatigue crack. The effect is independent of the stress gradients which also alter the peak width.

Table 5.1: Autofrettaged rings measurement dates

Date	Direction	Mask In(mm)	Slit out(mm)	C/UC†
7RDMA	(A/W≈0.14)			
22/4/87	H	2*2	$2^{s1}4^{d}$	UC
	R	2*2	$2^{s1}4^{d}$	UC
	A	2*2	$2^{s1}4^{d}$	UC
3/2/87	H	2*2	2^{d}	C
	R	2*2	2^{d}	C
	A	2*2	2^{d}	C
8RDMA	(A/W≈0.27)			
25/4/87	H	2*2	$2^{s1}4^{d}$	UC
	R	2*2	$2^{s1}4^{d}$	UC
	A	2*2	$2^{s1}4^{d}$	UC
3/11/87	H	2*2	$2^{s2}4^{d}$	C
	R	2*2	$2^{s2}4^{d}$	C
	A	2*2	$2^{s2}4^{d}$	C
9RDMA	(A/W≈0.50)			
7/2/87	H	2*2	2^{d}	UC
	R	2*2	2^{d}	UC
	A	2*2	2^{d}	UC
3/11/87	H	2*2	$2^{s2}4^{d}$	C
	R	2*2	$2^{s2}4^{d}$	C
	A	2*2	$2^{s2}4^{d}$	C
+ 9RDMA misc.				
7/11/87	H *(tip array)*	2*2	$2^{s2}4^{d}$	C

H - hoop
R - radial
A - axial
d - detector mask
s1 - exit slit near specimen, April
s2 - exit slit near specimen, November
† - cracked/uncracked side

5.5 Boundary integral method

The boundary integral (BIE) or boundary element method is a stress analysis tool which provides solutions to engineering problems for which no analytical solution is available. It is a numerical technique which converts the partial differential equations which describe the elastic behaviour of a material to a surface integral applicable over a boundary. The conversion is exact and approximation is only introduced by the subsequent numerical solution of the integral. By applying tractions and displacements to points on a boundary the distribution of tractions and displacements at other points on

the boundary can be predicted subject to any enforced conditions. The method is applicable to problems which involve stress concentrations or to contact problems.

The application of boundary integral methods to stress analysis is discussed by Fenner (1983). Boundary element methods combine the known solutions of simple problems to give solutions to more complicated problems. If a force of known direction and magnitude acts on a point on the boundary of a material then subject to the laws of elasticity an analytical solution exists for the forces and displacements which act on any other point. By considering the application of multiple individual forces the fundamental solution associated with each can be superposed and by applying boundary conditions the effective traction and displacement over the remainder of the boundary can be predicted.

Unlike finite element methods in which the whole of the relevant domain must be discretised only the boundary is considered. This simplifies the model and reduces the dimensionality of the problem by one. Fewer elements are needed than equivalent finite element models which reduces the preparation and computing time. No approximation of the internal region is necessary which improves accuracy and produces less unwanted information. Selection of an appropriate mesh makes it easier to focus on a region of interest. Cracks can be introduced by creating new boundaries which can be external or internal.

Within each element on the boundary the displacement and tractions are described by nodal values together with a shape function for interpolation. Integrations along the boundary can be complicated and the solution is usually effected using Gaussian quadrature applied to the boundary elements. Small strains are implicit otherwise the shape of the domain will be altered.

The boundary element method has successfully been applied for calculating stress intensity factors in autofrettaged rings (Webster, 1983). However when the crack face is shut the analysis must also consider contact constraints and solutions must be found which do not predict overlap of a crack face. Since the contact area is not usually known in advance, an iterative approach must be adopted (Becker, 1987).

5.6 Application of boundary integration to 9RDMA

Two features in the cracked rings are open to modeling using the elastic stress analysis provided by the boundary element method. These are the notch which initiates the fatigue crack and the presence of a crack in the tensile region. Removal of material to form a notch permits the faces to compress in response to the residual stress at the bore and no compressive load is transmitted between R=0 and R=2.5mm. Similarly when the crack has propagated beyond 25% of the wall thickness it relieves the tensile stress seen in figure 5.7a because the cracked region cannot transmit a tensile force. In the tensile region the crack is drawn open and the stress must redistribute. For 7RDMA and 8RDMA all or most of the crack remains in the compressive region and the modification to the measured hoop stress distributions is limited to the presence of the notch. Consequently the boundary element method was applied primarily to 9RDMA in which the crack relieves approximately 8mm of the original tensile hoop stress between R=7.5 and R=16mm.

A boundary element program developed by Watson (1982) was used for the calculations. The program assumes plane strain conditions and uses Hermitian cubic elements. Cubic variations of displacements and tractions are permitted along each element. In figure 5.10a the original autofrettaged hoop stress distribution is illustrated across the wall of a ring. In figure 5.10b the position of the crack tip in 9RDMA is indicated. In the shaded regions AB and CD corresponding to the notch compressive region and to tension across the crack the stresses are relieved.

The BIE program was used to predict the stresses induced in the regions BC and DE for an applied stress distribution corresponding to the shaded regions in figure 5.10b. Assuming superposition and adding the stress distribution in fig 5.10a to the predicted stress distribution due to the applied stresses in figure 5.10b the stresses in the region AB and CD are negated. The modified stresses in regions BC and DE are then the residual stresses of interest.

Symmetry requires that only half of the ring needs to be modeled. The mesh used for the calculations is shown in figure 5.11. A total of 58 nodes was used around the mesh with 20 on the flat part of the crack plane. The boundary conditions are shown

in figure 5.12. In regions AB and CD tractions are applied of equal magnitude but opposite sign to those existing in the uncracked ring (cf shaded areas in fig 5.10b) and the elements are permitted free displacement in the hoop direction. In regions BC and DE no tractions are applied and the elements are permitted no displacement normal to the crack plane (hoop direction). On the uncracked side (nodes 30 to 49 in figure 5.11) no tractions are applied and the nodes are also held to zero displacement in the hoop direction. All other nodes on the circular sections are completely free.

In the first analysis the BIE program predicted some overlap of the crack plane to the left of point C (corresponding to R=7.5 at the limit of the compressive hoop stress) in fig 5.10b. Overlap is not possible and consequently the reversed stress distribution was extended backwards to R=5.9mm. Physically this corresponds to the tensile stress holding the crack open at the end of the compressive zone. The crack tip (point D in figure 5.12) corresponded to R=16.3. The BIE prediction of the redistributed stress for 9RDMA is plotted with the measured values in figure 5.13.

To predict the changes expected on the uncracked side a calculation was also performed to examine the effect of removing the autofrettage distribution from the complete crack length in 9RDMA. This represented a worst possible case and a maximum change of only 15MPa was predicted on the uncracked side. This lies within the experimental error and is in accordance with the measured values in which no change was observed on the uncracked side, even for the longest crack length. Calculations in which only the stress over the notch was reversed predicted a sharp increase in the compressive stress near the notch which diminished with radial distance from the notch as might be expected.

5.7 Discussion

When the crack tip is assumed to lie at R=16.3mm and the crack face is drawn open to R=5.9mm qualitative agreement between the measured results and the BIE predicted values is achieved. In figure 5.13 the first node beyond point D (fig 5.12) is 0.5mm away. Refinement of the mesh to give the values closer to point D would predict larger tensile stresses which would improve the agreement with the observed data.

However, there is considerable discrepancy in the position of the crack tip. According to the experimental data the crack tip cannot lie beyond R=14.5mm (fig 5.13) since the crack cannot support a tensile stress. However this is shorter than the optical assessment of 16mm. The BIE prediction gives nodal values and strictly some account of the finite size of the sampling volume should be made. Taking the finite sampling volume of the neutron technique into account would improve the agreement between the BIE prediction and the measured values.

In the BIE prediction the stress in the originally tensile region along the crack plane is negated to leave zero stress. In practice there is apparently a constant compressive stress lying along the crack plane behind the crack tip. Its origin is unclear but may be associated with the plastic wake on either side of the crack plane. The limited hoop strain array in figure 5.8 supports this assertion. As might be expected the material removed from the notch displaces the compressive stress from the interior to larger radii.

Further work is suggested to investigate the nature of the compressive shoulder, in particular to assess whether it is associated with the plastic wake. Measurements should be made at the crack tip with improved spatial resolution to assess where the tip lies in the ring. Also the limited evidence for a shoulder in 8RDMA merits further examination. Finally the variation in peak widths noted in figure 5.9 potentially provides a valuable tool for assessing the plastic strain if it can be correctly calibrated.

5.8 Conclusions

Propagation of fatigue cracks through half the wall thickness of autofrettaged specimens have been shown to have negligible effect on the stress distribution on the uncracked side of the ring. Similarly cracks which remain in the originally compressive region of an autofrettaged ring ring show no detectable modification to the residual stress pattern except due to the artificially introduced notch. However when a crack is propagated through half the wall thickness a distinctive stress distribution is produced with an increased tensile stress ahead of the crack tip which reaches a maximum of 300MPa which is 3 times the value in an uncracked ring. Along the crack plane in the

originally tensile stressed region a constant compressive stress of -80MPa was observed. The start of the compressive shoulder appeared to coincide with the original limit of the compressive hoop stress between R=7 and R=8mm and extended to near the crack tip.

The uncertainty in spatial resolution for these measurements precluded more detailed attempts to model the stress distributions. However the redistribution caused by the longest crack has been addressed using a BIE and superposition approach. Qualitative agreement has been achieved for between the predicted and measured values.

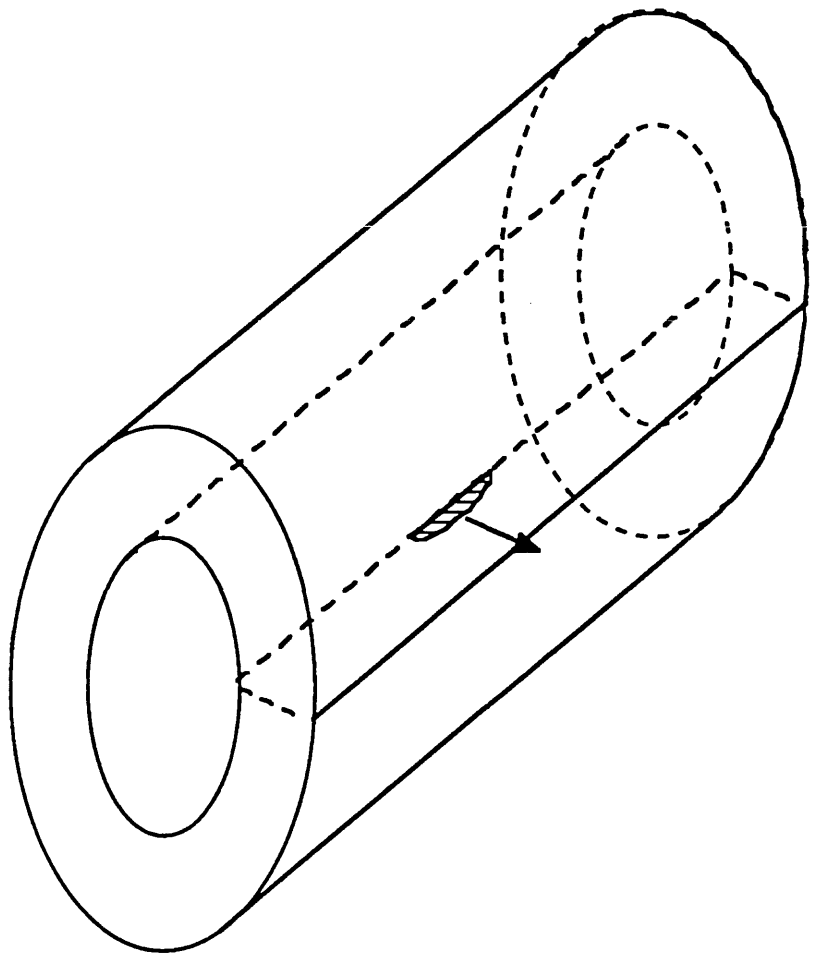


Figure 5.1: Fatigue crack growth from the bore of a thick walled tube

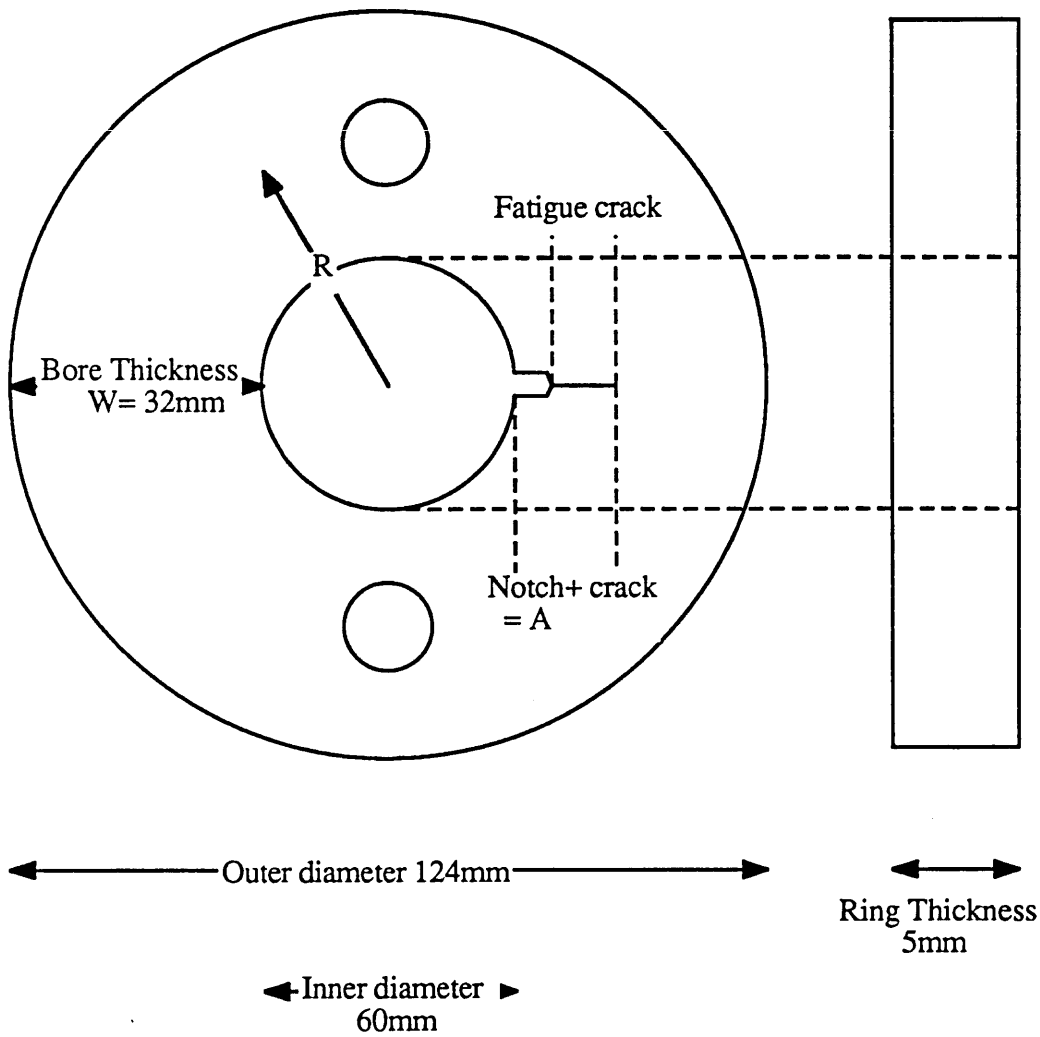


Figure 5.2: Dimensions of autofrettaged rings

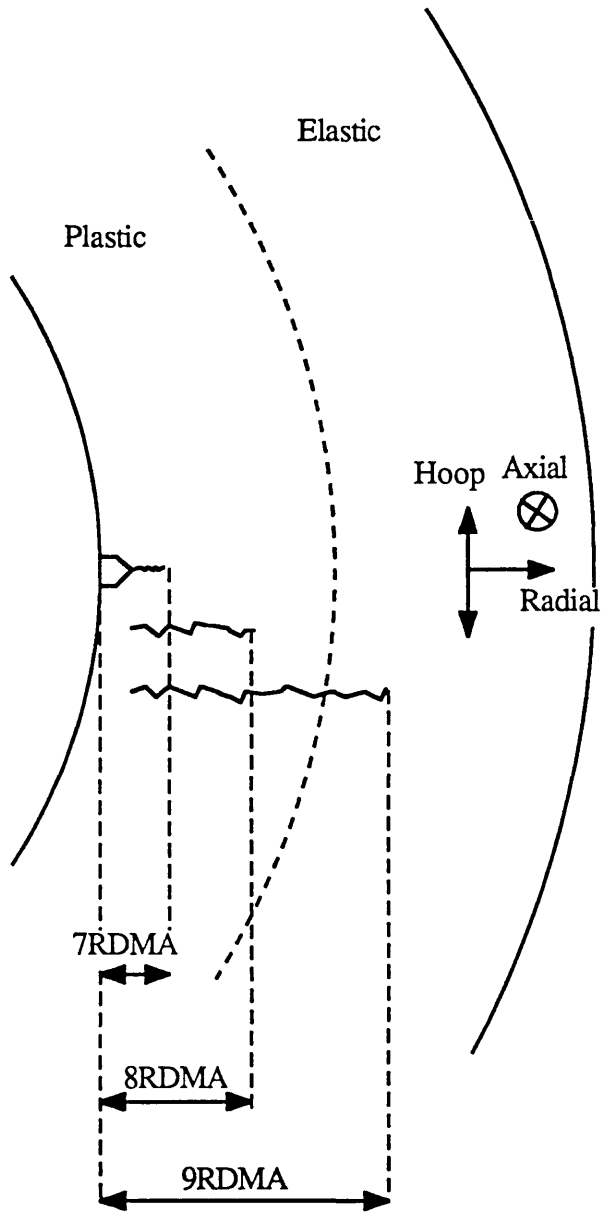


Figure 5.3: Crack lengths and direction definitions

Figure 5.4a: Hoop strain / uncracked sides of autofrettaged rings

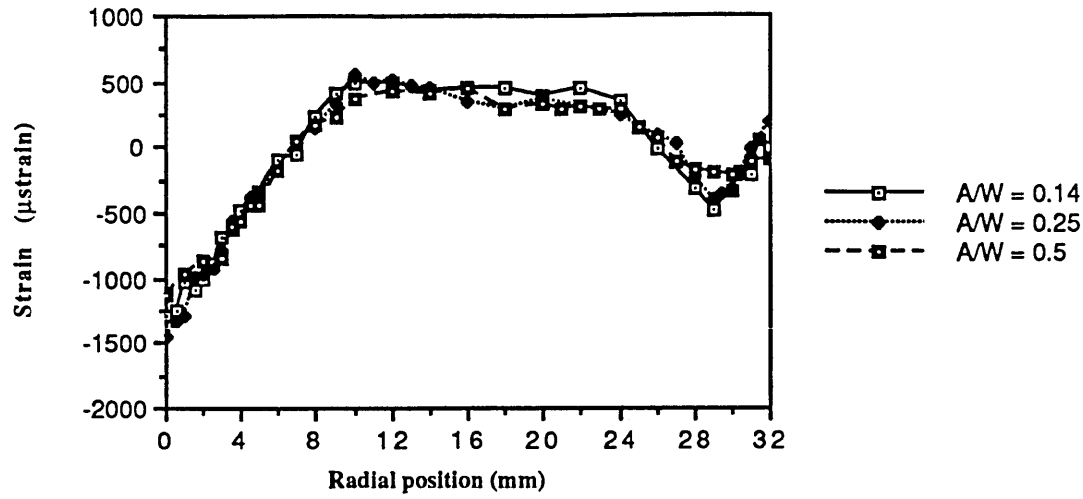


Figure 5.4b: Radial strains / uncracked sides of autofrettaged rings

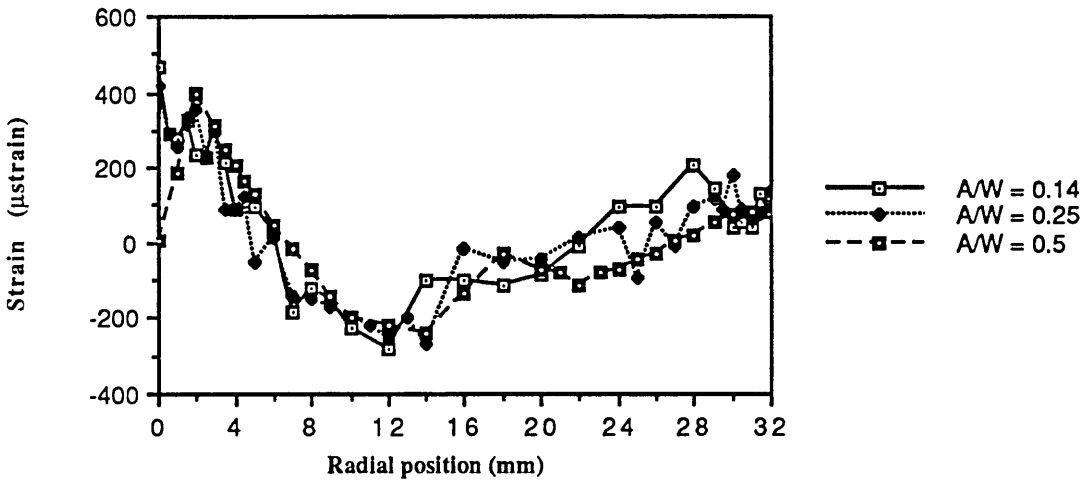


Figure 5.4c: Axial strain / uncracked sides of autofrettaged rings

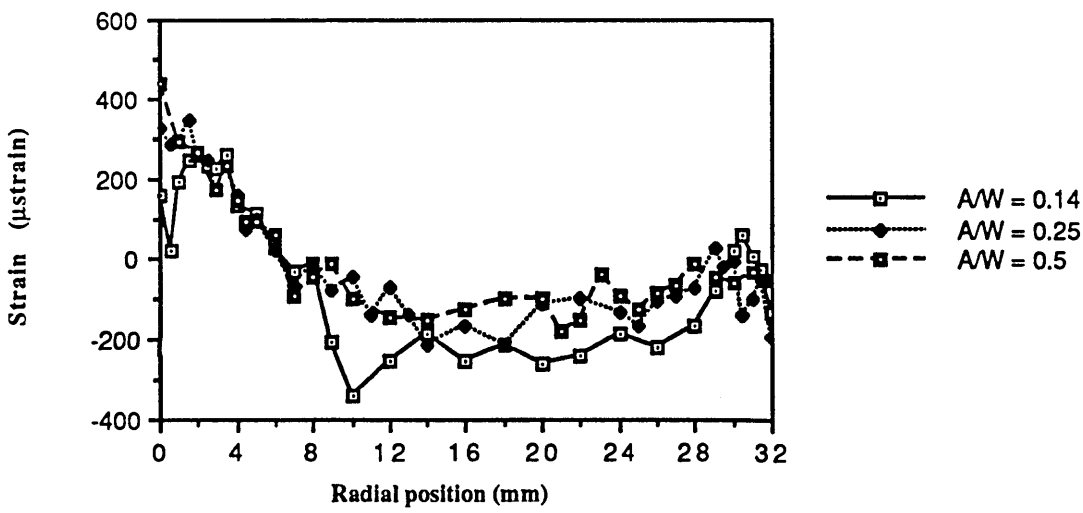


Figure 5.5a: Hoop strain / cracked sides of autofrettaged rings

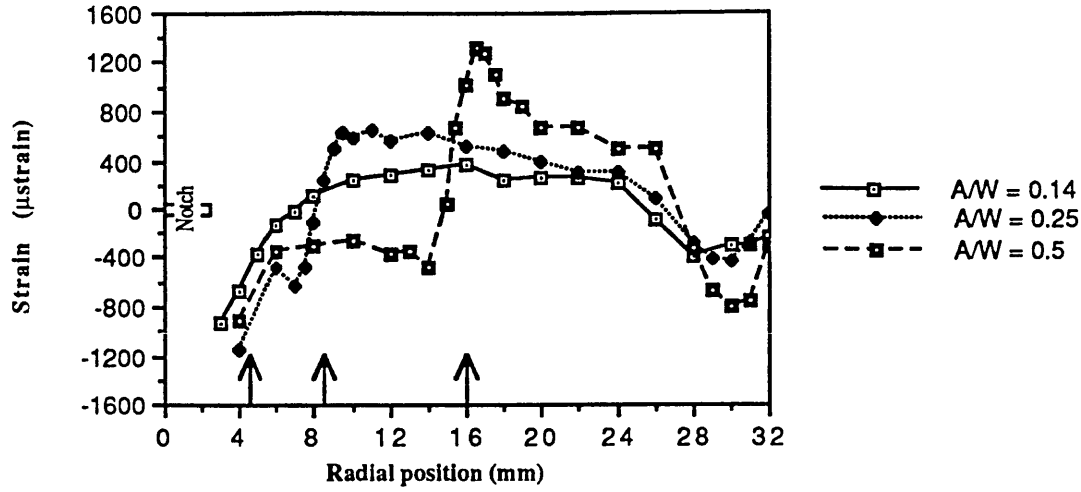


Figure 5.5b: Radial strain / cracked sides of autofrettaged rings

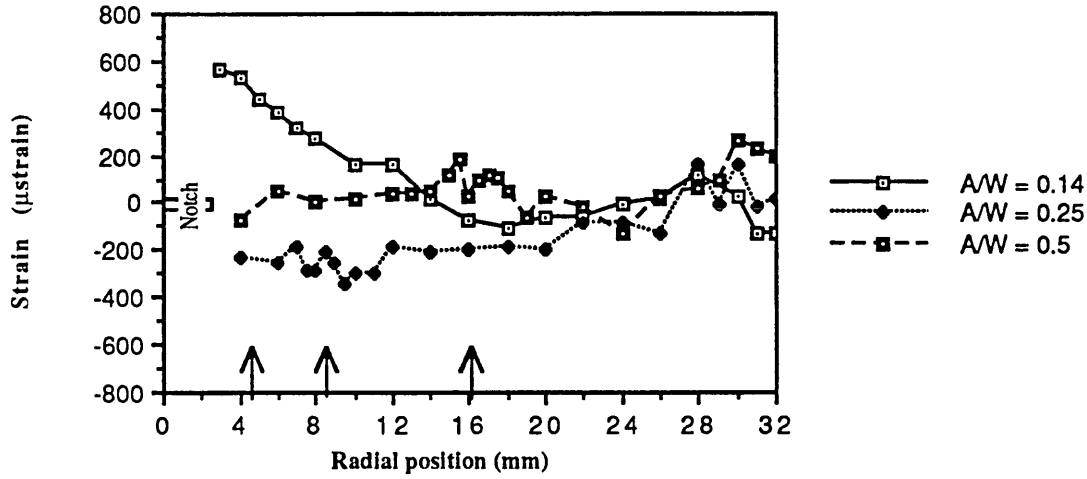


Figure 5.5c: Axial strain / cracked sides of autofrettaged rings

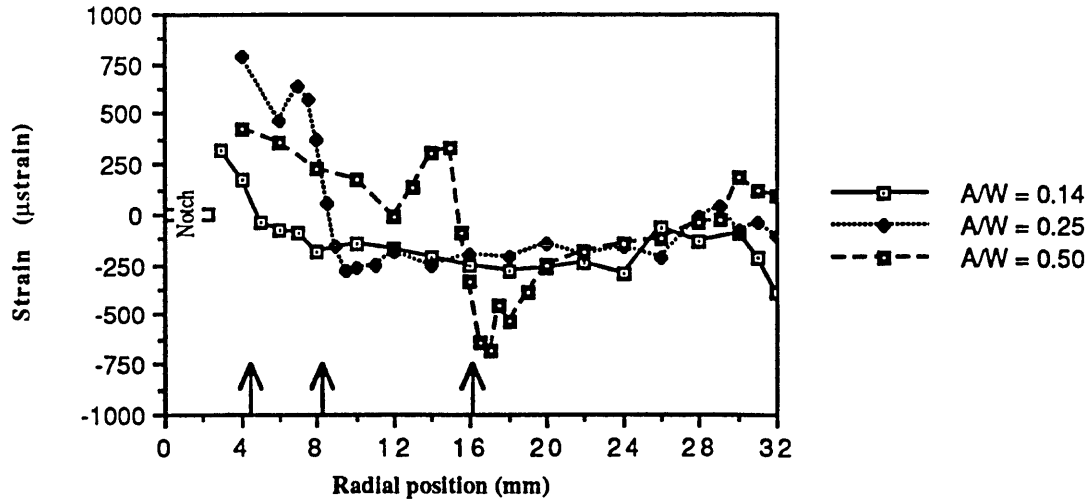


Figure 5.6a: Hoop stress / uncracked sides of autofrettaged rings

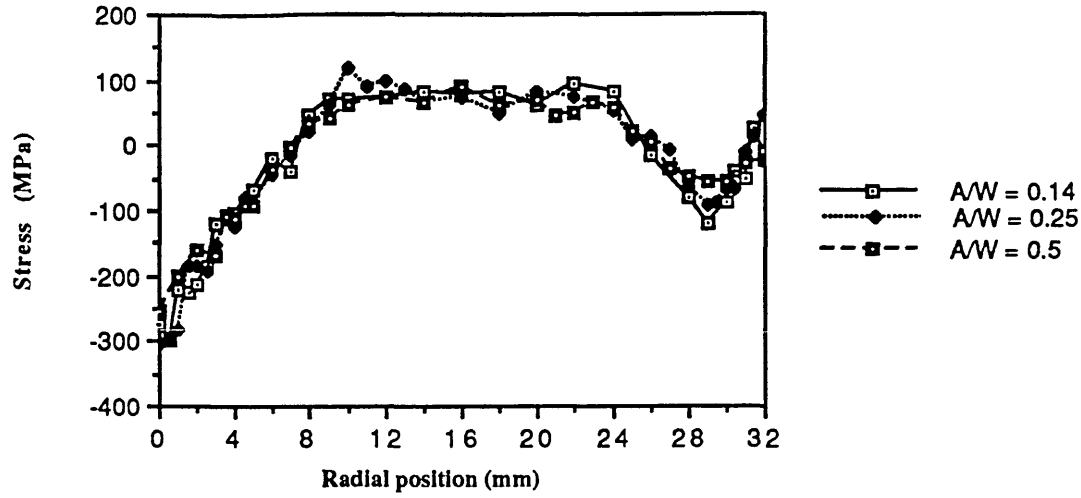


Figure 5.6b: Radial stress / uncracked sides of autofrettaged rings

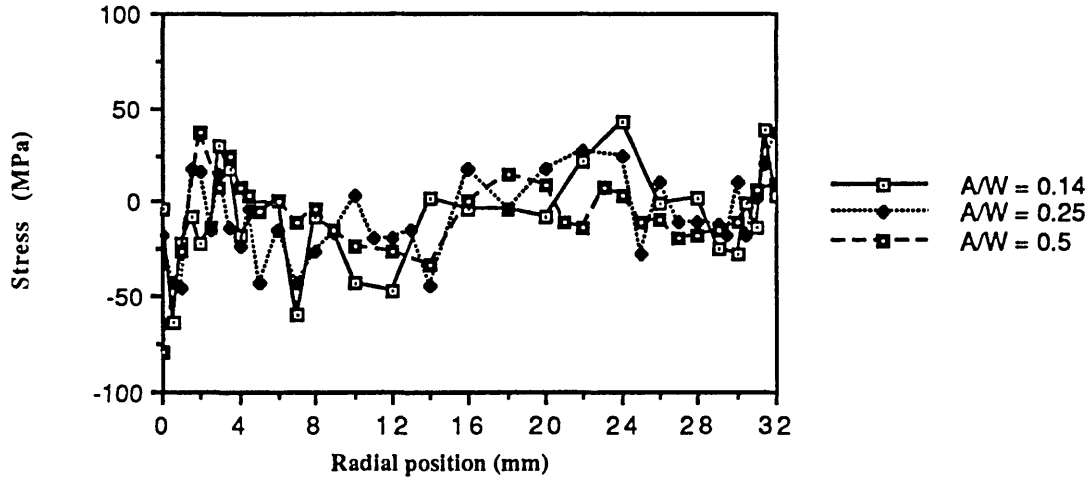


Figure 5.6c: Axial stress / uncracked sides of autofrettaged rings

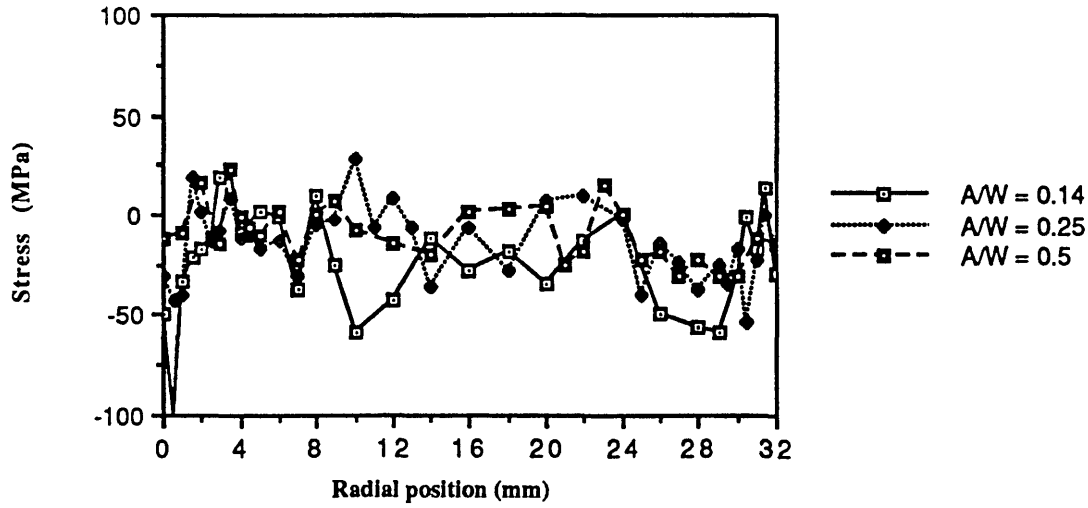


Figure 5.7a: Hoop stress / cracked sides of autofrettaged rings

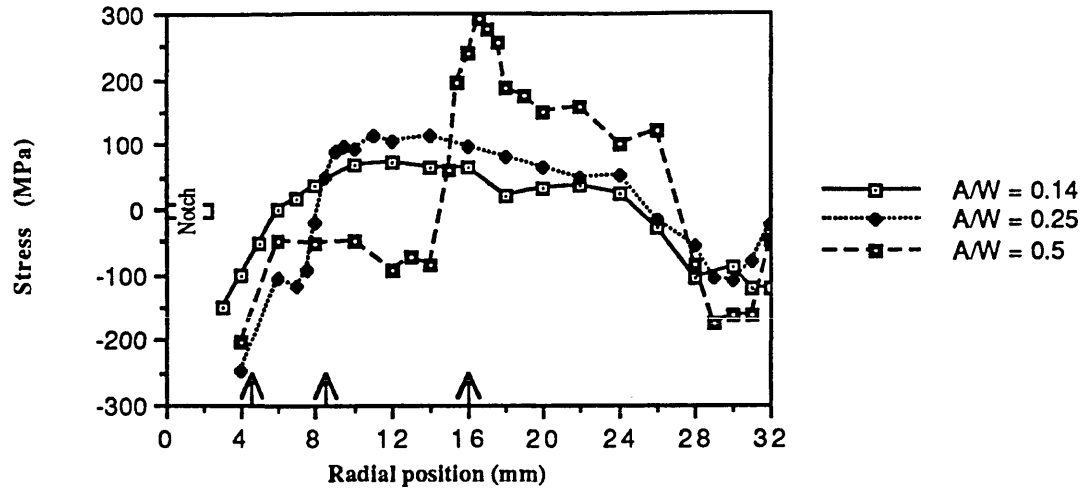


Figure 5.7b: Radial stress / cracked sides of autofrettaged rings

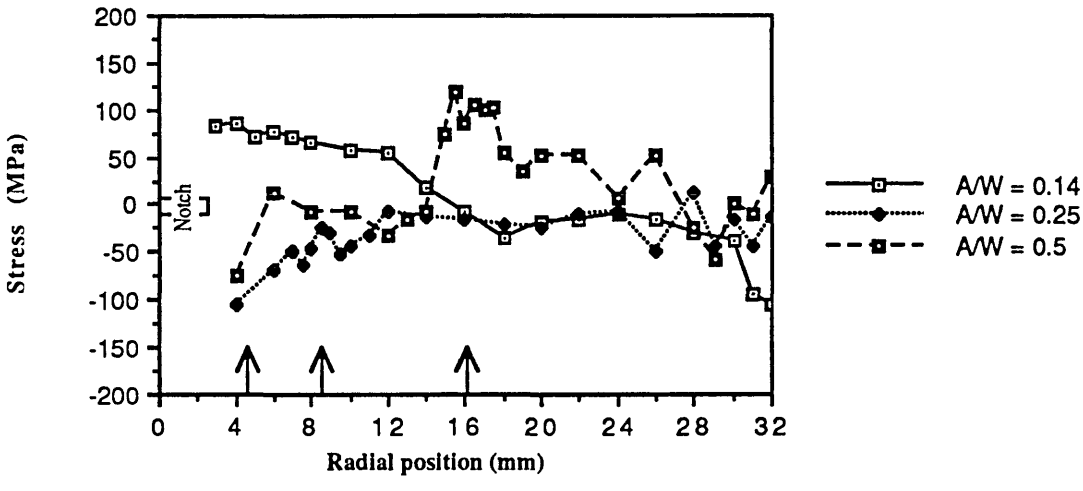
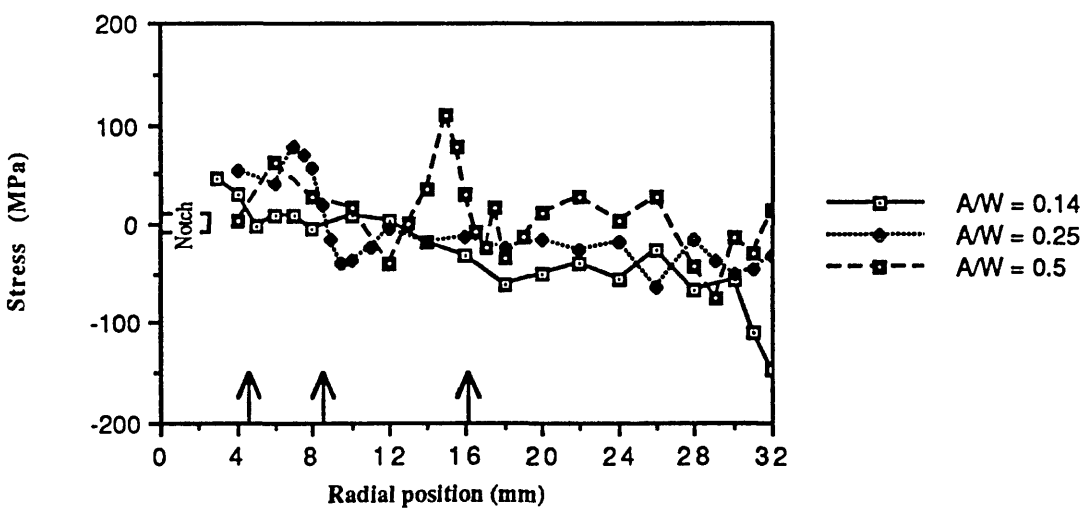


Figure 5.7c: Axial stress / cracked sides of autofrettaged rings



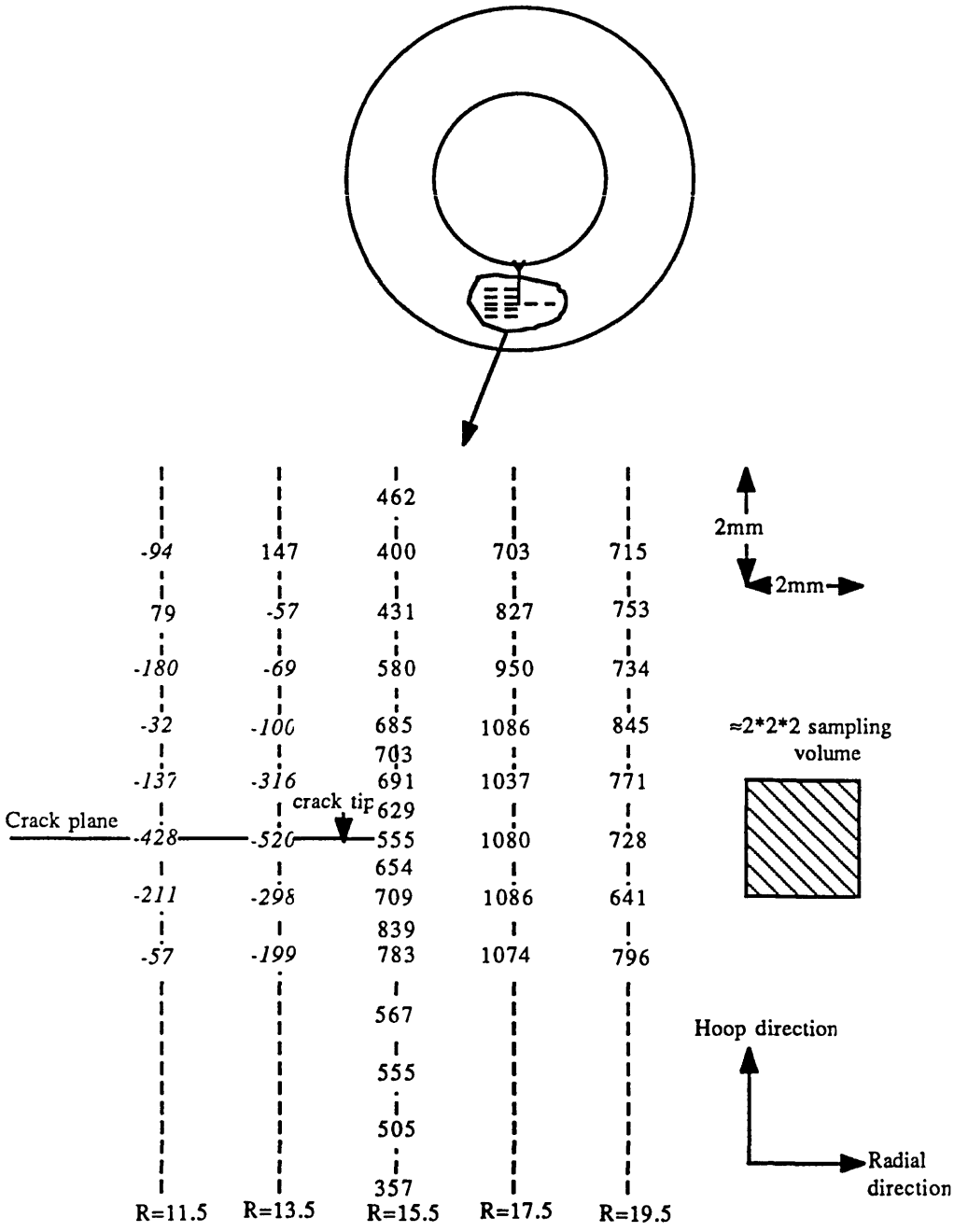


Figure 5.8: 9RDMA,(A/W = 0.5) Hoop strain array near crack tip

Figure 5.9a: Peak widths axial direction (A/W = 0.14)

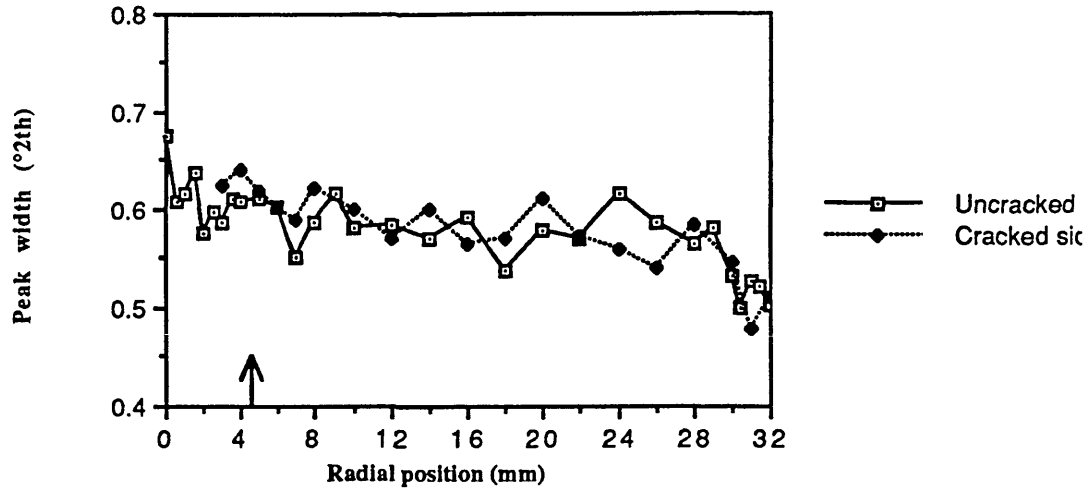


Figure 5.9b: Peak width axial strain (A/W = 0.5)

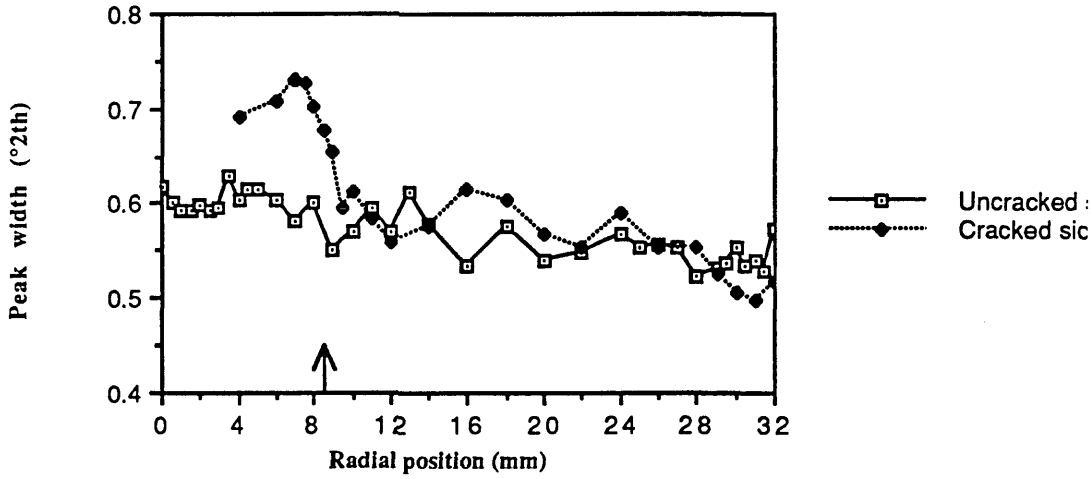
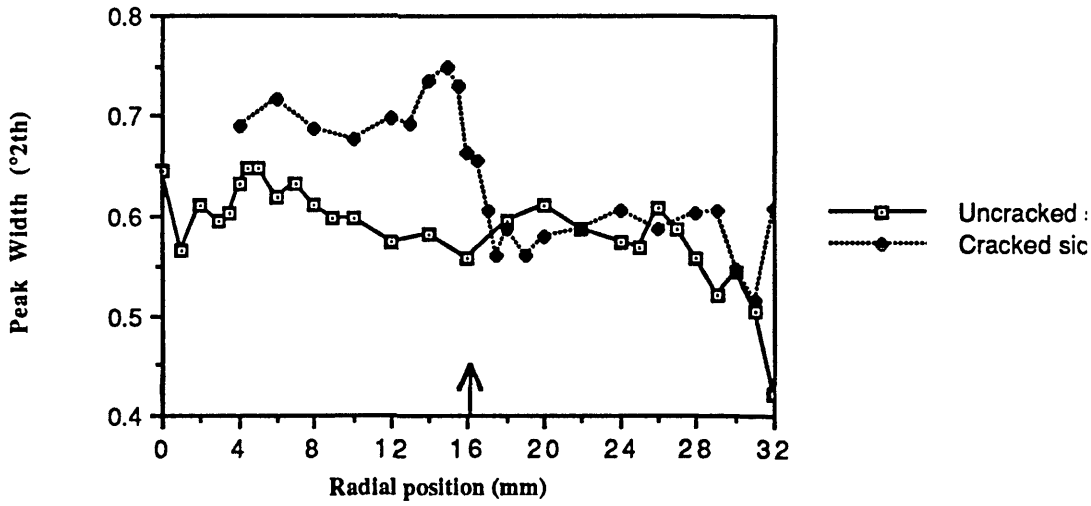


Figure 5.9c: Peak width axial strain (A/W = 0.5)



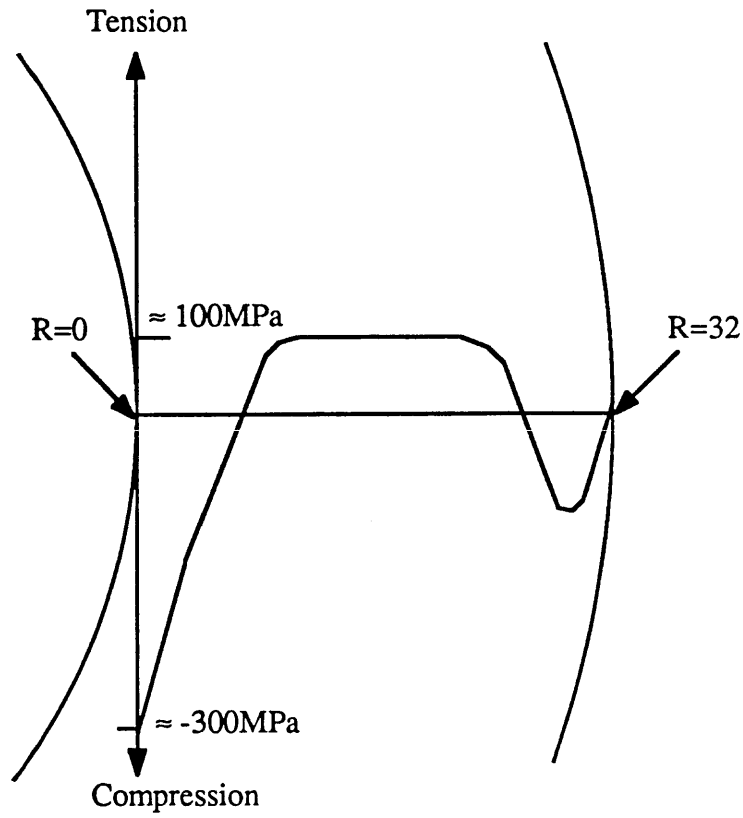


Figure 5.10a: Original hoop stress distribution

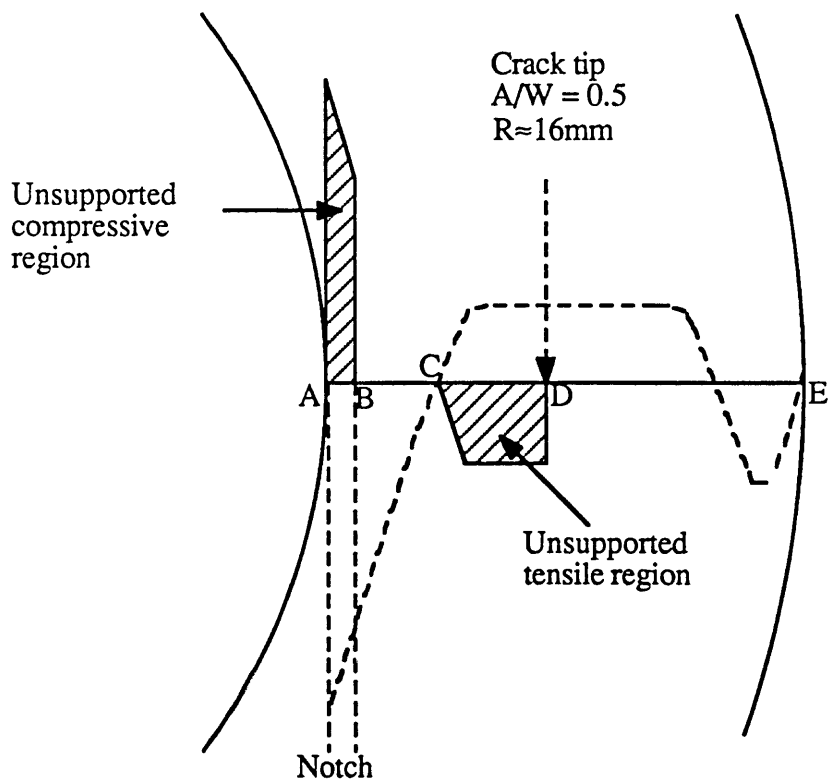


Figure 5.10b: Applied stress distribution (shaded) for BIE calculation

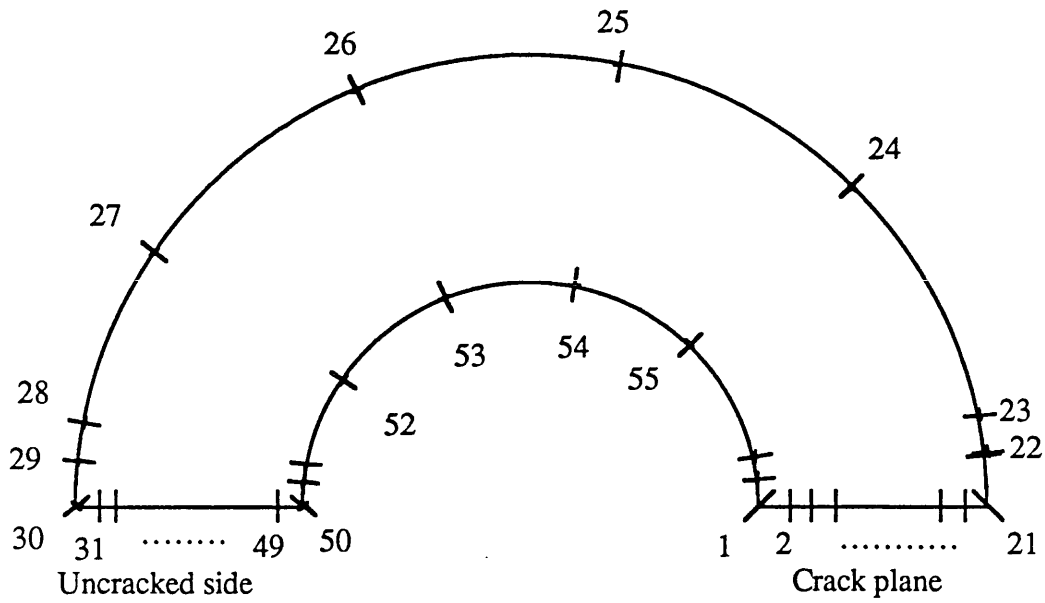


Figure 5.11: Boundary element mesh

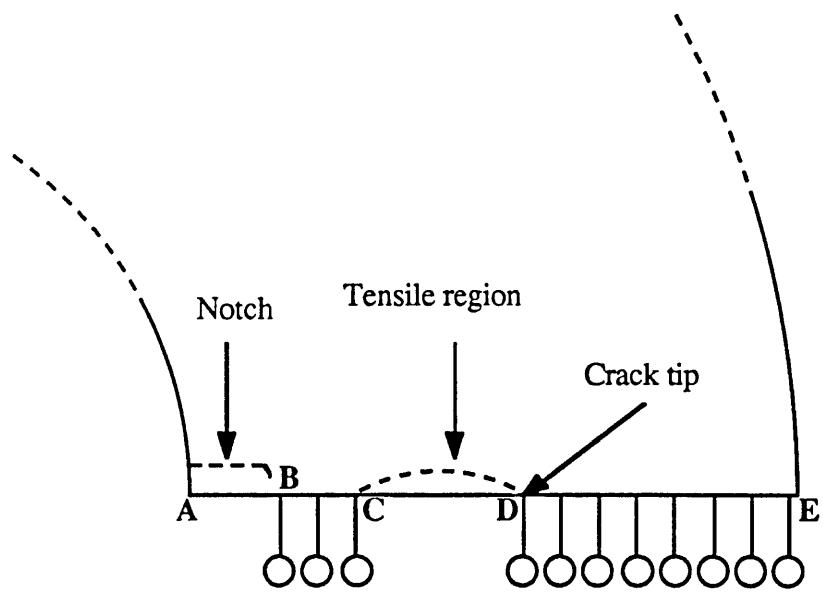
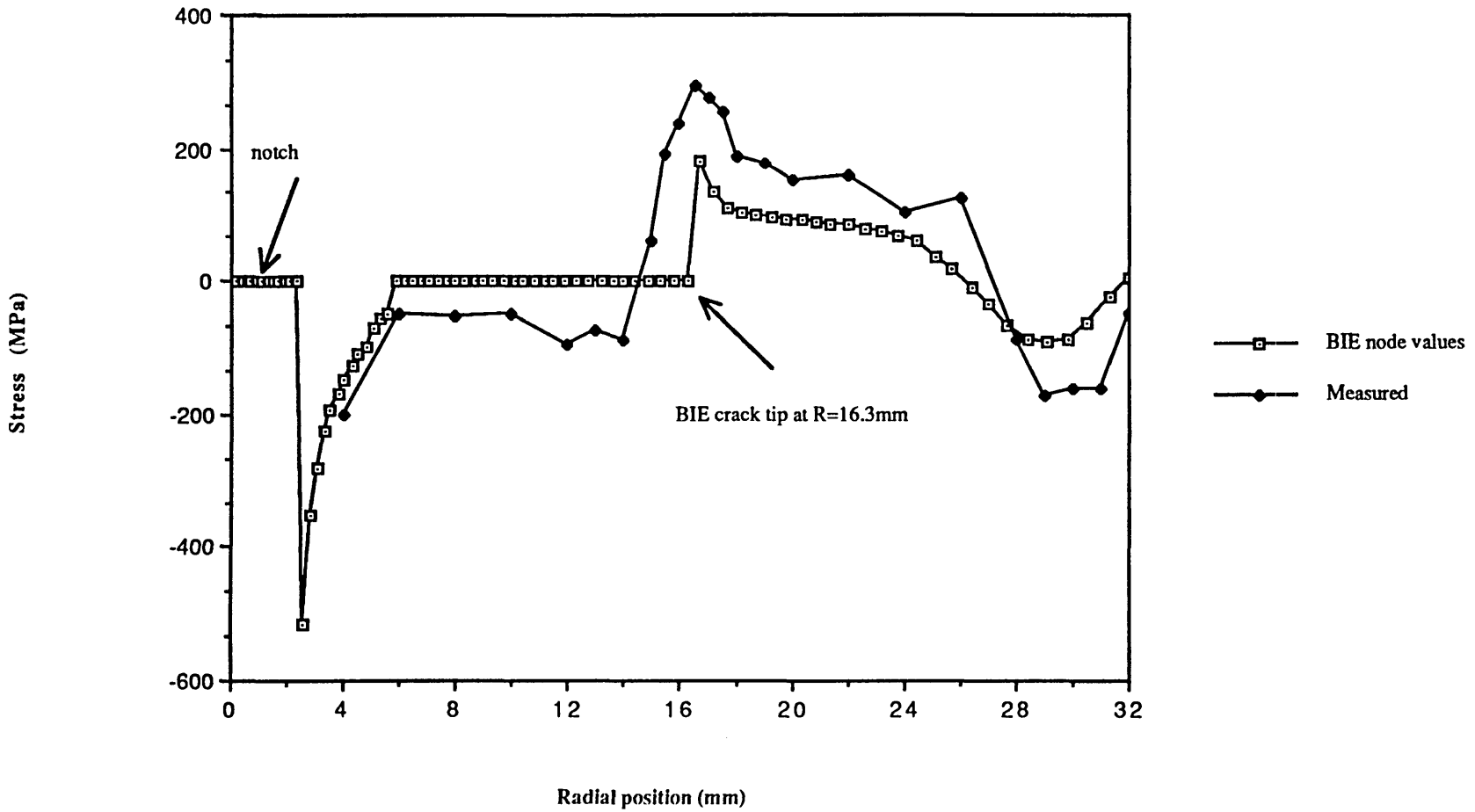


Figure 5.12: Boundary conditions on crack plane

Figure 5.13: Cracked side hoop stress measured (9RDMA) and BIE prediction



CHAPTER 6

Residual stress distributions in cracked beams

6.1 Introduction

Beneficial effects on structural integrity can result from proof loading tests, by the introduction of compressive residual stresses around flaws which inhibit their subsequent propagation under in-service loading conditions. Assessment of the benefits of overstressing requires a knowledge of the magnitude and extent of the compressive stress fields generated ahead of crack tips. However, experimental measurements are complicated by the rapid fall off and localised nature of the stress field adjacent to a defect. Neutron diffraction measurements are limited by the spatial resolution of the sampling volume and comparison with finite element predictions must take this into account.

Measurements have been made on D1A of the residual stress distributions in single edge notch bend (SENB) specimens of a low alloy ferritic steel. Fatigue cracks were introduced into two specimens, one of which was subsequently subjected to a warm pre-straining treatment. Relatively small stresses were noted in the fatigue-only specimen. In the prestrained specimen a zone of compressive residual stress was measured around the crack tip, which was less than finite element predictions. However the size of the plastic zone was in agreement with fracture mechanics estimates.

6.2 Background

Proof loading in the same sense but of greater magnitude than anticipated service load is often used to demonstrate the integrity of a structure. The preload induces plastic strain near defects in a surface, then on its removal, elastically strained material introduces a compressive stress in the deformed area. Subsequent in-sevice loading must overcome the residual compressive stress around the flaw before achieving a tensile stress sufficient to cause brittle fracture. The proof loading implications of preload are evident, however the benefit of residual stresses depend on their magnitude and rate of reduction ahead of and normal to a flaw. Provided that small spatial resolutions can be obtained, neutron measurements can offer a non-destructive

determination of their values.

The elastic stresses local to a crack can be determined from stress function solutions. In figure 6.1 a through thickness crack of length 2a is subjected to a remote stress, σ applied normal to the crack plane. In this case the elastic stresses are given by:

$$\sigma_{yy} = \frac{K}{\sqrt{2\pi r}} \cos\left(\frac{\theta}{2}\right) \left[1 + \sin\left(\frac{\theta}{2}\right) \sin\left(\frac{3\theta}{2}\right)\right] + \ldots\ldots\ldots\ldots \quad (6.1)$$

$$\sigma_{xx} = \frac{K}{\sqrt{2\pi r}} \cos\left(\frac{\theta}{2}\right) \left[1 - \sin\left(\frac{\theta}{2}\right) \sin\left(\frac{3\theta}{2}\right)\right] + \ldots\ldots\ldots\ldots \quad (6.2)$$

$$\sigma_{xy} = \frac{K}{\sqrt{2\pi r}} \cos\left(\frac{\theta}{2}\right) \left[\sin\left(\frac{\theta}{2}\right) \cos\left(\frac{\theta}{2}\right)\right] + \ldots\ldots\ldots\ldots \quad (6.3)$$

where r is the distance from the crack tip

θ is the angle to the crack plane (fig 6.1).

The stress intensity factor, K defines the singularity and for a SENB specimen, loaded in 3 point bending K is the mode I stress intensity factor. From equations (6.1 - 6.3), in the elastic region the stress varies as $r^{-1/2}$ with distance from the crack tip. At the crack tip there is a singularity where the stress tends to infinity. However, yielding and plasticity invalidate the elastic equations at small distances from the crack. If the crack tip remained sharp during loading then yield level residual compression would be expected near the crack tip region on unloading. However due to plasticity the crack tip will become blunted.

For small amounts of plasticity, fracture mechanics concepts give an estimate of the size of the plastic zone (Knott, 1976). The high local stresses at the crack tip are assumed to produce a circular plastic zone and if the Tresca yield criterion is applied, the radius is:

$$r_p = \frac{1}{2\pi}\left(\frac{K}{\sigma_y}\right)^2 \qquad \text{for plane stress} \quad (6.4)$$

$$r_p = \frac{1}{6\pi}\left(\frac{K}{\sigma_y}\right)^2 \qquad \text{for plane strain} \quad (6.5)$$

In practice the material behaviour will depend on effects like the Bauschinger effect and work hardening.

6.3 Specimens

Two SENB specimens were made with identical dimensions (fig 6.2). Both were fatigue pre-cracked from a notch 20mm deep leaving a fatigue crack approximately 5mm in length from the root of the notch. The maximum load applied in the final stage of fatigue cracking was 14kN. One specimen identified by the number 207 was left in the fatigue precracked condition and the second, numbered 206 was plastically deformed by three point bending in a servohydraulic test machine. During the prestrain treatment a clip gauge measured the crack mouth opening displacement (CMOD). A preload was applied to give a CMOD of 0.53mm, at a load of 51kN, and was then removed. The load-deflection curve is given in figure 6.3.

The original specimen thickness of 25mm gave prohibitively long count times because of absorption of the neutron beam. Consequently, both specimens were sectioned by spark erosion. The resultant pieces were approximately 12.5mm thick as shown in figure 6.2. The two halves were given an additional identification of A and B. The coordinate system for the specimens is illustrated in figure 6.2. The X direction is parallel to and lies along the crack, Y is perpendicular to and lies across the crack and Z is the through thickness direction. The crack tip is defined as X=5, Y=0 and the centre line of the specimen as Z=6.25mm.

The specimens were fabricated from a low alloy ferritic steel A533B class1, which is used in pressurized water reactor (PWR) vessels. The composition is given in table 6.1. The specimens were taken from a quenched and tempered steel plate with their major (Y) axes parallel to the rolling direction. A uniaxial tensile test at 20°C on a specimen taken from the same plate gave material properties: Young's modulus 207GPa, 0.2% proof strength 496MPa, tensile strength 672MPa and Poisson's ratio, 0.3.

Table 6.1 Chemical composition of A533B

Element	C	S	P	Si	Mn	Ni	Cr
Wt %	0.18	0.005	0.006	0.24	1.41	0.56	0.18
Element	Mo	V	Cu	Nb	Ti	Al	Sn
Wt %	0.48	<0.002	0.12	<0.002	<0.002	0.018	0.01
Element	Co	Fe					
Wt %	0.01	Balance					

6.4 Experimental results

6.4.1 Deformation response under reverse yield conditions

The effects of cyclic tensile and compressive loading for different levels of prior plastic strain was examined on a separate specimen. A servohydraulic testing machine was used under displacement controlled loading. The specimen was loaded in tension beyond the yield point, unloaded and then loaded beyond yield in compression to return to the zero displacement position. This loading sequence was repeated for increasing levels of applied displacement. The engineering stress-strain response is included in figure 6.4. The yield behaviour in tension and compression differs and compressive yield occurs at a smaller stress magnitude than the corresponding tensile yield. The phenomenon of different yield stresses and subsequent behaviour in cyclic tension and compression is known as the Bauschinger effect and occurs in real metals whenever there is a stress reversal.

The Bauschinger effect is commonly ignored in theories of plastic flow. Instead two idealised models are used to characterise the material behaviour, isotropic hardening and kinematic hardening. Isotropic hardening is characterised by a uniformly expanding yield surface in both tension and compression after the onset of plasticity. Thus if a material has been loaded beyond yield to maximum tensile stress of value of σ_{mt} it must then be reverse loaded to $-\sigma_{mt}$ before compressive yield occurs. The kinematic

hardening model assumes a yield surface which translates in stress space after yield but does not increase in size or volume. Thus the predicted yield in compression occurs at a stress equal to twice the yield stress below its current position on the tensile stress-strain curve. The material behaviour in figure 6.4 lies between the two limits.

6.4.2 Sampling volume and θ_0 determination

The physical extent of the sampling volume is critical for measurements in regions of steep stress gradient. In chapter 4 the dispersive effect on the beam profile for different positions of the input aperture was discussed. Consequently, prior to commencing strain measurements, the transmitted intensity profile of the neutron beam was recorded during vertical and horizontal traverses of a 0.5mm slit through the sample position. A square input aperture of side 2mm was used, approximately 14mm from the surface of the specimen. The input mask was not moved for the duration of each experiment. The profiles in figures 6.5a and 6.5b indicate that the input cross section of the beam is close to a square of side 2mm horizontally and 2.2mm vertically.

The orientations for the X, Y and Z strains are illustrated in figure 6.6. Figure 6.7 is a photograph of one of the specimens in position for an X strain measurement. The measurements were made with the (211) reflection at $2\theta_0 \approx 109.4°$2th using a wavelength of 1.95 Å. Since the diffraction angle is not 90° in plan view, the sampling volume is a rhombus (for an exit slit of 2mm). Consequently, when the specimens are rotated into different orientations small differences in the sampled volume occur. Close to the surface when the sampling volume was only partially immersed in the specimen, the measurement positions were corrected by reference to the intensity profiles. Some weak reflections have been omitted from the results because of systematic errors.

After spark erosion the path length for the neutrons through the specimen in the X and Y orientations was approximately 12.5 / sin 35.3° (22mm) In the Z orientation the path length was similar but varied for different positions in the sampling volume. Count times were typically 20 minutes for each scan. All measurements were made at the mid-thickness position (Z=6.25mm).

The strain-free reference angle, θ_0 was measured on a small ($\approx 1cm^3$) cube taken from the corner of one of the specimens. However the strains measured in different

directions in the cube indicated that it could not be treated as stress free. Fortunately, stress profiles were obtained on a plane through each sample and θ_0 can be inferred for force and moment balance across the section. The stresses were assumed to be constant in the through thickness direction. The difference in stress for θ_0 obtained from force or moment equilibrium is only 6MPa and if an average value of θ_0 is taken from the three directions of the cube, the stresses differ from force balance by 12MPa. All the quoted results employ a value of θ_0 determined by force balance.

Due to the symmetry of the specimens the principal stress directions were assumed to coincide with the X, Y and Z axes and the isotropic stress strain relationships (2.14) were used to convert the strains to stress.

6.4.3 Measurements ahead of the crack tip

The distance from the root of the notch along the crack to the outer edge is 30mm. Experimental measurements were made in the prestrained and as fatigued specimens along the crack plane, at intervals of 0.5mm near the crack tip and of 2mm through the surviving ligament. At each position the strain in the three orthogonal directions was measured. For the two specimens the strains on the plane ahead of the crack tip are superimposed for each direction in figures 6.8,6.9 and 6.10. Similarly the stress distributions are given in figures 6.11, 6.12 and 6.13. In each figure the tip of the fatigue crack is indicated by an arrow. For clarity the data error bars are not included. For the fatigued-only sample the stress errors are $\pm$ 11MPa and for the prestrained specimen are $\pm$ 20MPa.

Fatigue only specimen, 207:

Along the plane of the crack the X and Y stresses are small except in the crack tip region. The through thickness stress, σ_z is approximately -50MPa from approximately X=6 to X=30mm. (A similar compressive σ_z stress is observed in the prestrain specimen, 206 from X=12mm to X=30mm). In the region of the crack (X=0 to X=5mm) the through thickness stress, σ_z, rises to 80 MPa. This feature is not observed in the preload specimen, 206.

A small tensile stress perpendicular to the crack face is observed at

approximately X=4mm on the crack plane, 1mm before the crack tip (fig 6.12). It reduces to zero by X=10mm. Tensile stress over the crack plane is not possible and the observation is attributed to the effect of the finite sampling volume.

Prestrained specimen 206:

The pre-strain treatment introduced a maximum compressive stress normal to the crack of ≈180 MPa approximately 0.5mm ahead of the crack tip at X=5.5mm (fig 6.12). However this decreases rapidly away from the crack tip and becomes tensile at X=7.0mm.

At the free surfaces, X=30 and at the notch tip, X=0 the X stress must be zero. The preload specimen satisfied this constraint at X=30mm however at X=0 there is an anomalous tensile stress of 80MPa. This has also been attributed to sampling of extraneous material around the notch. A maximum tensile stress of ≈200MPa was observed in the Y direction at X=10mm and at X=30mm.

6.4.4 Measurements normal to the crack plane

In the preload specimen strains were also measured on a line normal to the crack plane on either side of the X=5.5mm position. A symmetrical scan from Y=12 to Y=-12mm was obtained. The symmetry of the scans about Y=0, provide a check of the position of the sampling volume relative to the crack plane. These results are discussed in the section 6.5.2 and 6.6.

6.4.5 Plastic zone sizes

Smith (1987) calibrated the relationship between prior plastic strain and peak width for simple compact tension and compression specimens of A533B. Prior plastic strain in either sense was shown to increase the width of diffraction peaks. By noting the peak widths an estimate of the plastically strained zone can be made. The widths corresponding to the Y strain ahead of and normal to the crack tip are given in figures 6.14 and 6.15 .

Care must be taken not to confuse the the effects of plastic deformation with the

broadening resulting from steep stress gradients. Experience suggests that some of the increase in peak widths observed in figures 6.14 and 6.15 may be attributed to plastic deformation. In the fatigue-only sample, 207 no variation beyond the experimental error was was seen for the peak widths near the crack tip.

6.5 Finite element prediction

6.5.1 FE description

Finite element analysis has been applied to the prestrained specimen 206. The aim of the modeling was to predict the shape and the extent of the residual stresses and to assess the size of the plastic zone at the crack tip. A two dimensional elastic plastic solution program (PLIPP) was used, which is part of the Welding Institute finite element system (WIFES) (Smith, 1981). PLIPP solutions for plane strain and plane stress conditions give upper and lower bounds for the global, load-displacement behaviour of SENB specimens.

The prestrained specimen 206 was modeled in 2 dimensions using 3rd order isoparametric quadrilateral elements. Symmetry around the crack plane permitted the use of a symmetric half mesh. The mesh which was focussed on the crack tip, was refined along the crack flank and the remaining ligament (fig 6.16). An isotropic hardening model was assumed despite the observed Bauschinger effect. Loads and reactions were assumed to act at single points and the Von-Mises yield criterion was applied. A more detailed description of the FE model is given by Smith (1989).

The material parameters used in the analysis were: Young's modulus 207GPa, first yield at 485MPA and Poisson's ratio 0.3. Beyond first yield at 485MPa the stress strain curve is non linear and the data were input as discrete coordinate pairs taken from the true stress-strain curve for the material.

Both plane stress and plane strain constraint conditions were applied. For plane stress, the model was incrementally loaded to the maximum observed CMOD then incrementally unloaded. The CMOD of the numerical model was defined as twice the axial displacement δ_y of the uppermost node on the crack flank (fig 6.16). In plane strain, the model was loaded incrementally to the maximum experimental load per unit

thickness then incrementally unloaded. To prevent loss of symmetry by overlap it was necessary to fix some nodes at the crack tip.

6.5.2 Residual stresses

The two-dimensional finite element analysis for a given load predicts a stiffer response in plane strain than in plane stress. Initial calculations for both constraint conditions predicted a high compressive stress normal to the crack. For the plane stress solution a maximum value of -1064 MPa was predicted at the crack tip and -1864 MPa for the plane strain solution. The preliminary solutions in the X and Y directions are given in figures 6.17 and 6.18. However, these are nodal values and to make a comparison with the experimental results the numerical stress distribution must be averaged to imitate the finite sampling volume ($\approx 8mm^3$) of the neutron measurements. By averaging the stress values at each numerical integration point which fell inside an appropriate area ($4mm^2$) the sampling process of the neutron method was simulated and an averaged numerical stress was obtained at each measuring position.

The averaging process reduced the peak compressive residual stresses. Figure 6.19 and 6.20 show the predicted X and Y stress, after the averaging process, along the crack plane for the two constraint conditions and the experimental data. The same averaging process was carried out for the numerical results normal to the crack plane and are included in figures 6.21 and 6.22.

6.5.3 Plastic region

The plastic zone predicted by the finite element model was determined by identifying the points where the equivalent plastic strains were no longer zero. The experimentally obtained peak widths (figs 6.16 and 6.17) were converted to plastic strain by reference to Smith's (1987) results. The experimental and predicted values for the plastic region parallel to and normal to the crack are given in figures 6.23 and 6.24.

6.6 Discussion

Even after account has been taken of the finite sampling volume the numerical method predicts a larger residual stress at the crack tip than is observed experimentally (figs 6.19-6.22). During the traverse parallel to the crack plane the maximum measured Y stress in the crack tip region is -180 MPa compared to the corrected numerical predictions of -480 and -510 MPa, for plane strain and plane stress respectively. The corresponding values for the peak stresses in the X direction are -60MPa for the measured value and -190 or -315 MPa for the plane stress or plane strain estimates.

Normal to the crack plane (fig 6.22) the Y stress changed from a compressive peak of -100 MPa near the crack tip to close to zero between 3 and 4mm on either side of the crack plane. The maximum value near the crack tip of -100MPa (fig 6.22) compared to -180MPa measured in the traverse parallel to the crack plane (fig 6.20) suggests that the positioning was in error in the X direction. In view of the steep decrease of the compressive stress field ahead of the crack tip only a small displacement in the X direction would result in a large reduction in the measured stress. In the Y direction the positioning is thought to be correct because the scans in figures 6.21 and 6.22 are symmetrical about about Y=0. The finite element calculations plotted in figures 6.21 and 6.22 were displaced 0.5mm to X=6.0mm to account for the discrepancy in the magnitude of the Y stress on the crack plane.

At distances greater than 5mm from the crack tip there is reasonable agreement between the predicted and measured stresses. In general, the high constraint plane strain solution predicts a stiffer response than the plane stress prediction for a given load and the two predictions bound the the experimental results.

In both orientations the averaged finite element analyses predict larger stress magnitudes and larger compressive regions on either side of the crack plane than were experimentally measured. For the Y stresses the ratio of the measured to the averaged, predicted value is typically 0.36. Parallel to the crack plane and approaching the crack tip the two constraint conditions predict different X stress behaviour. In plane stress the X stress became increasingly compressive and in plane strain increasingly tensile. In figure 6.19 the data appear closer to the latter.

The difference in magnitude between the experimental and predicted stresses at the crack tip may be attributable to the unrealistic isotropic hardening used in the FE model despite the fact that the material has shown a significant Bauschinger effect. Thus after initial tensile yielding during the three point bend procedure the yield in compression occurred at a lower stress than predicted by isotropic hardening. To correct the predicted data to the experimental results the yield stress in compression would have to be reduced to ≈40% of yield in tension, i.e. to about -200MPa. From figure 6.4 this is not unreasonable.

In the prestrained specimen a crack closure stress of approximately 50MPa in the Y direction was noted to within 0.5mm of the notch (fig 6.20). Also in both specimens a through thickness, Z stress was seen in the uncracked ligament (fig 6.13). However, the FE model is 2 dimensional and cannot be applied to this issue.

The finite element analysis indicates that the compressive Y stress resulting from the pre-strain will reduce to zero between 1 and 3mm ahead of the crack tip. Figure 6.20 supports this assertion and demonstrates the localised nature of the stresses at the crack tip. The compressive region may be estimated from the plastic zone size. The maximum stress intensity factor, K applied during the fatigue precracking was 27.6 MPa$\sqrt{m}$ and during the plastic overload was 100.6 MPa$\sqrt{m}$. For plane strain, from equation 6.5, the radii of the plastically deformed zones are 0.16mm and 2.15mm for the as-fatigued and prestrained specimens respectively. (The plane stress estimates are 0.48 and 6.75mm).

The predicted plastic zone in the fatigued-only specimen is considerably smaller than the sampling volume used for the experimental measurements. No variation in peak widths were observed near the crack tip of the fatigued only specimen. In the preloaded specimen the stress variation seen in figure 6.12 supports the fracture mechanics estimate of a plastic zone radius of ≈2mm. However using the peak width as an indicator of the plastic zone size gives a much larger estimate (figs 6.23 and 6.24). This is probably due to a contribution to the peak width arising from the stress gradient over the sampling volume and could be subtracted out.

6.7 Recommendations

If the compressive stress normal to the crack reduces from a maximum value at or near the crack tip to zero approximately 2mm away then the change from compression to tension can be contained within the sampling volume used for these measurements. Using better experimental resolution it may be possible to resolve the stress in the plastically strained zone. Spatial resolutions better than $1mm^3$ have been achieved, although the count time on these specimens would be several hours for each measurement to obtain similar accuracies.

The elastic plastic finite element program, PLIPP used in these calculations only incorporates isotropic work hardening. More accurate predictions could be achieved using a model which includes the Bauschinger effect and the change in work hardening behaviour on reverse loading.

6.8 Conclusions

Neutron diffraction measurements have resolved the residual stresses produced in a fatigue cracked pre-strained bar down to a cubic sampling volume of approximately $8mm^3$. The maximum measured compressive residual stress at the crack tip was -180MPa. Two unexpected phenomena were observed: in the prestrained specimen a compressive stress of approximately -50MPa exists across the crack plane, and for both specimens a through thickness stress is present for most of the uncracked ligament.

Initial comparison with an FE model indicated much smaller measured stresses than predicted. The correlation is improved by allowing for the finite spatial resolution of the neutron technique. The numerical results were averaged over points in the FE mesh to simulate the sampling volume. In regions away from the crack tip the volume averaged numerical data and experimental results showed similar behaviour with reasonable agreement both in the magnitudes of the predicted stresses and in the crossover points between tension and compression. However near the crack tip the averaged numerical data still predicted larger stresses than were observed. The differences are attributable to the unrealistic isotropic hardening model employed in the FE calculation. For effective modeling of the material behaviour at the crack tip a more realistic hardening rule is required. Nevertheless, the level of compressive stresses at

the crack tip suggest that there is less benefit from overstressing than might be hoped.

Predictions of plastic deformation were attempted from the width of the Bragg reflections. Apart from some agreement with fracture mechanics estimates and qualitative agreement with FE predictions further work is needed before effective use can be made of the peak shape profiles.

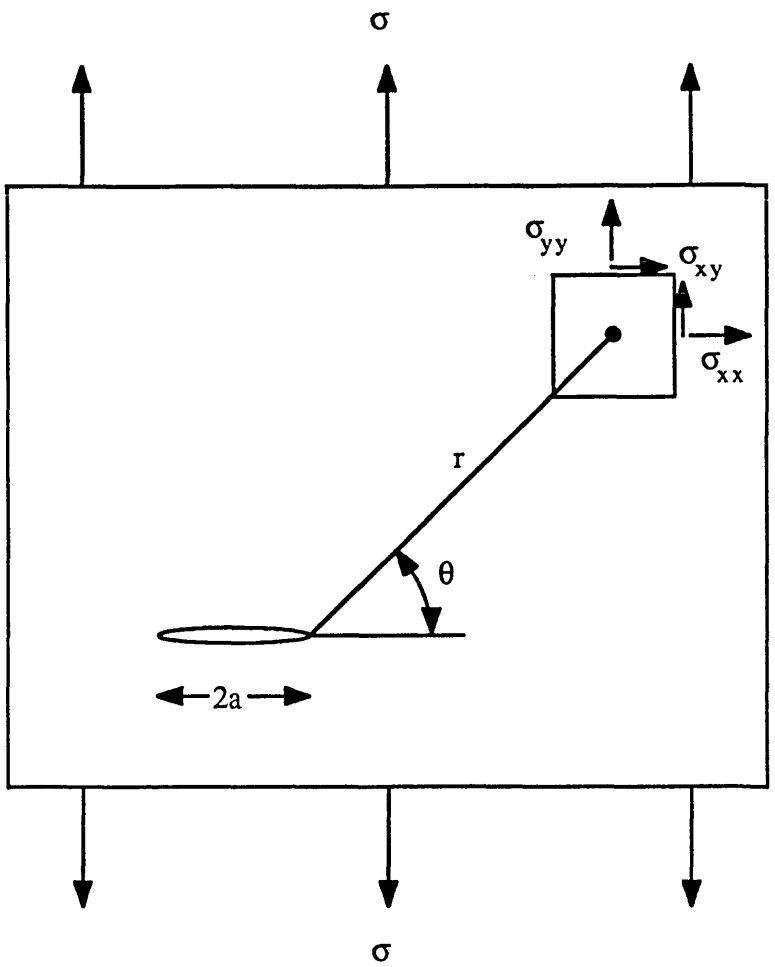


Figure 6.1: Elastic stress distribution ahead of a crack

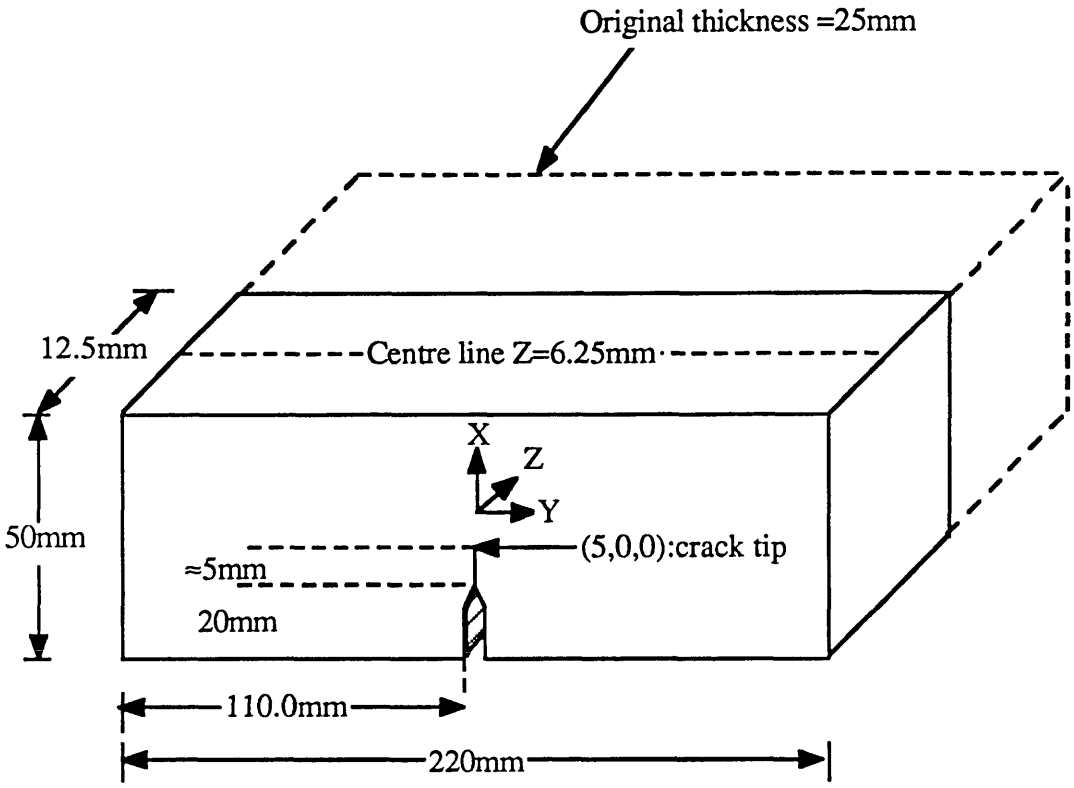
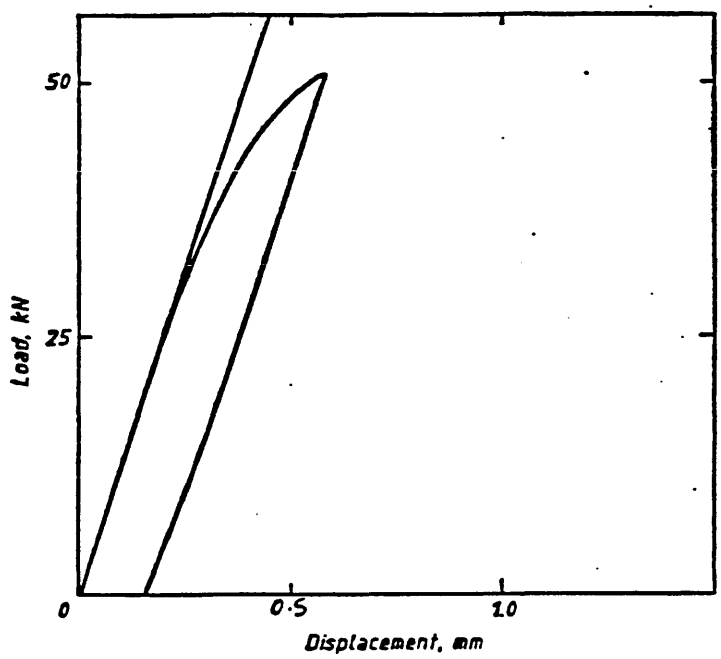


Figure 6.2: SENB specimens, dimension and coordinate system



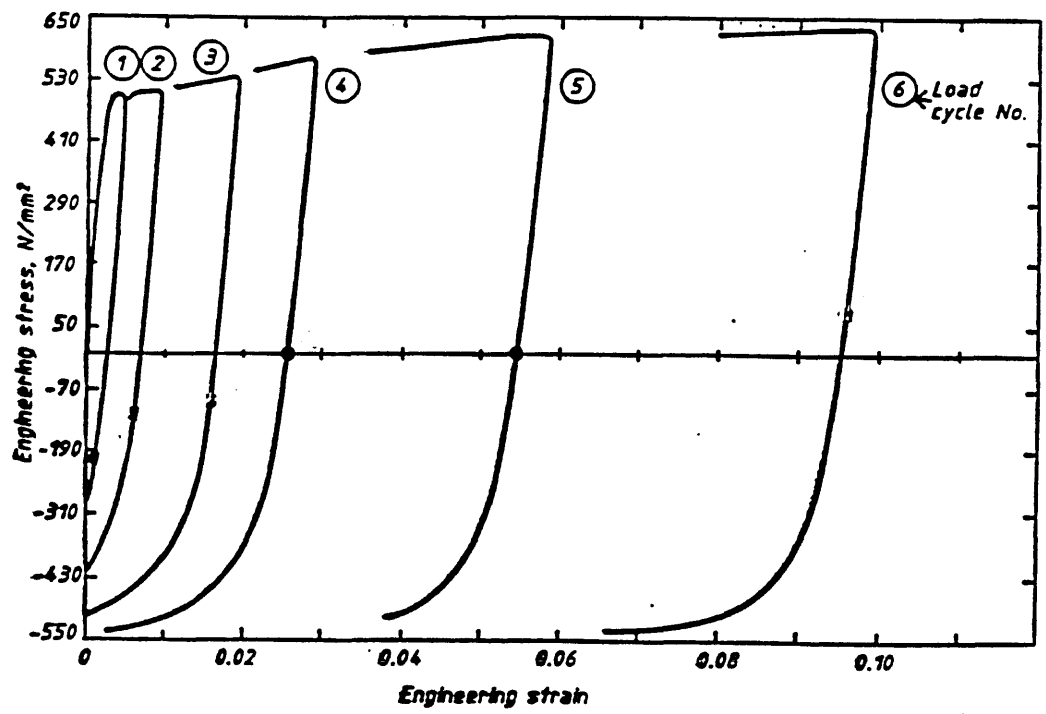


Figure 6.3 (TOP) Load displacement curve for preloaded specimen,

206

Figure 6.4 (BOTTOM) A533B material behaviour on reverse loading

Figure 6.5a: Transmitted profile: horizontal slit through 2*2mm beam

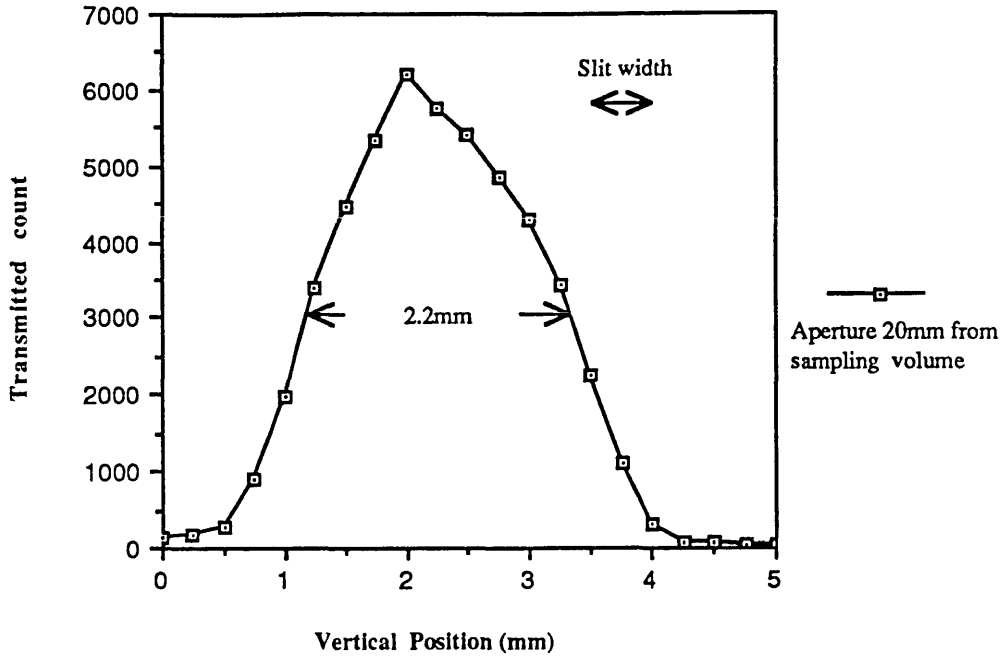
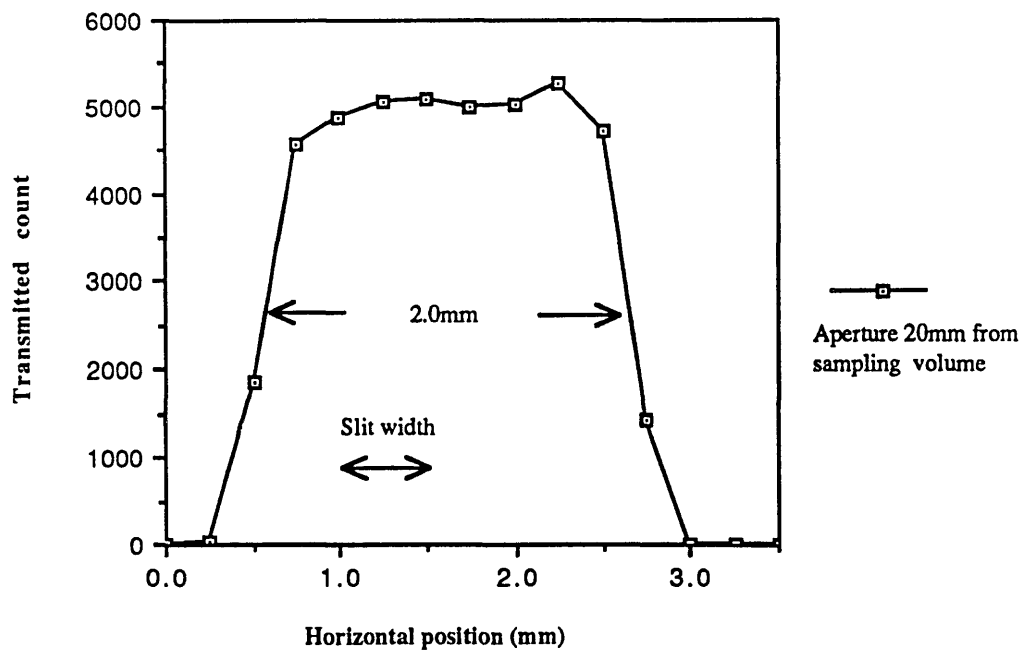


Figure 6.5b: Transmitted profile: vertical slit through 2*2mm beam



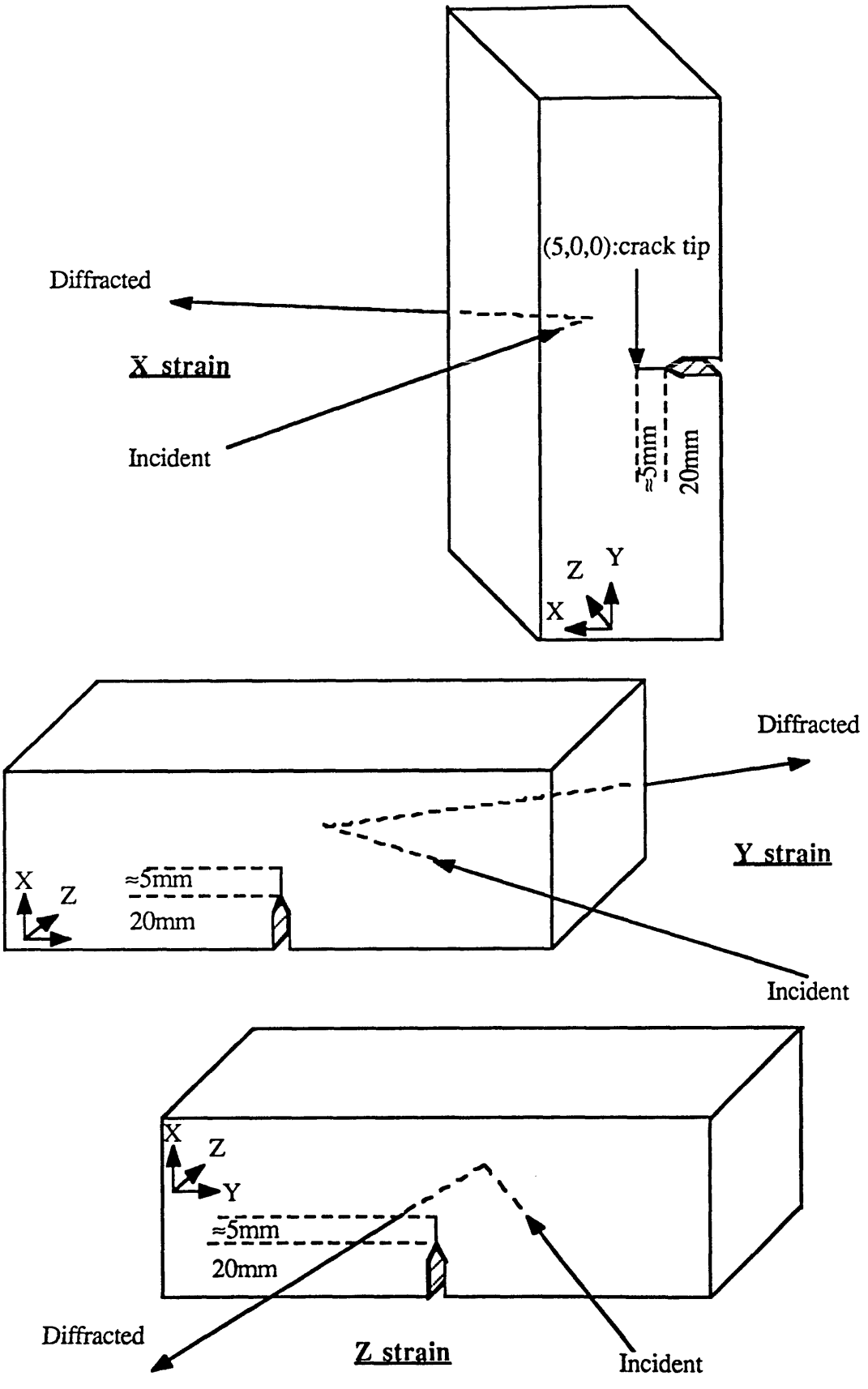


Figure 6.6 SENB orientation for X,Y,Z strain measurements

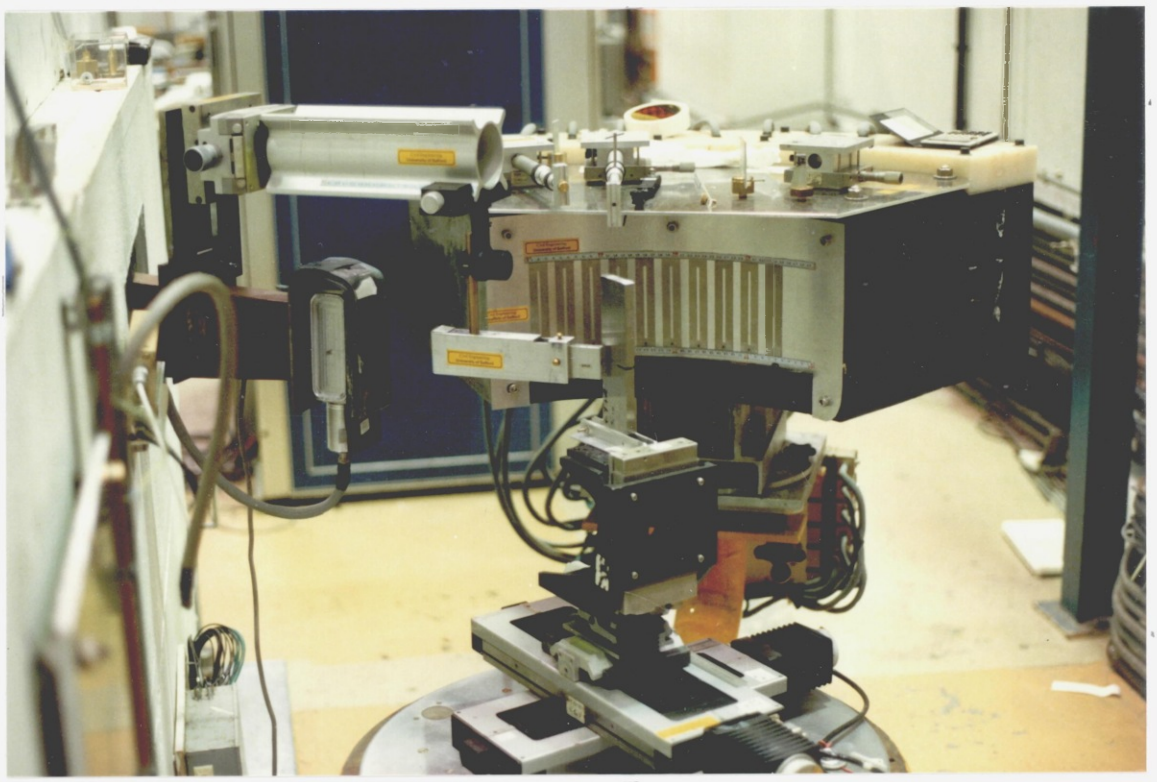


Figure 6.7: SENB specimen in position for X strain measurement

Figure 6.8: X strain ahead of crack plane (206&207)

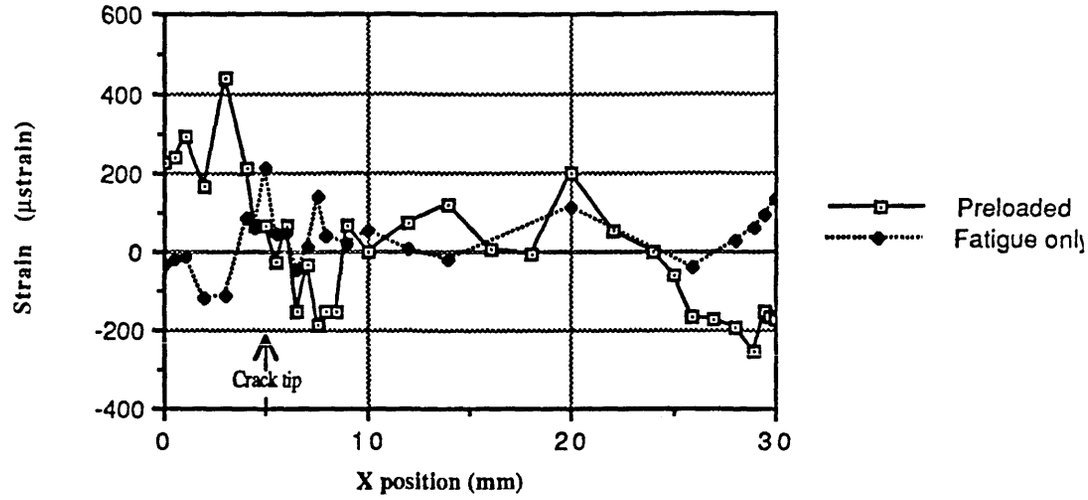


Figure 6.9: Y strain ahead of crack plane (206&207)

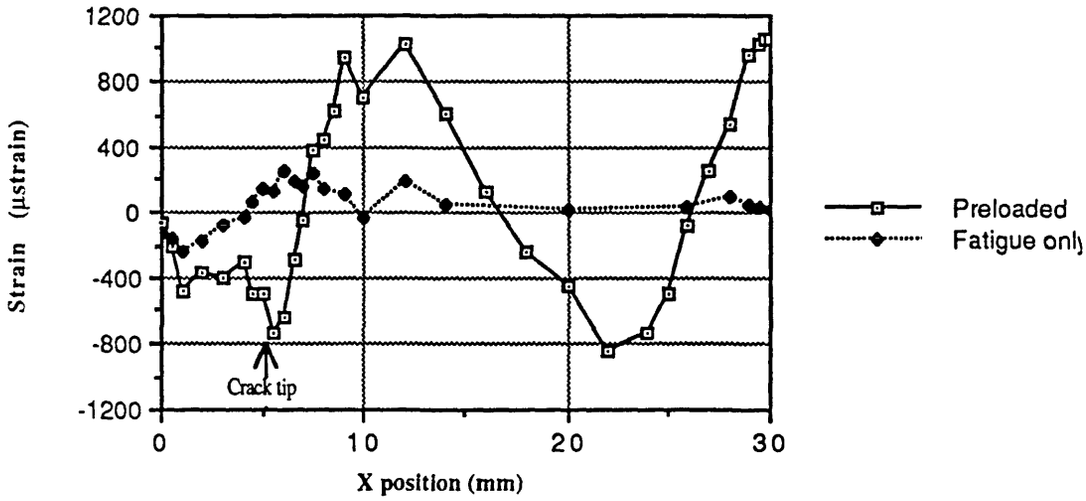


Figure 6.10: Z strain ahead of crack plane (206&207)

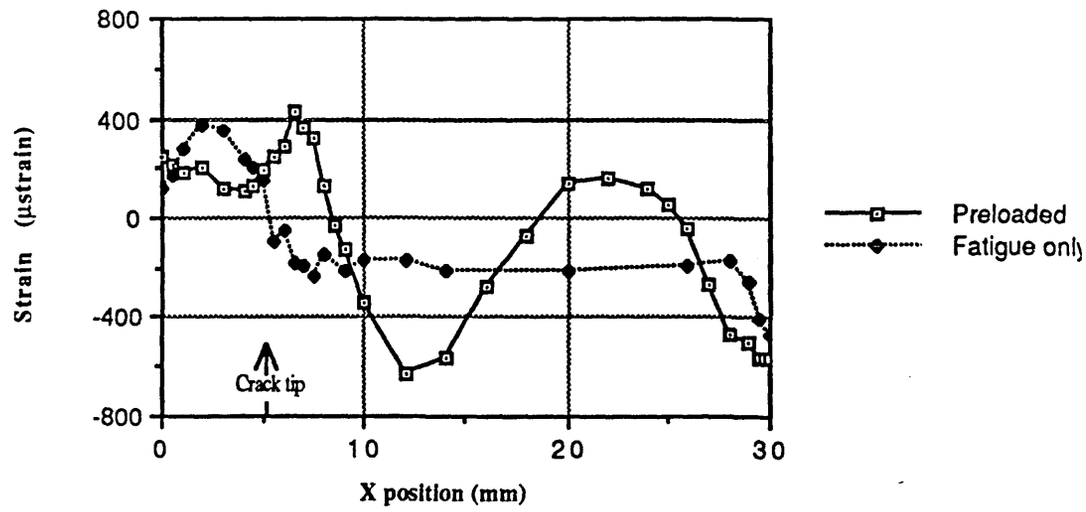


Figure 6.11: X stress ahead of crack plane

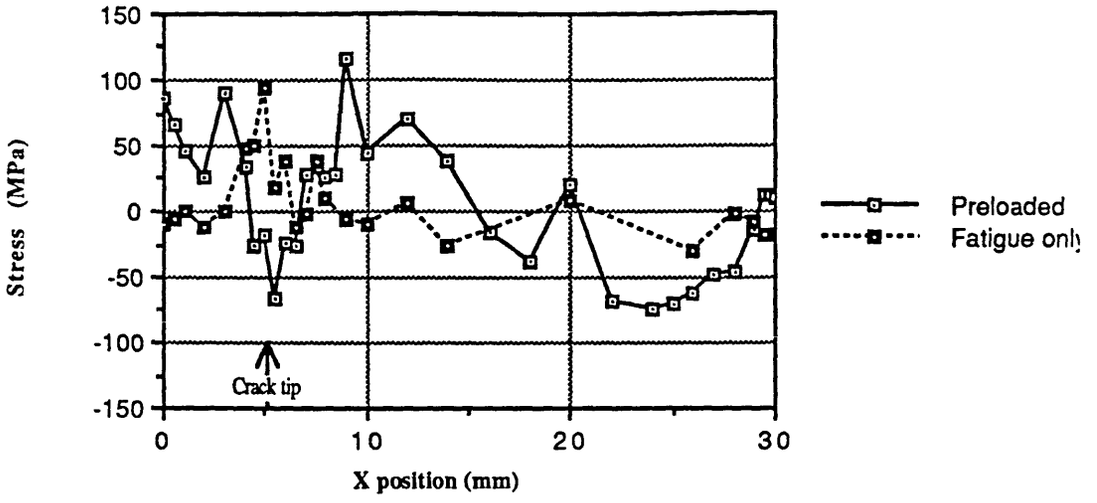


Figure 6.12: Y stress ahead of crack plane (206&207)

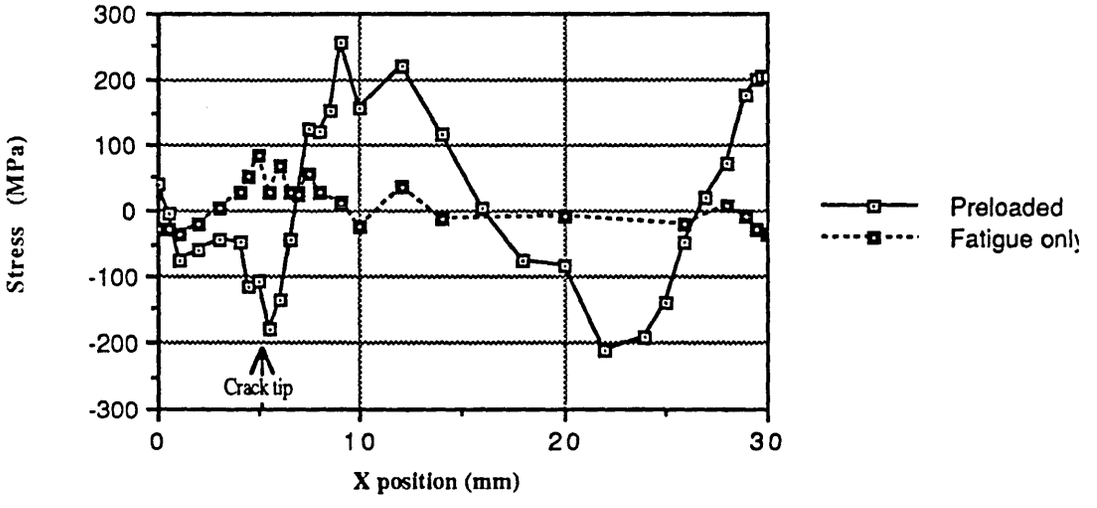


Figure 6.13: Z stress ahead of crack plane (206&207)

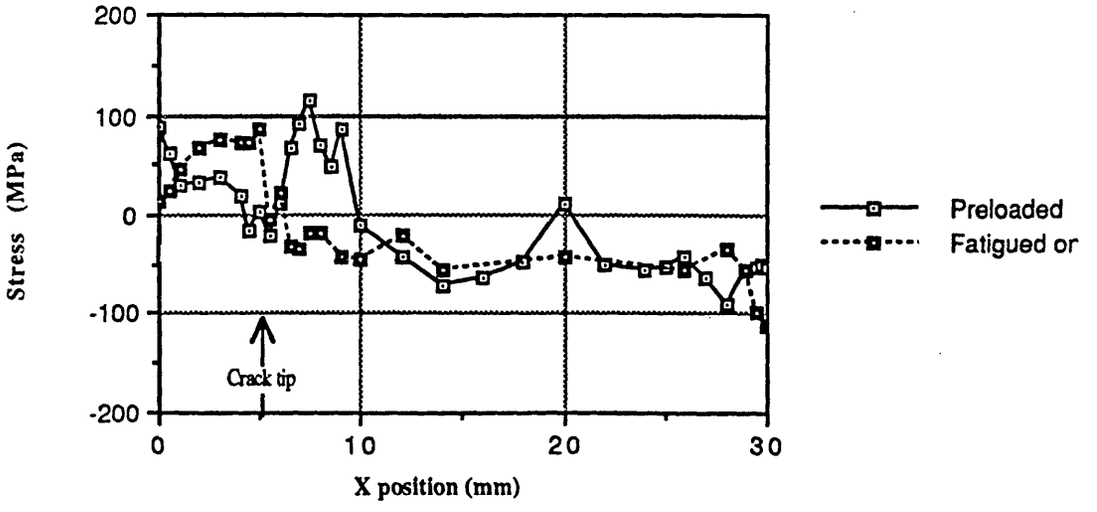


Figure 6.14: Y strain peak widths - traverse parallel to crack

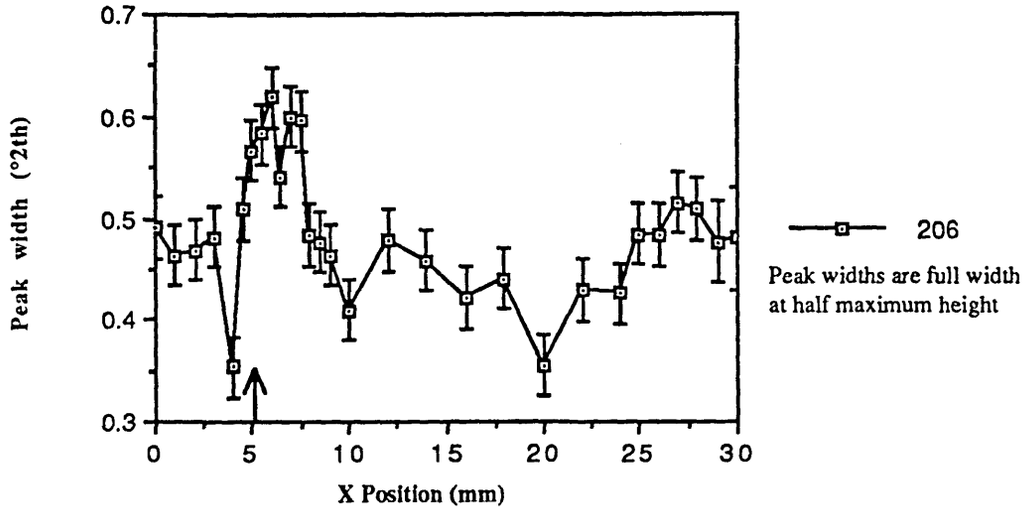
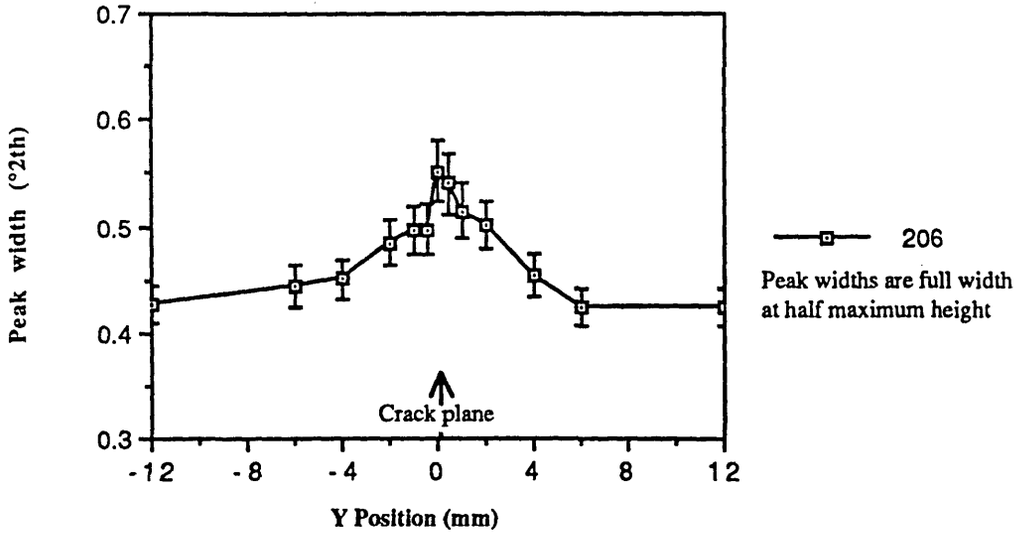


Figure 6.15: Y strain peak widths-traverse normal to crack



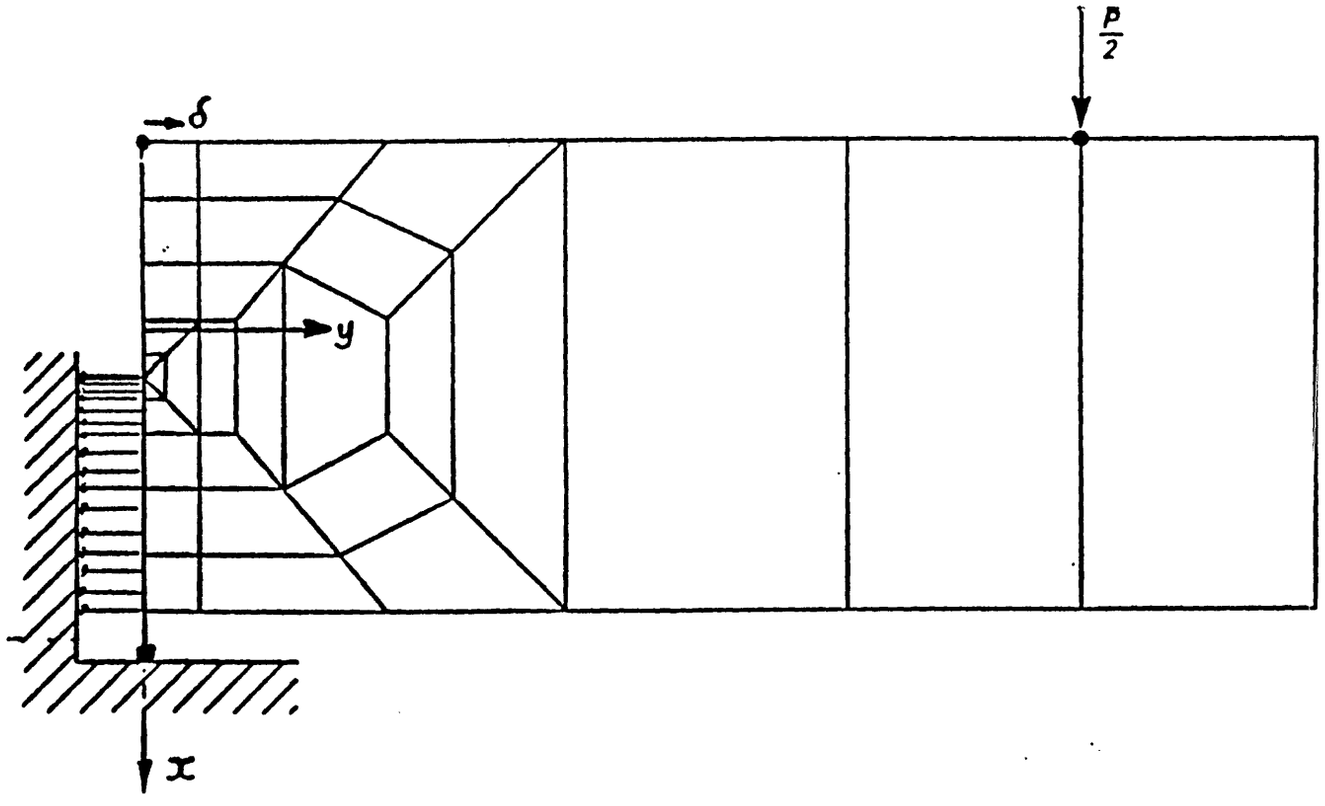
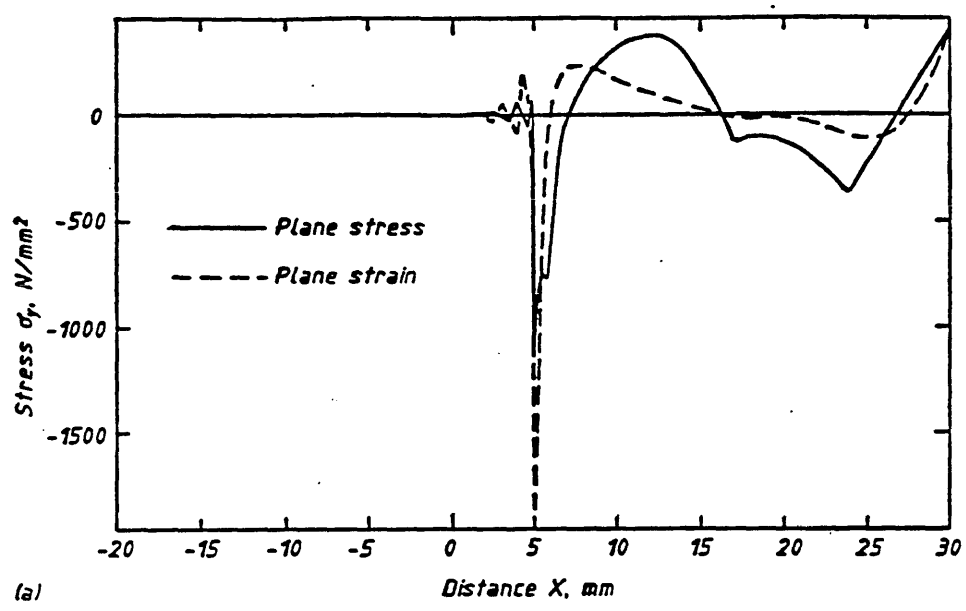


Figure 6.16: FE model with boundary conditions and applied loads



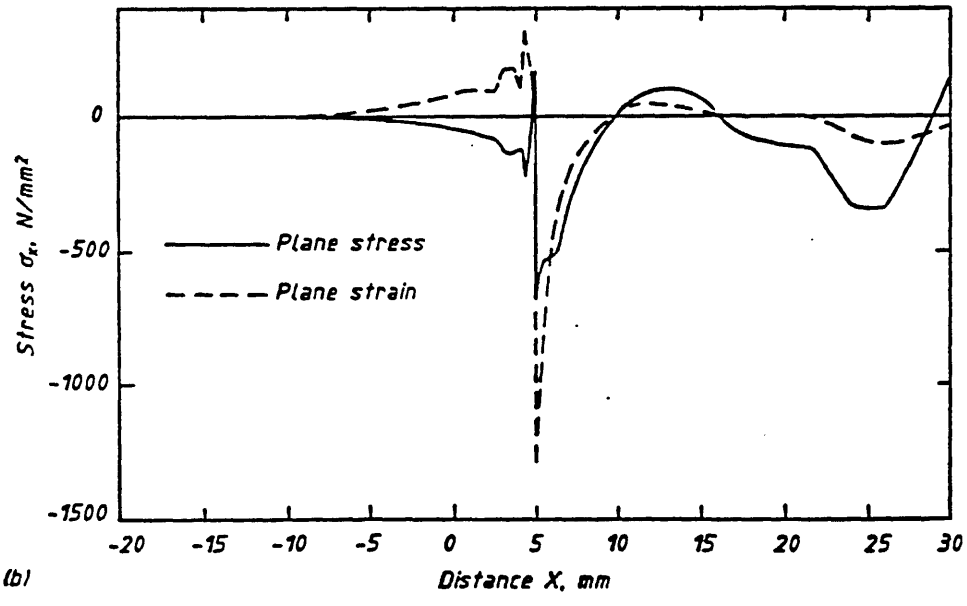


Figure 6.17 (TOP) FE residual node point stresses Y direction

Figure 6.18 (BOTTOM) FE residual node point stresses X direction

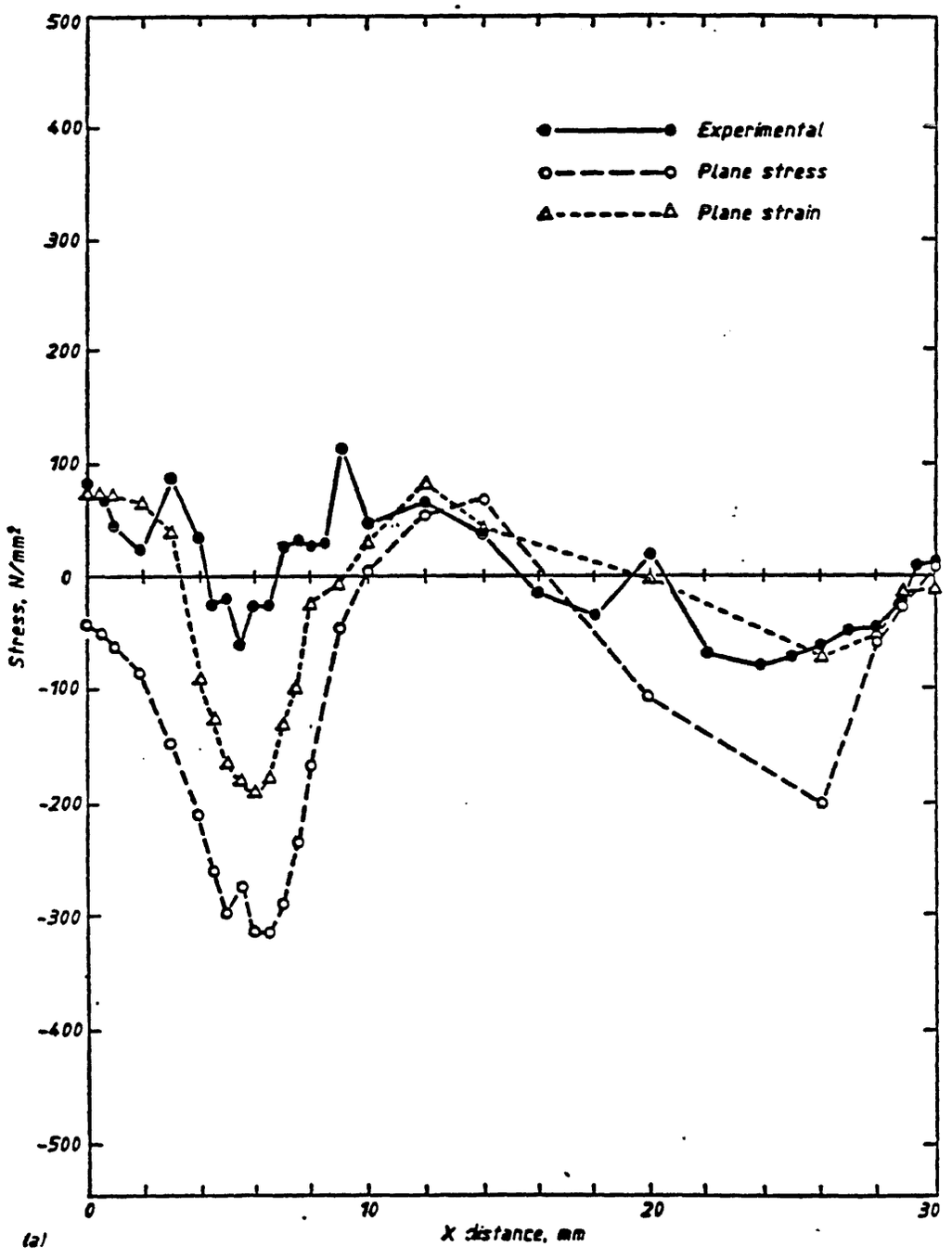


Figure 6.19: Experimental and averaged FE X stresses ahead of the notch tip

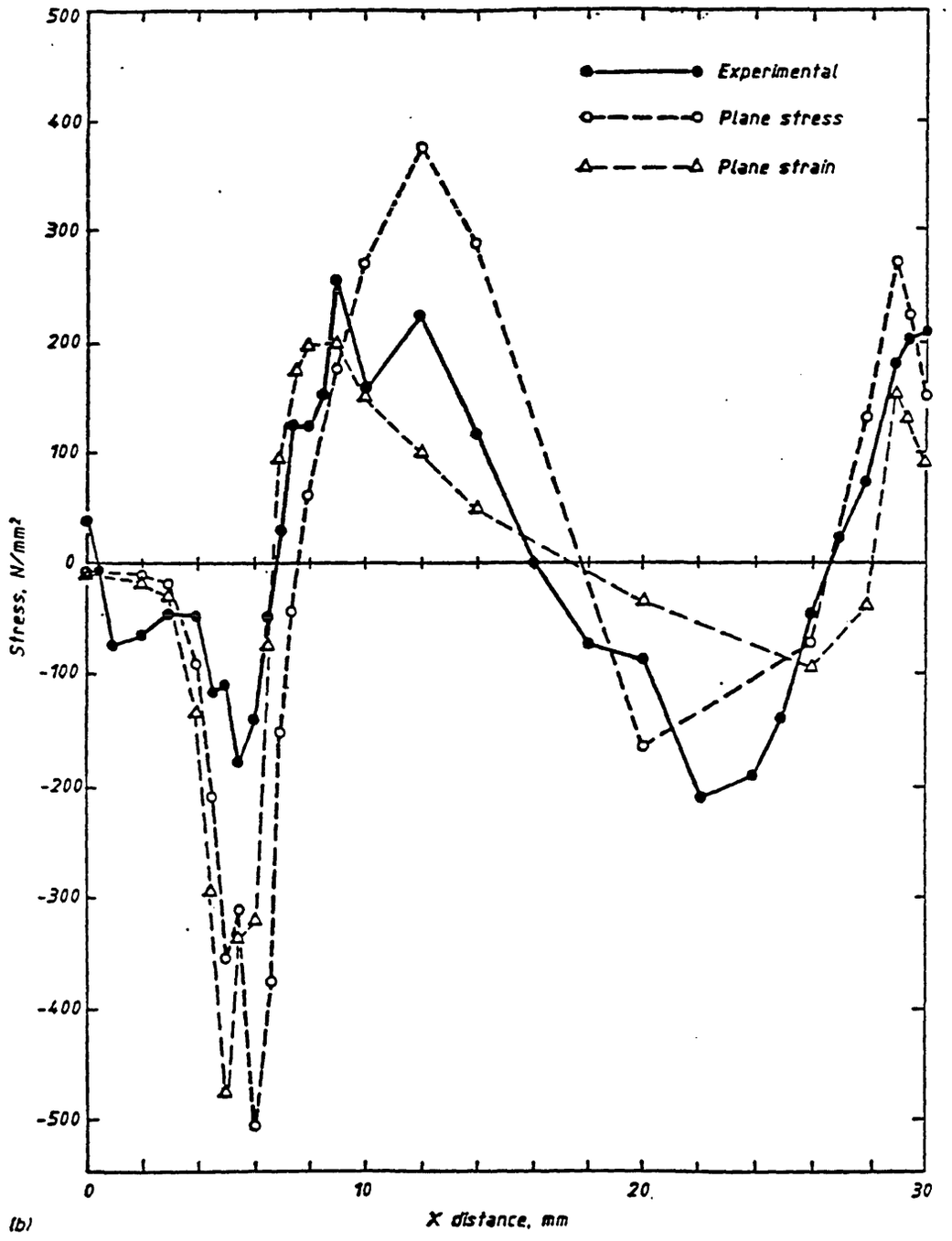


Figure 6.20: Experimental and averaged FE Y stresses ahead of the notch tip

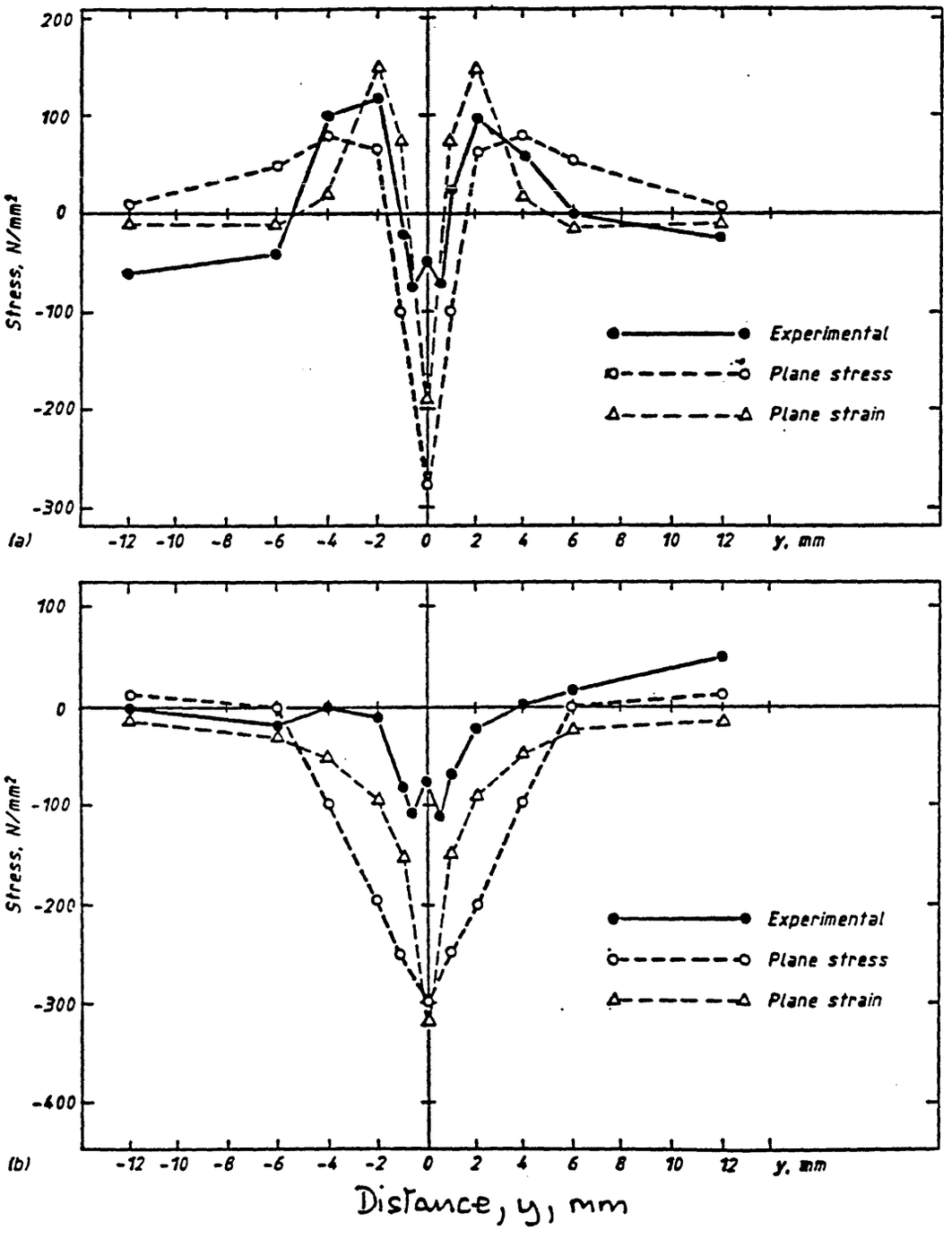


Figure 6.21 (TOP) Experimental and averaged FE X stresses normal to crack plane in 206

Figure 6.22 (BOTTOM) Experimental and averaged FE Y stresses normal to the crack plane in 206

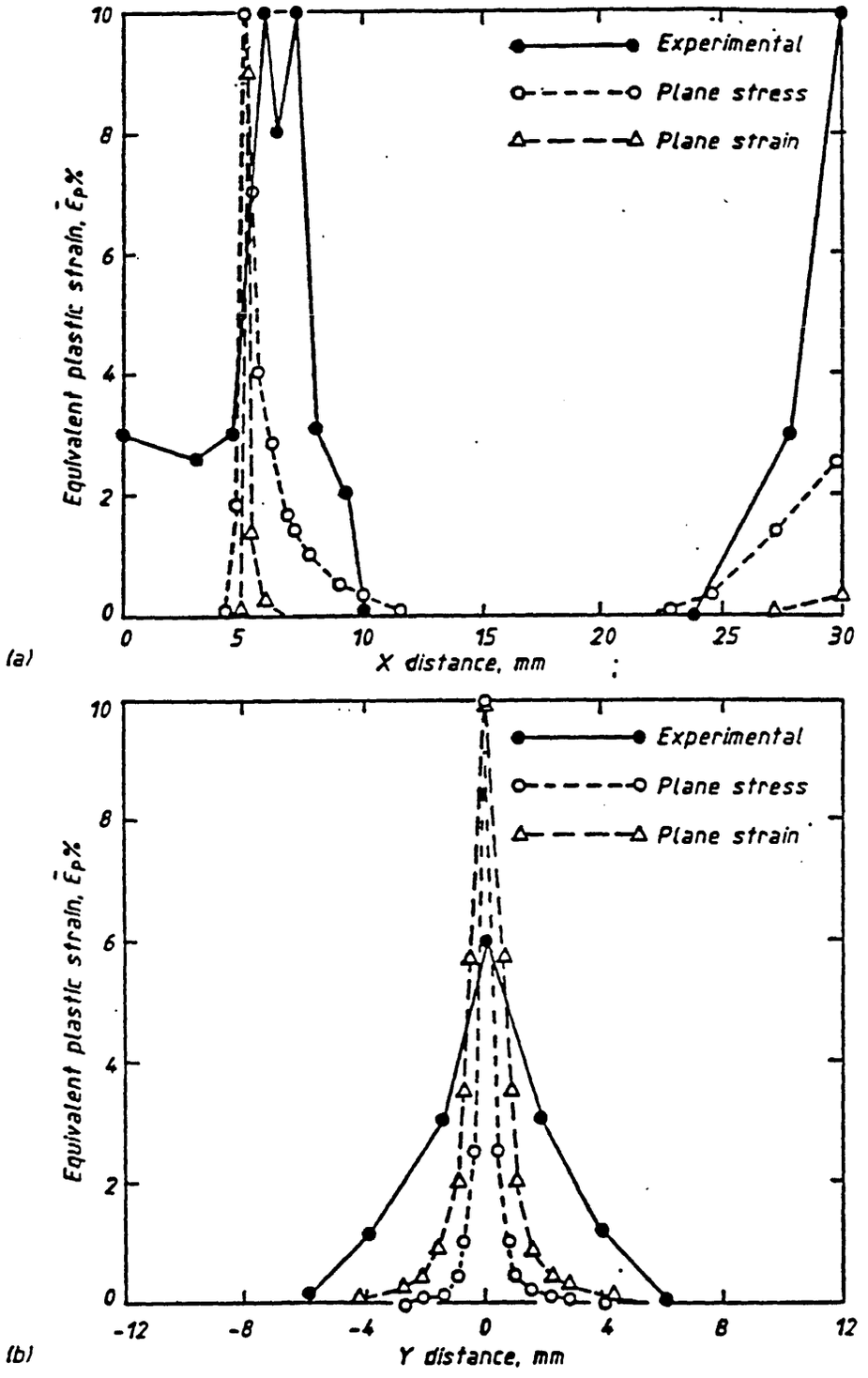


Figure 6.23 (TOP) Experimental and FE prediction of plastic region along crack plane in 206

Figure 6.24 (BOTTOM) Experimental and FE prediction of plastic region normal to crack plane in 206

CHAPTER 7

Residual stresses in railway rails

7.1 Introduction

Failure processes in railway lines are governed by a combination of live stresses resulting from the passage of trains and residual stresses in the rail. Superposition of the two contributions can move the combined stress into or away from a tensile stress state. Approximately 5000 defective rails are replaced in the United Kingdom every year. Many of these failures are due to fatigue cracks which are encouraged by the tensile residual stresses produced by fabrication processes or by plasticity in the rail head due to high surface loading. Conventional strain measurement in rails is performed by slicing and sectioning after attaching strain gauges. Large path lengths in original rail sections require the neutron technique to adopt some sectioning, although transverse slices are not further reduced. Neutron diffraction strain measurements have been made on a selection of specimens. The technique has been successful in measuring stresses in a cold expanded bolt hole (in a rail web) and due to roller straightening processes. Baseline measurements on unused head-hardened specimens containing little residual stress showed considerable scatter.

7.2 Background

Research into the metallurgy and behaviour of rail steel is motivated by safety and cost. The passage of trains on track can cause fatigue crack growth which may lead to complete or partial failure of a rail with serious consequences. The cost of replacement for failed or defective track is considerable. Railway research centres expend a large effort in improving the quality and treatment of rail to avoid defects. The dynamic plane strain crack arrest toughness is a key factor in lifetime prediction as are the residual stresses. The shape, direction and growth rate of fatigue cracks is a testimony to the importance of residual stress in their prediction. Safety analyses generally involve a combination of dynamic and residual stresses. The main issue for experimental measurement is to quantify the contribution to crack driving forces made by residual stresses.

The passage of a train over a rail will produce a large dynamic compressive stress field. In the contact patch between the rail and wheel, compressive stresses can exceed 2000MPa (Sawley, 1989). This could, by itself, be sufficient to induce fatigue crack growth in regions of tensile residual stress. However the stress fields are complicated by flats on the wheels (due to skidding during acceleration or braking), by shear stresses at the rail surface and by transient loads which occur at the joins of bolted track.

Failure studies, prediction and control are complicated by the large number of parameters which affect the state of the rail. These include the rail metallurgy, hardness, toughness, resistance to wear, treatment during fabrication and chemical composition. The physical condition of the track, the sleeper spacing, maintenance and usage are all factors. Different behaviour is expected from continuously welded or bolted rail and from different track curvatures. Finally, the loading history in terms of the speed, density and total tonnage over a line are also important. The number of variables is large and independent studies of a single variable are rare. Generally the characteristics of rail steels are: good "batter" resistance, low cost, weldability, acceptable dynamic fracture toughness and resistance to the bending and thermal stresses inherent in its use.

7.3 Residual stress in rails

Fabrication stresses in rails are caused by inhomogeneous cooling and associated thermal effects. Rails emerge from rolling mills with surface temperatures in excess of 1000°C. Their irregular cross section and contact with neighbouring sections complicates their cooling history. Superimposed on the thermal stresses are the effects of transformation induced plasticity (TRIP). TRIP is associated with phase transformation processes and is a localised microstress effect due to volumetric or shape changes. A computational analysis of thermal and TRIP effects in rails has been made by Fischer (1988). Using a model in which thermo-visco-elastic-plastic material laws are included and by considering the radiative and convective heat processes it was concluded that fabrication stresses are largely developed in the first twenty minutes of cooling and do not alter substantially on cooling from 500°C to room temperature. TRIP during the phase transformation from austenite to ferrite (between 680 and 600 °C) was

shown to influence the final residual stress state. A compressive longitudinal stress was predicted at the surface of the head which rapidly changed to tensile through most of the head. In the web and foot compressive and tensile longitudinal stresses were predicted respectively.

Other fabrication processes which lead to residual stresses include spray cooling and roller straightening. Under service loading conditions stresses are produced by plastic deformation at the surface of the rail, where the greatest shear stresses are expected. Repeated deformation leads to advanced work hardening of the surface layer and eventually the plastic flow becomes minimal and the stress reversal in the head surface remains elastic (Stone, 1982). Prediction of the surface residual stresses is complicated by the close relationship between their production and wear processes.

7.4 Failure mechanisms

The danger associated with a fatigue crack in a rail is that failure at one point will lead to an increase in the bending moment at an adjacent crack and ultimately cause failure of a complete section. Regional and international variations in residual stress distributions reflect the different prevailing physical conditions and usages. British Rail categorise failures and defects according to their position and origin (Allen, 1988). Proximity to joints, the position (in the head, web or foot) and the origin of failure (such as manufacturing defect or misusage) are noted in statistical surveys. The rate of occurrence of different failure modes evolves with time, with changing operating practices and with production methods. In the U.K. at present there are three dominant failure types; rail end bolt hole cracks, rolling fatigue contact defects (squats) and internally initiated railhead cracks (tache ovales).

Bolt hole failures are caused by dipped joints (fig 7.1). Failure usually occurs at the "running on" end of a rail with crack growth on a plane at 45° to the longitudinal axis. The driving forces are shear stresses in the web, magnified by the stress concentration of the hole. Commonly two cracks are formed, one growing towards the foot and the other towards the surface. The latter generally breaks through to the surface between 100 and 150mm from the rail end. During the passage of a train, bolt hole cracks respond to dynamic loadings which are affected by the inertial mass of the rail,

train speed and the resistance of the sleepers. With the increased usage of continuously welded rail the importance of bolt hole cracks is likely to diminish. However bolted sections will remain in regions of high curvature and at crossovers, so the problem will not disappear completely.

Squat failures initiate from the surface of the rail head and occur on sections of heavily utilised track. They are caused by wheel irregularities or from fine cracks produced by the severe shearing at the edge of the running band. A qualitative model of the driving force is illustrated in figure 7.2 Ingress of water into a crack as it is drawn open is followed by compression during the wheel passage and subsequent release (Bower, 1987). Initial propagation is at 45° to the rolling direction, and followed by longitudinal propagation. In response to the local microstructure the cracks subsequently either turn towards the surface, removing a blister of material or turn downwards towards the foot which can lead to complete fracture.

Tache ovale defects initiate from small hydrogen cracks in the rail head and may be caused by ingot moulds not being totally dry before casting. During their early growth stage they propagate at 20° to the vertical and residual longitudinal tensile stress in the head encourages their growth, although the compressive stress at the surface subsequently inhibits it. The increasing use of continuously cast rail means that tache ovales, like bolt hole failures, are likely to reduce in significance in the future.

7.5 Strain gauge results

Strain gauge sectioning has been widely adopted as the primary strain measuring technique in rails. The procedure for inferring the three dimensional state of stress from a combination of longitudinal and transverse sectioning measurements is well established. Typically two adjacent specimens are removed from the section of track of interest. One section, of length sufficient to assume the centre is free of end effects, is sectioned longitudinally. A second, thin transverse section is examined by X ray diffraction, hole drilling or dicing. The first test gives the longitudinal strains and in the second the transverse strains are obtained. The two sets of data are combined, taking into account the Poisson's ratio effect, to predict the original state of stress.

The size and bulk of rail specimens require that similar sectioning and slicing is

necessary for neutron measurements. Consequently discussions concerning the optimum thickness and length for the transverse and longitudinal slices for strain gauge measurements are also pertinent to the neutron technique. The assumptions inherent to sectioning are; that longitudinal measurements are free from end effects (i.e. shear stress does not act on transverse planes), that slicing does not induce residual stress and that material behaviour is isotropic linear homogeneous, described by Young's modulus and Poisson's ratio.

Gauge measurements made in the head of a new "gag" straightened rail indicated low transverse stress with a maximum tensile value of about 55MPa (Schilling, 1981). This compared with a peak transverse tensile stress from below the deformed region, in heavily used rail, of 186MPa. It was also concluded that the Poisson's ratio effect of the transverse stresses on the longitudinal stress obtained from plate samples was small. A comprehensive strain gauge investigation of the effects of tonnage, curvature and speed recorded high compressive stresses particularly at the edges of the wear pattern for rail removed after in-service loading. Internal tensile stresses were shown to increase with traffic tonnage over the rail (Groom, 1979).

7.6 Cold expanded bolt hole

Before neutron diffraction measurements were made on unused rail sections the technique was applied to a cold expanded bolt hole. Cold expansion of a bolt hole by forcing through a hard oversize tool gives simple and cost effective protection against the incidence of bolt hole cracks. Prior to expansion, a sleeve is inserted to prevent damage to the hole surface. Material near the bore is plastically deformed radially and circumferentially in a process similar to autofrettage. A residual stress distribution is produced with maximum compressive stress at the bore. Strain gauge measurements quoted by Cannon (1985) suggest that the hoop stress decreases linearly from the surface of the hole and even after considerable in service usage the compressive hoop stress is maintained.

A section of web containing a bolt hole was provided by British Rail. The hole had previously been expanded according to the recommended process. The material composition is given in table 7.1. The 0.2% proof stress was 420MPa with an ultimate

tensile strength of 710MPa. No in-service loading was applied. For convenience and to facilitate access for the neutron beam, sections of the head and foot were removed but the web was unmodified. The sample is illustrated in figure 7.3.

The sample was mounted in the neutron beam on D1A with AB vertical and the scattering vector aligned to measure strain in the Y (hoop) direction (fig 7.3). Vertical traverses were made to obtain strain measurements on radii parallel to AB, 1.5mm below the surface and on the centreline (fig 7.4). The distance AB from the top of the hole to the upper edge is 52mm and the bore and outer surface are defined as R=0 and R=52mm respectively. A sampling volume of approximately $8mm^3$ was used. The (211) reflection at 109.5°, gave a path length through the material of approximately 35mm for each measurement. Each measurement took approximately 90 minutes to give a peak height of about 100. The quality of the diffracted reflections was poor but single Gaussian peak fits were possible. A small cube taken from the edge of the specimen provided a strain-free reference angle.

The measured hoop strains are given in figure 7.5. The largest difference between the two penetrations occurs near the surface of the hole and may be due to a variation in the shape of the plastically deformed zone or to differences in the constraint conditions. The compressive stress may also vary according to the direction of travel of the tool. At distances greater than 15mm from the surface of the hole there is little difference between the two sets of measurements. Only hoop strain measurements were obtained. In the absence of radial or axial strain information the strains were converted to stress by assuming simple Hooke's law behaviour with a Young's modulus of 207GPa. In figure 7.6 the center line stresses for the neutron results are compared with strain gauge stresses quoted by Cannon (1988). In the compressive region the neutron and gauge measurements are in agreement but at distances greater than 20mm from the surface of the hole the gauge measurements suggest a more rapid increase into tension. In order to assess the differences between the neutron results near the hole surface and also the disparity with the gauge measurements at large distances from the hole a more comprehensive study is required. Triaxial strain measurements would give true stress values which might improve the agreement with the strain gauge values. Nevertheless

the neutron measurements have shown that realistic strains can be measured for comparatively low peak intensities and long path lengths which are likely to prevail in rail measurements.

Table 7.1 Chemical composition (%wt.) of normal rail steel

Element	C	Mn	Si	S	P	Fe
Wt %	0.45 / 0.60	0.95 / 1.25	0.05 / 0.35	1.41	0.05	balance

7.7 Representative rail specimen sizes

The path lengths in uncut rail sections are too large for neutron measurements in their bulk. Examination of the stress state necessitates sectioning into transverse and longitudinal specimens in which the longitudinal or transverse stresses respectively are relaxed. Limited neutron beam time requires that standard specimen sizes must be determined at the outset of experimental programs, since repeat measurements may not be possible. Optimum sample sizes are determined by a compromise between the count time to achieve a specified accuracy and stress relaxation effects. Standard specimens fall into three categories; longitudinal plates, transverse slices and gauge corner specimens (figs 7.7, 7.8 and 7.9). The gauge corner specimens were included in response to observed cracking processes.

A finite element analysis of the variation in stress distribution in longitudinal plates has been made by Ezeilo (1990). By applying an analytical load distribution to one end of a 2 dimensional plate and varying the height to length ratio it was shown that the predicted end effects are limited to distances less than the height of the plate. This suggests that a longitudinal plate longer than twice the height of the rail can be assumed to maintain the longitudinal stresses at its centre, apart from the relaxation of the transverse stresses. Experimental measurements on the 10mm thick plate, described in section 7.8.4, indicate that the longitudinal stresses are substantially stable at distances greater than 100mm from the cut end (Webster, 1990). An experimental survey of the effects of thickness on measurements in transverse slices proved inconclusive and for

practical purposes a slice thickness of 8mm was adopted in this study (Webster, 1989b).

7.8 Survey of an unused rail.

7.8.1 Overview

As part of an international research initiative (ORE D 173) in collaboration with British Rail, neutron diffraction measurements were made on a series of specimens removed from a head hardened rail which had not been subjected to any in service usage. The aim of the study was to assess the fabrication residual stresses and to provide a baseline for subsequent measurements on specimens of identical rail, removed after different amounts of service loading and from regions of different physical conditions. The residual stresses were not expected to be large in the transverse slices but straightening processes induce appreciable longitudinal stresses which vary with depth below the surface of the rail.

The rail under study was produced by a German company, Thyssen Stahl. Head hardening is induced to reduce wear at the rail surface. The head hardening is induced after the rail is produced by reheating the head surface by induction heating to 1080° and subsequently cooling the running surface using compressed air. This produces a refined pearlitic microstructure around the head profile. The microstructure is modified in a zone approximately 30mm in depth around the profile of the rail head. Hardness profiles measured by Thyssen on a transverse slice indicate a maximum hardness of 382 on a Brinell scale at the surface falling to between 250 and 300 at distances greater than 30mm from the surface (fig 7.10).

The rail fabrication begins with hot rolling, followed by roller straightening, head hardening, 3 point bend straightening and final roller straightening. The material composition differs slightly from normal rail steel and is given in table 7.2. The yield stress for the material is 821MPa and the U.T.S is 1244MPa.

Three rail specimens were provided by Thyssen. Each was 600mm long with a maximum foot to head height of 172mm. Only one specimen was examined which was identified by the designation 370HB. For ease of handling it was cut into two sections 350mm and 250mm long. Preliminary measurements were made on the 350mm section

prior to removing a transverse slice (8mm thick) approximately 170mm from one end. All cutting processes were performed with a lubricated mechanical hack saw. A separate longitudinal plate (340mm long and 10mm thick) and two gauge corner specimens (GCS) were also provided. The coordinate system adopted for the rail is illustrated in figure 7.7. X is the longitudinal direction, Y is the horizontal direction and Z is vertical from the surface of the head (increasing positive downwards). The surface of a rail head on the center line of a transverse slice is defined as (0,0,0). The principal stress axes were assumed to coincide with the X, Y and Z directions. All neutron measurements were made using the steel (211) reflection.

Table 7.2 Chemical composition (%wt.) of 370HB Thyssen rail

Element	C	Mn	Si	S	P	Cr	Fe
Wt %	0.79	0.97	0.25	0.009	0.015	0.05	balance

7.8.2 Stress free θ_0 for rail specimens

Accurate determination of an unstrained diffraction angle for this study was important since the strain variations were expected to be small. Three cubes were removed from different positions in a transverse slice of the rail as indicated in figure 7.11. The measured peak positions are given in figure 7.12 for different directions in the cubes before and after heat treatment at 650°C for 6 hours (followed by slow cooling to room temperature). A series of repeat measurements were made on cube 2 in the X direction prior to heat treatment which established that the errors quoted for individual measurements were consistent. The scatter of measurements on the different cubes and in different directions is considerable and a sizeable fraction of the total variations seen in the transverse and gauge corner specimens. No systematic effects were observed and the variations are larger than have been observed in other experimental programs. In response to this uncertainty a longitudinal plate was examined (section 7.8.4) since equilibrium constraints provide unambiguous determinations of θ_0 when applied to the bending stress induced by roller straightening. In practice the strain free zeros were

either obtained by force balance on the longitudinal plate or by averaging a selection of values from a heat treated cube. Consequently the absolute values of strains (and stresses) are subject to some uncertainty.

7.8.3 Longitudinal variations

If longitudinal strain variations exist along the rail section, the use of transverse slices would be invalidated. Before sectioning the rail the only direction in which strain can be measured in acceptable time periods lies normal to and within 20mm of the surface. At the surface of the head this corresponds to measurements of the Z strain. To examine the longitudinal stability of the stress distribution, Z strain measurements were made at 15mm intervals in the X direction. One end of the 350mm section was denoted, X=0 and Z strains were measured using a 2*2 input mask and a 2mm exit slit at 4 (Y,Z) positions; (10,2) (10,5) (20,5) (20,2) within the head and at 5 X positions along the rail; 145, 160, 175, 190, and 205mm (fig 7.13). The central plane of the section lay at X=175mm from where an 8mm transverse slice was subsequently removed. The change in peak centres for the measurements are given in figure 7.14. The maximum variation along an X profile corresponds to a strain difference of ≈200 μstrain (40MPa) with experimental error of ≈+- 40 μstrain (8MPa). Although a smaller variation would have been preferred this was not believed to seriously compromise the use of transverse slices. A series of hardness measurements over 100mm in the X direction performed by Thyssen at the surface of a separate specimen demonstrated the uniformity of hardness over the same length.

The neutron check of longitudinal continuity covered only 60mm and would not identify changes over longer distances. In practice the longitudinal stress may vary over metres due to fabrication effects and post-service specimens may show cyclic variations due to the sleepers or periodic variations in the track. A second set of Z strain measurements not included here showed evidence for the asymetry of the residual strain distribution about the Y=0 plane which may result from asymetric cooling. Consequently the rail is "handed" even before it is deformed under service conditions and ambiguity in the Y direction must be avoided during experimental measurements.

7.8.4 Measurement in a longitudinal plate

In the longitudinal direction stresses in excess of 100MPa are caused by roller straightening processes applied during fabrication. By making measurements on a plane from the head to the foot of a longitudinal plate specimen (fig 7.7) equilibrium conditions can be applied to calculate θ_0. On D1A 6 stress measurements (18 strains) were obtained between the head and the foot.

A thorough survey of the plate would have taken a prohibitively long time on D1A and consequently measurements were made on a second diffractometer D20 also at the I.L.L. D20 is a high flux diffractometer with reduced resolution compared to D1A but with higher count rates due to its proximity to the reactor and better efficiency due to the use of a position sensitive detector. Details may be found in the publication "Neutron research facilities at the I.L.L." which can be obtained from the I.L.L. The strain results are presented without discussing the measurements in further detail.

The longitudinal plate was 340mm long. Measurements on D20 were made on a vertical line 150mm from one end, from the surface of the head to the foot. Strains recorded on D20 are superimposed with D1A measurements in figure 7.15 abc. A photograph of the longitudinal plate on D1A is given in figure 7.15d. The D20 results demonstrate the longitudinal stress variation in more detail and identify a characteristic variation near the interface between the head and the web between Z=40 and Z=60mm. The longitudinal stresses measured on D1A, D20 and by Thyssen (on a separate sample using strain gauges) are given in figure 7.16. Tensile stresses exist in the head and the foot which are balanced by compressive stress through the web. The Thyssen gauge results predict a larger compressive stress in this region than the neutron measurements.

7.8.5 Measurement in a transverse slice

A transverse slice of thickness 8mm was removed from the 350mm section as described in 7.8.3. X, Y and Z strain measurements were made in the head on the centreline thickness using an $8mm^3$ sampling volume (fig 7.17). The strain results for an array of YZ positions are given in figure 7.18 abc using a θ_0 estimated from a "stress free" cube. A complete array of overlapping measurements was not achieved due to problems with the original movement system prior to the installation of the system

described in chapter 4. The arrays are too limited to make detailed statements concerning the overall state of the head. The X strains seen in the plate specimen are completely relaxed, and the Y and Z strains show compressive and tensile behaviour respectively. In view of the failure to achieve overlapping measurements over the strain array the stresses which can be calculated are limited. However where calculated the X stress shows a mixture of tensile and compressive behaviour with maximum values of 57MPa tensile and -49MPa compressive. The Y stresses were almost all compressive with a maximum value of -112MPa and an average value of -42MPa over the part of the array where triaxial measurements were made. The Z stresses were all tensile with a maximum value of 89MPa and an average of 46Mpa.

7.8.6 Measurement in a gauge corner specimen

In response to observed in-service cracking, two gauge corner specimens were removed from the unused rail as indicated in figure 7.9. Each specimen was approximately 100mm long in the X (longitudinal direction) with Y-Z dimensions of 21-27 and 21-19.3. The dimensions of the smaller specimen are indicated in figure 7.20a. During removal strain gauges were attached to the surface of the rail to record the relaxation which took place during the cutting process. The relaxed stresses measured by the gauges were less than 100MPa in magnitude but indicated that tensile stress was relieved in the top surface and compressive stress from the side face.

Measuring orientations and apertures sizes are indicated in figure 7.19 and photographs of the specimens in position are given in figures 4.4 and 4.5. Only the smaller specimen was examined in detail since it offered more favourable count times. The measured strains (in μstrain) are plotted in figure 7.20abc onto scale sections of the specimens. The approximate sampling volume in the YZ plane is indicated on the figures. In the X direction the sampling volume is distorted in a vertical direction due to the vertical dispersion of the neutron beam discussed in chapter 4. In the Y and Z orientations the sampling volume can be more accurately defined in the YZ plane since the sample can stand vertically permitting a vertical "matchstick" sampling volume to be used assuming that no longitudinal variation takes place along the rail length. The spot measurements in figures 7.20 show little overall trend although it is clear that the strains

are largest near the rail surface, notably a maximum compressive strain of -482 μstrain in the Y strain direction in figure 7.20b. Over most of the array the stress is less than 50MPa in magnitude. The stresses within 2 to 3 mm of the surface may exceed this but were not examined in detail.

7.9 Conclusions

Measurements in a rail web near a cold expanded bolt hole have demonstrated that strains can be obtained with neutron path lengths in excess of 30mm through rail steel. Procedures have been established for examining a variety of longitudinal, transverse and gauge corner specimens removed from rail sections.

A survey on an unused rail demonstrated that the residual stress is limited to the effects of roller straightening during fabrication. Little residual stress was found in the transverse or gauge corner specimens, however there were indications that larger strains do exist in the surface regions. The survey provides a base line for the residual stress associated with fabrication and may be followed by examinations on identical rail removed from service after having been subjected to different amounts of total usage.

Further work is needed to examine the near surface region and to assess the measurement of θ_0 more accurately.

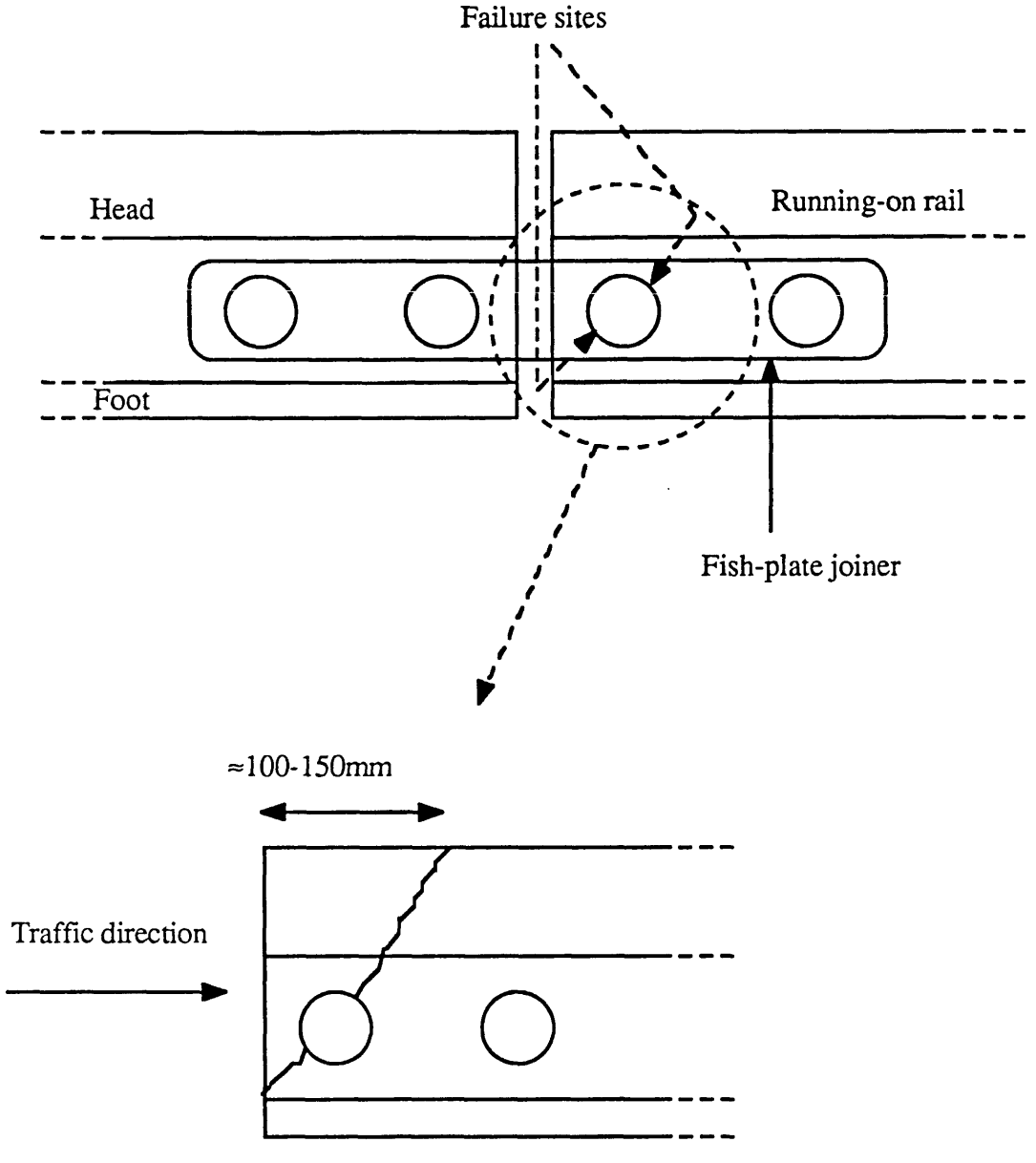


Figure 7.1: Side views of bolt hole failure sites

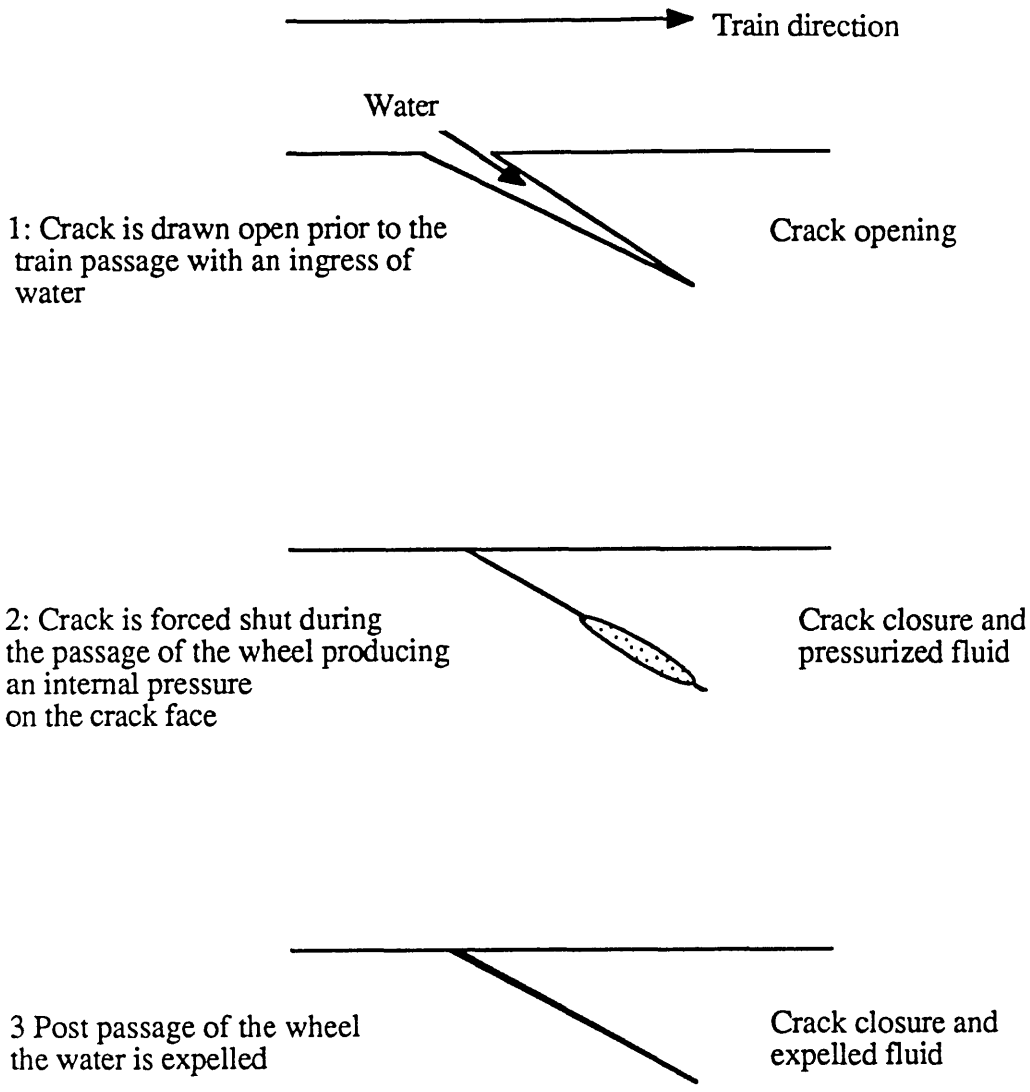


Figure 7.2: Qualitative model of driving force for squat failures

(After Bower PhD Thesis Cambridge, 1987)

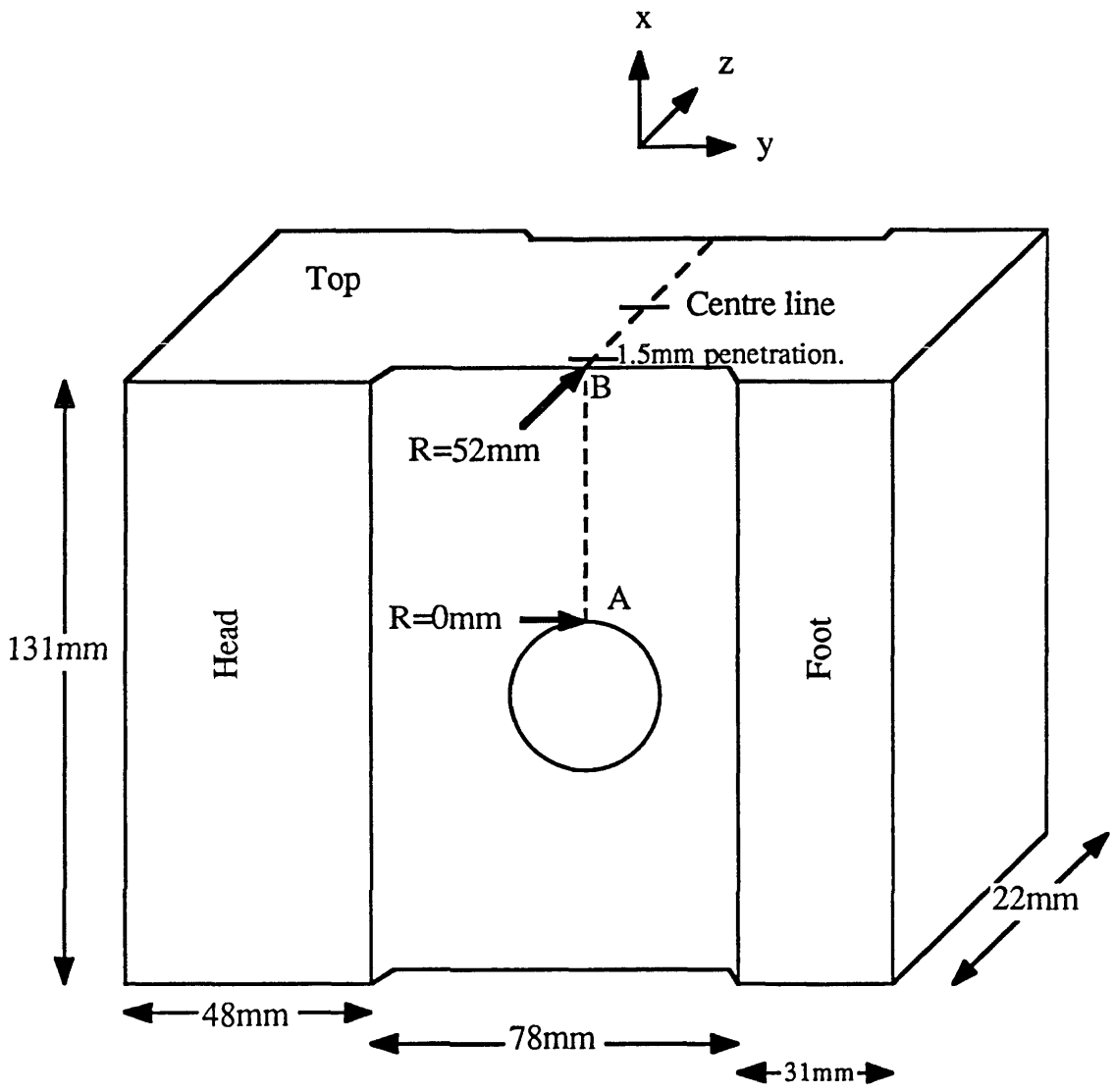
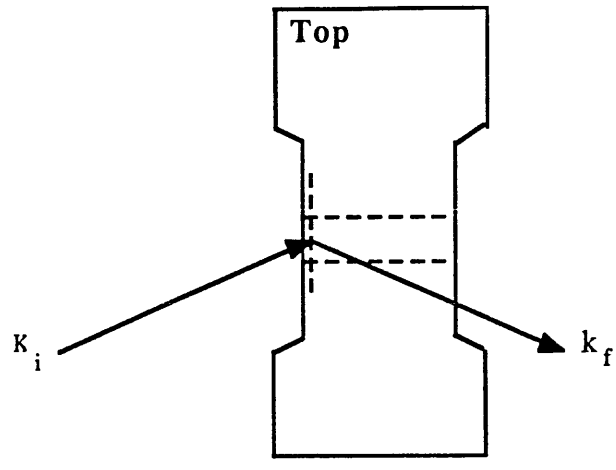
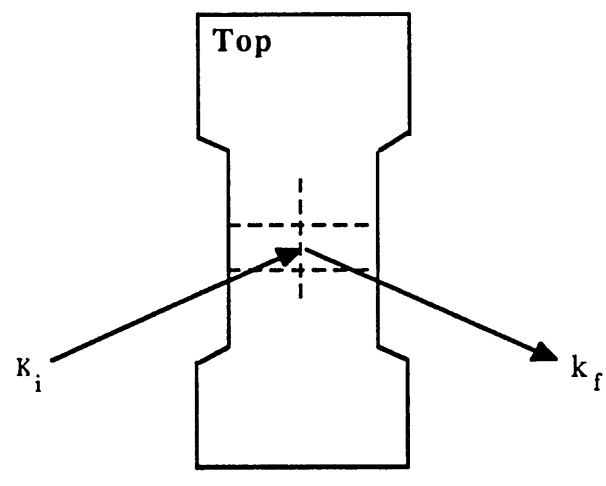


Figure 7.3: Cold expanded bolt hole



a) 1.5mm penetration below surface



b) central plane

Figure 7.4: Plan View of measuring planes in cold expanded bolt hole

Figure 7.5: Hoop strain near a cold expanded hole

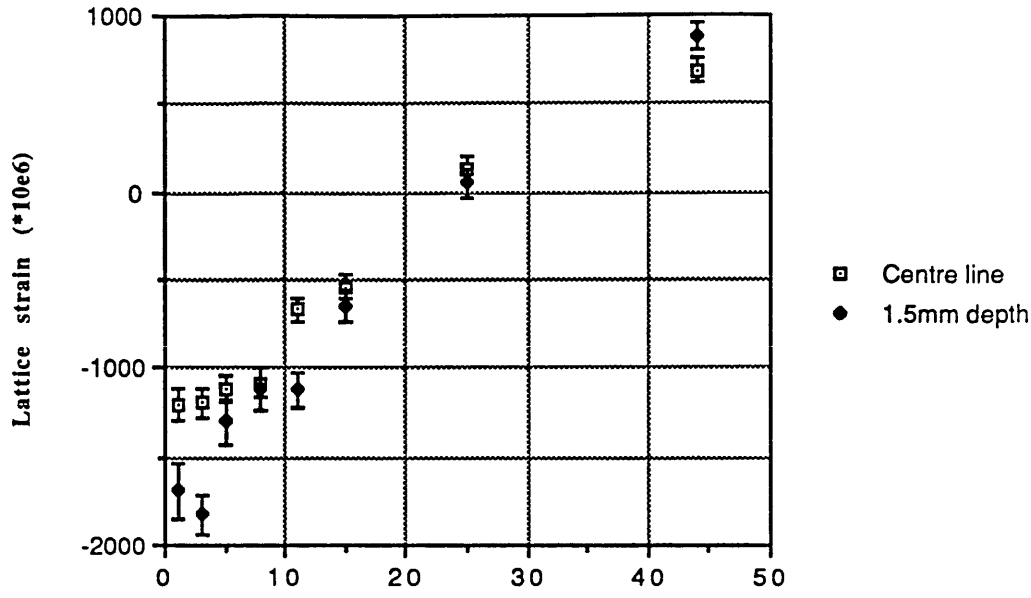
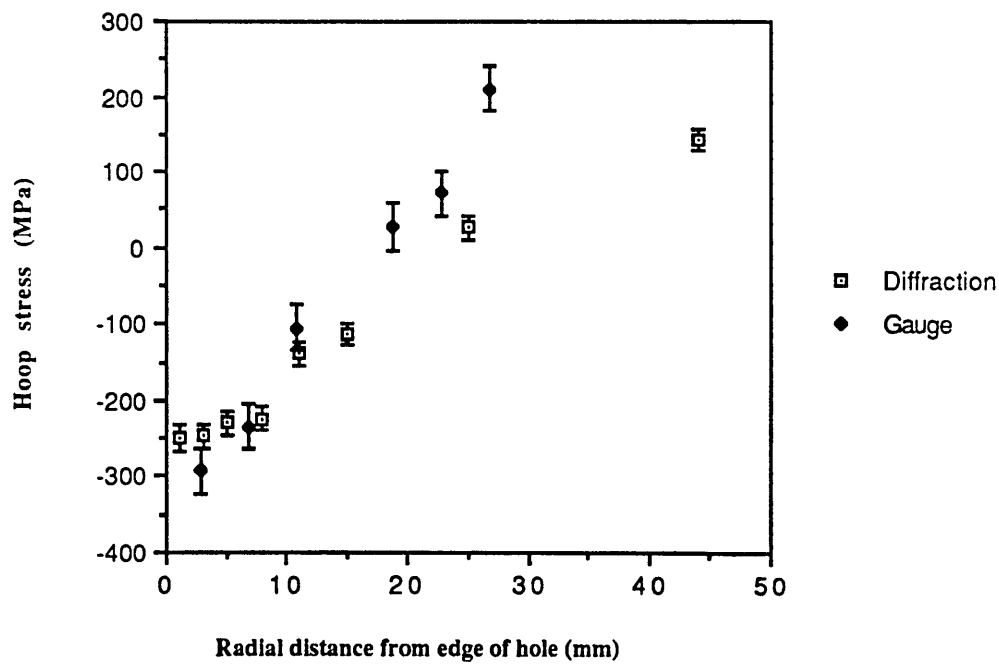


Figure 7.6: Hoop stress near expanded hole



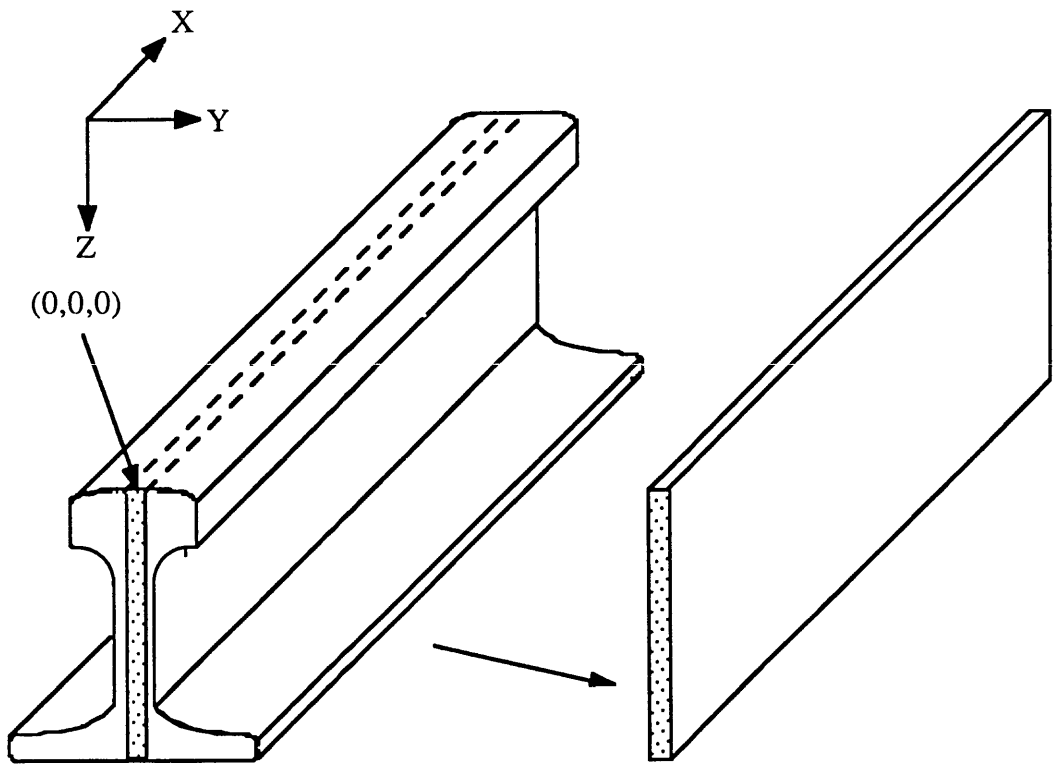


Figure 7.7 Longitudinal slice

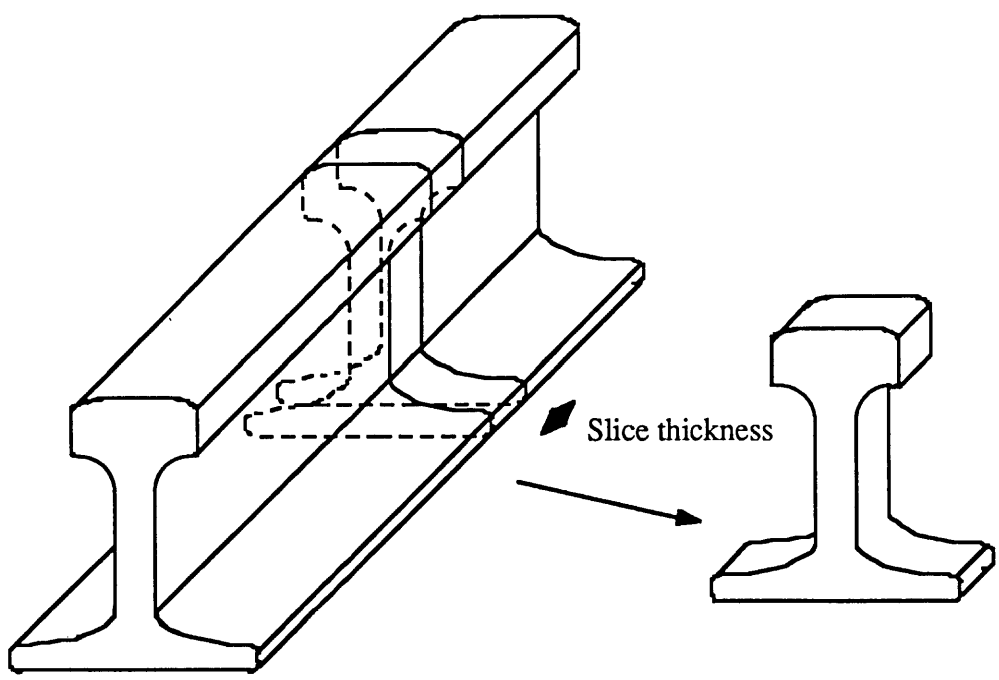


Figure 7.8 Transverse Slice

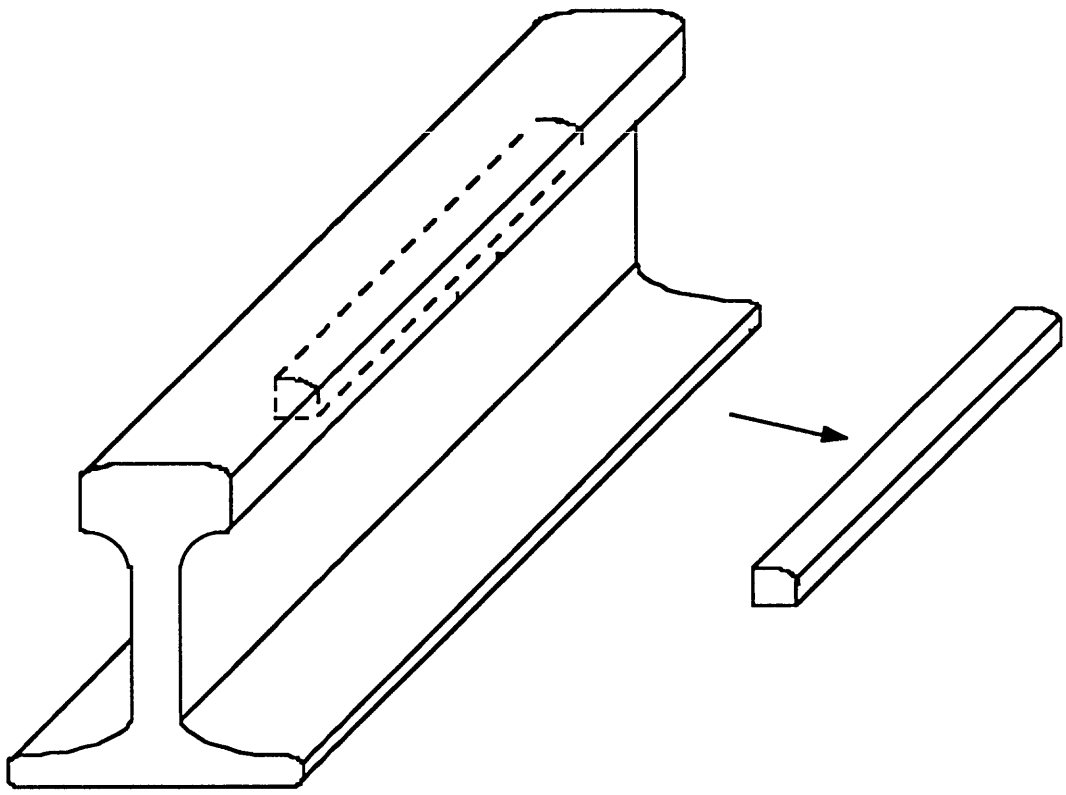


Figure 7.9: Gauge corner specimen

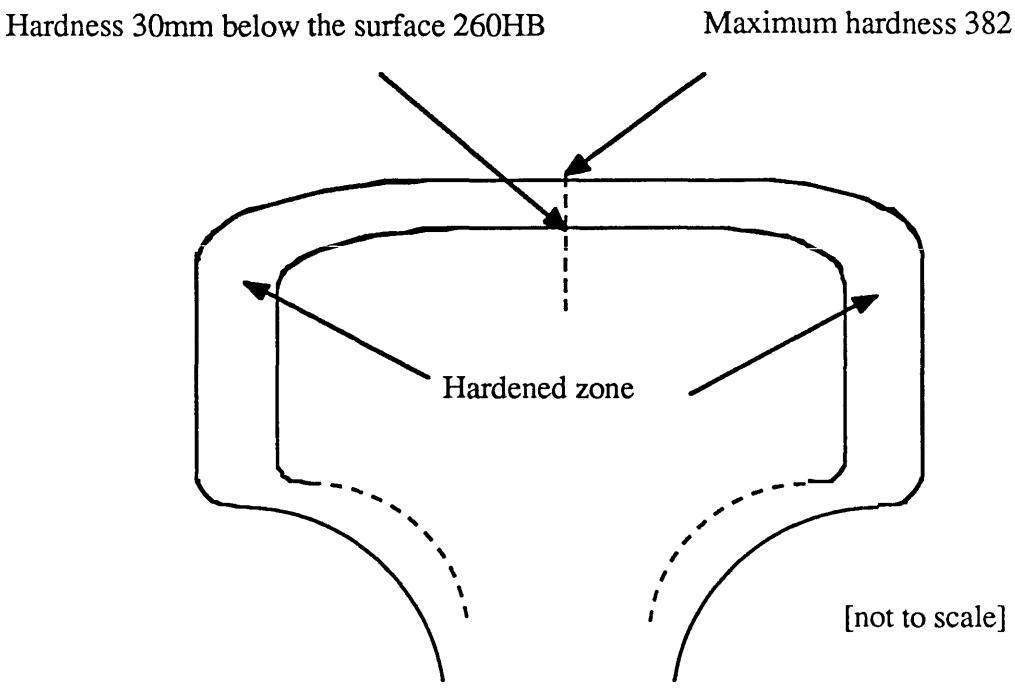


Figure 7.10 Rail head - hardened zone

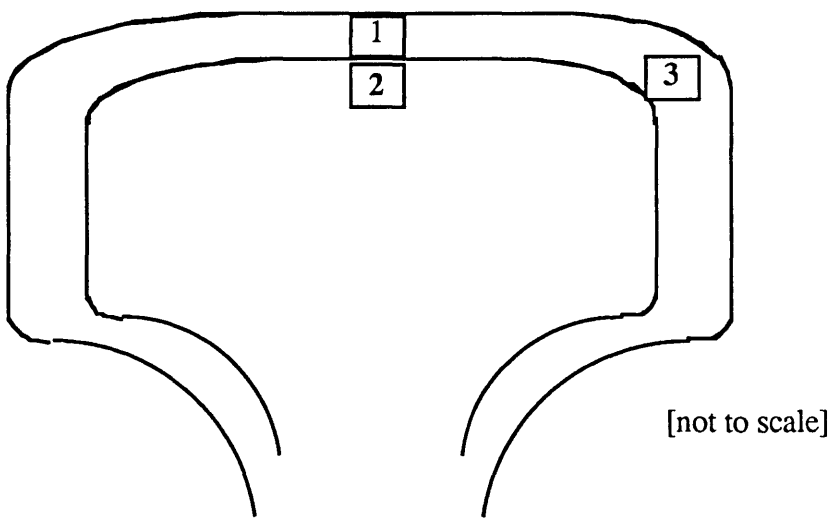
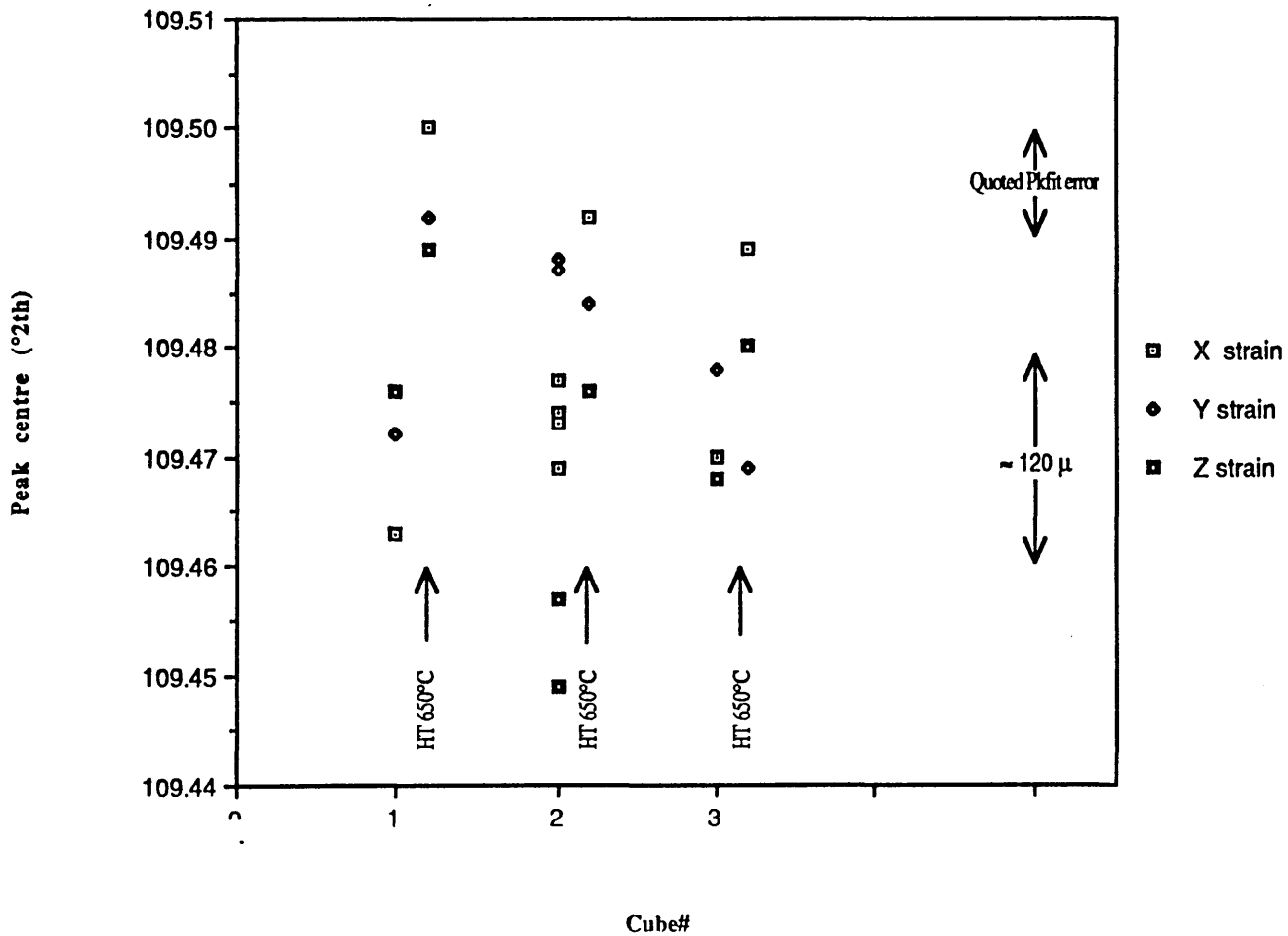


Figure 7.11: Positions of "stress free" cubes

Figure 7.12 "Stress free" cubes 1,2,3 pre and post heat treatment



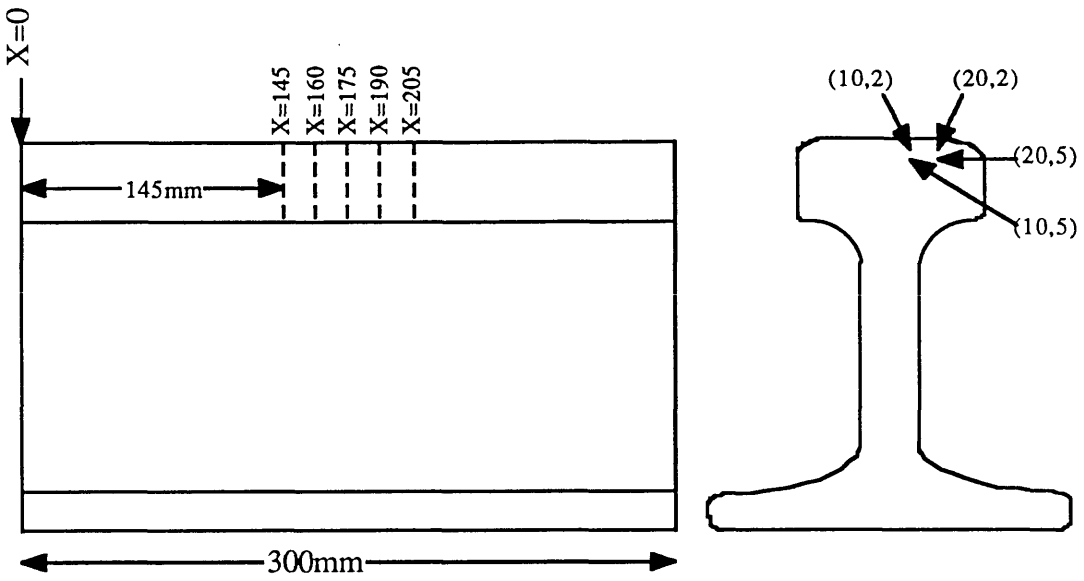


Figure 7.13: X positions and head positions for check of longitudinal variation

Figure 7.14: Longitudinal variation in Z strain

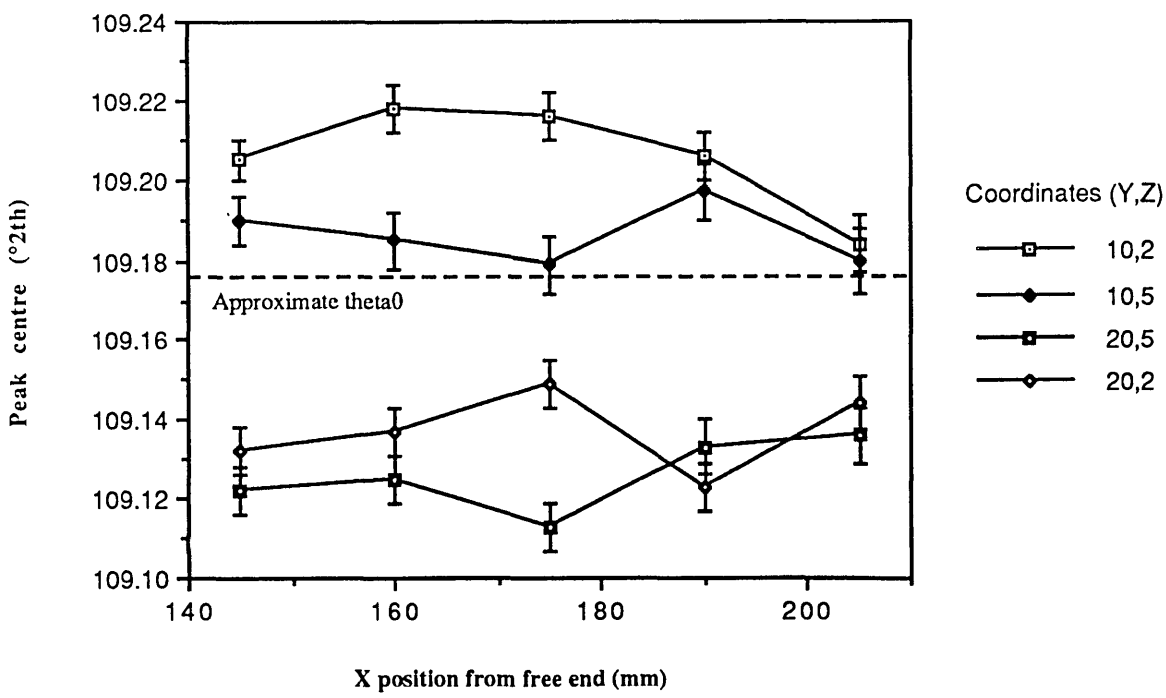


Figure 7.15a: Longitudinal plate X strain

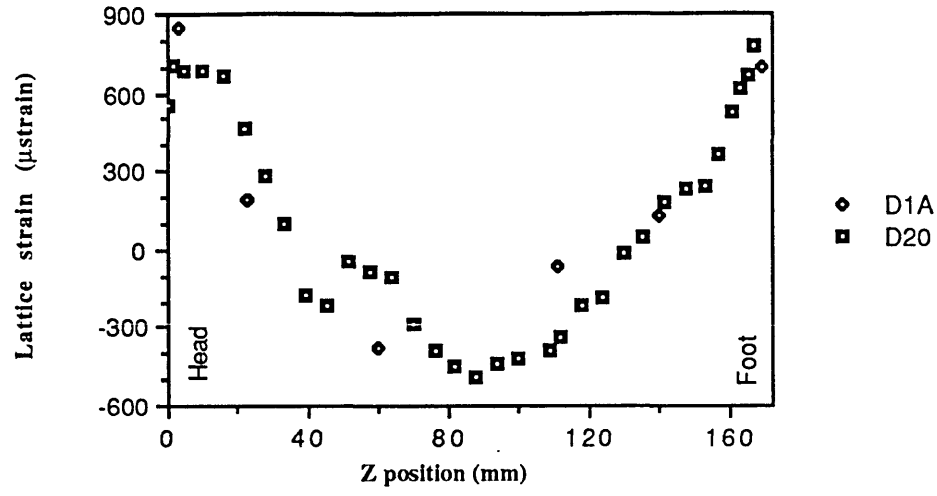


Figure 7.15b: Longitudinal plate Y strain

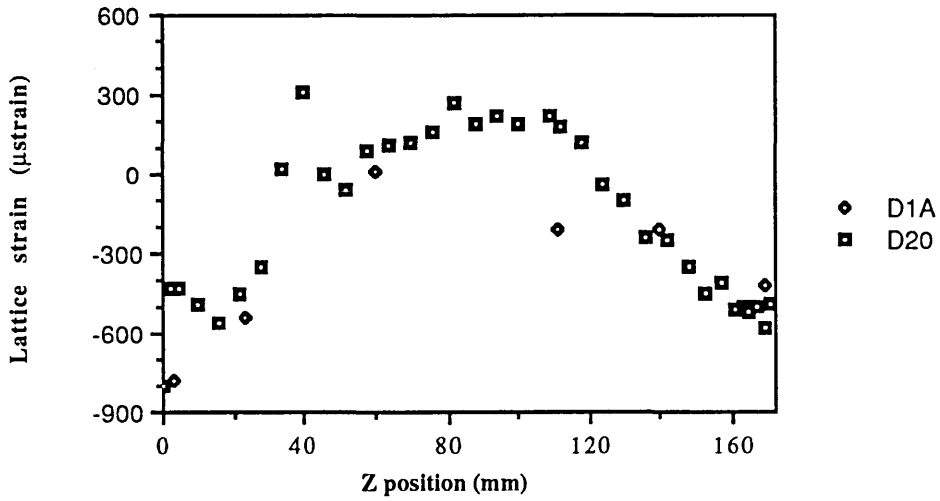
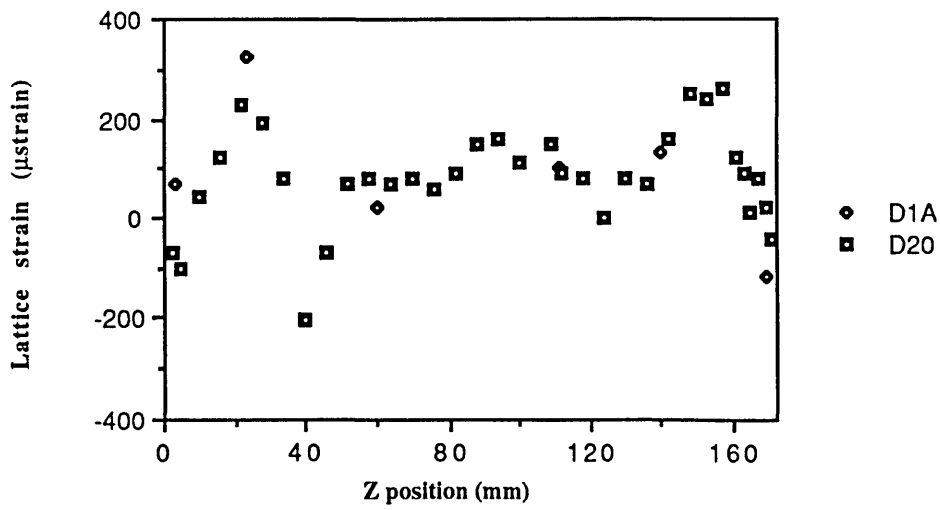


Figure 7.15c: Longitudinal plate Z strain



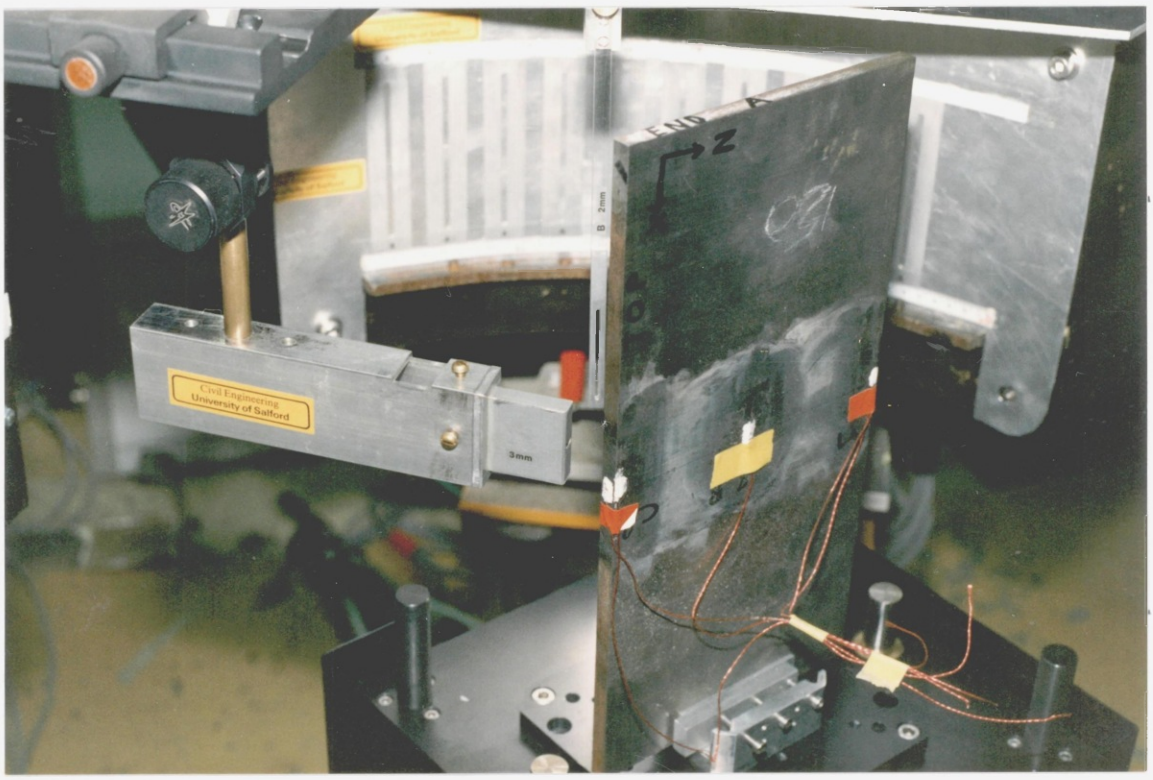
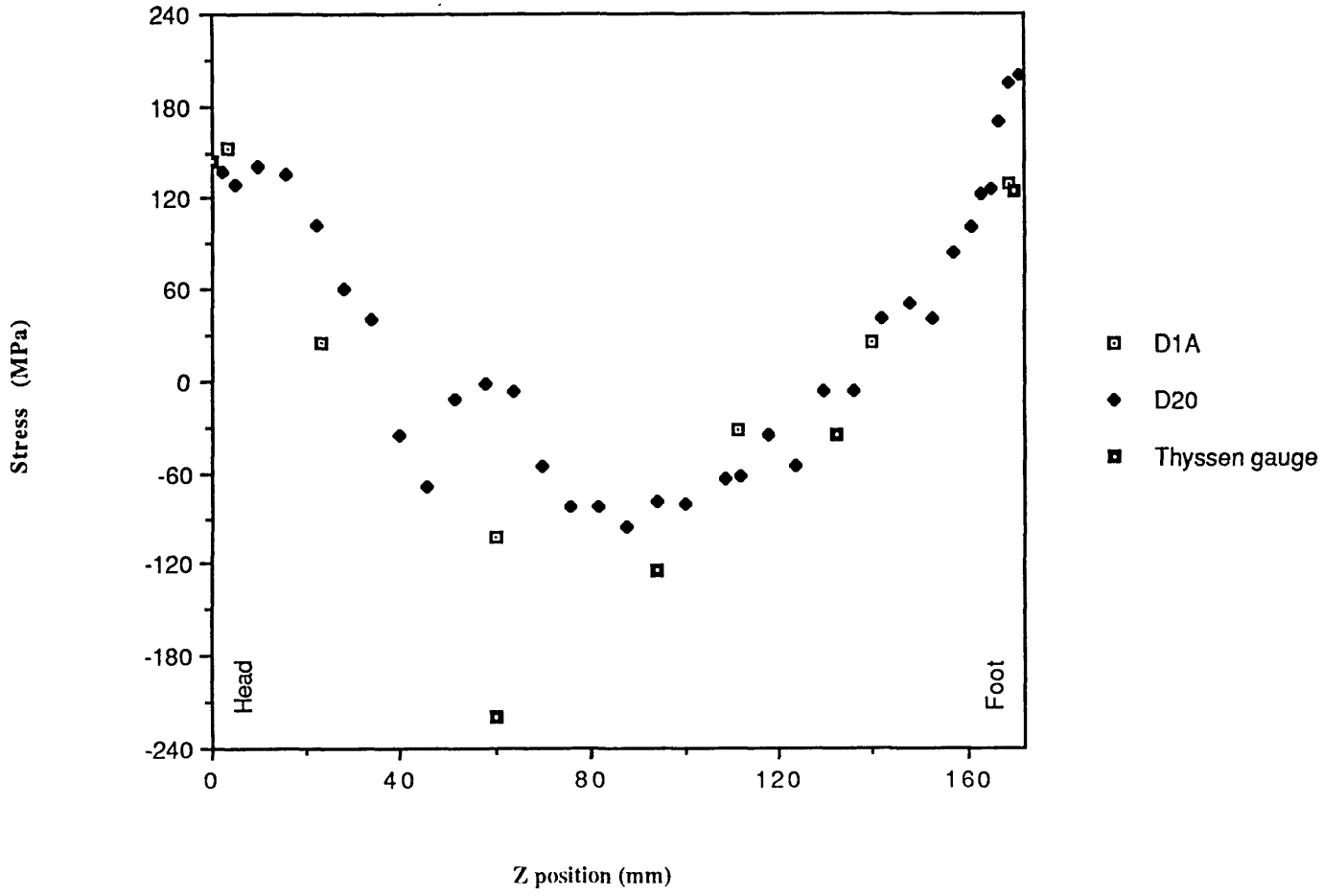


Figure 7.15d: Longitudinal plate from unused rail on D1A

Figure 7.16: X stress in the longitudinal plate from unused rail



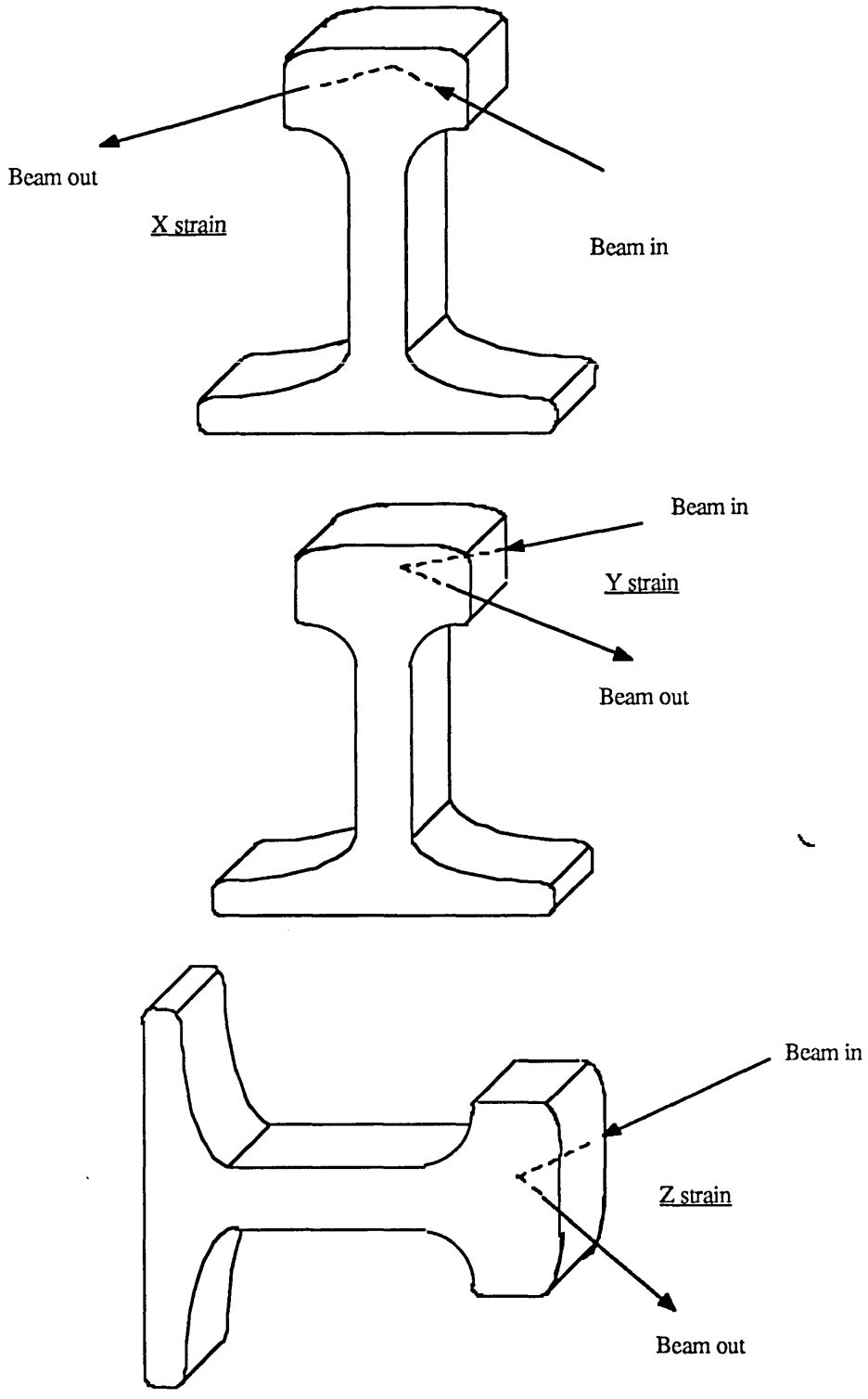


Figure 7.17: Transverse slices orientations for X, Y, and Z strain measurements

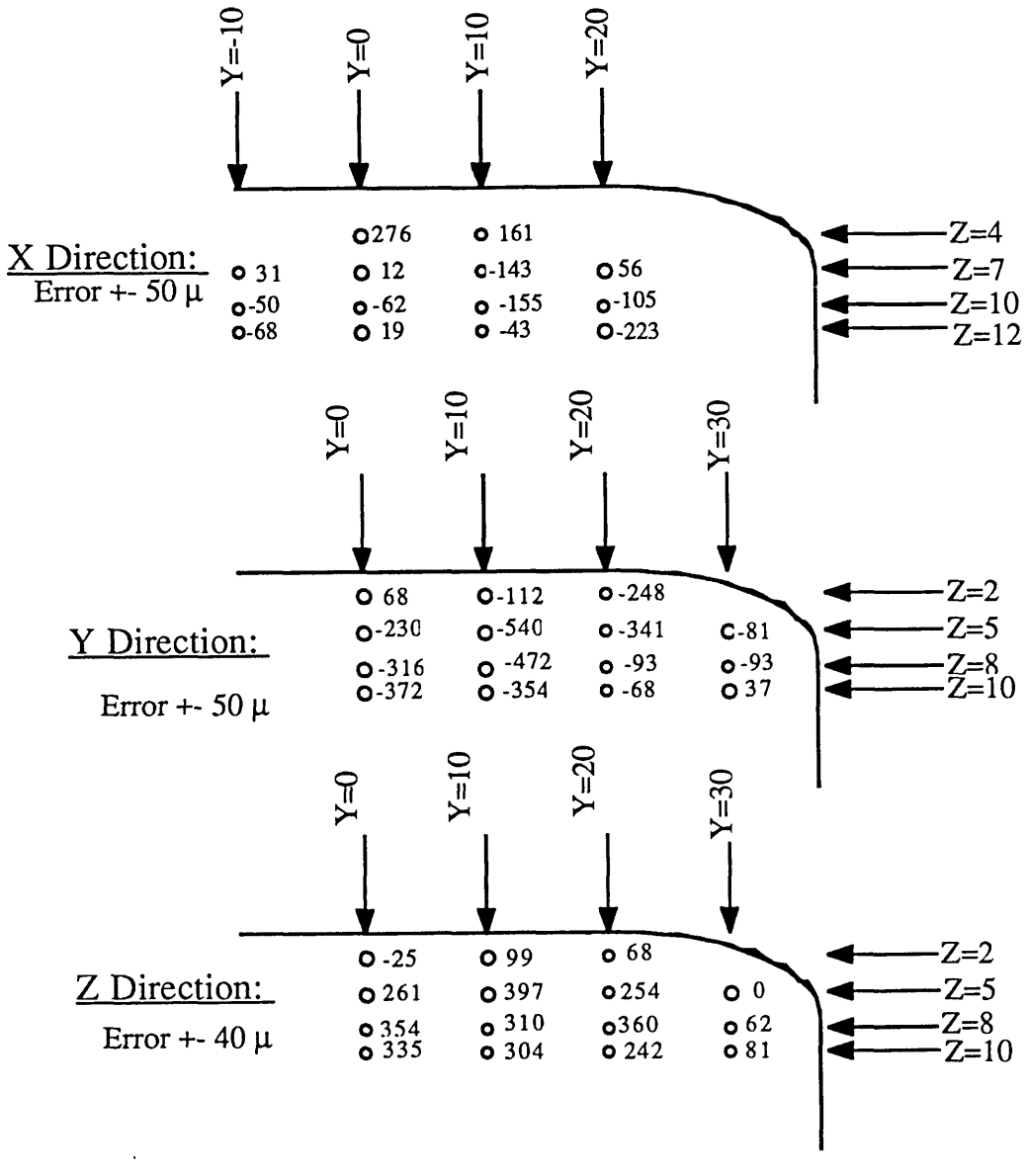


Figure 7.18: Strains in unused transverse rail slice

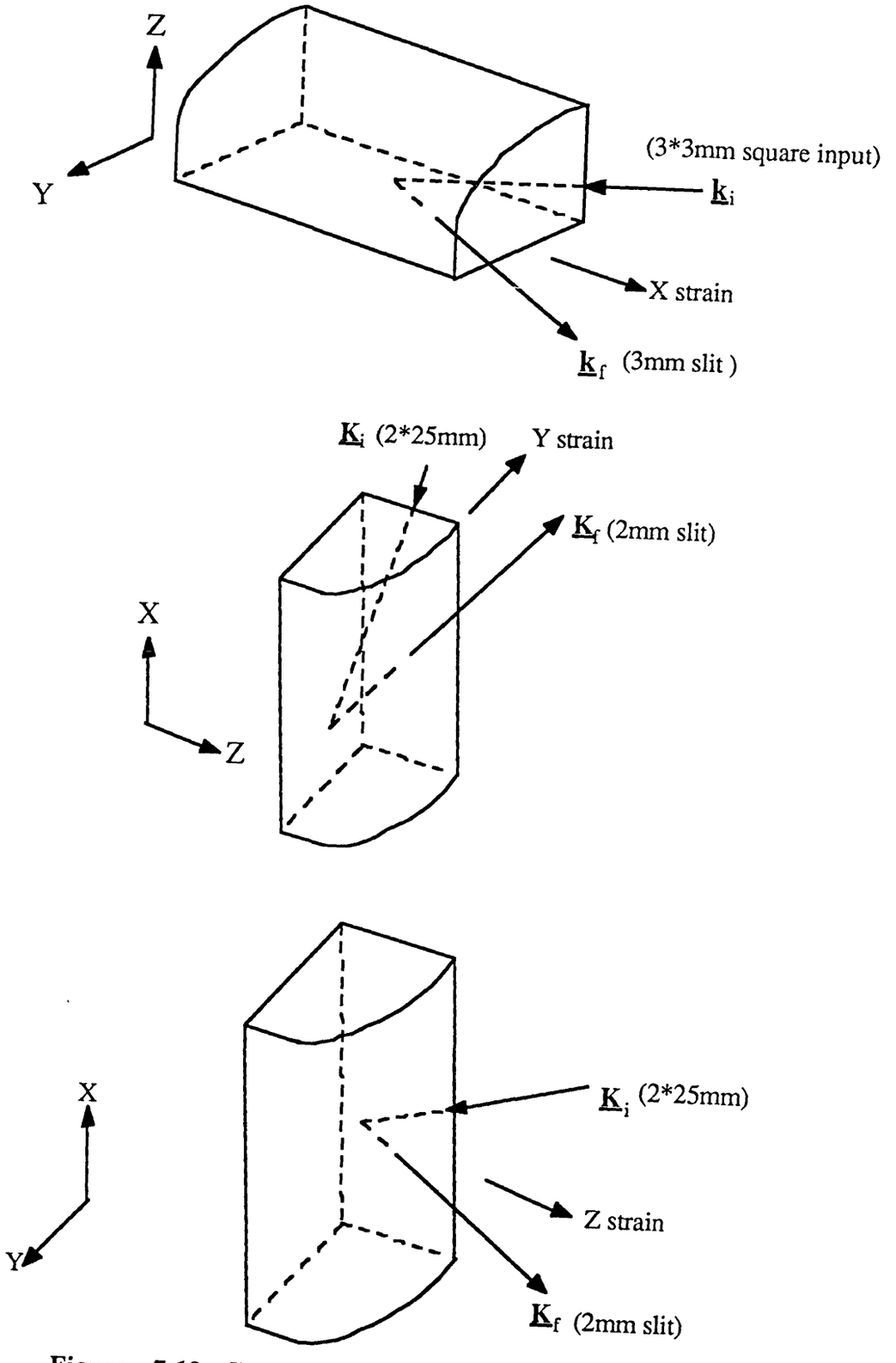


Figure 7.19: Gauge corner specimens orientations and aperture sizes

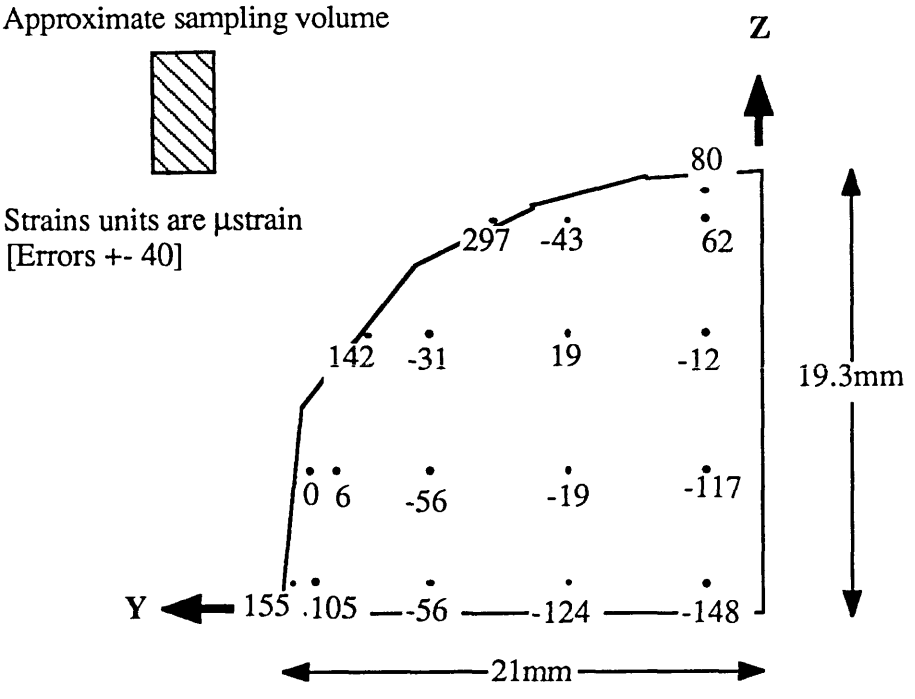


Figure 7.20a: Gauge corner specimen X strain

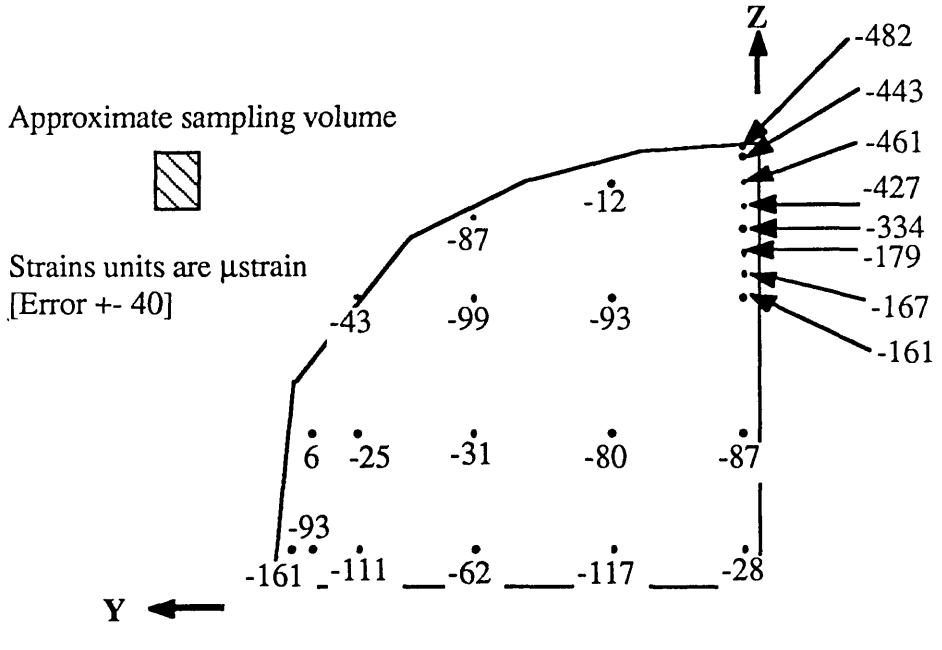


Figure 7.20b: Gauge corner specimen Y strain

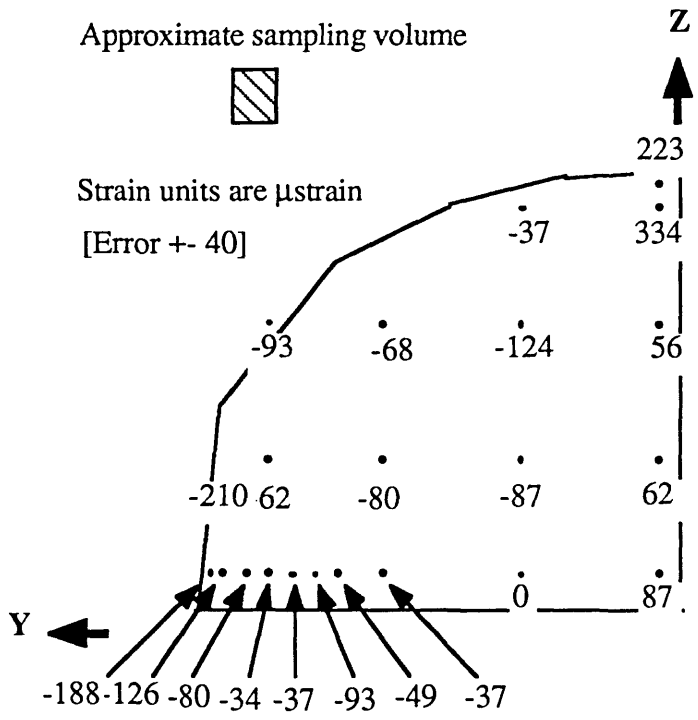


Figure 7.20c: Gauge corner specimen Z strain

CHAPTER 8

Strain measurements at ISIS

8.1 Introduction

Materials testing reactors (MTRs) provide relatively intense monochromatic beams of collimated thermal neutrons. However demand for beam time on reactor diffractometers is high. Recently pulsed neutron sources like ISIS at the Rutherford Appleton laboratory in the U.K. have become available as an alternative for engineering strain measurement. Although the principles of pulsed measurements are similar to those made on monochromatic sources, differences do exist. These include the ability to collect data for all lattice reflections in a single measurement and the possibility of simultaneously determining the strain in different directions using several detectors. These advantages are offset by longer count times and practical problems, which include definition of a sampling volume and determination of a strain free reference spectrum.

In this chapter the feasibility is assessed of using a pulsed source to examine residual stresses resulting from non-uniform plastic deformation. Trial measurements have been made using two instruments. Modifications to existing systems have enabled accurate definition of the incident beam and manipulation of simple engineering components. Despite some experimental problems, the radial variation of triaxial stresses has been measured in thin autofrettaged rings enabling a comparison to be made with measurements made on D1A at the I.L.L.

8.2 Background

In pulsed sources neutrons are produced by spallation, which occurs when energetic particles interact with target nuclei. Heavy element targets offer the best efficiency for emitted neutrons per unit energy of the incident pulse and at ISIS either a tantalum or a depleted uranium target is used. All the measurements recorded in this chapter were made using the tantalum target, which produces approximately 50% fewer neutrons than the uranium target. At ISIS protons are accelerated in bunches to 800MeV using a synchrotron and are subsequently directed at the target. The target nuclei are excited and "boil off" neutrons and lighter particles in an evaporation process. Each

incident "bunch" produces a pulse of highly energetic (up to 1MeV) neutrons, particularly in the forward direction. For diffraction, the fast neutrons from the initial pulse must be thermalised using a moderator.

The inherent difference between pulsed and continuous sources concerns the manner in which the scattered radiation is measured. If a neutron is created at a known time and position, its energy (and therefore wavelength) on detection can be determined from the distance it has travelled to the detector and the time taken to do so, called the time of flight (TOF). Measurements on pulsed sources are energy dispersive and for powder diffraction are independent of the scattering angle (although the resolution of individual detectors is dependent on the scattering geometry).

On monochromatic diffractometers such as D1A, the direction of the diffracted beam must be accurately defined. Consequently collimation is inherent between the specimen and the detector. For engineering measurement this facilitates the definition of a sampling volume, since a slit can be installed anywhere along a radial line between the sample and the detector (cf chapter 4). On pulsed sources position sensitive detectors (PSD) are used and for conventional experiments, there is no need for inherent exit collimation. However, definition of a sampling volume does require that the spatial extent of the diffracted beam is limited. This is achieved with an exit slit. If the exit slit is close to the PSD a large solid angle of detector may be obscured while if the mask is close to the sample the spatial resolution in the sample is reduced. Measurements described in this chapter suggest that for spatial resolutions of several mm^3 the former will be the limiting feature.

Using pulsed neutrons the lattice strain is determined by the relative change in TOF for the diffracted maxima between strained and unstrained material (chapter 2, section 2.6b). The diffracted maximum for each lattice reflection occurs at a discrete energy (flight time). Since the energy distribution in each neutron pulse is continuous, the diffracted spectra at any scattering angle contains all the Bragg reflections. On monochromatic diffractometers the diffracted peaks are limited to specific angles.

In chapter 3 the anisotropy due to differing compliances within the unit cell was examined for selected reflections. On a monochromatic source each reflection requires a

separate measurement, for which the specimen must be realigned to maintain the scattering vector in the same orientation. By contrast, each pulsed measurement records the complete strain response for all directions within the lattice. This is an advantage in studies of grain interaction stresses and helps to address the issue of yield in certain directions within the lattice. Grain interaction stresses in hexagonal crystal structures have been the subject of an investigation using time of flight neutrons by MacEwan (1983). They found that prior plastic strain in polycrystalline zircaloy induced peak shifts which could be explained by reference to texture and anisotropic yield.

Although interesting in its own right the study of grain interaction stresses was not the purpose of the measurements detailed here. The stresses of interest result from localised yield over several centimeters within engineering components and the objective was to establish a procedure for determining engineering residual stress. It will be shown that the grain interaction response may be obtained in addition to bulk strain measurements.

8.3 Instruments and profile refinement

The resolution of a powder diffractometer on a pulsed source is given by (Carpenter, 1984):

$$R = \frac{\Delta Q}{Q} = \left[\left(\frac{\Delta t}{t}\right)^2 + \left(\frac{\Delta L}{L}\right)^2 + (\cot\theta \Delta\theta)^2 \right]^{1/2} \qquad (8.1)$$

Where L is the flight path

t is the neutron time of flight

θ is the scattering angle

and ΔL, Δt and $\Delta\theta$ are the respective uncertainties.

From equation 8.1 the resolution can be improved in several ways. ΔL can be reduced by introducing a neutron absorber into the moderator to reduce the uncertainty in position corresponding to its origin. Alternatively by increasing the path length or the time of flight the resolution is improved. Optimal resolution is generally obtained by placing instruments at the end of long guide tubes. However the improved resolution is compromised by losses along the guide. Ultimately for very long guides "frame

overlap" occurs when slow neutrons from one pulse are overtaken by fast neutrons from its successor. In that case not all the incident pulses are used, for example on the high resolution powder diffractometer (HRPD) at ISIS only one pulse in four is accepted at the instrument. The 75% reduction in neutron flux severely limits engineering strain measurement for which small incident apertures and considerable attenuation are prevalent.

Two criteria must be met by an engineering strain measuring instrument at a neutron source. The incident flux must be sufficient for measurements, even after attenuation through up to 20mm in steel. Also it must be capable of resolving changes in lattice spacing in steel of 50 μstrain, to give a stress discrimination of 10MPa. At ISIS two instruments, HRPD and POLARIS, are potential candidates for engineering strain measurement. Both are powder diffractometers with position sensitive detectors surrounding the sample, including the 90° position. The work described in this chapter concentrates on the results obtained at 90°.

A schematic of the instruments around the pulsed source ISIS is given in figure 8.1. The distance between the moderator and the specimen is called the primary flight path, L_1. L_1 is 12m for POLARIS and approximately 100m on the HRPD. The relative proximity of POLARIS to the moderator gives a larger neutron flux than on the HRPD, which has better resolution. Schematic diagrams of the HRPD and POLARIS are included in figures 8.2 and 8.3. Figure 8.4 is a photograph corresponding to figure 8.3. The best spatial resolution in a sample is obtained at 90° and consequently the 90° detector bank is the most important for engineering applications. The 90° detector on the HRPD is made up of of 100 distinct scintillation elements each of which has dimensions 150 by 3mm. The elements are stacked in three rows and subtend an arc of 6° (from 87 to 93° 2θ) at the sample position. On POLARIS the 90° detector is made up of 20 ^{3}He tubes (≈30cm long and 2cm in diameter) stacked in array 5 across and 4 high. They subtend 2° at the sample position (from 89 to 91° 2θ). Unless detector elements are treated individually the integrated spectrum for all elements at 90° represents an average strain measurement, with a spread in direction corresponding to half the 2theta range of the detector (see fig 8.5). However on the HRPD the spread in Q by considering the

90° detector as a whole is only 3° and on POLARIS is only 1°. Since this is small by engineering standards and since measurements are often limited by low flux no attempt was made to attribute the spectra to individual elements.

All the diffracted neutrons which reach the detector on a pulsed source contribute to the measured spectrum. The presence of all the lattice reflections in each measurement means that profile refinement can be applied. If the crystal structure is known then the intensities and positions of the observed lattice reflections can be combined using the Rietveld method of profile analysis (Von Dreele, 1982). Using a least squares fit between the predicted and observed intensity profiles the atomic positions and lattice parameter a_0 can be determined. Thus residual strains can be obtained from the lattice parameter, which is specified to a better accuracy than the position of any individual reflection.

Anisotropic strain information in the lattice may be investigated by fitting individual reflections. The exact nature of the peak, fitted to the data, depends on many physical variables (Carpenter, 1986). At long times, low energies and in moderators that are not too small an exponential decay of the pulse will occur which will be faster in smaller moderators. Different functions are used to model the pulse shape as a function of energy.

8.4 Samples

The ring specimens, examined using the HRPD and POLARIS, were described in chapter 5. The residual stress distribution induced in thin rings by autofrettage has been examined by sectionning and using monochromatic neutrons on D1A (Chapter 5, and Stacey, 1985). Thin rings offer an appropriate geometry for preliminary examinations using pulsed neutrons because, in the absence of flaws, the stress distribution is axisymmetric and the stress gradients are sufficiently gradual to permit a large sampling volume. The small thickness (5mm) provided a self-limiting sampling volume in the axial direction which was important since no exit masking was attempted. All the measurements quoted in this chapter were made on the uncracked side of autofrettaged rings 7RDMA and 8RDMA.

8.5 Collimation and manipulation

The cross section of the incident beam on both POLARIS and the HRPD is several centimeters square. In order to make comparable measurements to D1A the relevant dimension of the incident beam was reduced to 2mm, relative to the radial direction in the ring. Preliminary measurements on the HRPD employed an incident boron carbide mask, containing a rectangular aperture (5mm horizontal and 2mm vertical), supported from the top plate of the sample tank (figure 8.6). The orientation of the mask could not easily be changed and the measurements were limited to the hoop and axial directions since the radial strain would have required reorientation of the aperture. The orientations of the rings with respect to the incident beam for different strain measurements are illustrated in figures 8.7 and 8.8. On POLARIS a remote controlled system was installed, allowing the aperture in the incident beam to be set to any rectangular shape up to the full beam profile. Unfortunately the size and shape of the input apertures used on both POLARIS and HRPD obscured the back scattering detectors.

Engineering strain measurements necessitate positioning of samples to accuracies of 0.1mm. Measurements are obtained at different positions by translating the specimen through a neutron beam of a defined cross section. The strain in different directions is measured by reorientating the specimen with respect to the detectors. On the HRPD the manipulation was limited to a manual rotation about a vertical axis and a single automated vertical motion. The system was upgraded on POLARIS to give added flexibility. Four remote controlled motions were installed: rotation about a vertical axis, two horizontal and a vertical translation (fig 8.9). A photograph of the manipulation system and automated input collimation system is given in figure 8.10. (Note that the automated input collimation is supported from the red top plate, unlike figure 8.9 in which the apertures are resting on the base of the sample tank).

One major impediment to the current measurements was the presence of a vacuum tank . Not only does it limit the installation of translation devices but it prevents optical positioning of the sample with respect to the aperture or a fixed datum. In practice, on both instruments, the position of the ring relative to the neutron beam was

determined by noting the change in the ratio of the transmitted to the incident intensity as the ring is moved into the beam. An example is given in figure 8.11.

8.6 HRPD results

Hoop strain measurements were made on the uncracked side of ring 8RDMA. Figures 8.12a is an example of a spectrum obtained on the back scattering detector without a mask on the incident beam. It is the product of 5 minutes count time. The spectrum in figure 8.12b was obtained on the 90 degree detector after installation of the input mask. It corresponds to an uninterrupted 11 hour count at an average beam current of 90μA. The scattering length geometry is different for the backscattering and 90° detectors hence the TOF spectra in figures 8.12a and figure 8.12b are displaced but the reflections have been labeled accordingly. The corresponding lattice spacings for figure 8.12a are given in table 8.1.

Comparison of figures 8.12a and 8.12b demonstrate the reduction in intensity resulting from absorption, scattering and masking of the incident beam. In figure 8.12b only the (110), (200) and (211) reflections are clearly visible. Subsequent reflections are too weak to be used for strain measurement. The low intensity of the spectrum in 8.12b is weaker than would be expected from a simple extrapolation of the intensities achieved in figure 8.9b. It is also too weak to attempt profile refinement and the residual lattice strains can only be deduced from the peak shifts of the individual reflections.

For the back scattered spectra (fig 8.12a) the reflections are intense with good statistics and were fitted using an Ikeda-Carpenter function which consists of the sum of a delta function and a decaying exponential convoluted with a slowing-down function. Peaks fitted in this way had errors ≈1μsec. However at 90°, after installation of the mask, the shape and low intensity of the reflections made peak fitting difficult. The poor statistical accuracy of the reflections did not warrant a sophisticated fitting routine and all fits were made with a single Gaussian. In some cases low intensity reflections were smoothed to enable a Gaussian to be fitted to noisy data.

Low count rates on the HRPD limited the number of measurements. The TOF and lattice spacing for five hoop strain measurements are given in table 8.2. A time of flight corresponding to zero strain for the (110) reflection of 71775 μsec was used by

assuming that zero strain occurs at a radial position 6.5mm from the bore, R=6.5 (as has been noted on D1A). Zero strain values for the (200) and (211) reflections were calculated for the same lattice parameter by $71775/\sqrt{2}$ and $71775/\sqrt{3}$ respectively.

The strains for the three reflections are plotted in figure 8.13 with measurements made using the (211) reflection at D1A. The D1A measurements were obtained with an $8mm^3$ sampling volume thus are not directly equivalent to the 71 mm^3 sampling volume on HRPD. However the residual strain distribution in the ring is axisymmetric and since the radial extent of the two measurements is the same reasonable agreement would be expected. In figures 8.13a and 8.13c the strains for the (110) and (211) reflections measured on the HRPD agree with the D1A results within the experimental error (except at R=24mm in figure 8.13c which was a very weak reflection). In particular the (110), which was the most intense of the three reflections measured, showed good agreement. The (200) reflection (figure 8.13c) shows larger strain variations than the D1A results. This may qualitatively result from strain anisotropy, as discussed in chapter 3.

Each D1A strain measurement for the (211) reflection took approximately 20 minutes to give an accuracy of $\pm$ 50 μstrain. On the HRPD at R=6.5mm after 11 hours the most intense reflection was the (110) which gave an accuracy of $\pm$ 111 μstrain.

Table 8.1: d spacings for back scattered peaks in figure 8.12a

Peak #	TOF (μsec ±1)	d † (Å ± 0.00002)	(hkl)
1	97959	2.02462	110
2	69283	1.43194	200
3	56571	1.16921	211
4	48995	1.01263	220
5	43824	0.90575	310
6	40005	0.82682	222
7	37036	0.76546	321

† d = TOF / 48384 for backscattering detector

Table 8.2: Hoop strains measured on the HRPD for 8RDMA-UC

R (mm)	TOF (μsec)	D† (Å)	Strain* (με)	Strain error ± (με)	Peak height (N/Å)
Reflection 110*1					
1.5	71685	2.00832	-1254	181	2.0
6.5	71771	2.01073	-55	111	17.5
10.5	71816	2.01199	571	289	1.8
24.5	71808	2.01177	460	195	2.0
30.5	71774	2.01081	-14	153	2.5
Reflection 200*2					
1.5	50635	1.41859	-1970	395	0.5
6.5	50707	1.42060	-906	197	4.5
10.5	50843	1.42441	1773	551	0.5
24.5	50814	1.42360	1201	650	0.6
30.5	50748	1.42175	-98	512	0.7
Reflection 211*3					
1.5	41373	1.15910	-1593	395	0.5
6.5	41442	1.16104	72	197	4.5
10.5	41466	1.16171	651	551	0.5
24.5	41483	1.16218	1061	650	0.6
30.5	41448	1.16120	217	512	0.7

† by d=TOF / 35694
*1 with t_0 =71775 assuming R=6.5mm is at zero strain
*2 with t_0 = 50753 by $t_0(110) / \sqrt{(2)}$
*3 with t_0 = 41439 by $t_0(110) / \sqrt{(3)}$

8.7 Polaris results

Measurements using POLARIS were made on the uncracked side of ring 7RDMA. Using the system described in section 8.5 the hoop, radial and axial strains were measured at different radial positions. A typical spectrum obtained on the 90° detector bank in 60 minutes is given in figure 8.14. In the absence of the incident mask the large sloping background at short TOF (high energy) was not observed. It is caused by scattering from the boron carbide mask which is placed within 5 centimeters of the sample position.

Count times for each measurement were specified by the integrated count on the

incident monitor from 2000 to 2200 μsec. The accuracy in the lattice parameter (quoted by profile refinement) has been converted to lattice strain and plotted against different monitor counts in figure 8.15. The accuracy appears independent of orientation and for a monitor count of 1 million is approximately ± 50 μstrain. On POLARIS with an uninterrupted beam current of approximately 100μA, this corresponds to a collection period of about one hour using a tantalum target.

The lattice parameters, a_0 for the measurements in the hoop, radial and axial directions were calculated by profile refinement and are given in figures 8.16. Clearly there is a large displacement between each strain direction. If the data for each direction were converted to strain using the same reference value of the lattice parameter, the radial results would be, on average, 5000 μstrain more tensile than the hoop strain measurements. This is unreasonable and disagrees with the measurements obtained on D1A (cf chapter 4). The disparity can be attributed to changes in the path length of diffracted neutrons which reach the detectors. Since no exit collimation is used, if the axis of rotation does not coincide with the neutron beam, then when the sample is rotated the effective sampling volume, defined by the intersection of the neutron beam with the ring, will be displaced. The difference between the mean lattice parameters for the hoop and radial directions is ≈0.013 Angstroms which corresponds to an increase in the path length of neutrons at the detector of ≈5cm. A displacement of the ring of this magnitude is not unlikely.

In figure 8.16 the lattice parameters were calculated assuming the same calibration constant between time of flight and lattice spacing for the different orientations. This appears not to be the case and without recalibration it is not possible to apply the same unstrained value for the lattice parameter in each direction. Hence for each orientation zero strain was assumed to occur at the same radial position as was observed on D1A (chapter 5). Strains calculated in this way for the POLARIS are superimposed on corresponding measurements using the (211) reflection on D1A in figure 8.17 abc.

On POLARIS the bulk strain can most accurately be calculated from the lattice parameter. However, as was noted for the HRPD results strain information for specific

lattice directions can be extracted by fitting individual reflections. The accuracy of measurement for the peak centres of intense reflections is adequate to make inferences concerning their strain response. In figure 8.18 the strains determined from the peak shifts of the first seven reflections are given. The data have been smoothed artificially which has the same effect as using a larger sampling volume and tends to reduce the magnitude of the maxima. The systematic displacement results from an error in the calibration which causes the successive displacements as the lattice spacing reduces.

8.8 Comparison with D1A and discussion

On the HRPD although the strains calculated for the three observable reflections are reasonable, the count rate is too low and the experimental error too great to make it viable as an instrument for measuring engineering strains. After data collection for eleven hours, in a single position, the peak fit accuracy on the most intense, (110) reflection was $\pm 111\mu$ strain which is 4 times the error obtained on D1A in twenty minutes. Measurements on thick samples would take prohibitively long times and if only three reflections are observed the HRPD would offer little extra information above a monochromatic measurement of a single reflection.

The results for POLARIS are more encouraging. One hour count times and a sampling volume of $70mm^3$ are adequate to give spectra on the 90° detector sufficient for profile refinement. The smooth variation of the strains calculated from the lattice parameter (figure 8.17) indicate that the accuracy obtainable on POLARIS measurements is competitive with D1A.

The greatest problem identified for TOF measurements on POLARIS is the determination of a strain free reference spectrum. Not only do strain-free specimens have to be identified but if a sampling volume is not defined, changes in path length can cause shifts in the TOF spectrum which can be misinterpreted as strain variations. Fortunately the differences seen in figure 8.16 were too large to be misinterpreted. In this case comparison with data sets for D1A were sufficient to infer strain free zeros but obviously this will not generally be the case. The only solutions is definition of a fixed sampling volume or the positioning of the sample relative to a fixed point to an accuracy better than 0.1mm. This is not currently possible.

When a TOF zero is assumed for the three measured strain directions the POLARIS data agree well with the strain inferred by the (211) reflection on D1A (fig 8.17). The absolute magnitude of the hoop strain measured in figure 8.17a is between 10 and 30% less than the D1A measurement. In view of the discrepancy of the sampling volume and that the lattice parameter may better reflect the bulk response of the material, the disparity is reasonable. What is is not understood are the surface discrepancies which occur at the bore and at the outer edge in the hoop and radial scans (figs 8.17a and 8.17b). Unfortunately the HRPD data (fig 8.13) are not detailed enough to support these anomalies.

On D1A the basic issue is selection of a reflection which will give a reliable value for the bulk stress. Generally a reflection whose behaviour is known to reflect the bulk material response is used. Figure 8.18 shows that a more complete probe can be made by measuring the strain anisotropy for multiple reflections. It would be interesting to modify the Rietveld program to allow for the assymetric deformation seen in the cubic lattice to account for the different strain responses of different lattice reflections.

In order to completely specify the stress tensor in a specimen, a minimum of 6 independent strain measurements are required. The ultimate aim for an engineering instrument should be simultaneous strain measurement in multiple directions. The practical constraints on such a goal result from varying sampling volume and varying specimen geometry which will inevitably obscure some directions because of excessive path lengths. Installation of soller slit collimation on a PSD can allow multiple simultaneous measurements along a line in a sample (Leffers, 1986). This is not possible on POLARIS since the individual elements of the detector do not offer sufficient spatial resolution to attempt multiple measurements, even if sufficient flux were available.

8.9 Recommendation for further study

Definition of a sampling volume must be attempted, primarily because of problems in determining the strain free reference spectrum but also because most engineering measurements require a spatial resolution of less than $10mm^3$. This will require installation of an exit mask in the diffracted beam within a few centimeters of the

sample.

Modification of the input mask system is attractive for two reasons. First, by installing upstream collimation the fraction of the incident beam masked at the sample position can be reduced, which should reduce the short TOF background noted in figure 8.14. Second, by making the input mask more compact, less of the back-scattering detectors will be obscured and it may be possible to collect usable spectra on these as well.

Attention must also be paid to sample positioning in the beam. Using the variation in intensity is satisfactory to position specimens of simple geometry but may not always be possible. Removal of the sample tank would enable optical positioning to be performed more effectively. This would also be attractive because it would allow more freedom of access and movement for bulky components.

Finally, a study of the effect of count time on the profile refinement would allow more efficient use of beam time to be made. Similarly, the peaks at 90° warrant further investigation since if their shape can be better understood then more accuracy can be achieved.

8.10 Conclusions

For applications where spatial resolution of less than $50mm^3$ is required the count rates on HRPD are too low to make measurements of engineering residual strain. However, using POLARIS, the residual strain distribution in a thin ring taken from a component of engineering interest has been successfully examined, with a resolution in one direction of 2mm. Profile refinement of TOF spectra offers the best means of extracting bulk strain information. Anisotropic effects can also be recorded by fitting individual reflections in a time of flight spectrum. For specific applications POLARIS appears to be equally applicable as D1A. Although the effective count rate was slower during these preliminary measurements it is likely that an increased understanding of the profile refinement and improvements in the experimental procedure will reduce the time required for measurements to a given accuracy. Currently the major experimental drawback is not the absence of a sampling volume, but in the apparent strain variation caused by rotation about an axis which is not coincident with the neutron beam.

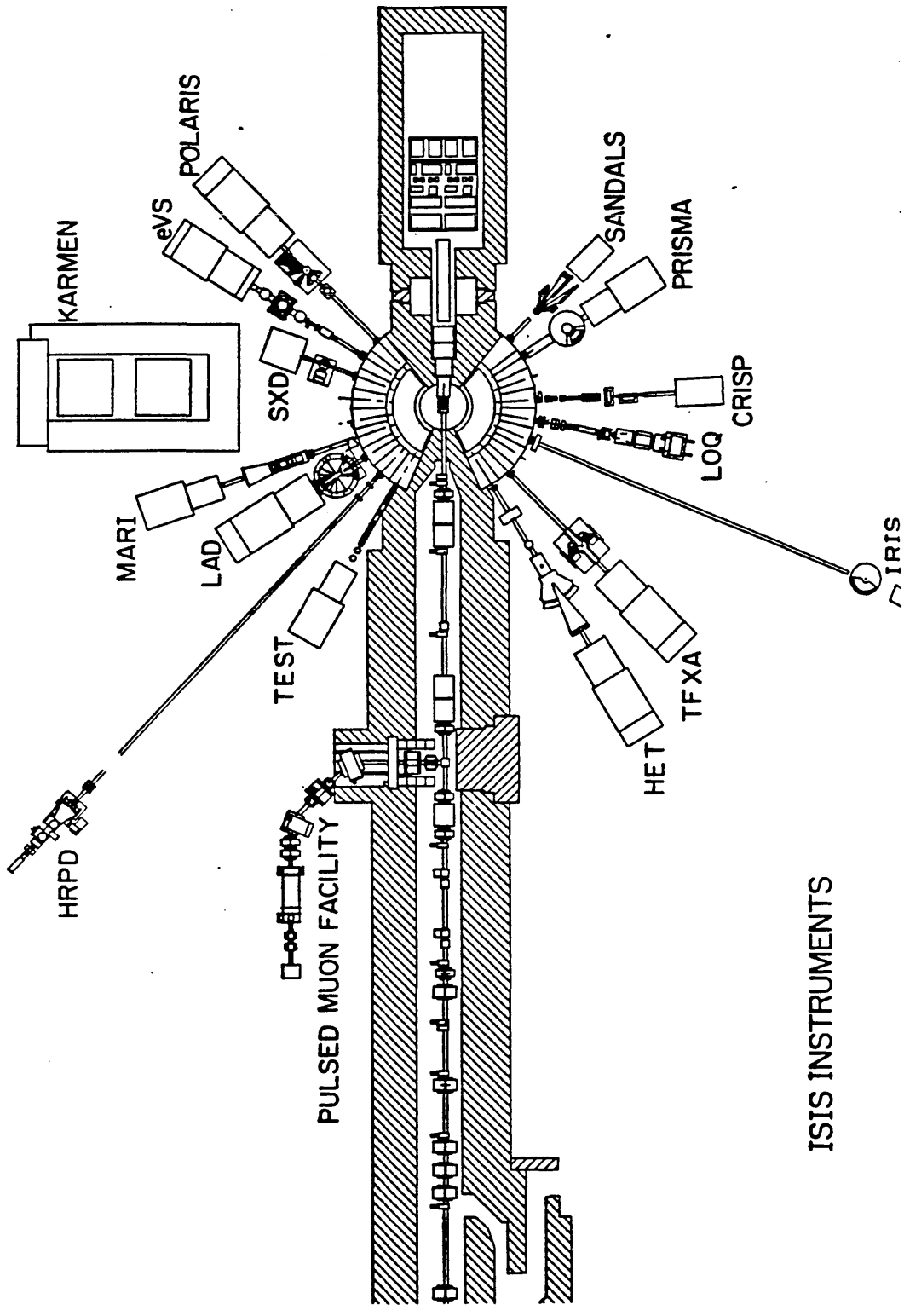


Figure 8.1: Instruments on the pulsed source ISIS

[from ISIS annual report RAL-89-050]

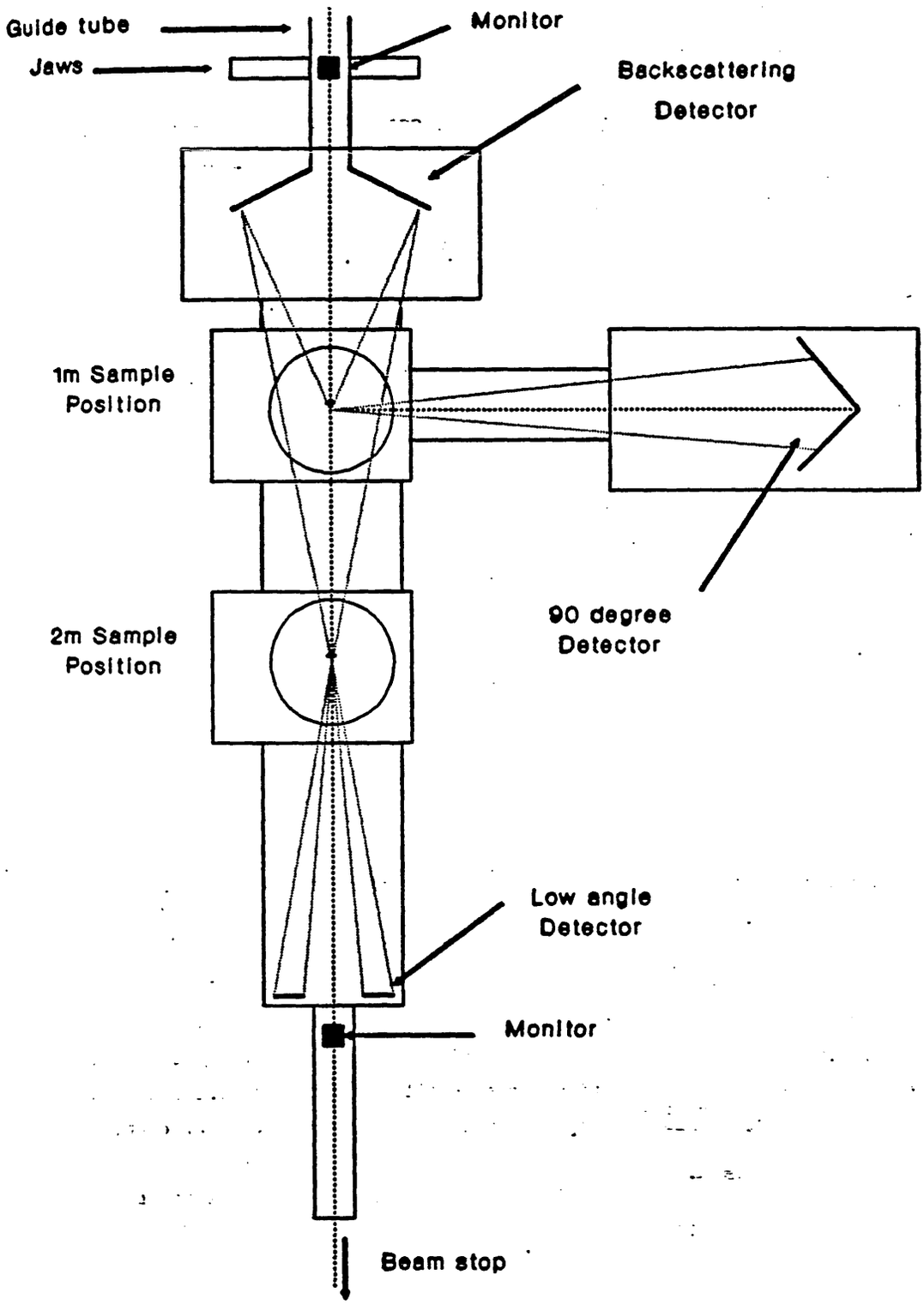


Figure 8.2:Schematic of the HRPD at ISIS

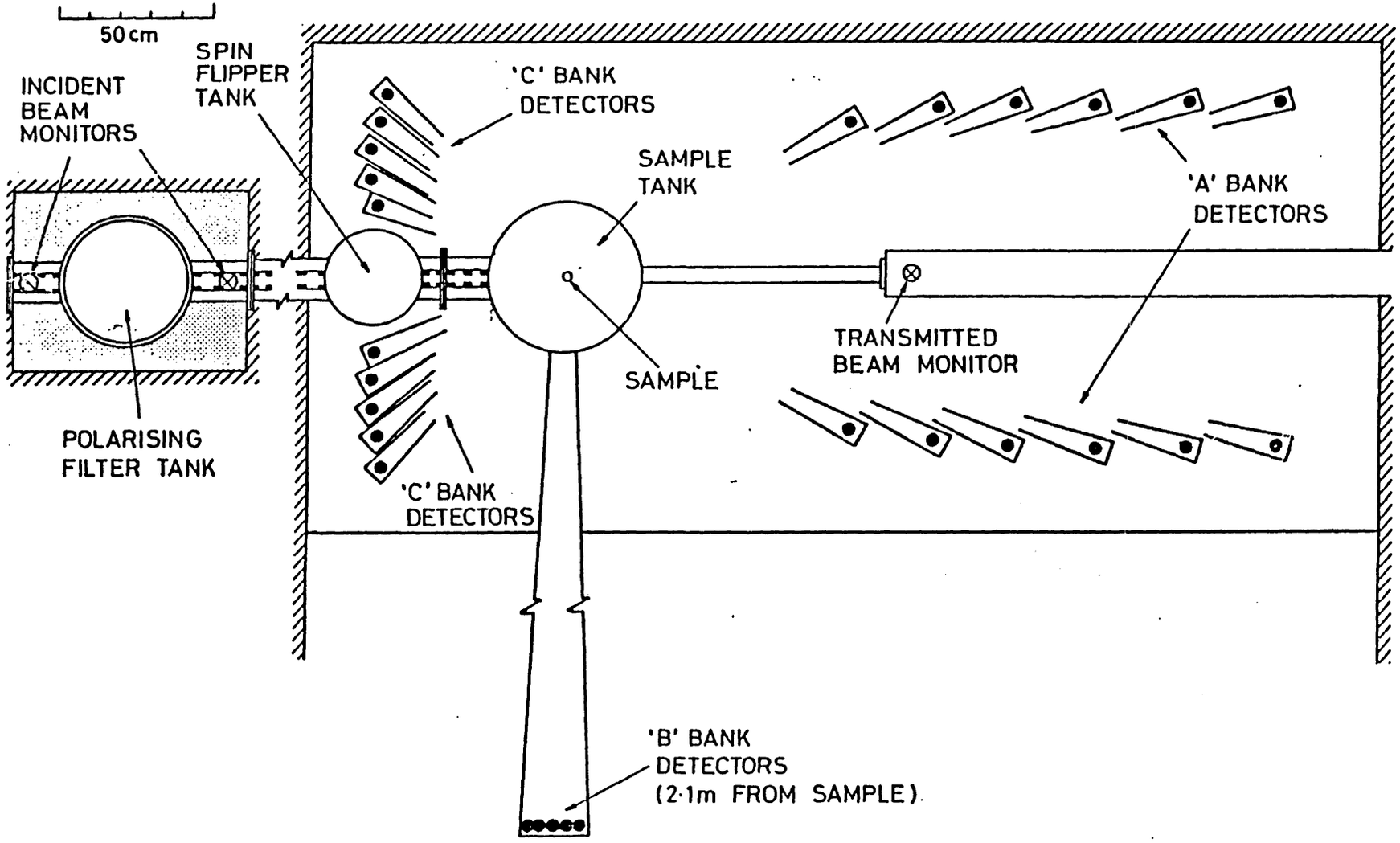


Figure 8.3:Schematic of POLARIS at ISIS

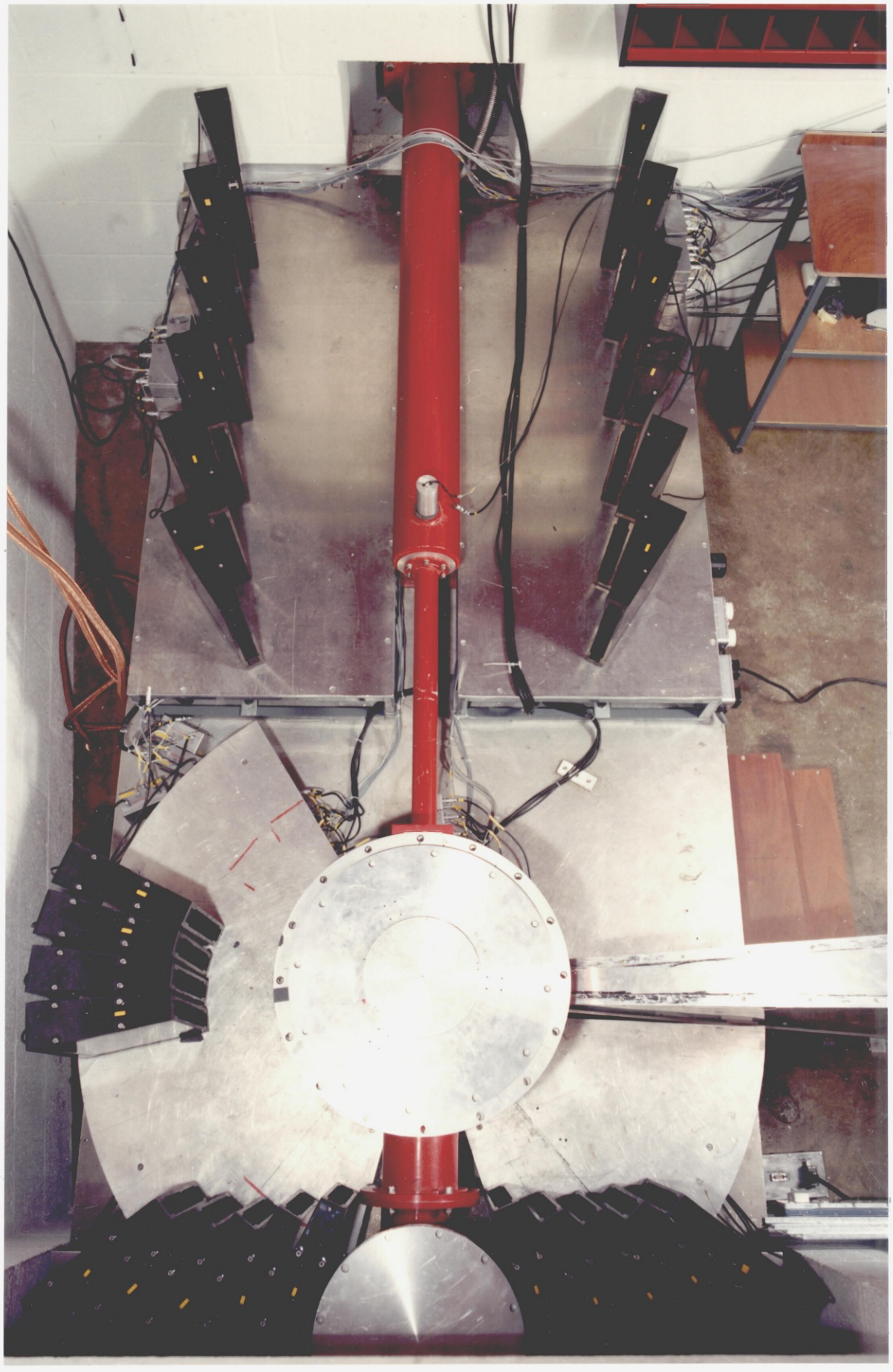


Figure 8.4: Overhead photograph of POLARIS

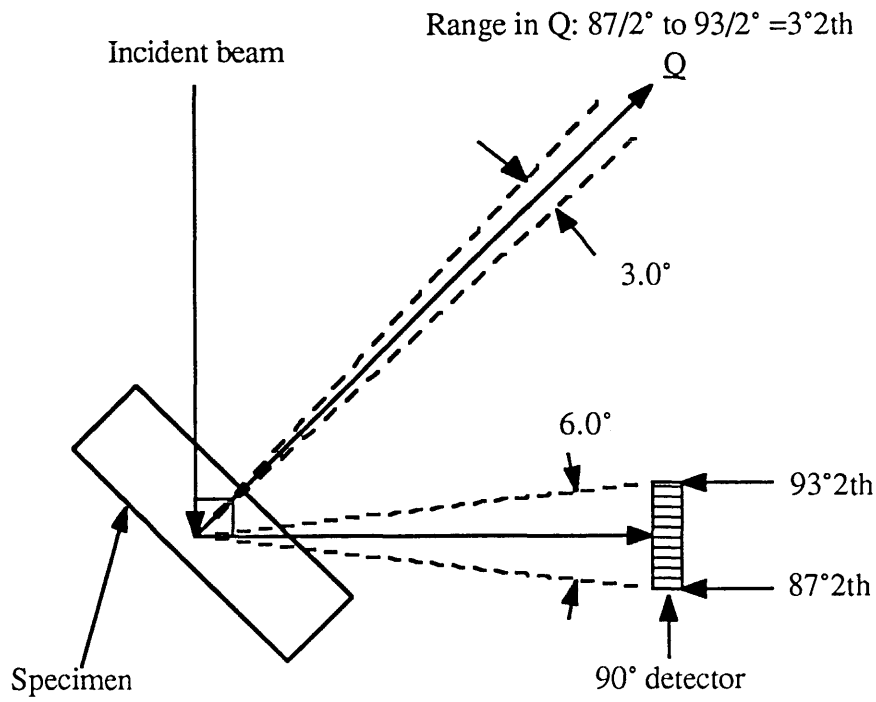


Figure 8.5: Range in scattering vector caused by integrating over all 90° detector elements

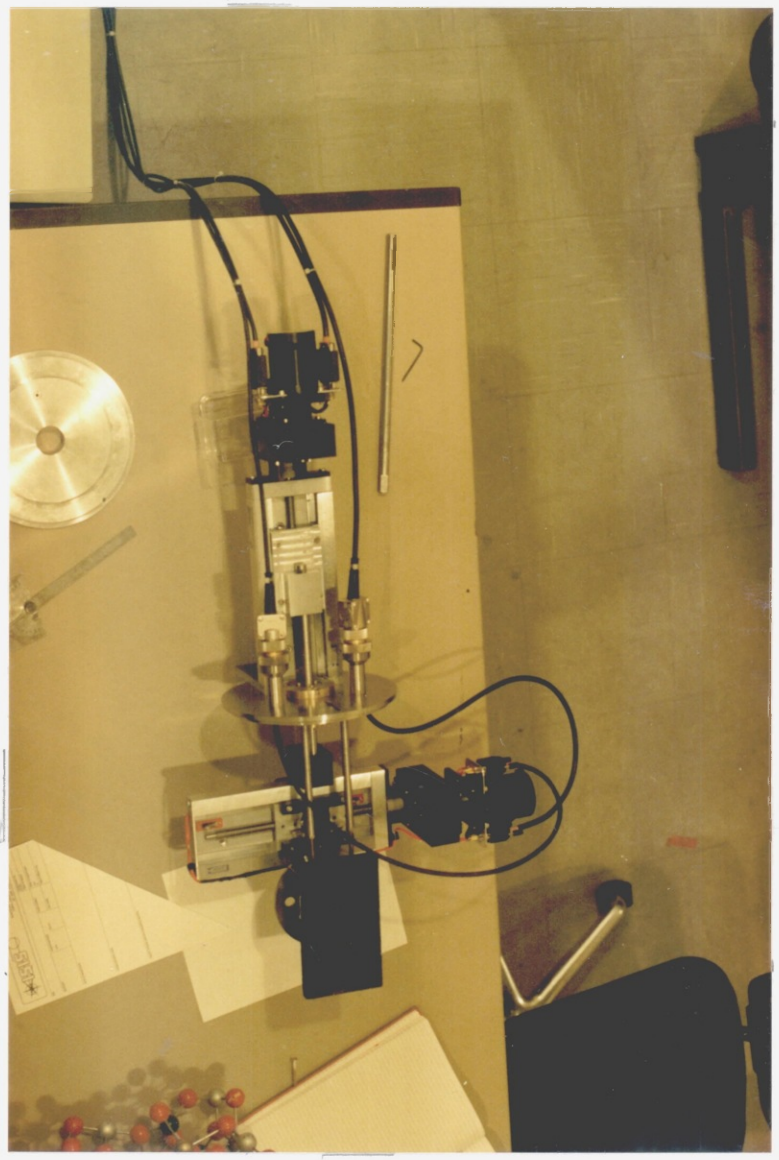


Figure 8.6: Original fixed mask and translator used on HRPD

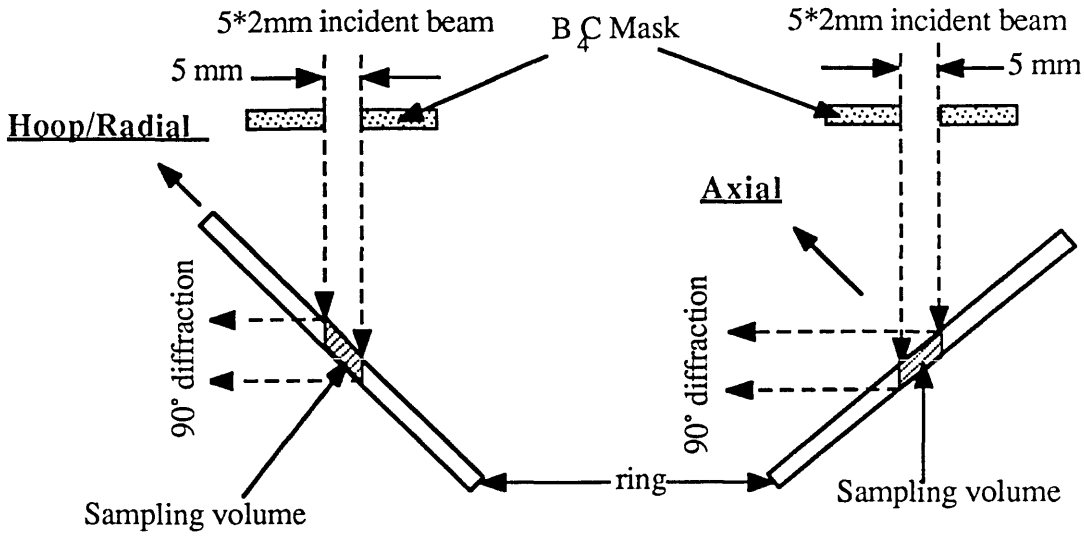


Figure 8.7: Plan view of ring orientations for different strain directions

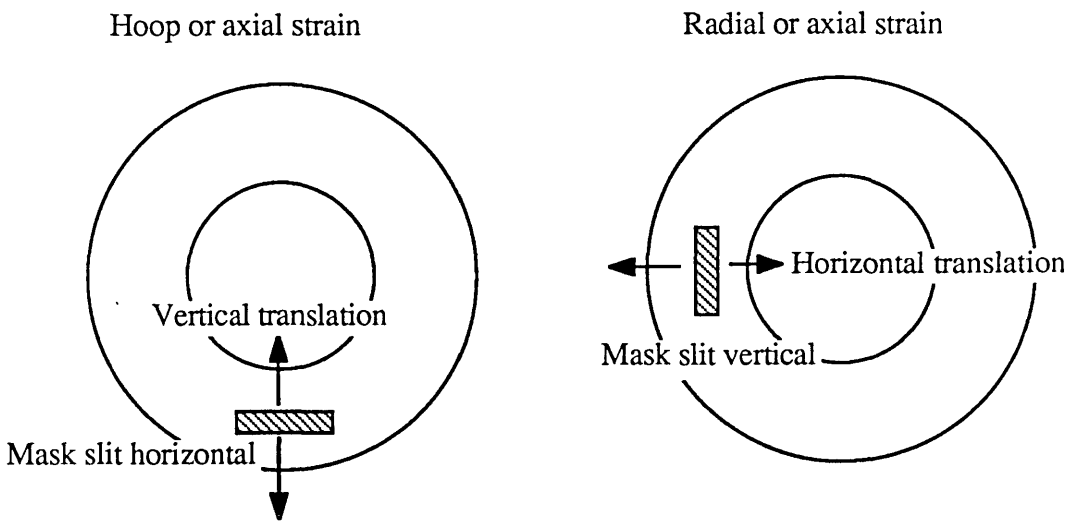


Figure 8.8: Beam projection onto the ring face showing traverse direction

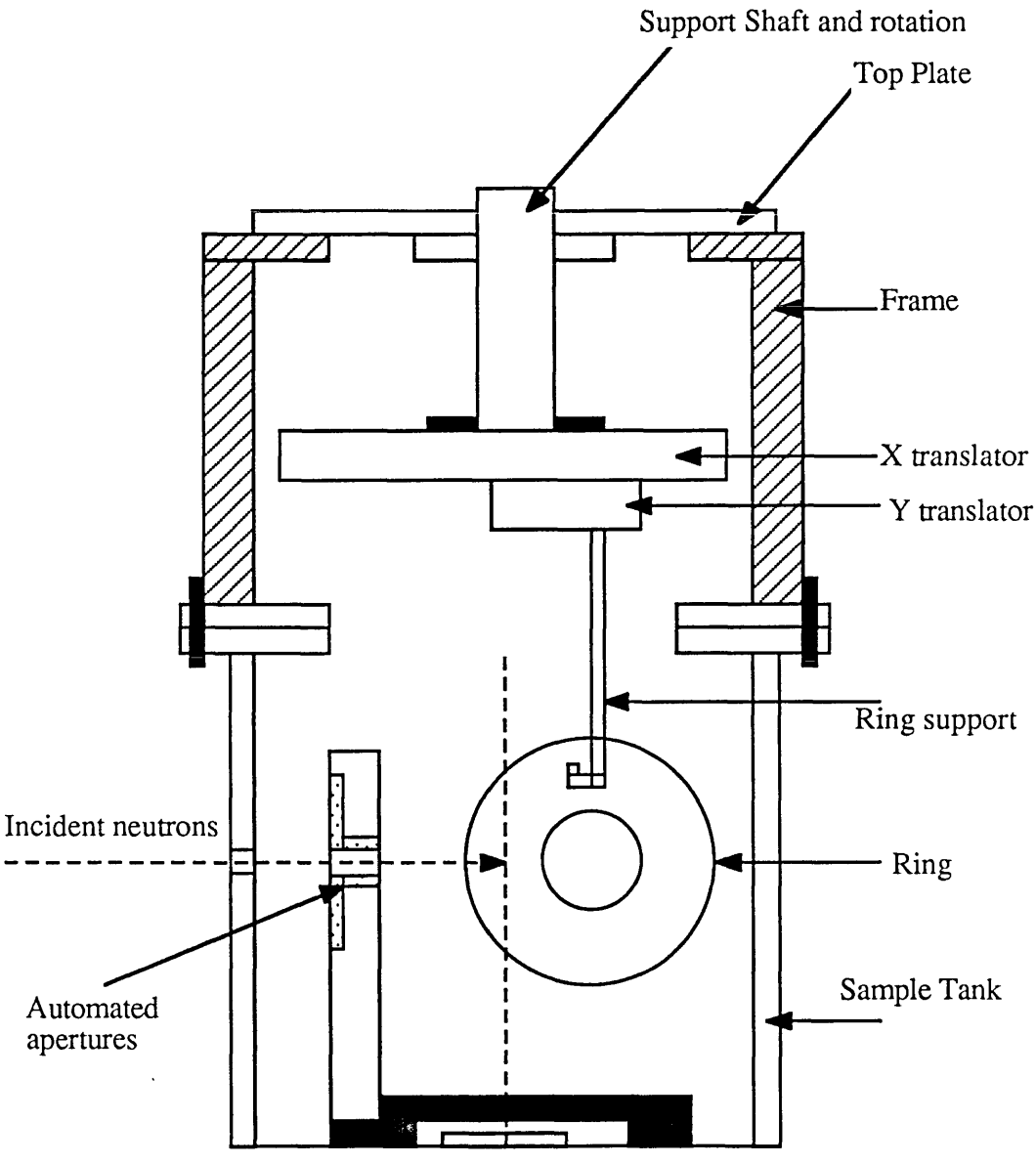


Figure 8.9: Schematic of experimental set up on POLARIS

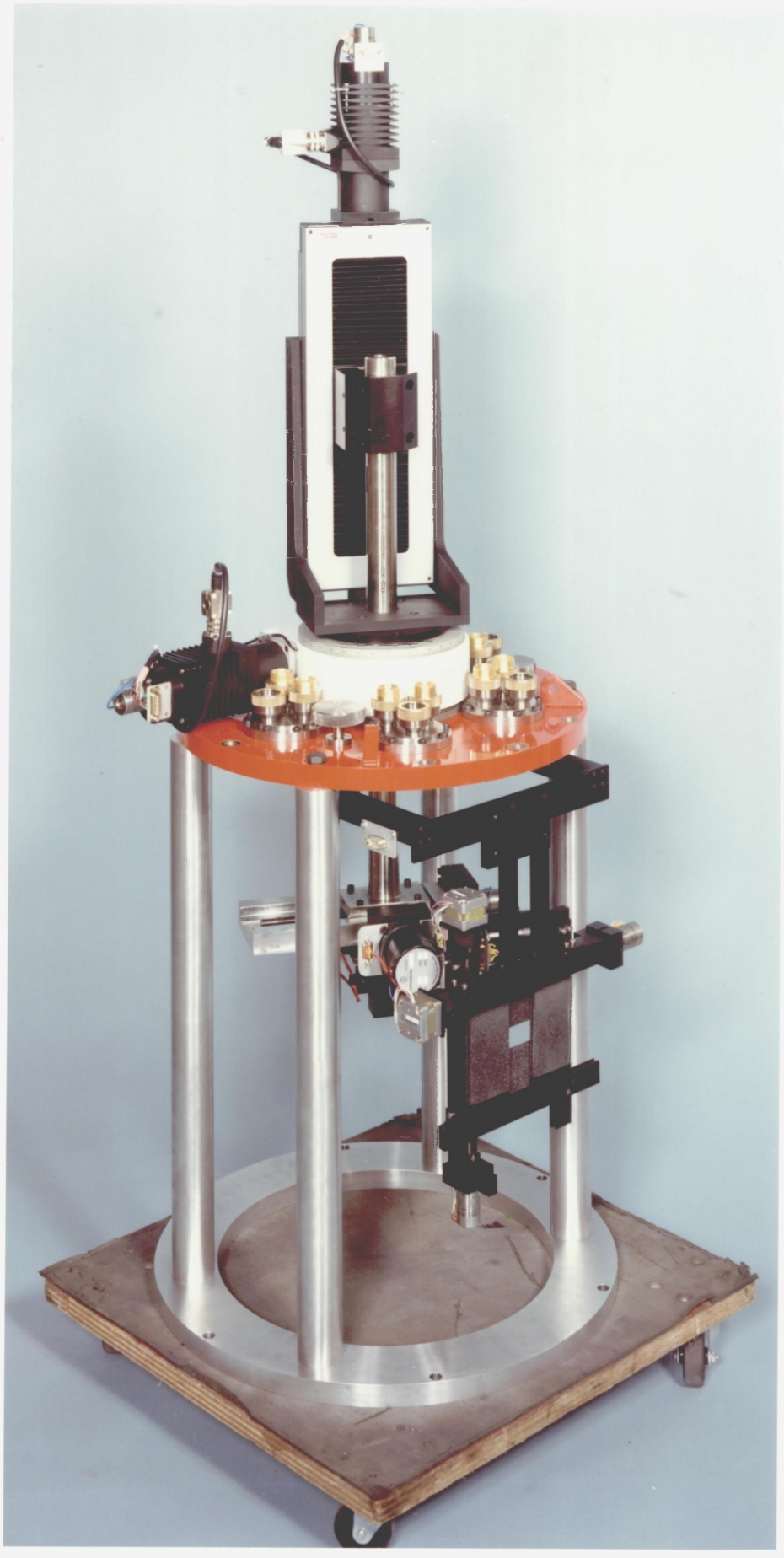
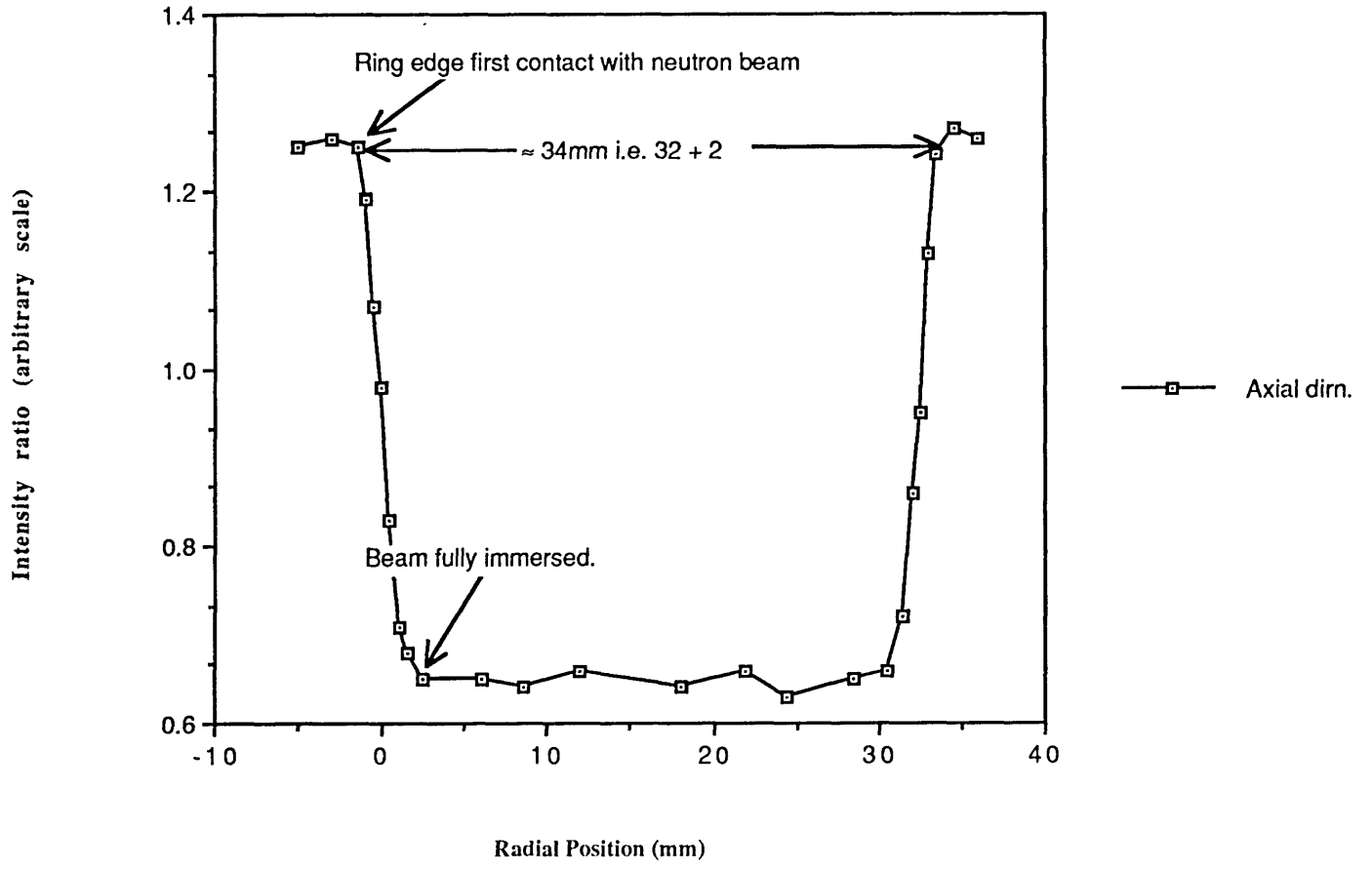


Figure 8.10: 4 Axis manipulator and automatic input collimation system for POLARIS

Figure 8.11: Transmitted / incident intensity ratio for a ring moved through the beam on POLARIS



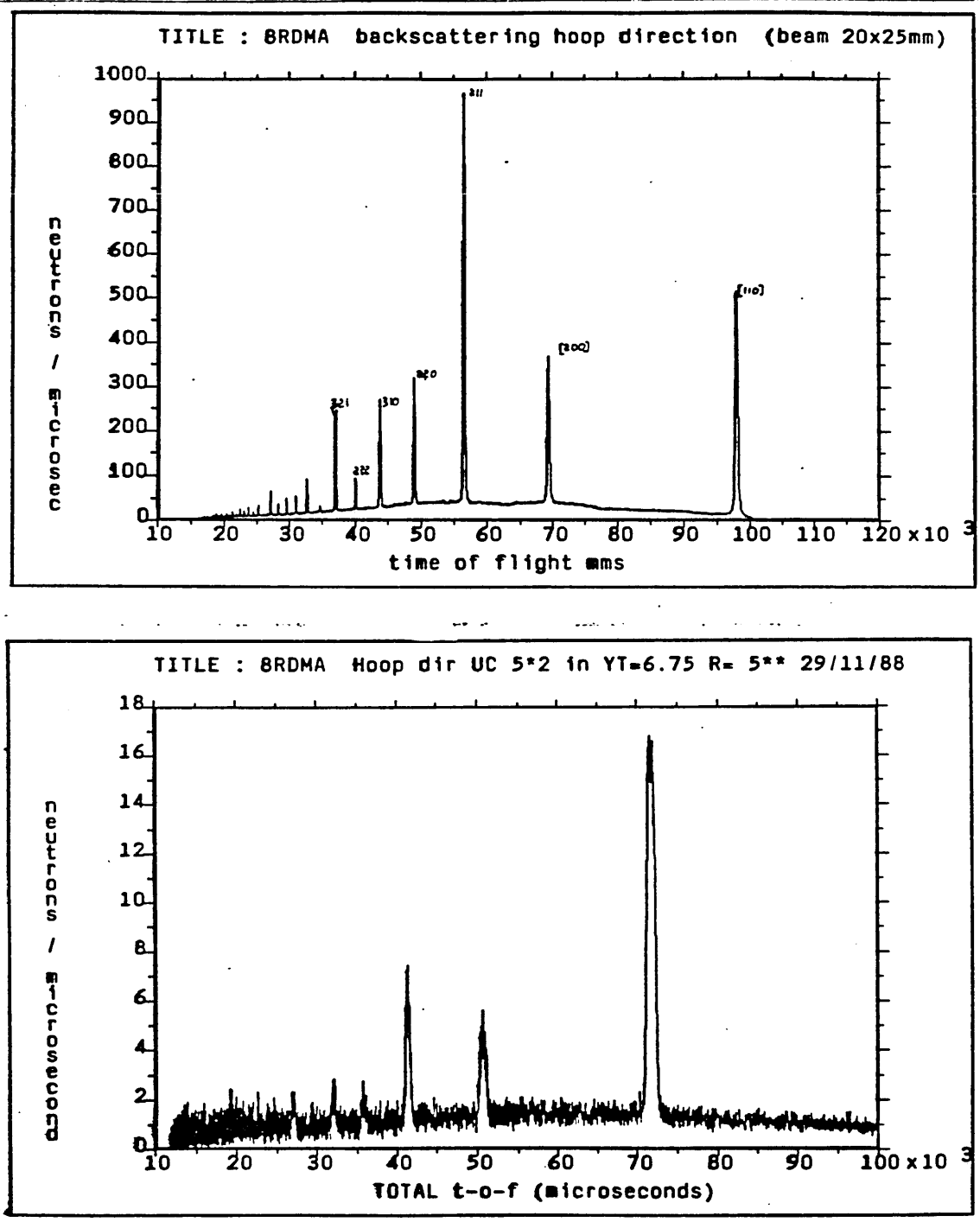


Figure 8.12a: (TOP) HRPD spectrum obtained on backscattering detector in 5 minutes

Figure 8.12b: (BOTTOM) HRPD spectrum from 90° detector with 5mm*2mm input aperture in 11 hours

Figure 8.13a: Hoop strain, uncracked side-8RDMA by [110] on HRPD

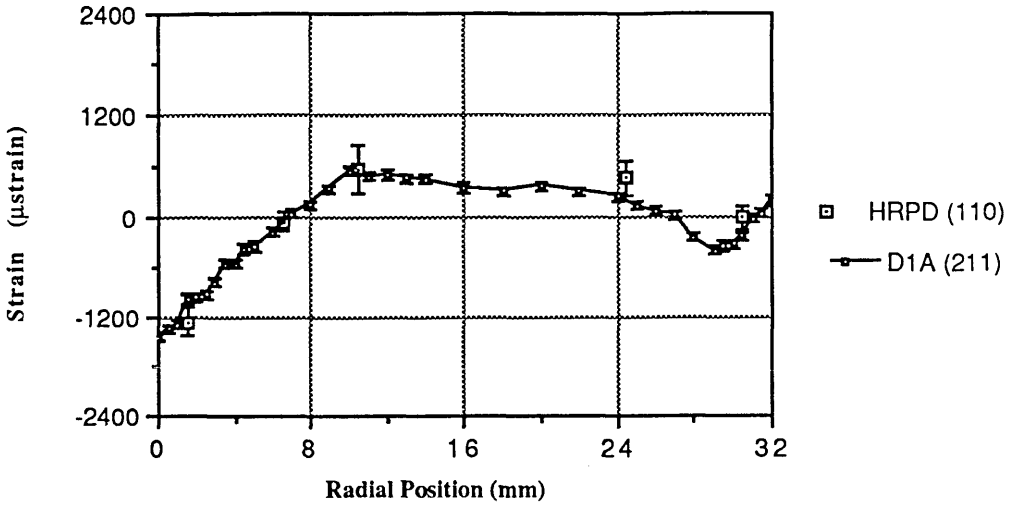


Figure 8.13b: Hoop strain, uncracked side-8RDMA by [200] on HRPD

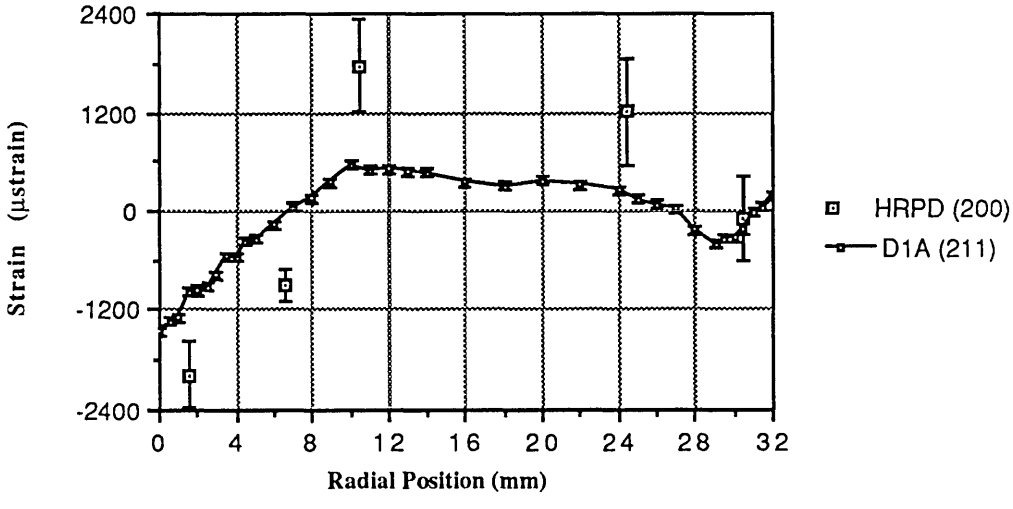
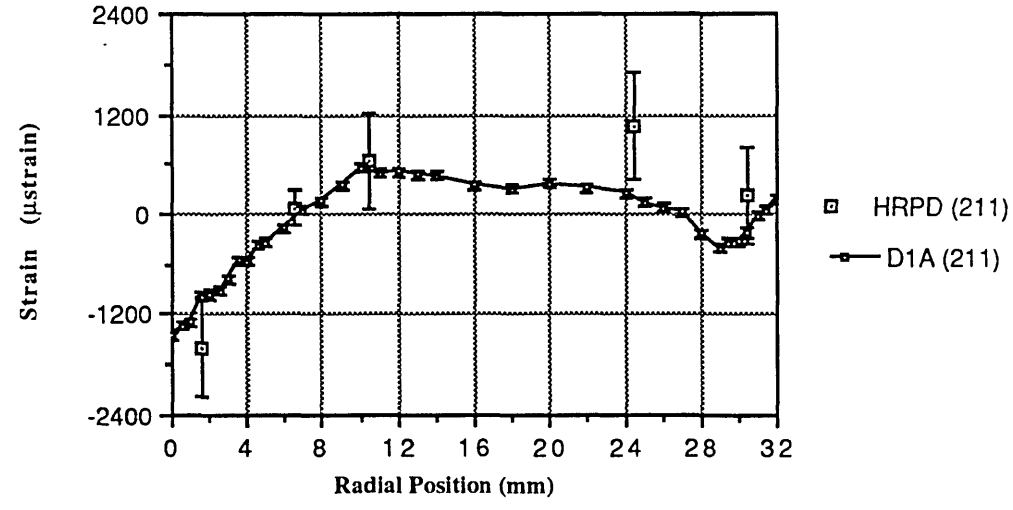


Figure 8.13c: Hoop strain, uncracked side-8RDMA by [211] on HRPD



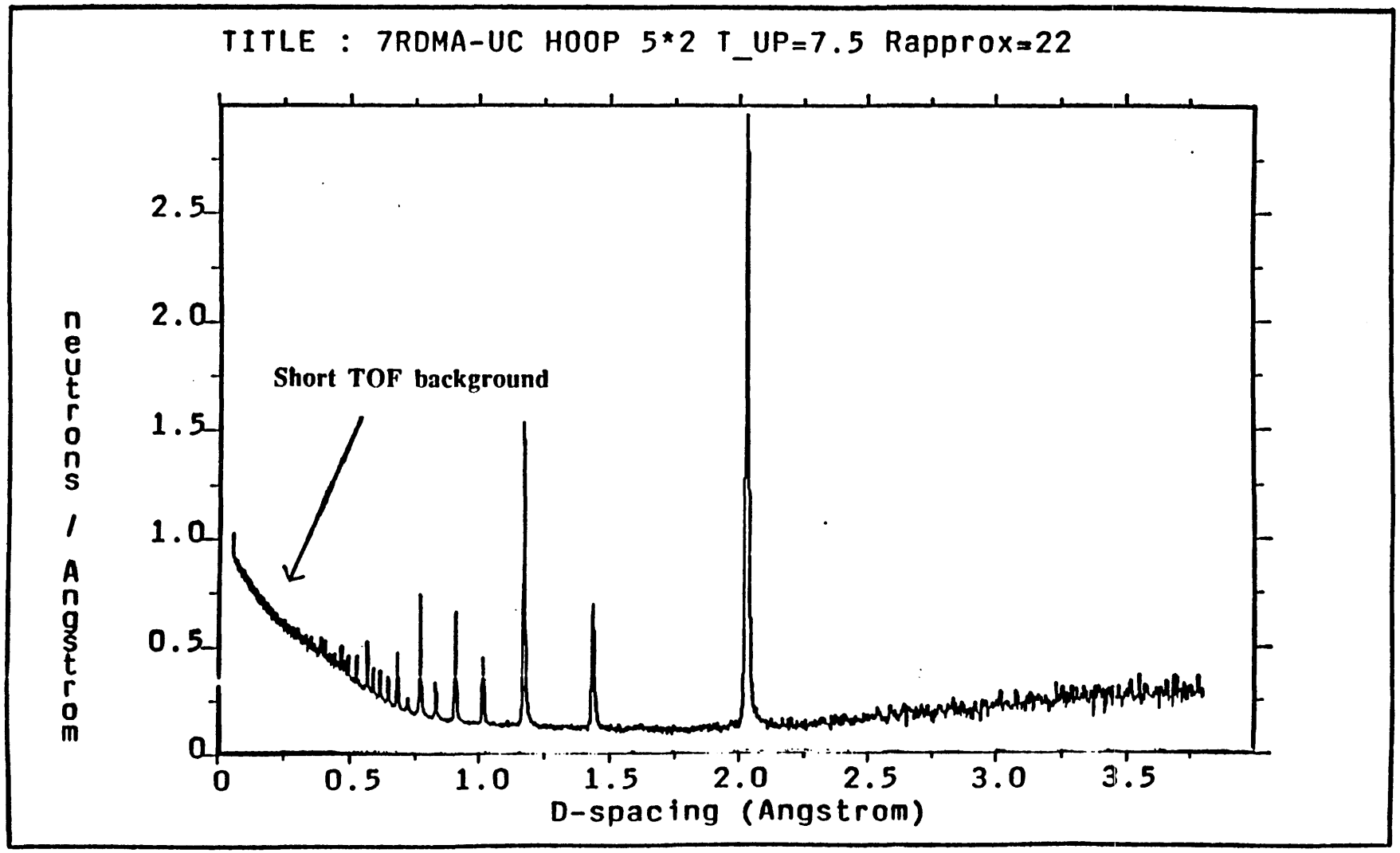


Figure 8.14: POLARIS spectrum on 90° detector 5*2 input mask count time 1hour

Figure 8.15: Standard deviation quoted by profile refinement for different count times

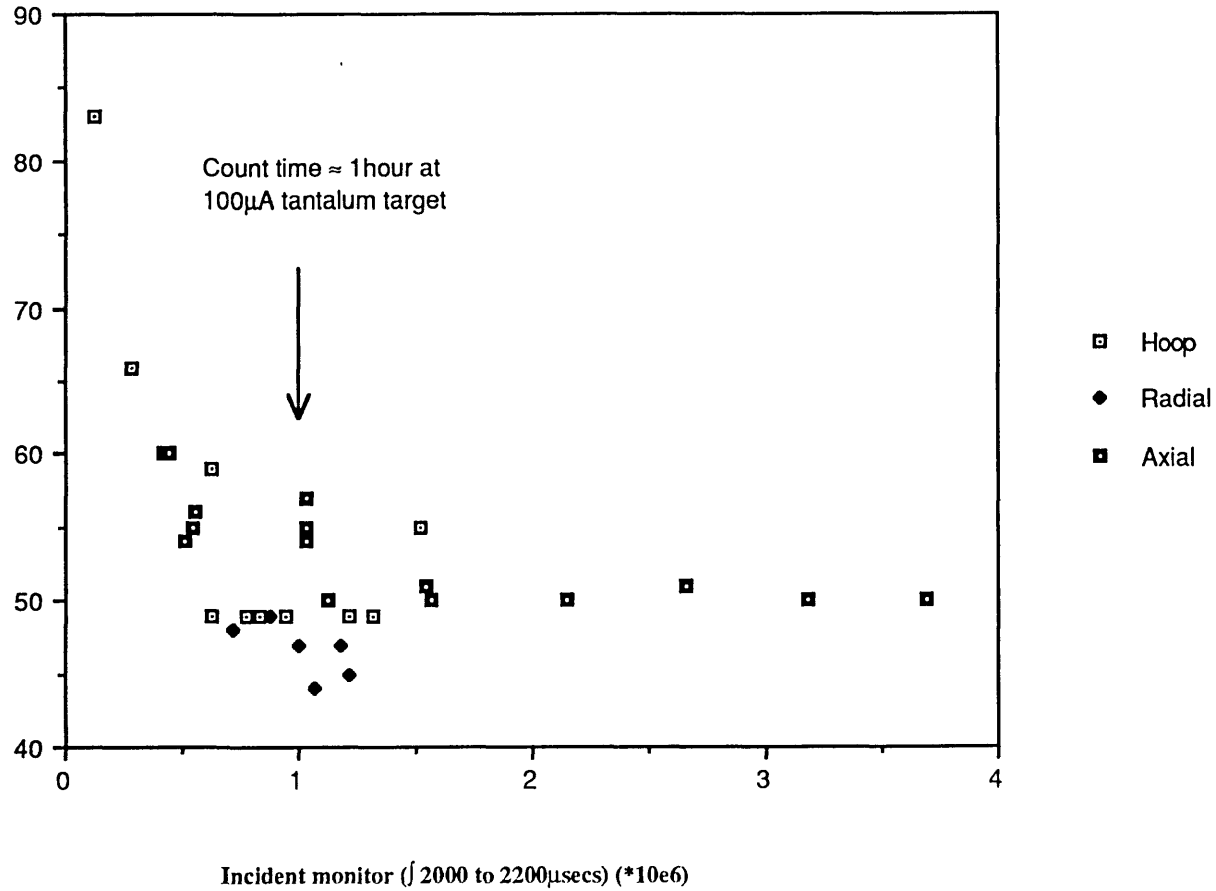


Figure 8.16: Lattice parameter-7RDMA assuming constant calibration factor on POLARIS

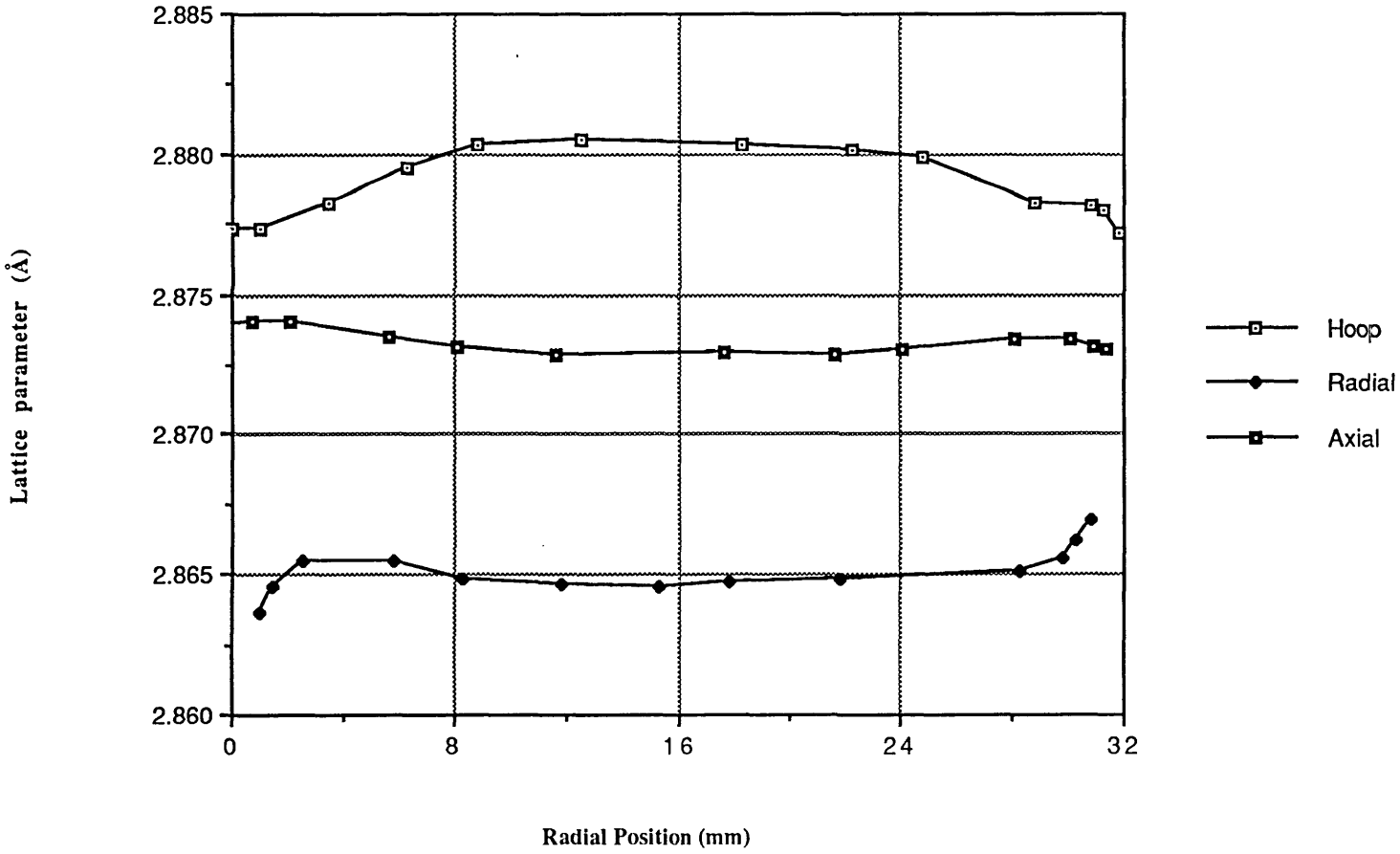


Figure 8.17a: Hoop strain in uncracked side of 7RDMA POLARIS by lattice parameter and D1A by (211)

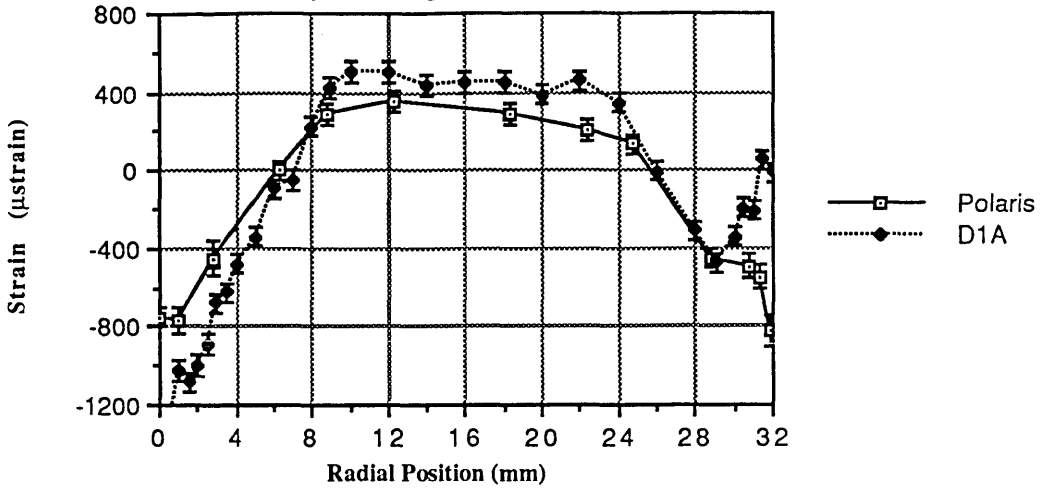


Figure 8.17b: Radial strain uncracked side of 7RDMA POLARIS by lattice parameter and D1A by (211)

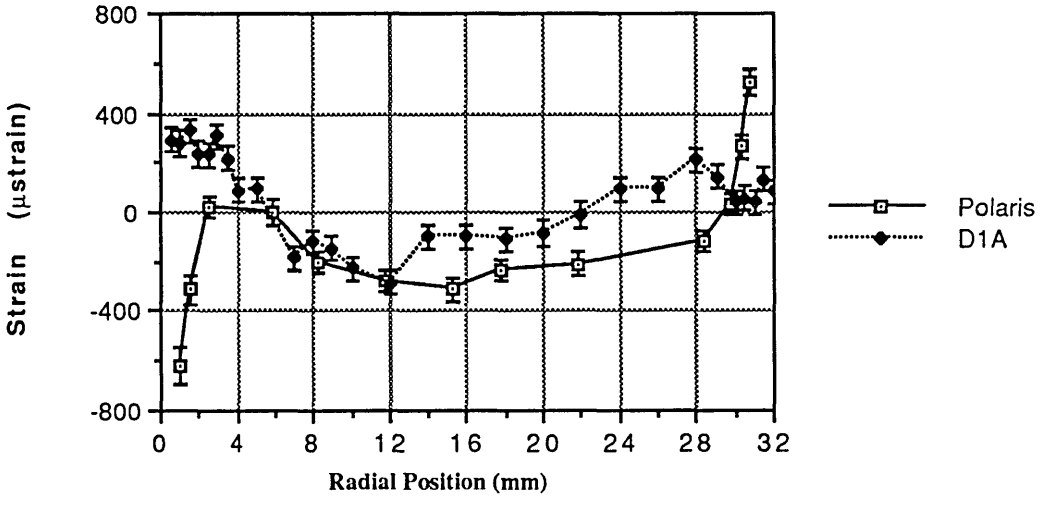


Figure 8.17c: Axial strain uncracked side of 7RDMA POLARIS by lattice parameter and D1A by (211)

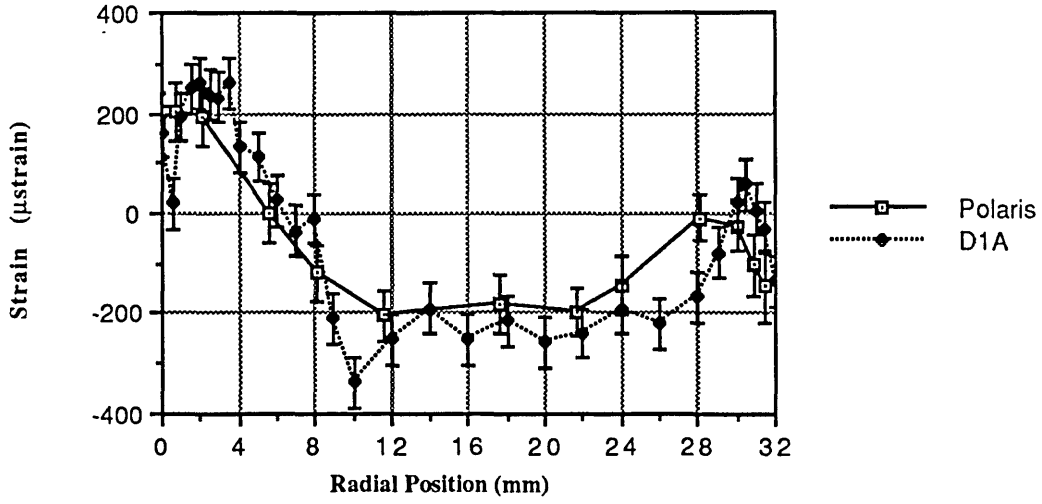
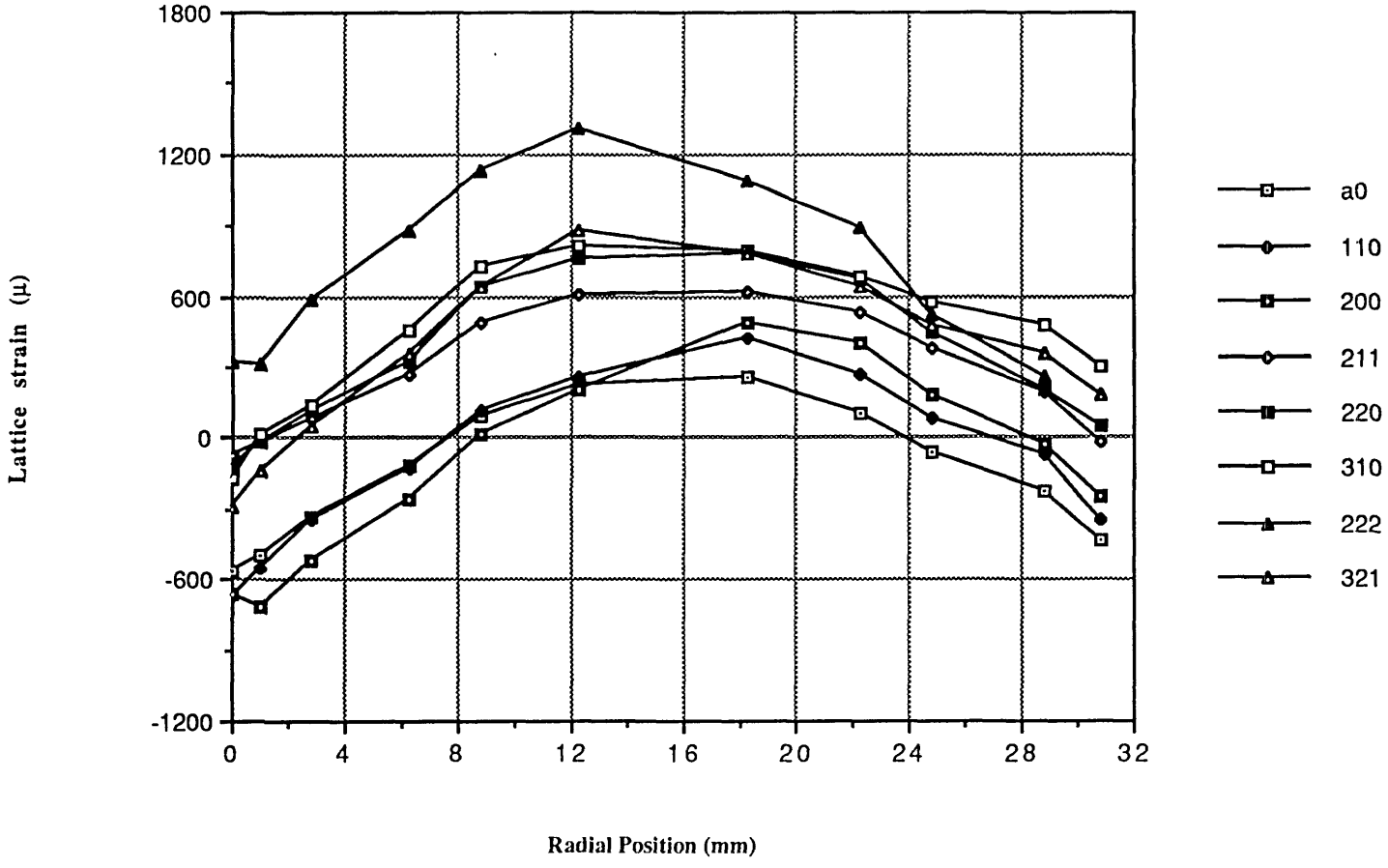


Figure 8.18: Smoothed hoop strain profiles for individual lattice reflections measured on uncracked side of 7RDMA on POLARIS



CHAPTER 9

Additional Measurements

9.1 Introduction

Additional experimental measurements are presented for two specimens of general interest with implications to the neutron technique and fracture mechanics. Surface stresses can change rapidly over distances that are small compared to the equivalent dimension of the sampling volume used in a neutron diffraction measurement. Measurements were successfully obtained from the surface of a shot-peened plate by moving the specimen into the sampling volume in small steps. Positional corrections are described to account for the partial immersion of the sampling volume. Good correlation with stress measurements made using the X-ray diffraction technique was achieved.

The introduction of tensile stresses by compressive loading is often overlooked and cyclic compressive loading can be associated with fatigue crack growth. A study of the stress distribution in a precompressed compact tension specimen is presented which demonstrates this effect.

9.2 Measurements in a shot-peened plate

9.2.1 Shot-peening

Peening is a surface treatment which can improve the total fatigue lifetimes of components and which usually, but not always, inhibits surface crack initiation (Mutoh, 1987). It is also beneficial in restricting stress corrosion cracking and intergranular corrosion (Tyler, 1987). The process is a cold working technique in which a surface layer is deformed by a high power jet of closely sized spherical particles. Plasticity in the surface induces a compressive residual stress parallel to the deformed region which can be an appreciable fraction of the yield stress. The deformation and stress reduces with depth into the material and the surface stress is balanced by internal tension. Parameters affecting the stress distribution were noted in chapter 1, section 1.3. The primary issues for comparison of different peening processes are the magnitude and

position of the maximum stress and its reduction with depth from the surface.

Two models describe the production of peening stresses; Hertzian pressure or direct plastic elongation of the surface (Wohlfahrt, 1982). The former is based on an elastic analysis of a round ball pressed on a flat sample, for which the maximum shear stress occurs below the surface. The latter assumes maximum deformation and thus maximum stress occurs at the surface. The relative importance of the two processes is determined by the respective hardness of the shot and workpiece.

9.2.2 Experimental results

Neutron diffraction measurements were made on an an aluminium shot peened sample as part of a test programme for the BSSM Residual Stress Technical Group for comparing measuring techniques (MacGillivray, 1987). The specimen was a plate 75mm square by 10.6mm thick. The specifications and treatment are given in table 9.1. Both major faces were peened to the same intensity. The peening was assumed to produce a uniform surface stress and a matchstick sampling volume geometry was employed (fig 9.1). A 20mm x 1.5 mm input aperture was used with a 2mm exit mask The specimen was moved through the sampling volume with the long dimension parallel to the surface. The extended sampling volume increased the diffracted intensity without compromising the spatial resolution which was significant because of the weak scattering of aluminium.

Shot peening produces a steep stress gradient and changes in strain were observed as the sampling volume progressively penetrated the material. Changes occurred over a distance smaller than the equivalent depth of the sampling volume, and the position of measurements were corrected for the progressive immersion of the sampling volume in the surface (fig 9.2). The dimension AD is approximately 2mm and the peening effect is substantially reduced before complete immersion has taken place. In figure 9.2b the sampling volume is half buried in the surface and neutrons are diffracted from the triangle FHI. Due to the triangular shape the measurement is weighted towards the surface away from point I. The corrected position corresponds to the centre of gravity of the shaded region and lies on line GI, at a point indicated by the arrow. In figure 9.2c immersion is complete and the the measurement is plotted at the

intersection of JM and KL. Before correcting the measurement positions, diffracted intensity was recorded at a distance of 0.5AD beyond each surface.

Strains were measured normal (Z) to the surface and for one in-plane (X) direction (the X and Y strains were assumed to be identical). In plan view the orientation for the measurements normal to and perpendicular to the surface are indicated in figures 4.9ab. Aluminium is face centered cubic and the (311) Bragg reflection was used at a wavelength of 1.905Å giving a scattering angle of 102.85°2θ. Measurements were made at a series of through-thickness positions with emphasis placed on the first millimeter below the surface where measurements were made in steps of 0.1 mm. In the interior of the sample 1mm steps were used. The measuring positions are illustrated in figure 9.3. All measurements lay on the dotted line normal to the peened surfaces, however for clarity the rectangles corresponding to the sampling volume are displaced vertically.

Measurements were made at the centre of the plate to avoid edge effects. Near the surface long count times were needed to ensure adequate statistics. Detailed examination was made of one face (A) and the traverses did not completely emerge from the back face (B). The peak centres are given in figure 9.4. θ_0 was determined by assuming a mirror image of the X stresses on the front and back faces and invoking axial equilibrium across the measurement plane. The principal axes were assumed to coincide with the X,Y and Z directions. Aluminium shows little strain anisotropy for different lattice reflections hence the bulk elastic modulus of ≈69GPa was used to convert from strain to stress. The stresses are given in figure 9.5.

X-ray measurements were made on the same sample using Phillips equipment at Rolls Royce, Derby (table 9.2). Surface stresses were measured in the X and Y directions on both peened faces using copper Kα and chromium Kα radiation. The intensity of X radiation in a material decreases exponentially with depth from the surface. By using X-rays of different wavelengths the attenuation coefficient and thus the penetration depth can be varied. Chromium Kα is less penetrating and approximately 95% of the radiation is diffracted within 27 microns of the surface. The equivalent value for Copper Kα is 84 microns. Neutron measurements for the first

millimeter are shown in figure 9.6 with an average of the X and Y stresses for side A, plotted at half the 95% diffraction limit. No allowance was made for the inherent variation in penetration depth due to the variation in angle of incidence during a single X-ray stress measurement.

Table 9.1: Material properties of shot-peened plate

Material	Aluminium alloy, 7071
Nominal Composition	4.5% Zinc, 2.5% Magnesium
Dimensions	75mm x 75mm x10.6mm
Heat Treatment	T651 aged beyond peak strength
Young's Modulus (E)	69GPa
0.2% Proof Stress	460MPa
Elongation at Fracture	12%
Poisson's Ratio (υ)	0.3
Peening Conditions	S 110 shot
Intensity	.008" - .012"
Coverage	125%

Table 9.2: X-ray stress measurement on peened sample

	Face A	Face B
Chromium Kα Radiation:		
X direction	-78	-94
Y direction	-81	-98
Copper Kα Radiation:		
	X direction	-107
-126		
Y direction	-112	-128

units of stress MPa

9.2.3 Discussion of measurements on peened plate

With the assumption that the stresses in the X and Y directions are equal and with θ_0 chosen to satisfy equilibrium, figure 9.5 indicates that the stress perpendicular to the surface, σ_z at side A is approximately zero as is required at a free surface. This provides an independent check of θ_0 Figure 9.6 shows that compressive residual stresses developed by the peening process are limited to a depth of about 0.5mm. The shallowest stress measurement corresponds 0.1mm below the surface and a compressive stress of 96MPa which is about 20% of yield.

The X-ray results confirmed the assumption that the X and Y strains in the plane of the plate are equal. Also, the stresses obtained with the more penetrating chromium radiation are in good agreement with the neutron measurements. The more shallowly penetrating copper radiation suggest the existence of a plateau in the stress distribution within 100 microns of the surface. This may reflect stress state effects or possibly reverse yielding at the surface.

These measurements are not comprehensive and refinement to improve resolution near the surface is possible. By adopting a glancing angle geometry and measuring the strain at an angle to the surface a dramatic improvement in resolution could be obtained. This could give an overlap between neutron and X-ray measurements which has not previously been possible. During the measurements some evidence of preferred orientation was noted and is reported elsewhere (Bourke, 1987). Micro hardness tests and polishing/etching processes could be used in understanding the nature of the texture variation through the material.

9.3 Compact tension specimen

9.3.1 Introduction

Compressive overload of a notched component can introduce a tensile residual stress at the notch root, in a process similar to but in the opposite sense to that described in chapter 6. The effect occurs when a crack or notch is originally open permitting localised compressive yield to occur. Subsequent compressive loading cycles may cause propagation of fatigue cracks from the root until they emerge from the tensile

stress field (Hermann, 1986). This is significant since cyclic compressive loading is often assumed to pose no risk for fatigue crack growth. Even the first cycle of a mild compressive fatigue cycle can act as a precompression. Sub-critical crack growth under cyclic compressive loading conditions can be correlated with the magnitude and extent of the residual stress field produced by overloading. The crack propagates through and sometimes beyond the original tensile region until the tensile residual stress is relaxed. In collaboration with Dr R. Hermann of the Open University an experimental examination was made of residual stress in an overstressed sample.

9.3.2 Experimental results

A mild steel compact tension specimen was machined according to the British Standards specification BS5447. The material properties are given in table 9.3. The line of the notch lay perpendicular to the rolling plane of the bar from which the specimen was removed. Prior to examination or precompression sub-critical annealing was applied for 1 hour at 600°C. The crystal structure was equiaxed ferritic with an average grain diameter of 40μm. A compressive overload of -55kN was applied by static loading using a servohydraulic machine. Material near the notch was deformed in compression and when the preload was removed a tensile stress was induced in the plastic zone. A slice of thickness 4.65mm was removed for neutron measurements and is illustrated in figure 9.7.

Strains were measured at 18 locations, coplanar with the notch and centered on the plane of central thickness. At each position the lattice strains in the X,Y and Z orientations, corresponding to the assumed principal stress directions, were obtained. The steel (211) reflection was employed with an $8mm^3$ sampling volume. Peak heights were in the range of 400 to 700. θ_0 was measured on a small nominally stress-free cube of the same material but was also calculated by assuming axial and moment equilibrium across the measuring plane. The values predicted for θ_0 by axial or moment equilibrium altered the stresses by less than 2MPa. The difference between the equilibrium checks and the stress-free cube implied a change in the stresses of approximately 8 MPa which is within the experimental error of $\pm$ 10MPa. All results were calculated using a θ_0 for axial equilibrium.

The X,Y and Z strains are plotted in figure 9.8. Correction for the partial immersion of the sampling volume has not been included and, strictly, the measurements at X=0 and X=27mm should be plotted at X=0.5 and 26.5mm respectively. The experimental errors for the Y strain are not visible on the scale used. By assuming that the X,Y and Z directions are the principle stress directions, and using 207 GPa for Young's modulus and 0.29 for Poisson's ratio the stresses were calculated (fig 9.9).

Table 9.3: Material properties - compact tension specimen

Material	:Mild steel BS 970,070 M20
Compressive preload	:-55 kN (B=25mm)
60° V notch profile	:0.1mm radius at the tip
Composition (wt%)	:C 0.16, Si 0.05, Mn 0.81.
Properties	
Tensile strength	: 460MPa
Yield strength	: 320MPa
Elongation	: 35%
Young's modulus	: 210 GPa
Poisson's ratio : 0.29	

9.3.3 Discussion

Favourable specimen dimensions gave strain accuracy of $\pm$ 30 μstrain for count times between 10 and 20 minutes for each measurement. The smooth strain profiles reflect the quality of the data. At the notch tip the tensile stress in the Y direction is 280MPa which is close to the yield stress. This falls to zero within 4mm and achieves a maximum compressive value of 200MPa 8mm from the notch. A second tensile region with a peak value of 100MPa is visible at X=22mm close to the outer edge. At the notch tip the X stress shows an anomalous value of 50MPa normal to the surface. This can be attributed to the finite sampling volume around the notch tip. At the opposite end (X=27mm) where the sampling volume emerges from a flat face, the X stress falls to

zero as it must at a free surface. The sample thickness was only 4.65mm and the Z stress remains close to zero except near the notch.

Conventional measurements on similarly treated specimens, made by observing the relaxation caused by spark erosion on the back face, gave excellent agreement with the results quoted above (Reid, 1990). Cyclic compression tests demonstrated that fatigue cracks propagated through the ligament of similarly precompressed specimens. In some cases the crack arrested at distances beyond the original tensile stress region which suggests that some stress redistribution is caused during the passage of the crack. One interesting feature observed during cyclic loading tests concerned the shape of the cracks which were longer at the surface than in the interior (Reid, 1989). This is consistent with the assumption that the plastic zone is larger at the surface due to reduced constraint and is pertinent to the neutron measurements which are made on a slice one fifth of the original thickness of the compact tension specimen.

9.4 Conclusions

Measurements of the stress distribution produced by shot peening demonstrated that stress variations changing over distances small compared to the sampling volume can be measured by neutron diffraction to an accuracy of $\pm$ 10MPa. A maximum compressive stress of -96MPa was recorded 0.1mm below the surface of an aluminium plate. X-ray measurements at the same position yielded a value of -110MPa although they originated from approximately half the depth of the neutron measurement. The neutron measurements did not show any evidence of a stress plateau beyond 0.1mm from the surface.

The stress distribution was measured in a standard compact compact tension specimen which had been subjected to a precompression sufficient to produce plastic deformation at the root of the notch. A maximum tensile residual stress of 280MPa was caused by the application of a -55kN compressive overload. The tensile stress reduced to zero 4mm from the notch which corresponds to approximately 14% of the surviving ligament.

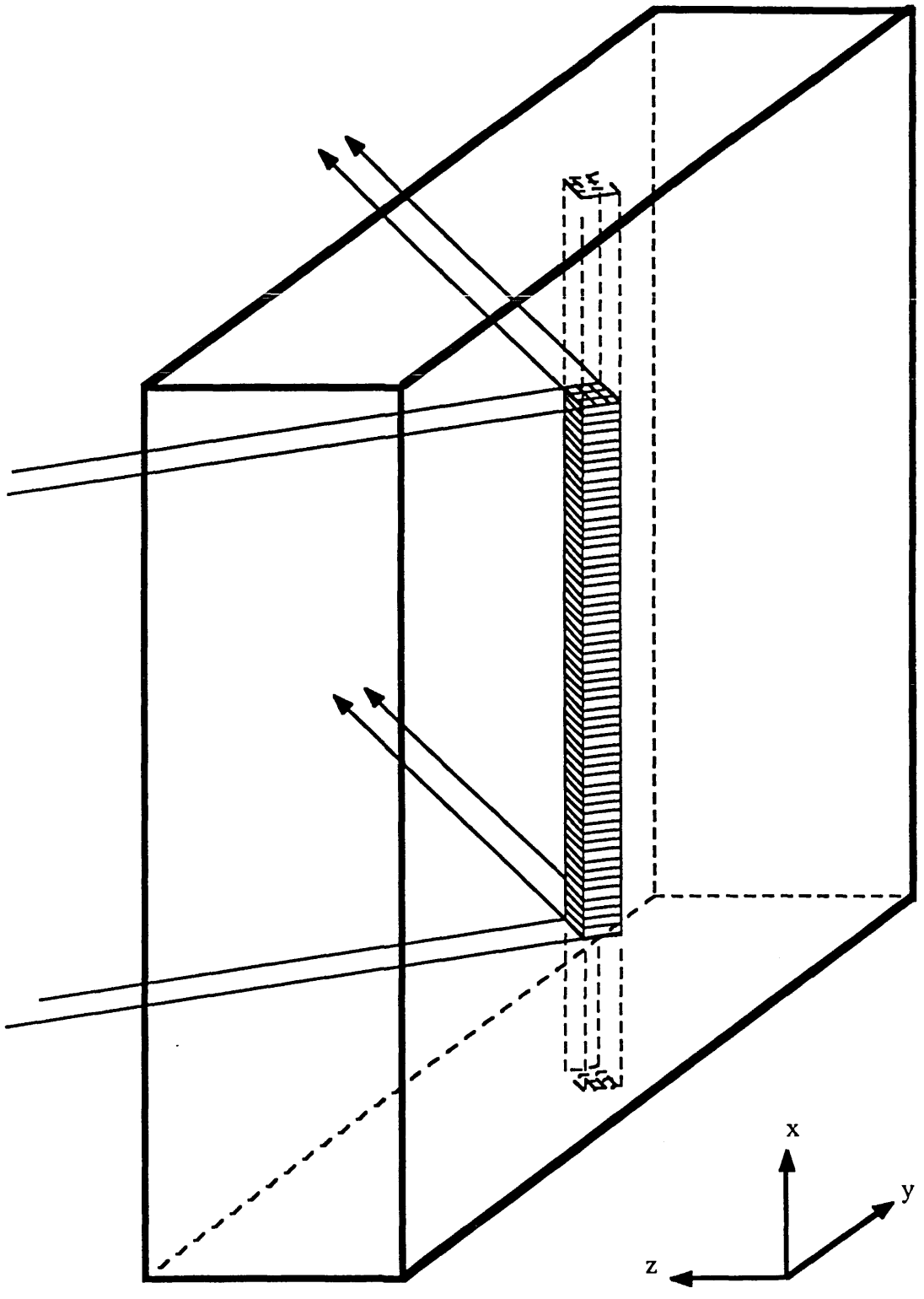
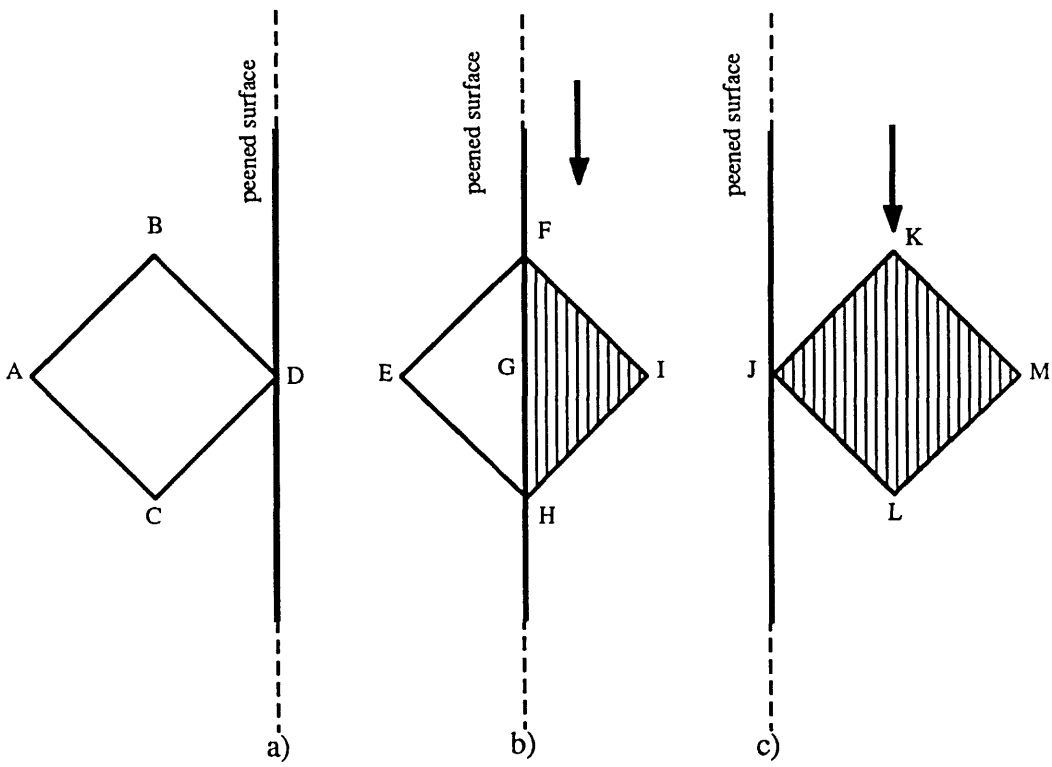


Figure 9.1: Sampling volume for strain measurement normal to the peened surface



[N.B. in reality plan view of sampling volume is a parallelogram]

Figure 9.2: Plan view of progressive immersion of sampling volume

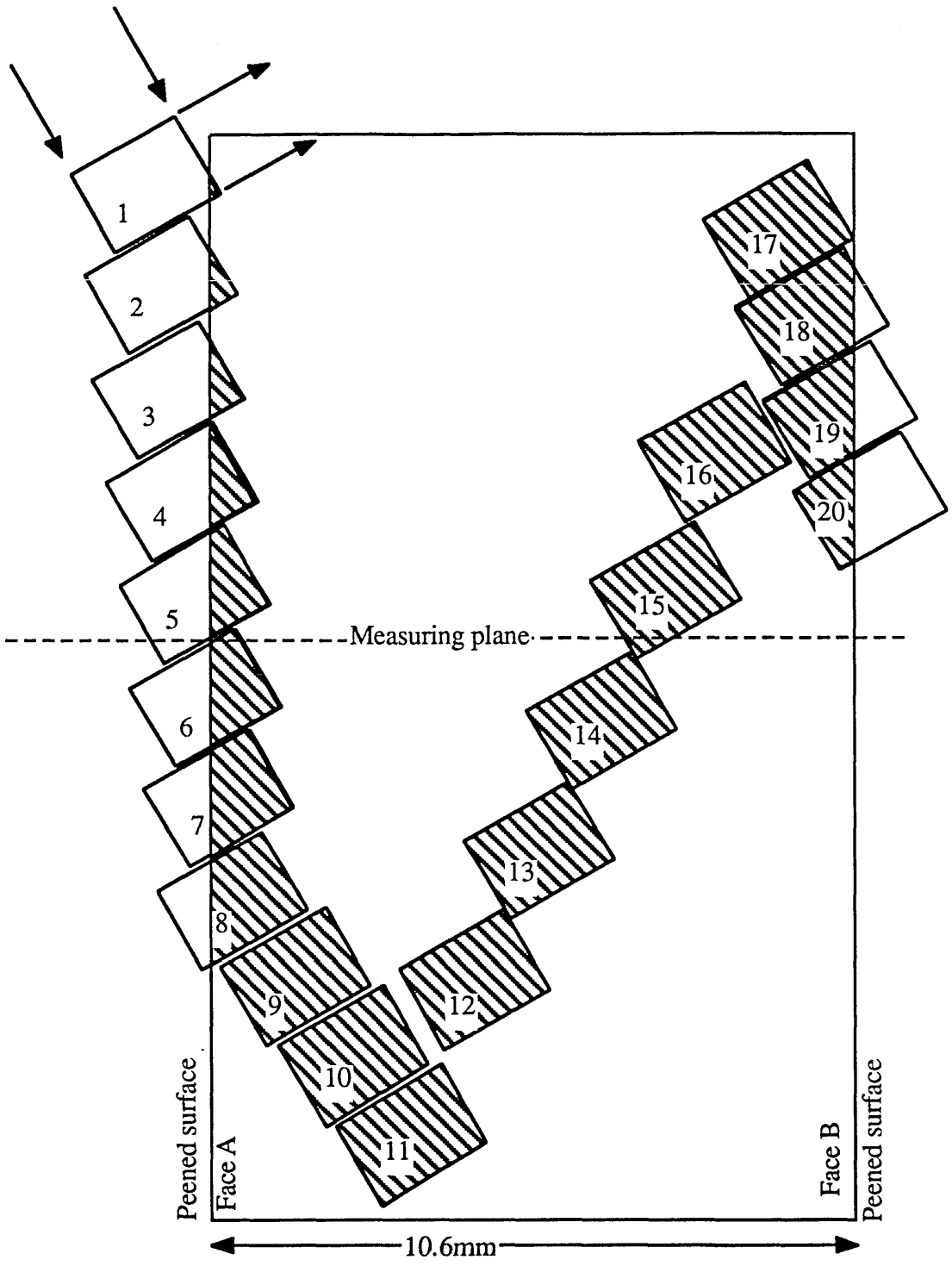


Figure 9.3: Measuring positions in peened plate

Figure 9.4: Peened plate diffraction peak centers

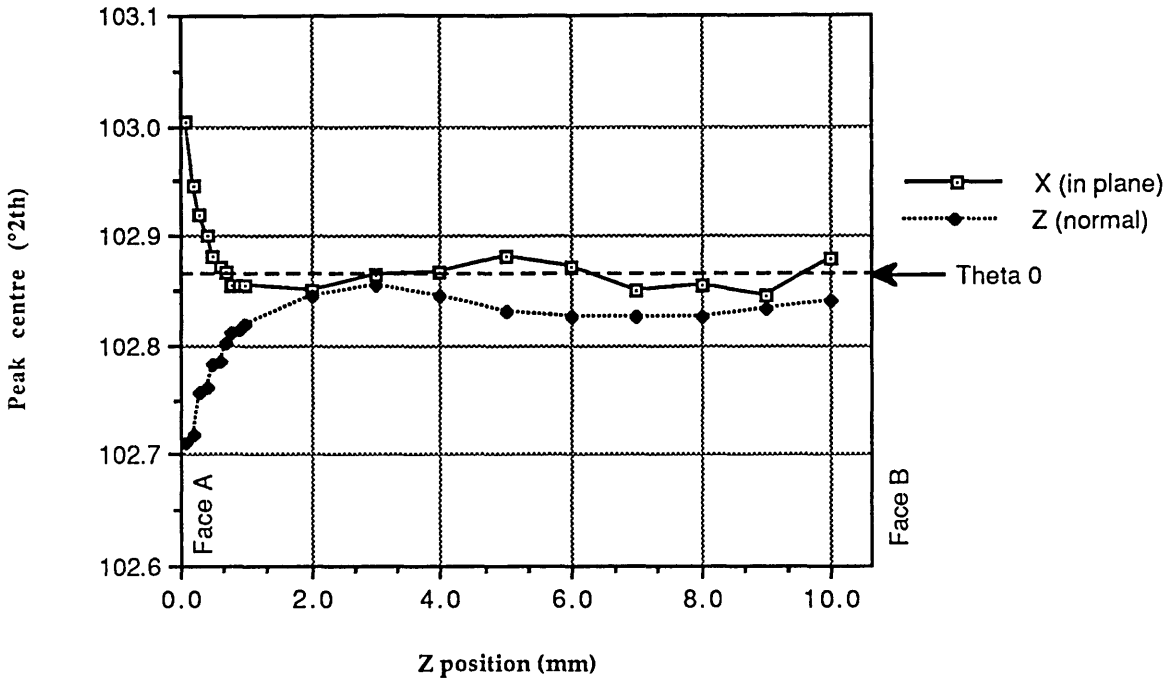


Figure 9.5: Peened plate stresses

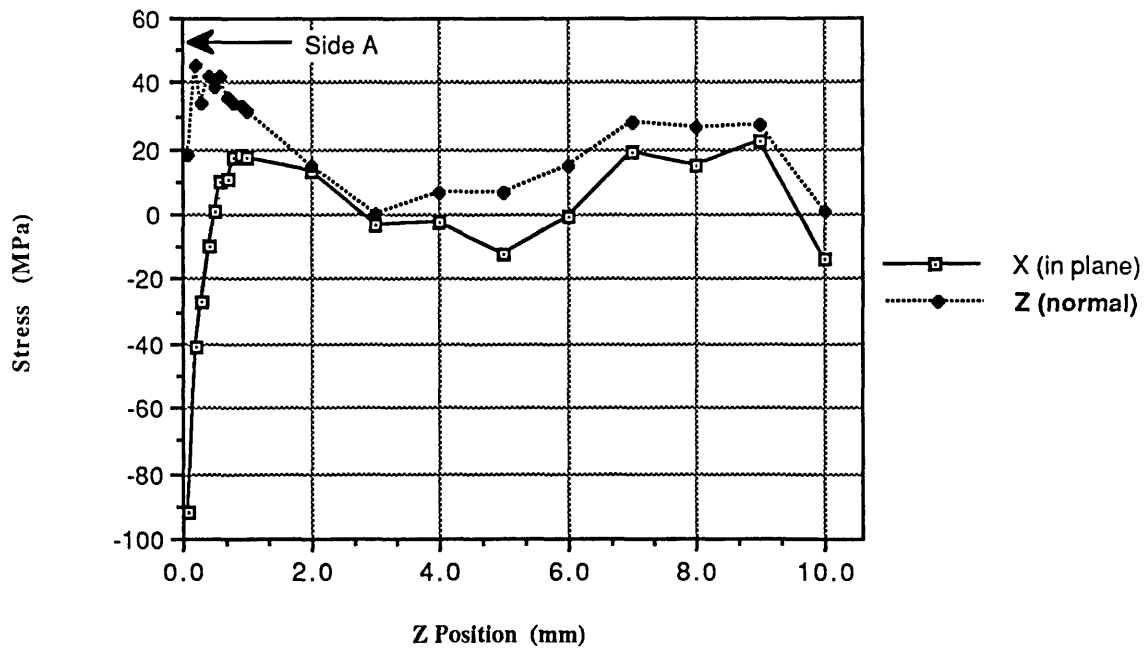
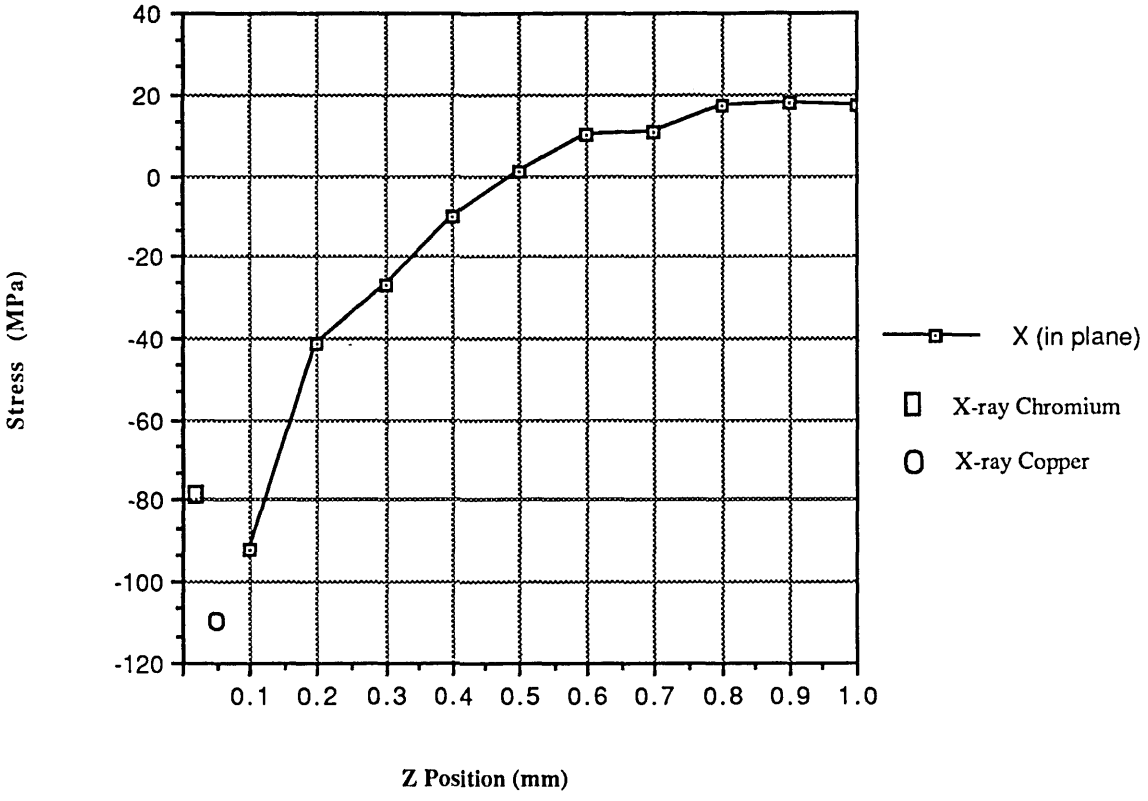
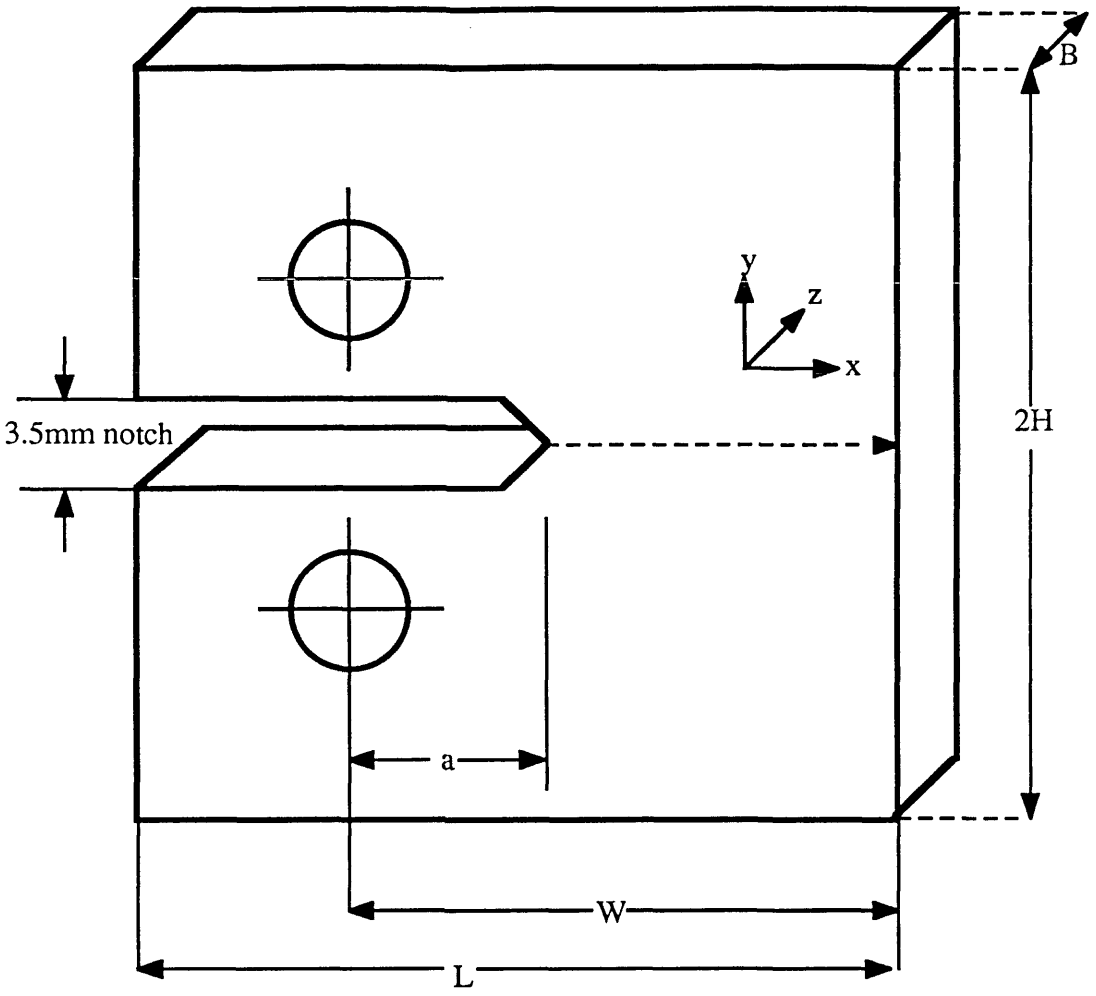


Figure 9.6: Near surface stress in a peened plate by X-rays and neutrons





L = 63mm
W = 50mm
a = 23mm

2H = 60mm
B = 4.65mm (original 25mm)
a/W = 0.46

Figure 9.7: Slice from compact tension specimen

Figure 9.8a: Precompressed C.T.S. , X strain

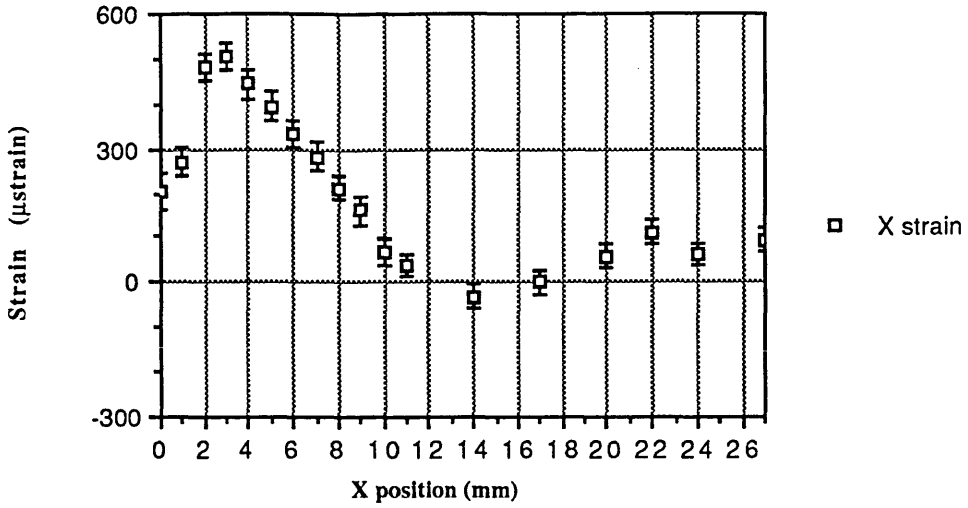


Figure 9.8b: Precompressed C.T.S. , Y strain

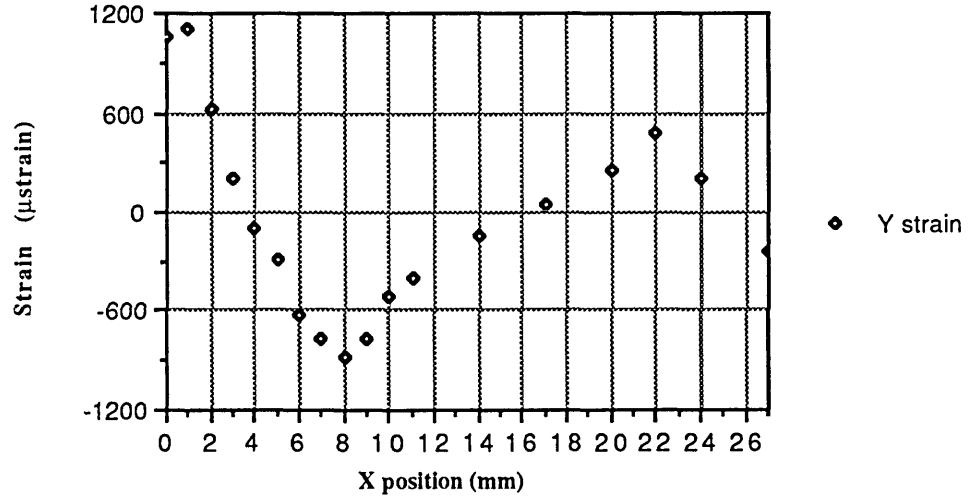


Figure 9.8c: Precompressed C.T.S. , Z strain

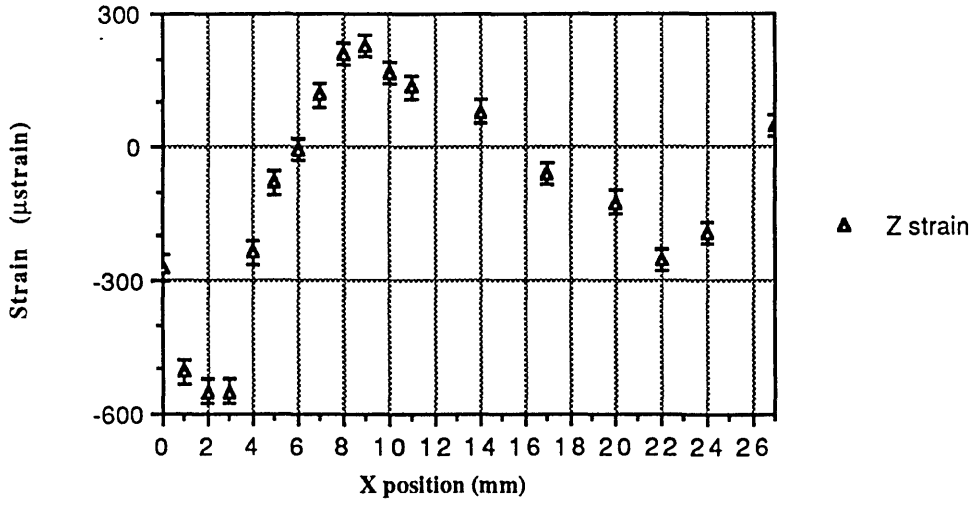
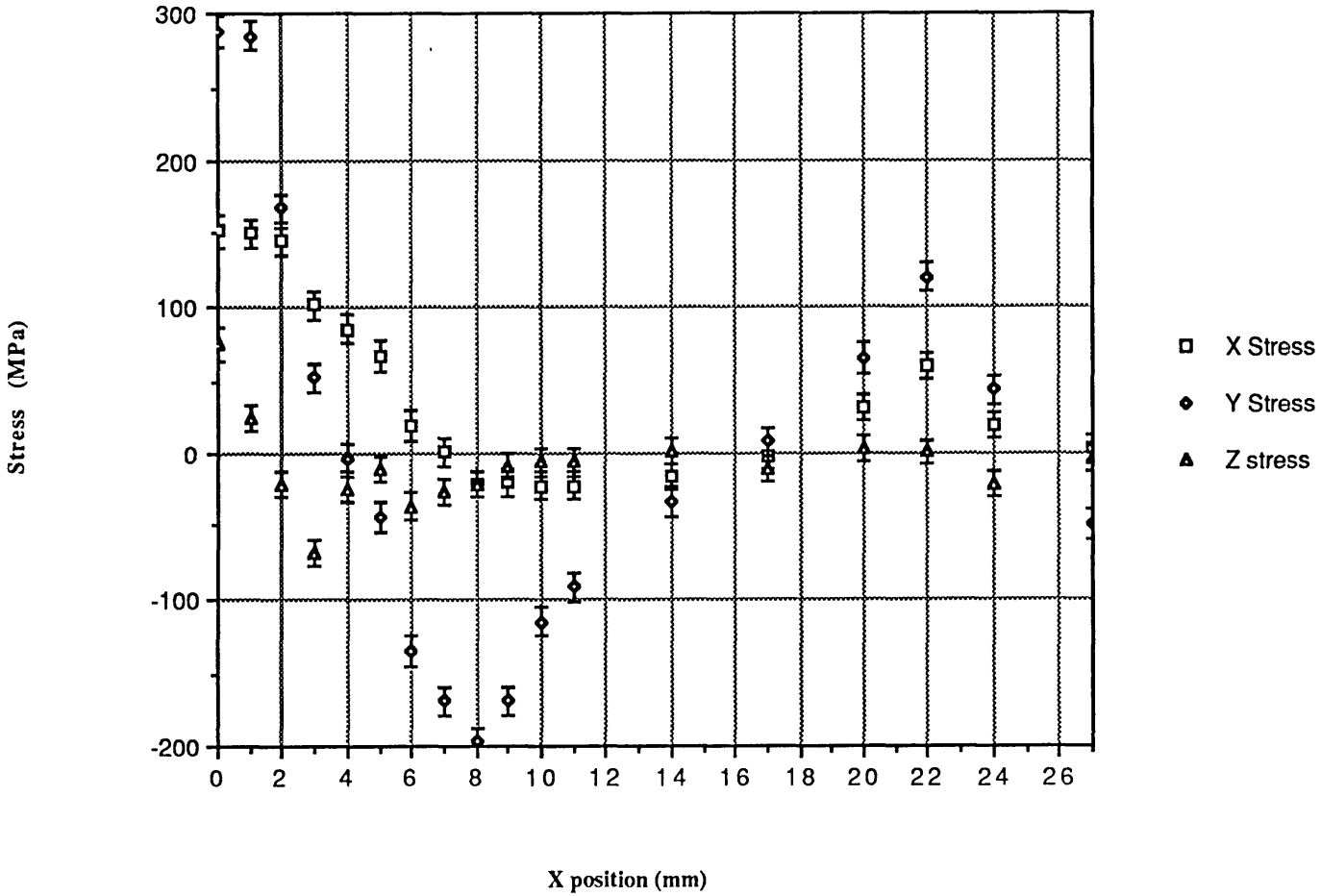


Figure 9.9: Stress in precompressed C.T. specimen



CHAPTER 10

Concluding remarks

10.1 General discussion

Many neutron measurements were initially limited to linear scans. However increasingly measurements are made on plane profiles. For example, strains recorded over a two dimensional array in the head of a transverse rail slice were described in chapter 7. Portraying data over two dimensions is facilitated by presentation techniques such as contour plotting or three dimensional perspective images. In figure 10.1 a colour contour plot shows the post-service transverse stress measured in a rail head. Alternatively in figure 10.2 a three dimensional perspective shows the stress near the edges of a peened plate. Improved efficiency on D1A and the higher neutron flux available on instruments such as D20 can generate many measurements in short periods and rapid assessment and presentation of the results is becoming increasingly important. In future, ideally all the parameters associated with each measurement, such as position, width, intensity etc will be transferred directly into programs capable of portraying them in different formats.

One issue which has been consistently neglected concerns the determination of an unstrained reference angle. When force or moment balance is assumed across a plane section an unambiguous determination of θ_0 is possible but in many cases measurements are not possible on plane sections. The physical constraint in which the stress normal to a surface must be zero is rarely an option for determining θ_0 since surface measurements involve low intensities are often complicated by steep stress gradients and can be unrepresentative of the bulk material. θ_0 values are usually measured in specimens which are less than $1cm^3$ and are small enough to be considered free of stress for an engineering analysis. In practice small specimens often show strains in different directions which exceed the experimental error and which compromise the measurements by giving an uncertainty in the absolute magnitude of the stresses. This is a problem when measuring small strains.

One possibility for examination is the variation of θ_0 associated with

microstructural changes. In homogeneous or low alloy materials the assumption of constant θ_0 throughout the material is reasonable. However in multiphase material this is less evident. Processes such as carburization can produce a gradient in the carbon content from the surface which may be associated with a change in θ_0. The efficacity of annealing for stress relief and the validity of using stress relieved measurements as strain free reference angles to non-stress relieved specimens must be examined. A standard and reliable technique for measuring θ_0 is urgently needed. Possibilities include; stress relief of a small sample, "tumbling" a sample during a measurement to average out any residual effects or measuring a powder removed from the specimen.

Recently there has been considerable interest in the possibility of installing an instrument for engineering strain measurement at a neutron source. The two features which most hamper strain measurement on conventional diffractometers or spectrometers are shortage of space and difficult definition of the incident beam. Since the manipulation, collimation and optical alignment systems are dismantled after each experiment, which may only last between 2 and 10 days, the set-up process must be repeated for each experiment. A dedicated instrument, probably with a position sensitive detector would offer many advantages including saving in time. Measurements on D20 and POLARIS have proved that in most cases the limiting feature for engineering strain measurements is neutron flux not instrumental resolution.

10.2 Recommendations for further work

Outstanding issues in the development of D1A include the sensitivity of stress measurement to differences in the sampling volume for coincident strain measurements in different directions. Diffraction through angles other than 90° produce sampling volumes which in plan view are parallelograms and as the specimen is rotated the actual material sampled is altered. Procedures must also be established for making measurements when the principal stress directions are unknown and linked to the data processing methods to give real-time analysis. Count times must be linked to required accuracy of measurement and confidence limits. In view of the repeated alignment procedure and the possible errors a reference sample could be adopted for examination at the start of each experiment. This would provide a comparison for results obtained on

different occasions.

The main hardware feature which requires development on D1A is the exit collimation system. Currently in most experiments a single exit slit is installed in front of one detector since this is sufficient for the measurement. Installing further slits is time consuming. However with improved design, exit slits could be installed in front of other detectors without unduly compromising the measuring time. This would permit extra strain information to be recorded from other lattice reflections for typically small increases in the scan range.

The development of POLARIS is less advanced than D1A. Measurements have demonstrated the potential of time of flight measurement and the ability to collect strain information for all lattice directions in each measurement. Before POLARIS can be used to examine the interior of thick components collimation of the diffracted beam is required. Limited access around the sampling volume impede the sample manipulation and it is hoped that the vacuum tank can be removed for subsequent measurements. Profile refinement of the spectra obtained on the POLARIS 90° detector gave excellent strain results for a thin autofrettaged ring. The count times to obtain similar accuracies appeared to be longer than on D1A but were not assessed in detail. A study should be performed to relate the accuracy specified for the lattice parameter by profile refinement to the count time. This is likely to show that shorter count times could be used, making POLARIS more competitive with D1A. However the issue of determining a value for t_0 must be addressed in particular its sensitivity to the path length to the sampling volume.

General areas of research suggested by the work recorded in this thesis are listed below. The cold expanded bolt hole and the shape of cracks in fatigue loaded compact tension specimens indicate that through thickness scans of thick deformed components might yield information concerning the shape and size of the plastic zone. By examining a specimen with a large plastic zone at a crack tip it may also be possible to resolve the residual stress in the plastic zone. The cracked autofrettaged ring containing a fatigue crack through half the wall thickness demonstrated an unexpected compressive stress along the part of the crack face which originally contained tensile residual stress. This may be related to the presence of the plastic wake and could be

examined by making measurements normal to the crack plane.

More research is needed concerning the nature of slip processes in polycrystals. Using a stress or bending rig measurements could be made near the bulk yield stress to assess the effects on different lattice directions. Alternatively by deforming larger components in the neutron beam localised areas of plastic strain could be identified. In-situ measurements of creep and fatigue processes could also be made at elevated temperatures or pressures for which examination by neutrons is particularly suited. Finally measuring procedures for coarse grained materials need to be established.

10.3 Overall conclusions

Neutron diffraction has been demonstrated as a specialist tool for non-destructive measurement of applied or residual macro stresses in the interior of isotropic or anisotropic crystalline materials. Although the limited number of neutron sources precludes its use for routine applications it is suited for calibration purposes or examinations for which conventional measurements are inconvenient. Measurements can be made and the specimen is still available for further testing. Strains are obtained without layer removal thus the technique is not vulnerable to plastic deformation during removal which introduce errors in conventional strain gauge measurements. For larger components sectioning is necessary to reduce the specimen geometry to give acceptable neutron path lengths through the material. The largest path length used in steel was 35mm. On D1A sampling volumes of $8mm^3$ are routinely obtained and measurements have been made with dimensions in the sampling volume of 0.5mm.

Calibration measurements using a uniaxial tensile stress rig showed anisotropic strain response of crystalline materials for applied loads. The strain in individual grains is related to their alignment relative to the applied load and to the single crystal compliance of the specific lattice direction. The strains in a metal matrix composite under an applied load were also found to be anisotropic.

A collimation and manipulation system has been installed on D1A which gives precise spatial resolution of the sampling volume. Specimens can now be positioned to within 0.1mm of a fixed point in space. Five axis manipulation of samples is possible using a modular series of translation and rotation stages.

Measurements were made in regions containing steep stress gradients near fatigue cracks. Experimentally measured stresses showed agreement with finite element models of crack tip behaviour and with boundary element predictions.

At present measurements using pulsed neutrons on POLARIS are most useful for assessing heat treatments, coatings or for multiphase specimens in thin samples. Automated definition of the incident beam on POLARIS has been installed. Three dimensional manipulation of specimens in the sample tank is also possible. Profile refinement has proved an excellent alternative to measuring individual Bragg reflections for obtaining strain information in the crystalline lattice.

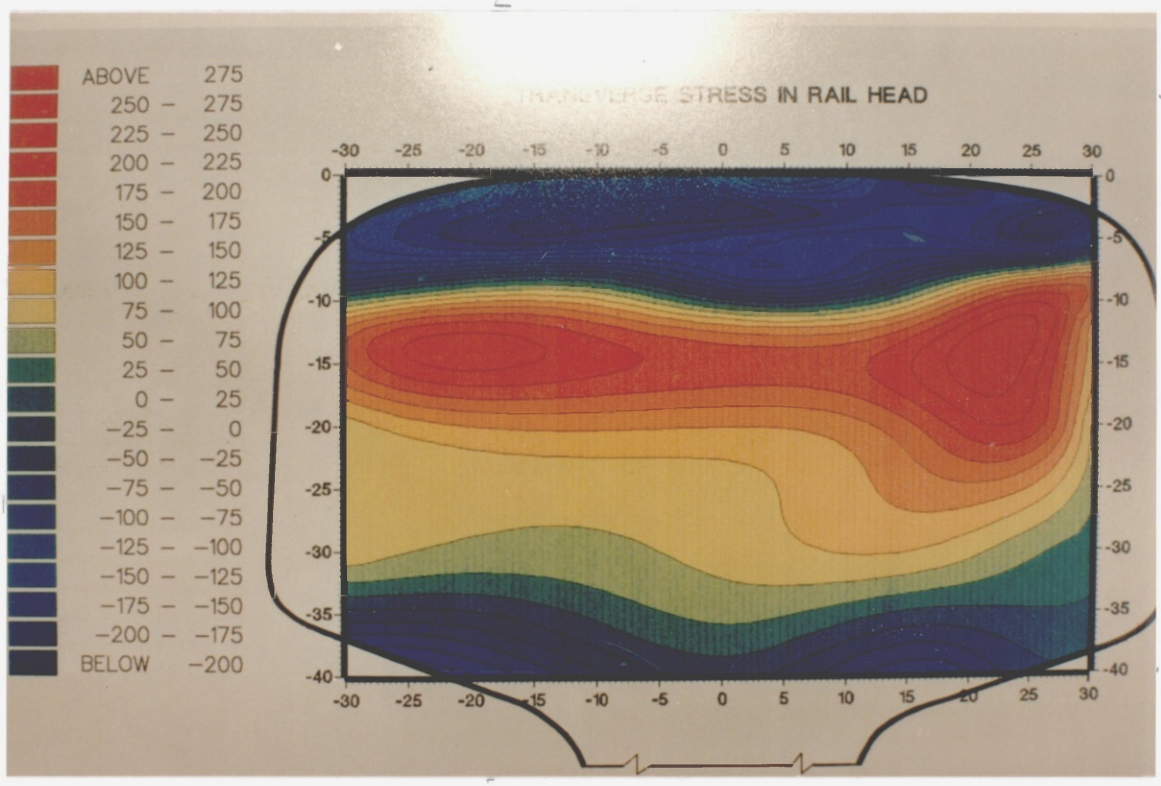


Figure 10.1: Contour plot of transverse stress produced near the surface of a rail head after service

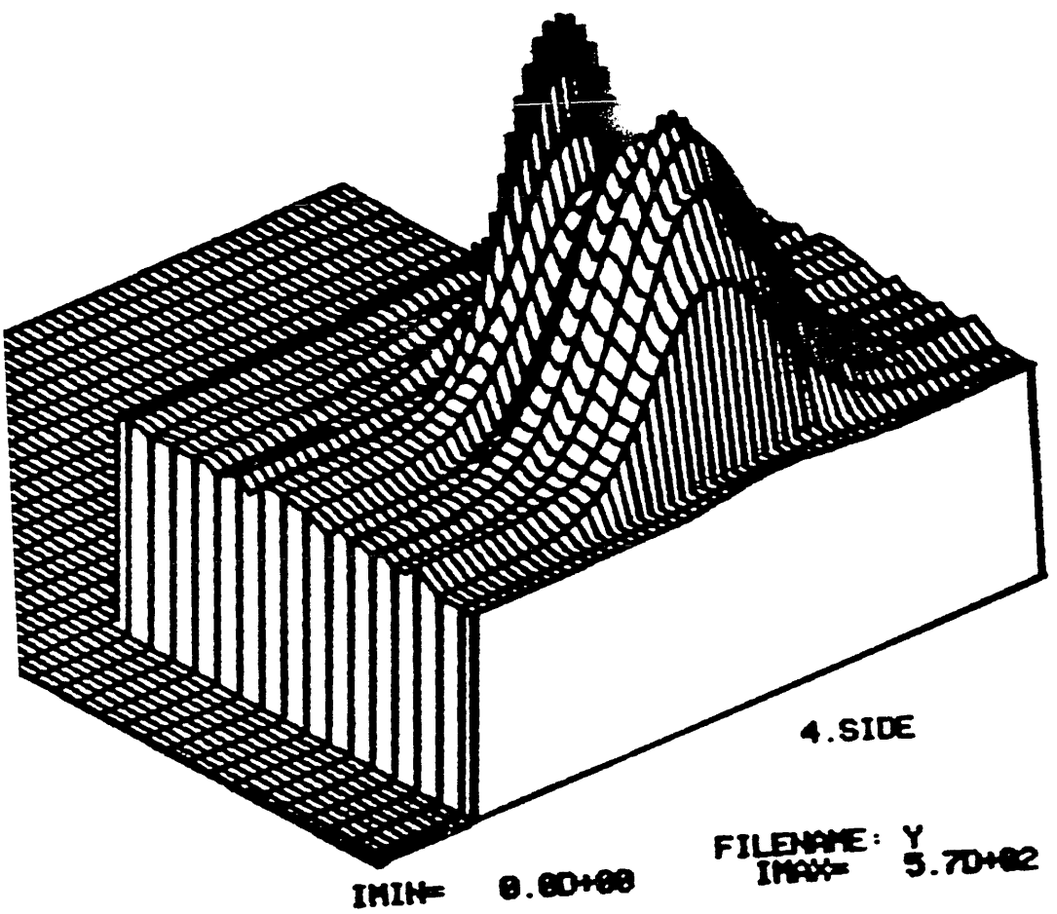


Figure 10.2: Three dimensional perspective of the stress near the edge of a peened plate

References

Allen, A.J., Hutchings, M.T., Windsor, C.G. & Andreani, C.
"Neutron diffraction methods for the study of residual stress fields",
Advances in physics, **1985**, Vol. 34, No4, 445-473.

Allen, A.J., Bourke, M.A.M., Hutchings, M.T., Krawitz, A.D. & Windsor,C.G.
"Neutron diffraction measurement of internal stress in bulk materials:- metal matrix composites",
Proceedings of the international conference on residual stresses, **1986**, Garmisch-Partenkirchen (FRG), 151-157.

Allen, A.J., Coleman, C.F., Conchie, S.J., Hutchings, M.T., & Smith, F.A.
"In the field NDT mapping of plastic damage in metal and alloy components using positron annihilation techniques and comparison with residual stresses",
AERE report, **1987**, MPD/NBS/331.

Allen, A.J., Bourke, M.A.M., Dawes, S., Hutchings, M.T. & Withers, P.J.
"The analysis of internal strains measured by neutron diffraction in Al/SiC metal matrix composites",
Submitted to Acta Met. **1990**.

Allen, R.J.
"Fatigue failures in rails"
B.R. Research / Chinese academy of railway sciences exchange meeting, **1988**, Beijing.

Bacon, G.E.
"Neutron diffraction",
2nd edition, **1962**, Oxford university press.

Beaney, E.M. & Proctor, E.
"Critical evaluation of the centre hole technique for the measurement of residual stresses"
Strain, **1974**, Vol 10, 7-15.

Becker, A.A. & Plant, R.C.A.
"Contact mechanics using the boundary element method"
Tribology conference, **1987**, Institute of mechanical engineers, C227/87, 975-980

Berns, H. & Weber, L.
"Fatigue crack growth in the presence of residual stresses"
Proceedings of the international conference on residual stresses, **1986**, Garmisch-Partenkirchen (FRG), 751-758.

Bourke, M.A.M., MacGillivray, H.J., Webster, G.A., Low, K. & Webster, P.J.
"Improving the resolution of neutron diffraction residual stress measurement in engineering components"
IITT , **1987**, International conference on fatigue and stress, Paris, France.

Bower, A.F.
"PhD Thesis"
1987, Cambridge.

Bynum, J.E.
"Modifications to the hole drilling technique of measuring residual stresses for improved accuracy and reproducability"
Experimental mechanics, Jan **1981**, 21- 33.

Cannon, D.F., Sinclair, J. & Sharpe, K.A.
"Improved fatigue performance of railway bolt holes by cold expansion"
A.S.M. conference proceedings, **1985**, "Fatigue life analysis and prediction", Utah, U.S.A.

Carpenter, J.M., Lander, G.H. & Windsor, C.G.
"Instrumentation at pulsed neutron sources",
Rev.Sci. Instrum., **1984**, 55 (7), 1019-1043.

Carpenter, J.M., & Yelon, W.B.
"Neutron sources",
Methods of experimental physics, **1986**, Vol 23, Part A, p99-p197.

Cheskis, H.P., & Heckel, R.W.
"Deformation behaviour of continuous-fiber metal-matrix composite materials",
Metallurgical transactions, **1970**, Vol 1, 1931-1942.

Clark, A.V. & Moulder, J.C.
"Ultrasonic determination of absolute stresses in aluminum and steel alloys",
Proceedings of the international conference on residual stresses, **1986**, Garmisch-Partenkirchen (FRG), 207-214.

David, W.I.F.
"Powder diffractometry",
Neutron scattering at a pulsed source, **1982**, Chapt 8, p189-232, Pbld by Adam Hilger.

Denton, A.A.
"Determination of residual stresses"
Metallurgical reviews, **1966**, Vol 11, 1-23.

Ericsson, T. & Hildenwall, B.
"Thermal and transformation stresses"
Sagamore army materials research conference proceedings, **1982**, Volume 28, 19-38.

Eshelby, J.D.
"The determination of the elastic field of an ellipsoidal inclusion, and related problems",
Proceedings of the royal society ,**1957**, Vol 241A, 376-396.

Ezeilo, A.

"Finite element analysis on rail slices"
1990, BRFE1, Unpublished research.

Fenner, R.T.

"The boundary integral equation (boundary element) method in engineering stress analysis"
"Journal of strain analysis, **1983**, Vol 18, No4, 199-205.

Fischer, F.D., Hinteregger, E, & Rammerstorfer, F.G.

"The cooling-down-process of hot-rolled railroad rails"
Published at the international seminar on the inelastic behaviour of solids, models and utilisation, August **1988**, Besancon, France.

Greenough, G.B.

"Residual lattice strains in plastically deformed polycrystalline metal aggregates",
Proceedings of the royal society A, **1949**, Vol 197, 556-567.

Greenough, G.B.

"Macroscopic surface stresses produced by plastic deformation",
Journal of the iron and steel institute, **1951**, Vol 169, 235-241.

Greenough, G.B.

"Quantitative X ray diffraction observations on strained metal aggregates",
Prog met Phys, **1952**, 176-219.

Groom, J.J.

"Determination of residual stresses in rails"
Final report to United States department of transport, **1979**, DOT-TSC-1426, Battelle Columbus Laboratories.

Harris, D.O.

"Stress corrosion crack growth in the presence of residual stresses"
Sagamore army materials research conference proceedings, **1982**, Volume 28, 273-295.

Hermann, R. & Reid, C.N.

"Slow crack growth in the presence of tensile residual stresses"
Proceedings of the international conference on residual stresses, **1986**, Garmisch-Partenkirchen (FRG), 759-766.

Honda, K., Sarai, T. & Hara,Y.

"Microscopic residual stress in metals deformed plastically under multiaxial stress",
JSME international journal, **1989**, Series 1, Vol 32, No 1, 128-135.

Hauk, V.M.

"X-ray methods for measuring residual stress"
Sagamore army materials research conference proceedings, **1982**, Volume 28, 117-138.

Knott, J.F.

"Fundamentals of fracture mechanics",
Butterworths, London **1976.**

Kroner, E.

Z. Phys, **1958**, 151, 504.

Zyczkowski, M.

"Combined loadings in the theory of plasticity",
Polish scientific publishers, **1981**, 58-62.

Leadbetter, A.J.

" Instrumentation for pulsed sources",
Proceedings of conference on neutron scattering in the nineties, **1985**, Julich, 219-245.

Leffers, T., Lorentzen, T., Jensen, D.J. & Kjems, J.

"Measurement of internal stresses by neutron diffraction using a position sensitive detector",
Proceedings of the international conference on residual stresses, **1986**, Garmisch-Partenkirchen (FRG), 143-150.

Love, A.E.H.

"Treatise on the mathematical theory of elasticity",
1944, New York: Dover

MacEwen, S.R., Faber, J. & Turner, P.L.

"The use of time of flight neutron diffraction to study grain interaction stresses",
Acta metall, **1983**, Vol 31, No 5, 657-676.

MacEwen, S.R., Holden, T.M., Hosbons, R.R. & Cracknell, A.G.

"Residual strains in rolled joints",
Proceedings of ASM's conference on residual stress in design, process and materials selection, **1987**, Ohio (USA), 183-191.

MacGillivray, H.J., Bourke, M.A.M., Webster, G.A., Low, K. & Webster,P.J.

"Recent advances in neutron diffraction residual stress measurements in engineering components"
International conference on advanced measurement techniques, **1987**, BSSM, London.

Macherauch, E. & Kloos, K.H.

"Origin, measurement and evaluation of residual stresses"
Proceedings of the international conference on residual stresses, **1986**, Garmisch-Partenkirchen (FRG), 3-26.

McMeeking, R.M. & Lee, E.H.
"The generation of residual stresses in metal-forming processes"
Sagamore army materials research conference proceedings, **1982**, Volume 28, 315-329.

Mutoh, Y., Fair, G.H., Noble, B. & Waterhouse, R.B.
"The effect of residual stresses induced by shot peening on fatigue crack propagation in two high strength aluminium alloys"
Fatigue fract. engng. mater struct., **1987**, Vol10, No 4., 261-272.

Noyan, I.C. & Cohen, J.B.
"Residual stress - Measurement by diffraction and interpretation"
Springer-Verlag, **1987**.

Priesmeyer, H.G.
"Strain tensor determination using neutron diffraction",
Proceedings of IITT conference on fatigue and stress, **1989**, 234-240.

Pintschovius, L., Jung, V., Macherauch, E., Schafer, R. & Vohringer, O.
"Determination of residual stress distributions in the interior of technical parts by means of neutron diffraction"
Sagamore army materials research conference proceedings, **1982**, Volume 28, 467-482.

Pintschovius, L., Macherauch, E., & Scholtes, B.'
"Determination of residual stresses in autofrettaged steel tubes by neutron and X-ray diffraction"
Proceedings of the international conference on residual stresses, **1986**, Garmisch-Partenkirchen (FRG), 159-165.

Reid, C.N.

"Deformation geometry for materials scientists"
Pergammon Press, **1973**.

Reid, C.N., Moffat, J., & Hermann, R.

"Fatigue crack growth in mild steel under cyclic compressive loads"
ICF7, **1989**, Houston, U.S.A. (D0070).

Reid, C.N., Moffat, J. & Hermann, R.

"Fatigue under compressive loading and residual stress"
Scripta Met, **1988**, Vol 22, No 11, 1743-1748.

Reuss, A.

"Berechnung der fliessgrenze von misch kristallen auf grund der plastizitatsbedingung fur einkristalle",
1924, Z. Angew, Math. mech., 9, 49.

Rooke, D.P. & Cartwright, D.J.

"Compendium of stress intensity factors"
HMSO, **1976**, London

Sayers, C.M.

"The strain distribution in anisotropic polycrystalline aggregates subjected to an external stress field",
Philosophical magazine A, **1984**, Vol49, No.2, 243-262

Sawley, K.J.

"Materials in railway engineering"
Metals and materials, April **1989**, 210-214.

Schilling, C.G. & Blake, G.T.

"Measurement of triaxial residual stresses in railroad rails"
Research report, March **1981**, R-477, United States steel corporation research laboratory.

Smith, D.J., Webster, G.A. & Webster, P.J.
"Measurement of residual stress and the effects of prior deformation using the neutron diffraction technique",
Welding institute research report, **1987**, 338/1987.

Smith, D.J., Legatt, R.H., Webster, G.A., Macgillivray, H.J., Webster, P.J. & Mills, G.
"Neutron diffraction measurements of residual stress and plastic deformation in an aluminium alloy weld"
Journal of strain analysis, **1988**, Vol 23, No 4, 201-211.

Smith, D.J., Bourke, M.A.M., Hodgson, A.P., Webster, G.A. & Webster,P.J.
"Residual stresses in cracked specimens subjected to prior loading"
Welding institute research report, **1989**, 7906.01/88/619.2

Smith, I.J.
"An introduction to WIFES- the welding institute finite element system"
Welding institute research bulletin, **1981**, 22 (5).

Sorem, Jr.J.R., Shadley, J.R. & Rybicki, E.F.
"Experimental method for determining through thickness residual stresses in thin walled pipes and tubes without inside access"
Strain, February **1990**, 7-14.

Stacey, A. & Webster, G.A.
"Fatigue crack growth in autofrettaged thick walled high pressure tube material"
High pressure in science and technology, **1984**, Mat. res. soc. symp. proc., Part III, Vol. 22, 215-219.

Stacey, A., MacGillivray, H.J., Webster, G.A., Webster, P.J. & Ziebeck,K.R.A.
"Measurement of residual stresses by neutron diffraction"
Journal of strain analysis, **1985a**, Vol. 20, No 2, 93-100.

Stacey, A.

"Prediction of fatigue crack growth in thick walled tubing"
PhD Thesis, **1985b**, University of London

Stone, D.H.

"Problems with residual stress in the railroad industry"
Sagamore army materials research conference proceedings,
1982, Volume 28, 341-353.

Swe-den Tsai, Schmerling, M. & Marcus, H.L.

"Residual stress measurement in metal matrix composites",
Sagamore army materials research conference proceedings,
1982, Volume 28, 425-438.

Theiner, W.A.,Brinksmeier, E., Stucker, E., & Nowack, H.

"Stress measurements on components with nondestructive ferromagnetic methods",
Proceedings of the international conference on residual stresses, **1986**, Garmisch-Partenkirchen (FRG), 167-174.

Tyler, D.

"Shot peening adds strength to component design"
Engineering materials and design, **1987**, 29-30.

Voigt, W.

"Lehrbuch der kristallphysik",
Leipzig: Teubner, **1928**, p962.

Von Dreele, R.B., Jorgensen, J.D. & Windsor, C.G.

"Rietveld refinement with spallation neutron powder diffraction data"
Journal of applied crystallography, **1982**, 15, 581-589.

Watson, J.O.

"Hermitian cubic boundary elements for plane problems of fracture mechanics"
Res. Mechanica., **1982**, No4, 23-42.

Webster, G.A., Klintworth, G.C. & Stacey, A.
"Stress intensity factors for cracked C-shaped and ring type test-pieces"
Journal of strain analysis, **1983**, Vol 18, No 4, 225-230.

Webster, G.A.
"Propagation of fatigue cracks through residual stress fields"
Fatigue and stress in materials and engineering, **1989**, pbld by IITT international.

Webster, G.A., Bourke, M.A.M., MacGillivray, H.J., Webster, P.J., Low,K.S., Cannon, D.F & Allen, R.J.
"Measurement of residual stresses in railway rails"
Proceedings of the international conference on residual stresses, **1989b**, Nancy (1988), pbld by Elsevier, 203-208.

Webster, P.J.
"Measurements on railway rail sections in 1989"
Report BRSCUIC01/89, **1990**.

Withers, P.J., Jensen, D.J., Lilholt, H. & Stobbs, W.M.
"The evaluation of internal stresses in a short fibre metal matrix composite by neutron diffraction",
Proc. ICCM, **1987**, 6,2,255.

Windsor, C.G.
"Experimental techniques"
Methods of experimental physics, **1986**, Vol 23, Part A, 197-257

Wohlfahrt, H.
"Shot peening and residual stresses"
Sagamore army materials research conference proceedings, **1982**, Volume 28, 71-92.

Zyczkowski, M

c.f P 235